Distribution Agreement

In presenting this thesis or dissertation as a partial fulfillment of the requirements for an advanced degree from Emory University, I hereby grant to Emory University and its agents the non-exclusive license to archive, make accessible, and display my thesis or dissertation in whole or in part in all forms of media, now or hereafter known, including display on the world wide web. I understand that I may select some access restrictions as part of the online submission of this thesis or dissertation. I retain all ownership rights to the copyright of the thesis or dissertation. I also retain the right to use in future works (such as articles or books) all or part of this thesis or dissertation.

Signature:

_____ _____

Dexter Myrick Date

The role of the histone demethylase LSD1 in hippocampal neuron survival and tau-mediated neurodegeneration.

By

Dexter Myrick
Doctor of Philosophy

Graduate Division of Biological and Biomedical Science
Neuroscience

_____
David J. Katz, PhD
Advisor

_____
Gary Bassell, PhD
Committee Member

_____
Victor Faundez, PhD
Committee Member

_____
James Lah, PhD
Committee Member

_____
Victor Corces, PhD
Committee Member

Accepted:

_____
Kimberly Jacob Arriola, Ph.D, MPH
Dean of the James T. Laney School of Graduate Studies

_____
Date

The role of the histone demethylase LSD1 in hippocampal neuron survival and tau-mediated neurodegeneration

By

Dexter Myrick
B.S., Emory University, 2010

Advisor: David J. Katz, PhD

An abstract of the role of the histone demethylase LSD1 in hippocampal neuron survival and tau-mediated neurodegeneration

A dissertation submitted to the Faculty of the
James T. Laney School of Graduate Studies of Emory University
in partial fulfillment of the requirements for the degree of
Doctor of Philosophy
in Graduate Division of Biological and Biomedical Sciences, Neuroscience
2020

Abstract

The role of the histone demethylase LSD1 in hippocampal neuron survival and tau-mediated neurodegeneration

By Dexter Myrick

We inducibly deleted the histone demethylase LSD1 in adult mice initially to investiagte mechanisms that maintained cell fate fully differentiated cells. We found that the loss of LSD1 led to transcriptional changes such as the reactivation of stem cell genes. Furthermore, we oberved transcriptional changes in common neurodegenerative pathways and substantial neurodegeneration of the hippocampus and cortex. These mice also displayed significant defects in learning and memory tasks. In adddition to this, all $Lsd1^{CAGG}$ mice eventually develop progressive hind-limb paralysis and expire prematurely. Here we have chosen to focus on hippocampal neuronal cell death and the potential link to human neurodegenerative disease. In addition to transcriptional changes that implicated potentially shared neurodegenerative pathways with AD and FTD, we find that LSD1 is mislocalized to pathological protein aggregates in these human cases. This raised the possibility that pathological protein aggregates such as hyperphosphorlated TAU could compromise the functions of LSD1. To investiagte this possibility, we utilized the P301S tauopathy mouse model to demonstrate that pathological tau can exclude LSD1 from the nucleus in neurons. Furthermore, we performed experiments in which we both reduced and increased the expression of LSD1 in P301S mice. The reduction of LSD1 highly exacerbated tau-mediated neurodegeneration and overexpression was sufficient to significantly delay neurodegeneration, even after the formation of TAU pathology. Taken together, these data suggest that the colocalization of LSD1 and TAU protein contributes to tau-mediated neurodegeneration via nuclear sequestration of LSD1.

The role of the histone demethylase LSD1 in hippocampal neuron survival and tau-mediated neurodegeneration

By

Dexter Myrick
B.S., Emory University, 2010

Advisor: David J. Katz, PhD

A dissertation submitted to the Faculty of the
James T. Laney School of Graduate Studies of Emory University
in partial fulfillment of the requirements for the degree of
Doctor of Philosophy
in Graduate Division of Biological and Biomedical Sciences, Neuroscience
2020

Acknowledgments

I would like to formally acknowledge and thank all those that made this dissertation possible. Starting with my mentor and advisor Dr. David Katz. Dave's mentorship and guidance has been essential to my PhD journey. The training and mentorship I have recieved has always gone above and beyond. Thank you for always beleiving in me and providing a research environment that fosters highly innovative and multidisciplinary science. And thank you again for your unwavering commitment to my success.

I would also like to thank the memebers my thesis committee (Dr. Gary Bassell, Dr. Victor Corces, Dr. Victor Faundez and Dr. James Lah) which have all provided invaluable guidance over the years. Your investment in my training, encouragment and intellectual contributions have been critical to my development as a scientist and all my accomplishments. I would like to specially thank Dr. Bassell for his encouragement and advice during the admissions process and always being in my corner. I would also like to thank Dr. Lah for his continued support of me and wife going all the way back to our undergraduate days, Dr. Corces for much needed guidance and expertise with ChIP experiments and bionformatics, and Dr. Faundez for always providing the support and encourgament I needed even at the darkest of times.

I am also very grateful to the entire Katz lab (current and past members). You guys are like my second dysfunctional family and I don't know what I would have done without you. In addition to providing a source of inspiration and technical advice, lab life was always fun and light-hearted. I would like to specifically thank Dr. Jadiel Wasson, Dr. Michael Christopher, Amanda Engstrom and Juan Rodriguez for the oppurtunity to work closely together and collaborate on some great projects. I also want to specially thank Dr. Ernest Ricks, Dr. Brandon

Carpenter for their invaluable friendship and support both personally and scientifically. I seriously couldn't have done it without you guys. I would also like to profusely thank the future Dr. Alyssa Scott for absolutely nothing.

My family has also been a critical part of my graduate school journey. My parents always instilled in me the value of hard work and education. Furthermore, their love, support and words of encouragement have always meant the world to me. You guys always supported my goals regardless of what they were and I love you both immensely. I wouldn't be the man I am today without you. Last but not least, I would like to thank my wife, Leila, and my two children, Arianna and Dexter III. You brighten my spirits after a hard day and you are always there to encourage and belive in me, even when I'm not believing in myself. Leila, you are my best friend and my everything and I dedicate this entire dissertation to you for all your relentless love and support. And please don't let Arianna call it "Daddy's sad book".

Table of Contents

List of Figures and Tables

Chapter 1

Chapter 2

Chapter 3

Chapter 4

Chapter 5

Appendix A

Chapter 1. Introduction and Background

1.1 Epigenetic transcriptional regulation

Epigenetic transcriptional regulation is critical to maintaining normal cell-specific gene expression in both senescent and actively dividing cells, including stem cells (1–4). Epigenetics can broadly be described as any genetic factor that influences gene expression in the absence of DNA sequence alteration. For example, post-translational modification of the amino-terminal tail of the histone can profoundly affect gene transcription (4). In the nucleus, DNA is packaged into nucleosomes forming chromatin. Nucleosomes contain histone protein octamers, which consist of dimers of the 4 histone proteins (H2A, H2B, H3, H4) (5).These N-terminal histone tails can be post-translationally modified in a myriad of ways, such as methylation, phosphorylation, acetylation and ubiquitylation (6). Here we will focus on the methylation of lysine residues on H3 N-terminal tails.

Histone methylation can consist of the addition of one, two or three methyl groups. The consequence of these modifications is varied and heavily depends on many other factors, such as distance from distinct genomic features (promoters, enhancers), the number of methyl groups and cell type (6). Unlike histone acetylation, which is exclusively correlated with euchromatin and active gene transcription (7, 8). In contrast, methylation of lysine 9 on histone H3 (H3K9me) is highly correlated with heterochromatin and the repression of transcription and methylation of lysine 4 on histone H3 (H3K4me) is correlated with active transcriptional states (9–11). Furthermore, studies have illustrated that H3K4me accumulates in gene bodies during active transcription and at enhancers that regulate tissue specific transcription (11). Based on this data, it has been postulated that H3K4me2 may establish a transcriptional memory to maintain patterns of transcription through cell division (12). This epigenetic signature may also play a critical role in maintaining normal cell-specific transcription in non-dividing cells, such as

neurons (Chapter 2) (13, 14). Moreover, these histone modifications are quite dynamic and can be added and removed by chromatin modifying enzymes to regulate transcription. For example, histone acetyltransferases (HATs) and methyltransferases (KMTs) add acetyl and methyl groups, respectively, onto N-terminal histone tails and histone deacetylases (HDACs) and demethylases (KDMs) remove these acetyl and methyl groups (15–17).

1.2 Lysine specific demethylase 1 (KDM1A/LSD1)

There are two distinct classes of histone demethylases. One being a large a family of jumanji proteins (which possess a JmjC domain) that removes tri-methylation from lysine residues. The other being amine-oxidase demethylases, of which there are only two, remove mono- and di-methylation (16, 17). These two enzymes are KDM1A (hereafter referred to as LSD1) and KDM1B (LSD2). To reiterate, LSD1 is an amine oxidase histone demethylase that in conjunction with CoREST removes mono- and di- histone methylation and will be the main focus this dissertation(17, 18).

LSD1 can function as an activator or repressor of transcription depending on the complex it interacts with in a cell-type specific manner. However, LSD1 canonically functions as a repressor of transcription by removing H3K4me that is associated with actively transcribed genes. LSD1 was discovered in association with the CoREST complex, which consists of scaffolding proteins and the histone deacetylases HDAC1 and HDAC2. Since LSD1 prefers hypoacetylated substrates, it is often in complex with HDACS (19, 20). Additionally, LSD1 alone cannot demethylate histone substrates. For example, association with RCOR1 within the CoREST complex is necessary for LSD1 demethylase activity. The CoREST complex has been shown to be critical for repressing the expression of neuronal genes in non-neuronal cell lineages (18, 20, 21)Further suggesting that LSD1 may play a critical role in the epigenetic regulation of cell-type specific transcription.

Additionally, LSD1 also functions as a repressor in the nucleosome remodeling and deacetylase (NuRD) complex. This complex contains many proteins, including HDACs and nucleosome remodelers. Targets of the NuRD complex include pathways involved with cell signaling, proliferation, and the epithelial-to-mesenchymal transition (21, 22). In association with the androgen receptor (AR) complex, LSD1 can also act as a transcriptional activator. In this context, LSD1 removes canonically repressive di-methylation of histone H3 on lysine 9 (H3K9me) in order to activate androgen receptor-responsive genes (23).

While LSD1's most characterized function is demethylating histones, it has also been described to demethylate non-histone targets. These proteins include p53, DNMT1, STAT3, and several others (24). By demethylating these targets, LSD1 has been shown to affect the stability and function of these proteins. The possibility of LSD1 interacting with non-histone proteins broadens the scope of potential LSD1 functions in the cell. LSD1 function can also be regulated by a microRNA, miR-137, in a regulatory feedback loop with TLX. miR-137 targets LSD1 mRNA for downregulation in neuroblastoma cells and cancer (25, 26). Together with TLX, LSD1 represses the expression of miR-137 (27).

1.2.1 Structure/Domains

LSD1 is a flavin-dependent monoamine oxidase histone demethylase. The overall structure of LSD1 closely resembles other flavin-dependent oxidases but it contains unique features that facilitate binding of nucleosome substrates and its complex members (17, 28, 29). Biochemical studies have illustrated that the structure of LSD1 contains three distinct domains. Additionally, there is an N-terminal unstructured domain of which not much is known about its function. The recombinant protein used in all biochemical analyses contains an N-terminal deletion (residues 172-833) of this unstructured domain (30). Presumably, because it is not

necessary for LSD1 complex formation or demethylation activity *in vitro* and the exclusion of the unstructured domain significantly impacts the solubility of the protein (31). Hereafter it can be assumed that LSD1 protein used in any structural study contains this N-terminal deletion.

LSD1 contains one SWIRM domain, two Amine oxidase (AOL) domains and a Tower domain. The SWIRM domain is frequently found associated with chromatin remodeling proteins. It is believed that, in general, SWIRM domains mediate the interaction between chromatin and protein complexes (28, 29). However, it is not completely clear what its role is in the structure of LSD1. Interestingly, separate preparations of the AOL and Tower domains do not yield any soluble protein without SWIRM domain present. Providing evidence that the domain confers some increased stability (29). Furthermore, in contrast to the general function of the SWIRM domain, within the structure of LSD1-CoREST complex bound to a nucleosome it is located too far away from both histones and extranucleosomal DNA to have any interaction (28).

AOL domains, in general, catalyze the oxidation of amines, polyamines, amino acids and methylated lysine side chains. AOL domains all also contain a FAD-binding motif/subdomain and a substrate-binding subdomain. Together these two subdomains create a cavity between them. This is referred to as the catalytic center of the structure. A distinct feature of the LSD1 catalytic center is the addition of a highly acidic surface near its entrance which facilitates interactions with the N-terminal tail of histone H3 (28).The Tower domain is an antiparallel coiled coil which protrudes out from the catalytic center without interacting with any other structural regions. The Tower domain is required for LSD1 protein to bind to the CoREST complex. The Sant2 domain present in CoREST is also necessary for the interaction to occur. Thus, the Tower domain is critical to the demethylase activity of LSD1 (28).

1.2.2 Biological roles

LSD1 is absolutely critical for development as evidenced by the knockout mouse phenotype. These mice arrest at e5.5 and fail to properly elongate the egg cylinder (21, 32). LSD1 ablation also has developmental phenotypes in yeast, arabadopsis, drosophila, C. Elegans and recently human patients (33–38). LSD1 is also critical for olfactory receptor choice in olfactory sensory neurons and regulation of circadian rhythms (39, 40). However, LSD1 most widely known for its critical role in stem cell differentiation (1–3, 21, 35, 41). Conditional loss of LSD1 has been demonstrated to disrupt plasma cell, hematopoietic stem cell, neural stem cell (NSC) and embryonic stem cell (ESC) differentiation *in vitro* (1, 2, 42). LSD1 must be poised at the enhancers of stem cells genes, such as Oct4, for normal ESC differentiation to occur. However, LSD1 is not required for survival of ESCs (2). LSD1 has also been shown to be critical for hematopoietic and trophoblast stem cells *in vivo* (1, 3). In contrast to this, LSD1 was also identified in a genetic screen as a neuroprotective agent and more recently several de novo LSD1 mutations were discovered in human patients exhibiting severe developmental delay (34, 43).

1.2.3 Germline

Additionally, the Katz lab has shown that LSD1 is essential for the switch from maternal to zygotic transcription in 2 cell embryos and maintenance and differentiation of spermatogonia stem cells (SSCs) in juvenile mice (Appendix A)(44, 45). In female mice, complete loss of LSD1 maternally causes embryonic lethality with complete arrest at the 1-2 cell embryonic stage. However, partial loss of LSD1 lead to alterations in DNA methylation status and expression of imprinted genes, such as Zac1 and Impact. We also observed perinatal lethality and abnormal behavior in adults. These abnormal behaviors included excessive digging and food harassing

behavior (45). In male mice, LSD1 is required to establish the male germline and ultimately produce spermatozoa. Furthermore, conditional deletion of LSD1 in the adult male testis lead to abnormal accumulation of meiotic spermatocytes, apoptosis and progressive germ cell loss (Appendix A). LSD1 is also a regulator of the classic stem cell gene, OCT4, in the mouse testis. In adult LSD1 mutant testis, OCT4 expression is inappropriately maintained in differentiating spermatocytes. Taken together, these data further suggest that H3K4me can act as a form of transcriptional memory and LSD1 is critical for the regulation of cell fate decisions (12, 44, 46).

1.2.4 Neural stem cells

We have also demonstrated that LSD1 is critical for neural stem cell differentiation (NSC) proliferation during development (Myrick, unpublished). Previous work demonstrated that LSD1 is expressed in NSCs and that following the administration of the LSD1 inhibitor, pargyline, NSC proliferation was significantly reduced *in vitro* (42). In order to elucidate the role of LSD1 in NSC's *in vivo*, LSD1 was conditionally deleted in NESTIN expressing radial glia (neural progenitor cells) by embryonic day 12.5 (e12.5). NESTIN is expressed in both early neural progenitors and adult neural stem cells (47). Interestingly, mice were born at the expected Mendelian frequency but no mutant mice survive to weaning age indicating 100% perinatal lethality. At birth they are significantly smaller than control littermates. By 8 days post-partum (8dpp) this size difference persists and mutants exhibit psychomotor defects such as star gazing. The oldest mutants ever observed were 12dpp but most expired by 8dpp. At this time point, we also observed ventricular expansion indicating significant loss of brain tissue (Myrick, unpublished).

To further investigate, we chose to focus on the specification of the motor neuron lineage. To accomplish this, primary motor neurons (pMN) were isolated from e13.5 LSD1 mutant and

control embryos and cultured for 3-5 days. Preliminary results suggest that there is significantly greater expression of NESTIN in LSD1 mutant motor neurons by quantitative PCR (qPCR) and immunofluorescence (Myrick, unpublished). Furthermore, we also observed significantly increased expression of the classic stem cell gene, *Sox2*, in these motor neurons. To investigate potential consequences of aberrant expression of stem cell genes in motor neurons, we performed electromyography (EMG) on the gastrocnemius (Gast) and tibialis anterior (TA) muscles of LSD1 mutant mice 10-12dpp. Evoked potentials were significantly lower (4-fold) in LSD1 mutants and latency was significantly increased (4-fold). Taken together, these preliminary data suggest that LSD1 is critical for normal neuronal progenitor differentiation and to repress the expression of critical stem cell genes *Nestin* and *Sox2* in differentiated motor neurons (Myrick, unpublished).

1.2.5 Alternative splicing

LSD1 function can also be altered through alternative splicing (48). LSD1 can be alternatively spliced to include a 60nt exon in intron 2 (E2a) or 12nt exon in intron 8 (E8a). While canonical LSD1 and LSD1+E2a are expressed ubiquitously, LSD1 +E8a (hereafter referred to as LSD1n) expression is neuronal specific. Furthermore, LSD1n has been reported to demethylate H3K9me1/2 when in complex with supervillin (SVL). However, LSD1n when associated with CoREST, will demethylate mono- and di-methly groups on histone H4 at lysine 20 (H4K20me1/2) (49, 50). Knockdown of LSD1n *in vitro* inhibits neurite morphogenesis, while overexpression increases neurite morphogenesis, suggesting a role for this isoform in neuronal development (48). Mice with deletion of LSD1n are viable, unlike the full LSD1 deletion. However, these animals show an impairment in spatial learning and memory (21, 32, 50). Collectively, LSD1's function as an activator or repressor is highly dependent on the cell-type

and complex it is associated with, as well as regulation of its transcription and translation (51). While LSD1 function is quite diverse, the theme remains that LSD1 plays a critical role in transcriptional regulation related to the maintenance and/or determination of cell fate.

1.3 LSD1 and Neurodegeneration.

Comparatively little is known about how LSD1 functions in fully differentiated cells. However, early studies demonstrating that the LSD1 complex, CoREST, is involved in the maintenance of cell fate by repressing transcription of neuronal genes in non-neuronal lineages and evidence of neuronal specific isoforms of LSD1 led us to hypothesize that LSD1 may play a role in the maintenance of adult differentiated neurons (18, 50). To address this possibility, we deleted LSD1 in the adult mouse brain (hereafter referred to as $Lsd1^{CAGG}$) using an inducible Cre/Lox genetic system. In $Lsd1^{CAGG}$ mice we observed massive neuronal cell death throughout the brain, especially in the hippocampus (Chapter 2). In addition to neuronal cell death, we also observed significant learning and memory defects. We then used genome-wide RNA-sequencing to further investigate LSD1 transcriptional regulation in the context of neurodegeneration. When comparing the hippocampus transcriptomes of $Lsd1^{CAGG}$ and littermate controls, we observed significant transcriptional dysregulation and even the evidence of inappropriate re-activation of stem cell transcription (Chapter 2). After comparing our dataset to existing human disease datasets in an unbiased fashion, we discovered that it most resembled a recent human study analyzing over 1500 late-onset Alzheimer's Disease (AD) patients (Chapter 2) (52). More specifically, our dataset indicated changes in key genetic modules in common with the Humphries et al. study: immune activation and oxidative phosphorylation. Furthermore, we found that LSD1 colocalized with hyperphosphorylated tau aggregates in human AD patients and TDP-43 inclusions in frontotemporal dementia (FTD) patients (Chapter 2) (53). To our

knowledge, this study provided the first experimental evidence linking LSD1 with human neurodegeneration.

Alzheimer's disease (AD) is characterized by progressive memory loss and significant cognitive decline caused by massive neuronal cell death in the hippocampus, temporal and frontal cortices. Postmortem analysis of human AD patients demonstrates significant reductions in brain volume, extracellular deposits of aggregated amyloid (amyloid plaques), and intracellular deposits of aggregated tau protein (neurofibrillary tangles) (54–57). The association of these pathological protein deposits with dementia led researchers to develop the β-amyloid hypothesis, according to which the buildup of pathological species of β-amyloid disrupts normal neuronal function (54, 55). Furthermore, pathological β-amyloid may interact with tau and cause excessive tau phosphorylation and aggregation (58). Tau is a microtubule-associated protein that is critical for the stabilization of microtubules in neurons (59). Recently, it has been reported that the presence of neurofibrillary tangles (NFTs) more closely relates to severity of cognitive decline in AD than β-amyloid (60–64). This association between NFT burden and cognitive decline suggests that tau pathology may potentially be more closely linked to the mechanism of neuronal cell death in AD.

Given the critical role that LSD1 plays in neuronal survival and our observation that LSD1 protein was mislocalized to cytoplasmic neurofibrillary tangles but not amyloid beta (Aβ) plaques in human AD cases, we hypothesized that the nuclear function of LSD1 in neurons could be disrupted by mislocalization to pathological tau aggregates. The PS19 P301S tauopathy mouse model was used to study how LSD1 may contribute to tau-mediated neurodegeneration (hereafter referred to as PS19 Tau). PS19 Tau mice exhibit a P301S mutant variant of human tau protein, which was first discovered in a patient with frontotemporal dementia with parkinsonism

(FTDP-17), which is controlled by the prion promoter throughout the nervous system (65). Without the presence of Aβ plaques, the P301S tau protein is prone to hyperphosphorylation and somatodendritic aggregation when produced in mice. PS19 Tau mice have a high pathological tau load and have been extensively studied for tau pathology development and disease-related characteristics (66, 67). However, the mechanism of pathogenic tau-induced neuronal cell death is still unknown.

The suppression of LSD1 activity leads to tau-induced neurodegeneration, according to functional evidence presented here. We showed that pathogenic tau sequesters LSD1 in the cytoplasm of neurons throughout the brain in PS19 Tau mice. LSD1 is depleted from the nucleus as a result of this. We also present genetic and molecular evidence that pathogenic tau disrupts LSD1 and thereby leads to neurodegeneration. Finally, we show that overexpressing LSD1 in hippocampal neurons is sufficient to prevent neuronal cell death even after the formation of pathogenic tau. Pathological tau, we believe, leads to neuronal cell death by sequestering LSD1 in the cytoplasm, thereby diminishing the nuclear reserve of LSD1 essential for neuronal survival.

1.4 References

1. M. A. Kerenyi, *et al.*, Histone demethylase Lsd1 represses hematopoietic stem and progenitor cell signatures during blood cell maturation. *Elife* 2, e00633 (2013).

2. W. A. Whyte, *et al.*, Enhancer decommissioning by LSD1 during embryonic stem cell differentiation. *Nature* 482, 221–225 (2012).

3. D. Zhu, *et al.*, Lysine-specific demethylase 1 regulates differentiation onset and migration of trophoblast stem cells. *Nat Commun* 5, 3174 (2014).

4. T. Kouzarides, Chromatin Modifications and Their Function. *Cell* 128, 693–705 (2007).

5. T. Jenuwein, C. D. Allis, Translating the Histone Code. *Science* 293, 1074–1080 (2001).

6. B. D. Strahl, C. D. Allis, The language of covalent histone modifications. *Nature* 403, 41–45 (2000).

7. A. L. Clayton, T. R. Hebbes, A. W. Thorne, C. Crane-Robinson, Histone acetylation and gene induction in human cells. *Febs Lett* 336, 23–26 (1993).

8. B. G. Pogo, V. G. Allfrey, A. E. Mirsky, RNA synthesis and histone acetylation during the course of gene activation in lymphocytes. *Proc National Acad Sci* 55, 805–812 (1966).

9. A. J. Bannister, *et al.*, Selective recognition of methylated lysine 9 on histone H3 by the HP1 chromo domain. *Nature* 410, 120–124 (2001).

10. T. S. Mikkelsen, *et al.*, Genome-wide maps of chromatin state in pluripotent and lineage-committed cells. *Nature* 448, 553–560 (2007).

11. H. Santos-Rosa, *et al.*, Active genes are tri-methylated at K4 of histone H3. *Nature* 419, 407–411 (2002).

12. S. C. Kerr, C. C. Ruppersburg, J. W. Francis, D. J. Katz, SPR-5 and MET-2 function cooperatively to reestablish an epigenetic ground state during passage through the germ line. *Proc National Acad Sci* 111, 9509–9514 (2014).

13. N. Ballas, *et al.*, Regulation of Neuronal Traits by a Novel Transcriptional Complex. *Neuron* 31, 353–365 (2001).

14. J. A. Chong, *et al.*, REST: A mammalian silencer protein that restricts sodium channel gene expression to neurons. *Cell* 80, 949–957 (1995).

15. K. Struhl, Histone acetylation and transcriptional regulatory mechanisms. *Gene Dev* 12, 599–606 (1998).

16. Y. Tsukada, *et al.*, Histone demethylation by a family of JmjC domain-containing proteins. *Nature* 439, 811–816 (2006).

17. Y. Shi, *et al.*, Histone Demethylation Mediated by the Nuclear Amine Oxidase Homolog LSD1. *Cell* 119, 941–953 (2004).

18. A. You, J. K. Tong, C. M. Grozinger, S. L. Schreiber, CoREST is an integral component of the CoREST- human histone deacetylase complex. *Proc National Acad Sci* 98, 1454–1458 (2001).

19. F. Forneris, C. Binda, M. Vanoni, A. Mattevi, E. Battagliol, 8 Demethylation pathways for histone methyllysine residues. *Enzym* 24, 229–242 (2006).

20. Y.-J. Shi, *et al.*, Regulation of LSD1 Histone Demethylase Activity by Its Associated Factors. *Mol Cell* 19, 857–864 (2005).

21. J. Wang, *et al.*, Opposing LSD1 complexes function in developmental gene activation and repression programmes. *Nature* 446, 882–887 (2007).

22. D. Patel, A. Shimomura, S. Majumdar, M. C. Holley, E. Hashino, The histone demethylase LSD1 regulates inner ear progenitor differentiation through interactions with Pax2 and the NuRD repressor complex. *Plos One* 13, e0191689 (2018).

23. E. Metzger, *et al.*, LSD1 demethylates repressive histone marks to promote androgen-receptor-dependent transcription. *Nature* 437, 436–439 (2005).

24. S. Amente, L. Lania, B. Majello, The histone LSD1 demethylase in stemness and cancer transcription programs. *Biochimica Et Biophysica Acta Bba - Gene Regul Mech* 1829, 981–986 (2013).

25. K. Althoff, *et al.*, MiR-137 functions as a tumor suppressor in neuroblastoma by downregulating KDM1A. *Int J Cancer* 133, 1064–1073 (2013).

26. F. Balaguer, *et al.*, Epigenetic Silencing of miR-137 Is an Early Event in Colorectal Carcinogenesis. *Cancer Res* 70, 6609–6618 (2010).

27. G. Sun, *et al.*, miR-137 forms a regulatory loop with nuclear receptor TLX and LSD1 in neural stem cells. *Nat Commun* 2, 529 (2011).

28. S.-A. Kim, J. Zhu, N. Yennawar, P. Eek, S. Tan, Crystal Structure of the LSD1/CoREST Histone Demethylase Bound to Its Nucleosome Substrate. *Mol Cell* 78, 903-914.e4 (2020).

29. Y. Chen, *et al.*, Crystal structure of human histone lysine-specific demethylase 1 (LSD1). *Proc National Acad Sci* 103, 13956–13961 (2006).

30. M. Yang, *et al.*, Structural Basis for CoREST-Dependent Demethylation of Nucleosomes by the Human LSD1 Histone Demethylase. *Mol Cell* 23, 377–387 (2006).

31. V. Uversky, Amyloidogenesis of Natively Unfolded Proteins. *Curr Alzheimer Res* 5, 260–287 (2008).

32. J. Wang, *et al.*, The lysine demethylase LSD1 (KDM1) is required for maintenance of global DNA methylation. *Nat Genet* 41, 125–129 (2009).

33. D. J. Katz, T. M. Edwards, V. Reinke, W. G. Kelly, A C. elegans LSD1 Demethylase Contributes to Germline Immortality by Reprogramming Epigenetic Memory. *Cell* 137, 308–320 (2009).

34. S. Pilotto, *et al.*, LSD1/KDM1A mutations associated to a newly described form of intellectual disability impair demethylase activity and binding to transcription factors. *Hum Mol Genet* 25, 2578–2587 (2016).

35. S.-T. Su, *et al.*, Involvement of Histone Demethylase LSD1 in Blimp-1-Mediated Gene Repression during Plasma Cell Differentiation. *Mol Cell Biol* 29, 1421–1431 (2009).

36. D. Jiang, W. Yang, Y. He, R. M. Amasino, Arabidopsis Relatives of the Human Lysine-Specific Demethylase1 Repress the Expression of FWA and FLOWERING LOCUS C and Thus Promote the Floral Transition. *Plant Cell* 19, 2975–2987 (2007).

37. T. Rudolph, *et al.*, Heterochromatin Formation in Drosophila Is Initiated through Active Removal of H3K4 Methylation by the LSD1 Homolog SU(VAR)3-3. *Mol Cell* 26, 103–115 (2007).

38. L. D. Stefano, J.-Y. Ji, N.-S. Moon, A. Herr, N. Dyson, Mutation of Drosophila Lsd1 Disrupts H3-K4 Methylation, Resulting in Tissue-Specific Defects during Development. *Curr Biol* 17, 808–812 (2007).

39. D. B. Lyons, *et al.*, An Epigenetic Trap Stabilizes Singular Olfactory Receptor Expression. *Cell* 154, 325–336 (2013).

40. H. J. Nam, *et al.*, Phosphorylation of LSD1 by PKCα Is Crucial for Circadian Rhythmicity and Phase Resetting. *Mol Cell* 53, 791–805 (2014).

41. S. Saleque, J. Kim, H. M. Rooke, S. H. Orkin, Epigenetic Regulation of Hematopoietic Differentiation by Gfi-1 and Gfi-1b Is Mediated by the Cofactors CoREST and LSD1. *Mol Cell* 27, 562–572 (2007).

42. G. Sun, *et al.*, Histone Demethylase LSD1 Regulates Neural Stem Cell Proliferation. *Mol Cell Biol* 30, 1997–2005 (2010).

43. C. Dai, *et al.*, Functional Identification of Neuroprotective Molecules. *Plos One* 5, e15008 (2010).

44. D. A. Myrick, *et al.*, KDM1A/LSD1 regulates the differentiation and maintenance of spermatogonia in mice. *Plos One* 12, e0177473 (2017).

45. J. A. Wasson, *et al.*, Maternally provided LSD1/KDM1A enables the maternal-to-zygotic transition and prevents defects that manifest postnatally. *Elife* 5, e08848 (2016).

46. B. S. Carpenter, *et al.*, Caenorhabditis elegans establishes germline versus soma by balancing inherited histone methylation. *Development* 148, dev196600 (2021).

47. J. Dahlstrand, M. Lardelli, U. Lendahl, Nestin mRNA expression correlates with the central nervous system progenitor cell state in many, but not all, regions of developing central nervous system. *Dev Brain Res* 84, 109–129 (1995).

48. C. Zibetti, *et al.*, Alternative Splicing of the Histone Demethylase LSD1/KDM1 Contributes to the Modulation of Neurite Morphogenesis in the Mammalian Nervous System. *J Neurosci* 30, 2521–2532 (2010).

49. B. Laurent, *et al.*, A Specific LSD1/KDM1A Isoform Regulates Neuronal Differentiation through H3K9 Demethylation. *Mol Cell* 57, 957–970 (2015).

50. J. Wang, *et al.*, LSD1n is a H4K20 demethylase regulating memory formation via transcriptional elongation control. *Nat Neurosci* 18, 1256–1264 (2015).

51. C. Martinez-Gamero, S. Malla, F. Aguilo, LSD1: Expanding Functions in Stem Cells and Differentiation. *Cells* 10, 3252 (2021).

52. B. Zhang, *et al.*, Integrated Systems Approach Identifies Genetic Nodes and Networks in Late-Onset Alzheimer's Disease. *Cell* 153, 707–720 (2013).

53. A. S. Chen-Plotkin, *et al.*, Variations in the progranulin gene affect global gene expression in frontotemporal lobar degeneration. *Hum Mol Genet* 17, 1349–1362 (2008).

54. J. Hardy, D. J. Selkoe, The Amyloid Hypothesis of Alzheimer's Disease: Progress and Problems on the Road to Therapeutics. *Science* 297, 353–356 (2002).

55. S. H. Barage, K. D. Sonawane, Amyloid cascade hypothesis: Pathogenesis and therapeutic strategies in Alzheimer's disease. *Neuropeptides* 52, 1–18 (2015).

56. G. S. Bloom, Amyloid-β and Tau: The Trigger and Bullet in Alzheimer Disease Pathogenesis. *Jama Neurol* 71, 505–508 (2014).

57. C. Duyckaerts, B. Delatour, M.-C. Potier, Classification and basic pathology of Alzheimer disease. *Acta Neuropathol* 118, 5–36 (2009).

58. Z. He, *et al.*, Amyloid-β plaques enhance Alzheimer's brain tau-seeded pathologies by facilitating neuritic plaque tau aggregation. *Nat Med* 24, 29–38 (2018).

59. Y. Wang, E. Mandelkow, Tau in physiology and pathology. *Nat Rev Neurosci* 17, 22–35 (2016).

60. A. Bejanin, *et al.*, Tau pathology and neurodegeneration contribute to cognitive impairment in Alzheimer's disease. *Brain* 140, 3286–3300 (2017).

61. N. Okamura, K. Yanai, Applications of tau PET imaging. *Nat Rev Neurol* 13, 197–198 (2017).

62. R. F. Buckley, *et al.*, Region-Specific Association of Subjective Cognitive Decline With Tauopathy Independent of Global β-Amyloid Burden. *Jama Neurol* 74, 1455 (2017).

63. H. Braak, K. D. Tredici, Are cases with tau pathology occurring in the absence of Aβ deposits part of the AD-related pathological process? *Acta Neuropathol* 128, 767–772 (2014).

64. K. A. Johnson, *et al.*, Tau positron emission tomographic imaging in aging and early Alzheimer disease. *Ann Neurol* 79, 110–119 (2016).

65. Y. Yoshiyama, *et al.*, Synapse Loss and Microglial Activation Precede Tangles in a P301S Tauopathy Mouse Model. *Neuron* 53, 337–351 (2007).

66. M. Iba, *et al.*, Tau pathology spread in PS19 tau transgenic mice following locus coeruleus (LC) injections of synthetic tau fibrils is determined by the LC's afferent and efferent connections. *Acta Neuropathol* 130, 349–362 (2015).

67. A. Bellucci, *et al.*, Induction of Inflammatory Mediators and Microglial Activation in Mice Transgenic for Mutant Human P301S Tau Protein. *Am J Pathology* 165, 1643–1652 (2004).

Chapter 2. LSD1 protects against hippocampal and cortical neurodegeneration

Adapted from Michael A. Christopher***, Dexter A. Myrick*** Benjamin G. Barwick, Amanda K. Engstrom, Kirsten A. Porter-Stransky, Jeremy M. Boss, David Weinshenker, Allan I. Levey and David J. Katz. LSD1 protects against hippocampal and cortical neurodegeneration. Nature Communications. 2017 Oct 9;8(1):805**. *Authors contributed equally**

Author Contributions**: D.A.M**, M.A.C and D.J.K **worked together on the design and execution of the experiments as well as the writing of the manuscript**. K.P., A.K.E and D.W. assisted with experiments. The manuscript was edited by all the coauthors. B.G.B and J.M.B. contributed to all of the bioinformatics analyses. A.I.L assisted with obtaining and analyzing the human pathology and provided guidance throughout.

2.1 Abstract

To investigate the mechanisms that maintain differentiated cells, we inducibly deleted the histone demethylase LSD1/KDM1A in adult mice. Loss of LSD1 leads to paralysis, along with widespread hippocampus and cortex neurodegeneration, and learning and memory defects. Here, we focus on the hippocampus neuronal cell death, as well as the potential link between LSD1 and human neurodegenerative disease. We find that loss of LSD1 induces transcription changes in common neurodegeneration pathways, along with the reactivation of stem cell genes, in the degenerating hippocampus. These data implicate LSD1 in the prevention of neurodegeneration via the inhibition of inappropriate transcription. Surprisingly, we also find that transcriptional changes in the hippocampus are similar to Alzheimer's Disease (AD) and Frontotemporal Dementia (FTD) cases, and LSD1 is specifically mislocalized to pathological protein aggregates in these cases. These data raise the possibility that pathological aggregation could compromise the function of LSD1 in AD and FTD.

2.2 Introduction

LSD1/KDM1a (hereafter referred to as LSD1) is an amine oxidase histone demethylase. In conjunction with the CoREST complex, it specifically demethylates mono- and di-methylation of lysine 4 on histone H3 (H3K4me1/2), but not H3K4me3[1,2]. Alternatively, when associated with the Androgen Receptor complex, LSD1 has been shown to demethylate H3K9me2[3]. LSD1 homozygous mutant mice arrest at embryonic day 5.5 and fail to properly elongate the egg cylinder, before being resorbed by embryonic day 7.5[4,5]. In addition, loss of LSD1 results in olfactory receptor choice[6] and circadian rhythm defects[7] when conditionally deleted in mice, along with defects in plasma cell[8] and hematopoietic differentiation[9] *in vitro,* and pituitary[4], hematopoietic stem cell[10] and trophoblast stem cell[11] differentiation defects *in vivo.* These defects, along with developmental phenotypes in yeast[8], *Arabidopsis*[12], *Drosophila*[13,14] and *C. elegans*[15], indicate that LSD1 may function during changes in cell fate. For example, in mouse embryonic stem cells (ES cells), LSD1 binds to the promoter and enhancers of the critical stem cell genes, *Oct4, Sox2, Klf4* and *Myc*[16]. Upon differentiation, LSD1 is required to remove H3K4me1 to repress the transcription of these stem cell genes and enable proper ES cell differentiation[16]. Similarly, LSD1 has also been implicated in regulating stem cell gene transcription during the differentiation of hematopoietic stem cells[10].

Although LSD1 has many roles throughout development, little is known about its function in differentiated cells. However, one hint comes from studies of the LSD1-containing CoREST complex, which has been implicated in the maintenance of cell fate by repressing the transcription of neuronal genes in non-neuronal cell types[17,18]. Based on this finding, we hypothesized that LSD1 may function similarly in the maintenance of other differentiated cell types. To address this possibility, we inducibly deleted *Lsd1* in adult mice. Loss of LSD1 leads

to paralysis, along with widespread neuronal cell death in the hippocampus and cortex, and associated learning and memory deficits. Here we have chosen to focus on the function of LSD1 in preventing hippocampus neurodegeneration, and the potential link to human neurodegenerative disease. In the degenerating hippocampus, we detect transcriptional changes in pathways implicated in human neurodegeneration. This suggests that LSD1 may prevent neuronal cell death by repressing common neurodegenerative pathways. In the degenerating neurons, we also detect the inappropriate expression of stem cell genes. This indicates that LSD1 may be part of an epigenetic maintenance program that continuously prevents inappropriate transcription. Surprisingly, we also find that LSD1 mislocalizes with pathological aggregates specifically in Alzheimer's Disease (AD) and Frontotemporal dementia (FTD) cases, and the genome-wide transcriptional changes in the degenerating *Lsd1* hippocampus specifically correlate with those found in AD and FTD cases. These data raise the possibility that LSD1 function could be affected in these dementias.

2.3 Results

2.3.1 LSD1 is continuously required to prevent neurodegeneration

To determine if LSD1 is required in terminally differentiated cells within the brain, we inducibly deleted *Lsd1* in adult mice by crossing floxed *Lsd1* mice[4,6,19-21] to the *Cagg-Cre* tamoxifen inducible *Cre* transgene[22-26] (hereafter referred to as $Lsd1^{CAGG}$). LSD1 is expressed widely in the mouse brain. Specifically, immunofluorescence detected LSD1 protein in the nuclei of NeuN positive neurons throughout the brain, including the hippocampus and cerebral cortex (Supplementary Fig. 1a-l). LSD1 protein is also present in astrocytes (Supplementary Fig. 2a-d, i-l) and oligodendrocytes (Supplementary Fig. 3a-d, i-l, q-t), but not microglia (Supplementary Fig.4a-h). Tamoxifen injection in $Lsd1^{CAGG}$ animals resulted in the widespread

loss of LSD1 protein in hippocampal and cerebral cortex neurons between 4 and 9 weeks after the final injection (Fig. 1a-d). However, surprisingly, at this time point LSD1 protein remained unchanged in astrocytes (Supplementary Fig. 2e-h, m-p) and oligodendrocytes (Supplementary Fig.3e-h, m-p, u-x) throughout the brain. Thus, within the brain, LSD1 loss is confined to neurons. As a result, *Lsd1*^{CAGG} animals enable us to interrogate the result of losing LSD1 specifically in these neurons.

We do not observe any defects in non-tamoxifen-injected *Cre* positive *Lsd1*^{CAGG} mice, nor in tamoxifen-injected *Cre* minus *Lsd1*^{CAGG} littermate controls (hereafter used as controls in all subsequent experiments). However, all (n = 45) tamoxifen-injected *Lsd1*^{CAGG} mice developed a severe motor deficit between 4 and 9 weeks after deletion, characterized initially by weakness in the hindlimbs followed by weakness in the forelimbs. These deficits are associated with hindlimb clasping, failure to maintain body posture, docile behavior, an inability to keep eyes open and ultimately, death (Fig. 1e-g, and Supplementary Movie 1 showing the terminal phenotype used in subsequent assays). Development of this motor defect occurred rapidly, with generally one week elapsing between initial onset and full defect. Importantly, the full motor defect occurred within 4 to 9 weeks after tamoxifen injection regardless of age at *Lsd1* deletion (Fig. 1g). This suggests that LSD1 is required throughout adulthood to protect against the development of these deficits. Though both males and females ultimately exhibit the motor defect, the number of days after tamoxifen injection to reach the terminal motor phenotype was longer in males compared to females (Fig. 1g inset). It is unclear at the moment why there is a small sex specific difference in the timing of this defect.

To investigate this phenotype further, we examined the spinal cords, neuromuscular junctions, muscles, and brains of *Lsd1*^{CAGG} mice. Mutant spinal cords appeared morphologically

normal and the number of motor neurons in the spinal cord did not significantly differ from control littermates (Supplementary Fig. 5a,b). We also did not detect any defects in the morphology of neuromuscular junctions, or in myelination of the spinal cord (Supplementary Fig. 5c-f). Upon examination of limb muscles, we observed severe atrophy in the soleus muscle, as indicated by the much smaller diameter of the muscle cells, and moderate atrophy of the tibialis anterior muscle (Supplementary Fig. 5g-j). However, we did not find any evidence of muscle degeneration, suggesting the motor defect is not due to complications in muscles.

Although we do not detect degeneration in the spinal cord or hind limb muscle, we find widespread severe neurodegeneration in the hippocampus and cerebral cortex of *Lsd1*^{CAGG} mice (Fig. 1h,i). As a result, we have initially focused here on the function of LSD1 in preventing this neurodegeneration. Within the hippocampus, many neuronal nuclei of the CA1, CA3, dentate gyrus, and cerebral cortex were pyknotic, and displayed a corresponding loss of the dendrite marker MAP2, as well as the axon marker Tau (Fig. 1j-s). Of these hippocampal regions, the CA1 was the most affected with 77.3±5.2% pyknotic nuclei (average with s.e.m.), while the CA2 and CA3 were moderately affected (Supplementary Fig. 6a,b). Within individuals, the percent of condensed nuclei in all regions of the hippocampus was higher in the posterior of the brain and less affected anteriorly (Supplementary Fig. 6c-f). Between individuals, the dentate gyrus was more variably affected, with the nuclei sometimes being completely pyknotic, completely unaffected, or intermediately affected (Fig. 1n,o and Supplementary Fig. 6g-j). In addition, we consistently observed pyknotic neuronal nuclei in the cerebral cortex, amygdala, thalamus and motor cortex, though the effect in the amygdala and thalamus was less severe than the hippocampus or cortex. (Fig. 1h,i,p,q and Supplementary Fig. 6k-r). Within the cerebral cortex, most of the pyknotic nuclei were typically found in layers II/III, IV and VI (Supplementary Fig.

6k,l). It is possible that the neurodegeneration in the motor cortex contributes to the observed paralysis phenotype. However, at the moment it is not possible to determine definitively if this is the case. Finally, in the cerebral cortex of *Lsd1*^{CAGG} mice, and to a lesser extent in the hippocampus, we observed a strong reactive gliosis response (Fig. 1t-w), an effect previously associated with neuronal distress[27].

To confirm that the pyknotic nuclei in the hippocampus and cortex of *Lsd1*^{CAGG} mice have undergone cell death, we performed TUNEL. Nearly every pyknotic nucleus exhibited positive TUNEL staining, indicating that they were undergoing or had undergone cell death (Fig. 1x-aa). Also, the neuronal cell death was observed at the terminal phenotype regardless of the age of the mice when *Lsd1* was inducibly deleted. These data indicate that LSD1 is continuously required for the survival of hippocampal and cortex neurons.

Immunohistochemistry verified that LSD1 protein is lost in the degenerating neurons of *Lsd1*^{CAGG} mice. Specifically, LSD1 was undetectable in most cortical nuclei and nearly all hippocampal nuclei, including all of the pyknotic nuclei in both regions (Fig. 1a-d). In contrast, LSD1 persisted in the remaining normal uncondensed nuclei within these brain regions (Fig. 1b,d, Supplementary Fig. 7a-d). The reciprocal relationship between LSD1 protein and pyknotic nuclei indicates that the neuronal cell death is likely due to the cell autonomous loss of LSD1. To confirm that hippocampal neurodegeneration is cell autonomous, we also induced deletion of *Lsd1* in *Lsd1*^{CAGG} mice using a single low dose tamoxifen injection. In contrast to the widespread LSD1 protein loss that we observe in the hippocampus with multiple higher dose tamoxifen injections (Supplementary Fig. 7a-d), 10 weeks after tamoxifen injection the low dose injection resulted in the loss of LSD1 protein in only a small number of neurons within the hippocampus (Supplementary Fig. 7e-f). Nevertheless, the few neuronal nuclei that lack LSD1 still become

pyknotic, indicating that they have undergone neurodegeneration (Supplementary Fig. 7e-f). These results suggest that within the hippocampus, the neuronal cell death is cell autonomous.

Despite the severe neurodegeneration of the hippocampus and cortex in *Lsd1*^{CAGG} mice, the cerebellum appeared normal. This can be seen, for example, by the absence of pyknotic nuclei and the normal distribution of the dendrite marker MAP2 (Supplementary Fig. 8a-d). To determine whether the lack of neuronal cell death in this region could be due to the failure of *Lsd1* deletion there, we performed quantitative PCR to assess the extent of remaining undeleted *Lsd1* in different brain regions. This analysis demonstrated high levels of deletion in the hippocampus and to a lesser extent in the cerebral cortex. However, there was very little *Lsd1* deletion in the cerebellum (Supplementary Fig. 8g). Overall, the extent of deletion matches the level of remaining LSD1 protein in each brain region at the terminal stage, with very little LSD1 in the hippocampus, low levels of LSD1 in the cortex, and higher levels of LSD1 in the cerebellum (Fig. 1a-d and Supplementary Fig. 8e,f). This distribution suggests that the brain region specificity of the neurodegeneration in *Lsd1*^{CAGG} mice may be due to the specificity of *Lsd1* deletion. Notably, though *Lsd1* deletion in the hippocampus occurred within the first 24 hours after tamoxifen injection (Supplementary Fig. 8g), the loss of LSD1 protein in the hippocampus occurred much later. For example, in the hippocampi of mice just beginning to display hindlimb weakness (approximately one week before the terminal phenotype) we observed some remaining LSD1 immunoreactivity and far fewer pyknotic nuclei (Supplementary Fig. 8h,i). This indicates that there is slow RNA or protein turnover in hippocampal neurons, a finding that is consistent with the continuous requirement for LSD1 in these cells.

Many previous mouse models of neurodegeneration display moderate levels of neuronal loss over an extended period of time (many months)[28,29], so the extent of neuronal cell death that

we observed in *Lsd1*^{CAGG} mice within nine weeks was striking. Therefore, we considered the possibility that LSD1 is generally required for cell viability. If this were the case, deletion of *Lsd1* throughout the mouse would be expected to result in a similar disruption in other organs and cell types. To address this possibility, we examined the liver and kidneys of terminal *Lsd1*^{CAGG} mice using dual IF. Hepatocytes and nephron epithelial cells lacking LSD1 appeared morphologically normal (Supplementary Fig. 9a-l). Additionally, Purkinje neurons lacking LSD1 in the cerebellum did not display any morphological signs of cell death despite the absence of LSD1 (Supplementary Fig. 8e,f). Taken together, these data suggest that LSD1 is not required for general cell viability. This conclusion is consistent with what has been reported in the literature elsewhere[4,6,9-11,16,30]. Thus, the continuous requirement for LSD1 to prevent neuronal cell death in the hippocampus and cortex appears to be specific to these neurons.

2.3.2 Loss of LSD1 results in learning and memory defects

To determine, whether LSD1-dependent neurodegeneration leads to learning and memory deficits, we assessed female *Lsd1*^{CAGG} mice in the Morris water maze and fear conditioning assays, 28 days after tamoxifen injection (prior to the onset of motor defects). Compared to littermate controls, *Lsd1*^{CAGG} mice had significant defects in the latency to mount the platform in the water maze assay on Day 5 (Fig. 2a). This is despite the fact that *Lsd1*^{CAGG} mice swam at speeds not significantly different than their littermate controls (Supplementary Fig. 10a, Supplementary Movie 2). Also, on Day 5, there is an increase in overall distance traveled as *Lsd1*^{CAGG} mice swim randomly rather than locating the platform (Supplementary Fig. 10b). Together these results suggest that the impaired performance of *Lsd1*^{CAGG} mice in the water maze is not due to motor deficits. On Day 6, when the platform was removed, controls spent nearly half of their time swimming in the platform quadrant, while *Lsd1*^{CAGG} mice spent approximately

equal time swimming in each of the four quadrants (Fig. 2b). These data suggest that *Lsd1*^{CAGG} mice have reduced spatial learning and reference memory capacity. *Lsd1*^{CAGG} mice were also impaired in contextual fear conditioning, spending less time freezing (30.0±8.3% average with s.e.m.) compared to controls (47.9±4.5% average with s.e.m.) (Fig. 2c). The contextual fear conditioning was reduced in *Lsd1*^{CAGG} mice at all points, and this reduction was statistically significant at 120,180 and 360 seconds (Fig. 2c). However, *Lsd1*^{CAGG} mice froze normally in response to a conditioned tone during cued fear conditioning (Fig. 2d). These data suggest that *Lsd1*^{CAGG} mice have defects in contextual, but not cued, learning and memory. This specificity is consistent with the observed pattern of neuronal cell death in the brains of these mice. Notably, though we do not detect any evidence of visual impairment, it is possible that a slight defect in visual impairment also contributes to the deficit observed in the water maze and contextual fear conditioning assays.

2.3.3 LSD1 inhibits reactivation of stem cell transcription

Previous work has implicated the LSD1 containing CoREST complex in repressing neuronal genes in non-neuronal cell types[17,18]. This raised the possibility that LSD1 may be functioning similarly in terminally differentiated hippocampal neurons to block the expression of genes associated with alternative cell fates. To test this possibility, we examined hippocampal gene expression changes in terminal *Lsd1*^{CAGG} mice by RNA-seq. At this terminal stage, there was no difference in the number of pyknotic nuclei in *Lsd1*^{CAGG} mutants versus the number of normal nuclei in unaffected controls, indicating that neurons in *Lsd1*^{CAGG} were actively undergoing neuronal cell death, but not yet cleared (Supplementary Fig. 11a). Comparison of global gene expression by unsupervised hierarchical clustering and principle components analysis in two *Lsd1*^{CAGG} mutants and two tamoxifen-injected *Cre* minus littermate controls,

showed that the expression states were similar between biological replicates, but different between *Lsd1*^{CAGG} mutants and controls (Supplementary Fig. 11b,c and Supplementary Data 1). Also, analysis of differentially expressed genes between *Lsd1*^{CAGG} mutant and control hippocampi revealed more significantly upregulated (281) than significantly downregulated (124) genes (Supplementary Fig. 11d,e, Supplementary Data 1, FDR < 0.05).

LSD1 has previously been shown to repress the expression of several critical stem cell genes during differentiation in multiple stem cell populations[9,11,16]. Therefore, we hypothesized that LSD1 may also be continuously required in terminally differentiated neurons to repress the transcription of stem cell genes to block the re-initiation of a stem cell fate. To address this possibility, we examined the expression of stem cell genes in our *Lsd1*^{CAGG} hippocampus RNA-seq dataset (Supplementary Data 1). Remarkably, three pluripotency genes (*Klf4, Myc,* and *Foxo1*), two of which are induced pluripotent stem cell (iPSC) factors[31], were amongst the most significantly upregulated genes in *Lsd1*^{CAGG} mice (Fig. 3a-c and Supplementary Data 1). Immunohistochemistry (IHC) analysis confirmed that KLF4 and FOXO1 proteins were reactivated widely in the degenerating pyknotic neurons, as well as in some of the remaining non-condensed nuclei, but not in controls (Fig. 3e,f,i,j). In contrast, c-MYC was reactivated only in a few nuclei (Fig. 3g,h). Therefore, to confirm that these c-MYC positive cells are neurons, we performed dual IF with the neuronal marker NeuN. This analysis confirmed that c-MYC is reactivated in neuronal nuclei (Supplementary Fig. 12a-h). Interestingly, although we did not observe increased *Oct4* expression in our RNA-seq dataset (Fig. 3d), one out of four mice analyzed displayed reactivation of OCT4 protein throughout the pyknotic hippocampal nuclei (Fig. 3k,l). This expression pattern appeared to be specific, as it was not observed in any of the controls or in other brain regions of the affected animal. These results suggest that LSD1 is

continuously required to repress the inappropriate expression of stem cell genes in hippocampal neurons.

Amongst the most highly activated genes in our RNA-seq dataset we also noticed the up regulation of the neuronal stem cell genes *Vimentin* and *Nestin* (Supplementary Fig. 12i,j). To determine whether VIMENTIN and NESTIN may also be reactivated in the dying neurons of $Lsd1^{CAGG}$ mice, we performed IHC to detect the expression of these proteins. IHC detected VIMENTIN protein in a subset of hippocampal neurons, though at a higher frequency in $Lsd1^{CAGG}$ mice than controls, while NESTIN protein is found in the reactive glia of the $Lsd1^{CAGG}$ hippocampus and cortex (Supplementary Fig. 12k-p).

2.3.4 Loss of LSD1 induces common neurodegeneration pathways

To identify additional pathways associated with the hippocampal neuronal cell death, we also performed gene ontology (GO) and Gene Set Enrichment Analysis (GSEA) on our RNA-seq datasets. Amongst the pathways that are affected by the loss of LSD1, we observed the upregulation of inflammatory response genes and complement cascade genes, along with the downregulation of oxidative phosphorylation genes and genes involved in neurotransmission (ion transport) (Supplementary Fig. 11f,g). All four of these pathways have been previously linked to neurodegeneration. For example, several studies have implicated the inflammatory response pathway in neurodegeneration. Activation of the inflammatory response pathway could contribute to neurodegeneration via macrophage mediated phagocytosis[32]. There is also evidence linking the complement cascade pathway to neurodegeneration. Activation of the complement cascade pathway could lead to neuronal cell death through axonal pruning[33]. In addition, impaired neurotransmission could contribute to neuronal cell death through the loss of electrical potential[34]. Finally, a defect in oxidative phosphorylation, with the accompanying mitochondrial

dysfunction, could lead to neurodegeneration via the generation of reactive oxygen species[35]. To determine the extent that these four neurodegeneration-associated pathways are misregulated in our *Lsd1*^{CAGG} hippocampus RNA-seq, we plotted the enrichment of these gene sets in our dataset for each of these four pathways. This analysis demonstrated that all four of these common neurodegeneration pathways are highly affected (Fig. 4a-d). Importantly, while each of these pathways has been implicated in neurodegeneration, it is difficult to determine whether these pathways contribute to neuronal cell death, or whether they may simply be a consequence of the neurodegeneration.

2.3.5 *Lsd1*^{CAGG} expression changes overlap with AD and FTD cases

The common neurodegeneration pathways affected by loss of LSD1 are also affected in human neurodegeneration patients. For example, systems biology approaches in human late onset Alzheimer's Disease (LOAD) brains have identified a critical microglia and immune transcription network upregulated in AD cases[36]. Interestingly, we noticed that many genes in the LOAD microglia and immune gene signature, including the critical receptor *Tyrobp*, are highly enriched in the *Lsd1*^{CAGG} hippocampus (Supplementary Data 1). Also, many of these microglia and immune genes are amongst the 281 most significantly upregulated genes in our RNA-seq dataset (Supplementary Data 1). Therefore, to determine if the LOAD microglia and immune response module is similarly misregulated in our mice, we compared the expression changes in the *Lsd1*^{CAGG} hippocampus to previously published expression changes at orthologous loci in LOAD cases[36]. This analysis demonstrated that loss of LSD1 in the mouse hippocampus leads to microglia and immune response gene expression changes that are highly similar to those that occur in the prefrontal cortex of LOAD cases. The microglia and immune expression changes in

the *Lsd1*^{CAGG} hippocampus also highly overlap with those that occur in the frontal cortex of FTD cases with progranulin mutations (FTD-progranulin)[37] (Fig. 4e,f).

Surprisingly, a similar correlation with AD and FTD cases is also found with the other neurodegeneration pathways that are misregulated in our RNA-seq dataset. For example, in the Kyoto Encyclopedia of Genes and Genomes (KEGG) complement cascade genes, expression changes in the *Lsd1*^{CAGG} hippocampus highly overlap with the upregulation that occurs in the prefrontal cortex of AD and FTD cases (Fig. 4g,h). A correlation is observed in pathways that are downregulated in the *Lsd1*^{CAGG} hippocampus as well. For example, we find a large overlap with expression changes in the neurotransmission genes (Synaptic Transmission Module) that were also identified using systems biology approaches in LOAD cases (Fig. 4k,l)[36]. Similarly, we observe a high correlation with the transcriptional changes in oxidative phosphorylation genes (Fig. 4i,j).

Finally, amongst the top upregulated genes in the *Lsd1*^{CAGG} hippocampus we noticed the cell cycle gene *PCNA* (Fig. 4m, and Supplementary Data 1). Evidence for the potential re-initiation of the cell cycle has been found in AD cases[38]. Therefore, to determine if PCNA, and other cell cycle markers, are being reactivated in degenerating *Lsd1*^{CAGG} neurons, we performed IHC analysis. This analysis confirmed the reactivation of PCNA protein, along with that of another cell cycle marker, H3S10p, specifically in the remaining non-pyknotic hippocampal nuclei (Fig. 4n-q). Intriguingly, the observation that c-MYC, PCNA and H3S10p were reactivated predominantly in the remaining uncondensed nuclei of the *Lsd1*^{CAGG} hippocampus raises the possibility that these neurons may be attempting to re-initiate the cell cycle prior to neuronal cell death.

The high degree of overlap within multiple neurodegeneration pathways between *Lsd1*^{CAGG} mice and human dementia cases was unexpected. Thus, we considered the possibility that the expression changes in our mice might overlap more broadly with AD and FTD cases. To address this possibility, we next compared the expression changes in the *Lsd1*^{CAGG} hippocampus with the expression changes in AD and FTD cases genome-wide. Remarkably, we found that the genome-wide expression changes in the prefrontal cortex of LOAD cases highly correlate with the expression changes in the hippocampus of *Lsd1*^{CAGG} mice (Fig. 5a). Likewise, the correlation was highly significant when compared to the frontal cortex of FTD-progranulin (Fig. 5b).

The genome-wide correlation in expression changes with AD and FTD cases could indicate the possible involvement of LSD1 in these diseases. However, it is also possible that the overlap is being primarily driven by the consequences of neuronal cell death. To address this second possibility we compared the expression changes in the *Lsd1*^{CAGG} hippocampus with other neurodegenerative diseases that have similar levels of neuronal cell death. If the genome-wide correlation is being driven by a common underlying mechanism, rather than neuronal cell death, we would expect the correlation to be less significant in these comparisons. Importantly, we observe relatively little overlap with the expression changes in the substantia nigra of Parkinson's disease (PD), a region with extensive neuronal cell death (Fig. 5c)[39]. We also see relatively little overlap with the expression changes that occur in the motor neurons of Amyotrophic Lateral Sclerosis (ALS) cases (Fig. 5d)[40]. Furthermore, compared to the high degree of correlation that we observe in FTD-progranulin cases, we find a dramatic reduction in the correlation when compared to sporadic FTD cases, despite the fact that these sporadic FTD cases have levels of neuronal cell death that are the same as FTD-progranulin cases (Fig. 5g). The large decrease in gene expression overlap, that we observe in PD, ALS and sporadic FTD

cases, suggests that the genome-wide overlap in expression with AD and FTD cases, is not simply due to neuronal cell death. Finally, we also compared *Lsd1*^{CAGG} hippocampus expression changes to changes in the cerebellum of AD and FTD cases. Compared to the prefrontal cortex, the cerebellum is relatively unaffected in AD and FTD cases. In both AD and FTD, we find that expression changes in the cerebellum overlap much less than the prefrontal cortex (Fig. 5e,f). This discrepancy indicates that within AD and FTD cases, the overlap in expression may be driven by the neurodegeneration, rather than brain region.

2.3.6 LSD1 is mislocalized in human dementias

The RNA-seq data suggest that deletion of *Lsd1* alone is sufficient to recapitulate transcriptional changes observed in the affected brain regions of AD and FTD-progranulin cases, including many of the individual gene categories that have previously been implicated in the etiology of these dementias. These data potentially implicate the loss of LSD1 function in these human dementias. As a result, we wondered whether LSD1 might be affected in AD and FTD patients. AD is characterized by protein aggregates of amyloid β (Aβ) and Tau, while FTD is associated with aggregates of either Tau or Tar DNA binding protein 43 (TDP-43)[41-43]. These pathological aggregates are thought to lead to downstream pathways of neurodegeneration, but it remains unclear mechanistically how these aggregates are linked to neuronal cell death.

To determine if LSD1 may be affected in AD and FTD patients, we examined the localization of LSD1 in post-mortem AD, FTD with TDP-43 inclusions (FTD-TDP43), and age-matched control cases. We also examined the localization of LSD1 in Parkinson's disease (PD) cases, as a disease control with pathological protein aggregates. Similar to the expression in mice, LSD1 immunoreactivity was found in neuronal nuclei throughout the frontal cortex and hippocampus of age-matched control cases (Fig. 6a,b). In contrast, in all 14 AD cases analyzed,

LSD1 was found both in neuronal nuclei as well as inappropriately associated with cytoplasmic tangle-like aggregates and neurites, (Fig. 6c,d). This pattern is highly reminiscent of the neurofibrillary tangles and neuropil threads marked by pTau in the same AD cases (Fig. 6c-f). In addition, in all 14 FTD-TDP43 cases analyzed, LSD1 was abnormally associated with neurites in the frontal cortex, and cytoplasmic inclusions in the hippocampus (Fig. 6j,k). This pattern is highly similar to the pTDP-43 aggregation observed in FTD-TDP43 cases (Fig. 6j-m). To confirm the co-localization of LSD1 with pTau and pTDP-43 we performed dual IF. This analysis demonstrated that LSD1 co-localizes with pTau in 56.3% of neurofibrillary tangles in AD (n = 14 patients), and with pTDP-43 in 52.4% of neurites in FTD-TDP43 (n = 5 patients) (Fig. 6g-i,n-q). Within AD cases the extent of co-localization ranges from 19%-76%, while in FTD-TDP43 cases, the co-localization ranges from 43%-71%. The finding that LSD1 is localized to pathological aggregates raises the possibility that it could be increasingly sequestered in the cytoplasm. This could result in less LSD1 being available to function in the nucleus of affected neurons in AD and FTD cases.

To confirm the specificity of the LSD1 localization, we performed several controls. Preincubation of the LSD1 Antibody (Ab) with its target LSD1 peptide completely abrogated the immunoreactivity (Supplementary Fig. 13a,b). We also did not observe the localization of LSD1 to the amyloid β core of senile plaques in the same AD cases where we observed co-localization with pTau (Supplementary Fig. 13c,d). Nor do we observe LSD1 localized to any Lewy body-like structures (aggregates of α-synuclein), or any other abnormal localization of LSD1, in the substantia nigra of PD cases (Supplementary Fig. 13e-h). These results suggest the mislocalization of LSD1 to neurofibrillary tangles in AD, and pTDP-43 inclusions in FTD cases, is specific. Notably, the co-localization of proteins with these pathological aggregates is

exceedingly rare. For example, though many proteins have been recently described as enriched in the insoluble fraction of AD brains, only one was confirmed to be co-localized with neurofibrillary tangles[44].

2.3.7 *Lsd1^{CAGG}* mice do not have protein aggregates

Since LSD1 associates with pathological aggregates in AD and FTD-TDP43 cases, we considered the possibility that the neuronal cell death that we observe in the *Lsd1^{CAGG}* mice could be due to the induction of pathological aggregates in the mice. To test this possibility, we performed IHC on the brains of terminal *Lsd1^{CAGG}* mice using antibodies to Aβ, pTau, and pTDP-43, along with Gallyas (silver, nonspecific aggregates) staining (Supplementary Fig. 14a-h). We find no evidence of any pathological protein aggregates or tangles associated with the degenerating neurons or otherwise. This suggests that if loss of LSD1 is involved in AD and/or FTD, it is likely downstream of pathological aggregation. This finding is consistent with the mislocalization of LSD1 to pathological aggregates in the human cases (Fig. 6).

2.3.8 Increased stem cell gene expression in AD and FTD patients

The loss of LSD1 in mice is associated with the surprising reactivation of stem cell transcription in hippocampal neurons. If LSD1 is affected in AD and/or FTD, these diseases could be associated with a similar increase in stem cell gene expression. To test this possibility, we re-examined the expression of stem cell genes in previously published microarray experiments from LOAD and FTD-progranulin post-mortem cases[36,37]. This analysis revealed a significant increase in the expression of *Klf4*, *Myc, Oct4, Foxo1*, and *Vimentin* in LOAD cases compared to controls (Supplementary Fig. 15a,c,e,g,k,), while *PCNA* expression was unchanged (Supplementary Fig. 15i). In FTD-progranulin cases there was also a significant increase in the expression of *Klf4* and *Foxo1*, as well as a trend toward the increased expression of *Myc, Oct4,*

PCNA and *Vimentin* (Supplementary Fig. 15b,d,f,h,j,l,). These data are consistent with the possibility that LSD1 function could be compromised in AD and FTD patients.

2.4 Discussion

Despite its well-known role throughout development, LSD1 protein can also be found in terminally differentiated cells throughout the brain. To determine if there is an ongoing role for LSD1 in these terminally differentiated cells, we conditionally deleted *Lsd1* in adult mice. Surprisingly, within the brain at the terminal time point, the inducible loss of LSD1 in $Lsd1^{CAGG}$ mice results in loss of LSD1 protein only in neurons. This indicates that neurons may be more vulnerable to LSD1 protein or RNA turnover, a specificity that mirrors what occurs in AD and FTD cases.

Within the brain, the selective vulnerability of neurons in $Lsd1^{CAGG}$ mice enables us to specifically interrogate the function of LSD1 in these cells. Loss of LSD1 in $Lsd1^{CAGG}$ mice results in widespread hippocampus and cortex neuronal cell death. This demonstrates that loss of LSD1 in hippocampus and cortex neurons is sufficient to induce neuronal cell death. This conclusion is consistent with our high/low tamoxifen mosaic experiments which indicate that LSD1 acts cell autonomously in hippocampal neurons. Thus, we propose that LSD1 functions continuously in hippocampal and cortex neurons to prevent neurodegeneration.

To further investigate the neuronal cell death in the hippocampus, we examined gene expression changes genome-wide. Previous analyses of human neurodegeneration cases and experimental models have implicated common pathways leading to neuronal cell death. These include; activation of genes in the microglia and immune pathways, a defect in oxidative phosphorylation, loss of synaptic transmission, and failure to maintain cell cycle arrest.

Remarkably, the loss of LSD1 affects all of these common neurodegenerative pathways. Therefore, it is possible that the loss of LSD1 creates a perfect storm where multiple neurodegenerative pathways are affected simultaneously, with one or more of these pathways leading to the observed neuronal cell death.

The prevailing view in developmental biology is that cells are irreversibly committed to their differentiated cell fate. Indeed, the very word "fate" promotes the idea that a differentiated cell has reached its final destiny. However, there may be a requirement for differentiated cells to actively maintain their differentiated status. The LSD1-containing CoREST complex has been previously implicated in repressing neuronal genes in non-neuronal cells[17,18]. Based on this, we considered the possibility that LSD1 could be similarly required to maintain terminally differentiated hippocampus and cortex neurons by repressing gene transcription associated with alternative cell fates. In the degenerating neurons of *Lsd1*^{CAGG} mice, we detect the re-activation of stem cell transcription factors, such as KLF4, OCT4, c-MYC and FOXO1. This demonstrates that LSD1 is continuously required in terminally differentiated neurons to block the re-activation of these factors. Also, we detect a widespread decrease in the expression of neuronal pathways. This suggests that LSD1 is also required, directly or indirectly, to maintain the expression of these genes. Therefore, we propose that LSD1 is a key component of an epigenetic maintenance program that reinforces the differentiated state of hippocampal neurons by continuously restraining the re-activation of factors associated with alternative cell fates.

At this moment, we cannot definitively determine why the loss of LSD1 results in a severe motor defect. Nevertheless, *Lsd1*^{CAGG} mice develop a motor defect that is similar to a tauopathy mouse model[28]. For example the P301S mice, which overexpress an aggregation prone form of human Tau, have a motor defect that is reminiscent of *Lsd1*^{CAGG} mice[28]. The

concordance of phenotypes between P301S mice and *Lsd1*^{CAGG} mice is consistent with Tau and LSD1 acting in a common pathway. Also consistent with this possibility, we find that that LSD1 inappropriately mislocalizes to cytoplasmic aggregates of pTau in AD, and global gene expression changes in the degenerating *Lsd1*^{CAGG} hippocampus correlate with changes in AD and FTD-progranulin cases. Finally, the re-examination of stem cell genes that are specifically affected by the loss of LSD1 in the mouse hippocampus demonstrates that these genes are also increased in AD and FTD cases. Together these data indicate a potential link between the loss of LSD1 and these human dementia cases. This could occur through the following potential model: as neurons age, the accumulation of protein aggregates sequesters LSD1 in the cytoplasm, and interferes with the continuous requirement for LSD1. Normally, LSD1 maintains terminally differentiated neurons, and prevents the activation of common neurodegenerative pathways, by continuously repressing the transcription of inappropriate genes. As a result, the inhibition of LSD1 by the pathological aggregates in the aging neurons of AD and FTD brains creates a situation where neurons are subject to an onslaught of detrimental processes. This results in neuronal cell death and dementia.

2.5 Methods

All mouse work, including surgical procedures, were approved by and conducted in accordance with the Emory University Institutional Animal Care and Use Committee. The post-mortem human samples were provided by the Alzheimer's Disease Research Center (ADRC) Brain Bank at Emory University and were obtained with signed informed consent in accordance with institutional guidelines.

2.5.1 Tamoxifen injections

Mice were intraperitoneally injected with 75.0 mg tamoxifen per kilogram of body mass dissolved in corn oil once a day on days 1, 2, 4, 5, and 7 of a seven day period. This injection protocol was used for all assays, except the single low dose tamoxifen injection, which was performed with 1mg tamoxifen per 40 grams of body mass.

2.5.2 Mouse Tissue Fixation

Mice were given a lethal dose of isoflurane via inhalation, then transcardially perfused with ice cold 4.0% paraformaldehyde in 0.1M phosphate buffer. Brain, spinal cord and muscle tissues were dissected and post fixed in cold paraformaldehyde solution for 2 hours. Tissues were then either cryoprotected by sinking in 30% sucrose and frozen embedded in O.C.T. Compound (Tissue Tek), or serially dehydrated and embedded in paraffin.

2.5.3 Histology

For hematoxylin and eosin, and thionin staining was performed according standard procedures (1% thionin, pH4.0). For Gallyas staining, sections were dewaxed then treated with 5% periodic acid for 5 minutes, followed by washing and one minute alkaline silver treatment. Sections were then developed for 30 minutes, followed by 0.5% acetic acid and water rinses. Finally, sections were treated with Schiff's reagent for 30 minutes, washed, counter stained with hematoxylin and coverslipped.

2.5.4 Mouse Immunofluorescence

Frozen mouse brain tissue was sectioned at 12μm and washed with TBS, then treated with 0.8% sodium borohydride for 10 minutes to reduce background. Antigen retrieval was performed by microwaving at 10% power 3X for 5 minutes in 0.01M sodium citrate. Slides were then cooled and washed with TBS, then permeabilized in 0.5% Triton X-100 for 20 minutes, followed by

blocking in 10% goat serum for 1 hour. Primary Abs (Supplementary Table 1) were incubated overnight at 4°C. Slides were then washed and incubated in secondary Abs (Goat α Mouse Alexa Fluor 488, 1:500, Invitrogen A11001 and Goat α Rabbit Alexa Fluor 594, 1:500, Invitrogen A11012) for 1 hour at room temperature followed by washes with TBS and DAPI, then coverslipped.

2.5.5 Mouse Immunohistochemistry

Paraffin embedded tissue was dewaxed with xylenes and serial ethanol dilutions then treated with 3% hydrogen peroxide at 40°C for 5 minutes to quench endogenous peroxidase activity, blocked in 2% serum at 40°C for 15 minutes, and incubated with primary Ab (Supplementary Table 1) overnight at 4°C. Slides were washed then incubated with biotinylated secondary Ab (Biotinylated Goat α Rabbit, 1:200, Vector Labs BA-1000 and Biotinylated Goat α Mouse, 1:200, Vector Labs BA-9200) at 37°C for 30 minutes. Signal amplification was then carried out by incubating at 37°C for 1 hour with Vector Labs Elite ABC reagent (PK-6200). Slides were then developed with DAB for 2-5 minutes, counterstained with hematoxylin and coverslipped.

2.5.6 Human Immunohistochemistry

Frozen free floating sections of 20-50μm thickness were washed of cryoprotectant followed by quenching of endogenous peroxidase activity by incubating in 3% hydrogen peroxide for 15 minutes. Sections were permeabilized and blocked in 0.1 Triton X-100 and 8% goat serum, then incubated with primary Abs (Supplementary Table 1) overnight at 4°C followed by incubation with biotinylated secondary Ab (Biotinylated Goat α Rabbit, 1:200, Vector Labs BA-1000 and Biotinylated Goat α Mouse, 1:200, Vector Labs BA-9200) and amplification with Vector Labs Elite ABC reagent. Sections were then treated with DAB (Sigma) for 3-4.5 minutes then mounted on slides, dried overnight and serially dehydrated and coverslipped with Permount.

2.5.7 Human Immunofluorescence

For immunofluorescence, sections were prepared as with IHC, except that tissue was incubated with two primary antibodies (Supplementary Table 1) overnight, and with two secondary antibodies, fluorescent goat anti-mouse (1:500, Invitrogen A11001) and biotinylated goat anti-rabbit (1:200, Vector Labs BA-1000). Fluorescent signal amplification of the biotinylated secondary was carried out with Vector Labs Elite ABC reagent and developed with PerkinElmer TSA Plus Cyanine 3 System diluted 1:100. Sections were treated with autofluorescence inhibitor (Millipore 2160) after mounting on slides.

2.5.8 Immunohistochemistry with Peptide block

For peptide block, the LSD1 primary antibody (1:500, Abcam 17721) was preincubated for 24 hours at 4°C with 74 fold molar excess of target peptide (Abcam 17763).

2.5.9 TUNEL Assay

Frozen embedded brain tissue was sectioned at 12µm thickness. Slides were permeabilized in 0.1% Triton X-100, 0.1% sodium citrate for 2 minutes followed by washes in PBS. For antigen retrieval, slides were microwaved for 1 minute at 10% power in preboiled 0.1M sodium citrate then rapidly cooled by adding deionized water. Slides were then washed in PBS and blocked for 30 minutes at room temperature in 0.1M Tris, 3.0% BSA, 10% goat serum. Slides were washed twice then incubated with 50µL of TUNEL labelling solution (Roche *In situ* Cell Death Detection Kit, Fluorescein) for 1 hour at 37°C. Slides were then washed with PBS and DAPI (0.5 mg/ml) then coverslipped.

2.5.10 Neuromuscular Junctions

Frozen tibialis anterior tissue was sectioned at 20 µm and blocked with 10% goat serum for 1 hour. Slides were then incubated with SV2 primary antibody (1:50, Developmental Studies

Hybridoma Bank) in blocking buffer for 72, replacing antibody every 24 hours. Slides were then washed and incubated with secondary antibody (1:500, Invitrogen A11001) for 2 hours, washed, then incubated with rhodamine conjugated α-bungarotoxin (Life Technologies T-1175) for 1 hour, washed and coverslipped.

2.5.11 Quantification of LSD1 Colocalization with pTau and pTDP-43

Three random fields per section that contained NFTs marked by pTau at 20X and pTDP-43 inclusions at 40X were manually examined. Beginning with the pTau/pTDP-43 fluorescence channel, each aggregate structure was visually inspected. Then, the microscope was switched to the LSD1 fluorescence channel and inspected for LSD1 signal. Structures were scored as positive for LSD1 colocalization if the LSD1 staining pattern was localized to a majority of the aggregate structure. 535 NFTs and 103 pTDP inclusions were scored.

2.5.12 Motor Neuron Counting

Thionin stained spinal cord sections were imaged and cropped to include just the ventral horn. Motor neurons were manually counted by appearance for each image then calculated as a percent of the total number of nuclei, which were counted by converting the image to binary then counting particles using ImageJ.

2.5.13 CA1 Nuclei Counting

Hematoxylin or DAPI stained nuclei of hippocampal sections were scored as normal, pyknotic, or intermediate. Counts were limited to the most dorsal region of the CA1 in the field of a Zeiss Axiophot ocular graticule grid. Three randomly selected sections were counted per animal. Investigator was blind to genotype.

2.5.14 *Lsd1* Deletion Quantification

Intact *Lsd1* alleles from hippocampus, cortex, and cerebellum were quantified from phenol extracted genomic DNA using BioRad CFX96 Real-Time System using the following primers: *Lsd1* forward: 5'-CCAACACTAAAGAGTATCCCAAGAATA-3'; *Lsd1* reverse: 5'-GGTGATTATTATAGGTTCAGGTGTTTC-3'; *Actb* forward: 5'-AGCCAACTTTACGCCTAGCGT-3'; *Actb* reverse: 5'-TCTCAAGATGGACCTAATACGGC-3'. The *Lsd1* reverse primer anneals to exon 6 of *Lsd1*, which is deleted in $Lsd1^{CAGG}$. Results were normalized to *Actb*.

2.5.15 Morris Water Maze

Training was carried out in a round, water-filled tub (52 inch diameter). Mice were trained with 4 trials per day for 5 days with a maximum trial length of 60 seconds and a 15 minute intertrial interval. Subjects that did not reach the platform in the allotted time were manually guided to it. Mice were allowed 5 seconds on the platform to survey spatial cues. Following the 5 day training period, probe trials were performed by removing the escape platform and measuring the amount of time spent in the quadrant that originally contained the escape platform over a 60 second trial. All trials were videotaped and performance analysed by means of MazeScan (Clever Sys, Inc.).

2.5.16 Fear Conditioning

On Day 1, mice were placed in a fear conditioning apparatus (Colbourn) and allowed to explore for 3 minutes. Following this habituation period, three conditioned stimulus-unconditioned stimulus pairings were presented with a 1 minute intertrial interval. The conditioned stimulus consisted of a 20 second 85db tone and the unconditioned stimulus consisted of a 2 second foot shock that co-terminated with each conditioned stimulus. On Day 2, subjects were presented with a context test by placement in Day 1 conditioning apparatus and amount of freezing

behavior was recorded by camera and quantified by Colbourn software. On Day 3, subjects were presented with a tone test by exposure to conditioned stimulus in a novel context. Mice were allowed to explore novel context for 2 minutes then presented with the 85db tone for 6 minutes with freezing behavior recorded.

2.5.17 RNA Sequencing

Mice were anesthetized with a lethal dose of isoflurane, followed by decapitation and hippocampus dissection. Hippocampi were snap frozen with liquid nitrogen in 1mL Trizol and stored at -80°C. For RNA isolation, samples were thawed at 37°C then kept on ice prior to homogenization with a Polytron homogenizer with a 5 second pulse. After a five minute incubation at room temperature, one tenth the sample volume of 1-bromo-3chloropropane was added, mixed by inversion and incubated for three minutes at room temperature. Samples were then centrifuged at 13,000 X g for 15 minutes at 4°C to separate the aqueous and organic layers. As much of the aqueous layer was recovered as possible, then RNA was precipitated with isopropanol. Pellets were then washed with 75% ethanol and resuspended in 50µL deionized water. RNA library preparation and sequencing were performed by HudsonAlpha Genomic Services Lab. RNA was Poly(A) selected and 300bp size selected. Libraries were sequenced for 25 million 50bp paired end reads.

2.5.18 RNA-seq Analysis

Short read FASTQ files were quality trimmed using FASTX toolkit (v. 0.0.14) to trim three bases from the 5' end of the reads. Paired-end reads were then mapped to the mm9 genome using tophat2 [45] and the UCSC knownGene gtf file. The following parameters were used in the tophat2 call "-N 1 –g 1 –read-gap-length 1 –mate-inner-dis 170". Reads that had the same starting location and strand with mate-pairs that also had the same location and strand were considered to

be PCR duplicates and removed from subsequent analyses using Picard tools (v. 1.103). Differentially expressed transcripts were determined using Cufflinks and Cuffdiff (v2.1.1) [46]. Downstream analyses were performed in R/Bioconductor [47] and used gene summarized expression levels normalized using Fragments Per Kilobase per Million (FPKM) from Cufflinks. Hierarchical clustering was performed using the pvclust R package were significance was determined using bootstrapping[48]. Principle Components Analysis (PCA) was conducted using the "prcomp" function of the stats package in R/ Bioconductor. Enriched gene ontologies were determined using the package "GOstats" (v. 3.1.1)[49]. Gene Set Enrichment Analysis (GSEA) was performed using a pre-ranked gene list determined by cuffdiff and GSEA (v. 2.1.0)[50]. Hierarchical clustering of gene expression data was performed using average clustering in the heatmap.2 package. UCSC-style display of gene expression data were plotted using the "rtracklayer" package [51] and custom R scripts to display RNA sequencing reads as histograms (available upon request). FastQ files for RNA sequencing experiments can be found in the GEO dataset GSE98875.

2.5.19 Comparison to Human Gene Expression Data

Normalized gene expression data from late onset Alzheimer's disease (LOAD)[36], frontal temporal dementia (FTD)[37] and Parkinson's disease (PD)[39] patients were downloaded from Gene Expression Omnibus gene sets GSE44772, GSE13162 and GSE20295, respectively. Comparison to *Lsd1*^{CAGG} gene expression data was performed by mapping mouse and human genes using the NCBI homologene database[53]. Correlation of *Lsd1*^{CAGG} gene expression changes and those found in LOAD, FTD and PD patients were assessed using Spearman's rank correlation (ρ). *P*-values were determined by analysis of variance (ANOVA).

2.6 References

1 You, A., Tong, J. K., Grozinger, C. M. & Schreiber, S. L. CoREST is an integral component of the CoREST- human histone deacetylase complex. *Proceedings of the National Academy of Sciences of the United States of America* **98**, 1454-1458 (2001).

2 Shi, Y. *et al.* Histone demethylation mediated by the nuclear amine oxidase homolog LSD1. *Cell* **119**, 941-953 (2004).

3 Metzger, E. *et al.* LSD1 demethylates repressive histone marks to promote androgen-receptor-dependent transcription. *Nature* **437**, 436-439 (2005).

4 Wang, J. *et al.* Opposing LSD1 complexes function in developmental gene activation and repression programmes. *Nature* **446**, 882-887 (2007).

5 Wang, J. *et al.* The lysine demethylase LSD1 (KDM1) is required for maintenance of global DNA methylation. *Nature genetics* **41**, 125-129 (2009).

6 Lyons, D. B. *et al.* An epigenetic trap stabilizes singular olfactory receptor expression. *Cell* **154**, 325-336, doi:10.1016/j.cell.2013.06.039S0092-8674(13)00778-2 [pii] (2013).

7 Nam, H. J. *et al.* Phosphorylation of LSD1 by PKCalpha is crucial for circadian rhythmicity and phase resetting. *Mol Cell* **53**, 791-805, doi:10.1016/j.molcel.2014.01.028S1097-2765(14)00111-7 [pii] (2014).

8 Su, S. T. *et al.* Involvement of histone demethylase LSD1 in Blimp-1-mediated gene repression during plasma cell differentiation. *Mol Cell Biol* **29**, 1421-1431, doi:MCB.01158-08 [pii]10.1128/MCB.01158-08 (2009).

9 Saleque, S., Kim, J., Rooke, H. M. & Orkin, S. H. Epigenetic regulation of hematopoietic differentiation by Gfi-1 and Gfi-1b is mediated by the cofactors CoREST and LSD1. *Mol Cell* **27**, 562-572, doi:S1097-2765(07)00483-2 [pi10.1016/j.molcel.2007.06.039 (2007).

10 Kerenyi, M. A. *et al.* Histone demethylase Lsd1 represses hematopoietic stem and progenitor cell signatures during blood cell maturation. *Elife* **2**, e00633, doi:10.7554/eLife.0063300633 [pii] (2013).

11 Zhu, D. *et al.* Lysine-specific demethylase 1 regulates differentiation onset and migration of trophoblast stem cells. *Nat Commun* **5**, 3174, doi:10.1038/ncomms4174 [pii] (2014).

12 Jiang, D., Yang, W., He, Y. & Amasino, R. M. Arabidopsis relatives of the human lysine-specific Demethylase1 repress the expression of FWA and FLOWERING LOCUS C and thus promote the floral transition. *Plant Cell* **19**, 2975-2987, doi:tpc.107.052373 [pii]10.1105/tpc.107.052373 (2007).

13 Rudolph, T. *et al.* Heterochromatin formation in Drosophila is initiated through active removal of H3K4 methylation by the LSD1 homolog SU(VAR)3-3. *Mol Cell* **26**, 103-115 (2007).

14 Di Stefano, L., Ji, J. Y., Moon, N. S., Herr, A. & Dyson, N. Mutation of Drosophila Lsd1 disrupts H3-K4 methylation, resulting in tissue-specific defects during development. *Curr Biol* **17**, 808-812 (2007).

15 Katz, D. J., Edwards, T. M., Reinke, V. & Kelly, W. G. A C. elegans LSD1 demethylase contributes to germline immortality by reprogramming epigenetic memory. *Cell* **137**, 308-320 (2009).

16 Whyte, W. A. *et al.* Enhancer decommissioning by LSD1 during embryonic stem cell differentiation. *Nature* **482**, 221-225, doi:nature10805 [pii]10.1038/nature10805 (2012).
17 Chong, J. A. *et al.* REST: a mammalian silencer protein that restricts sodium channel gene expression to neurons. *Cell* **80**, 949-957 (1995).
18 Ballas, N. *et al.* Regulation of neuronal traits by a novel transcriptional complex. *Neuron* **31**, 353-365 (2001).
19 Macfarlan, T. S. *et al.* Endogenous retroviruses and neighboring genes are coordinately repressed by LSD1/KDM1A. *Genes & development* **25**, 594-607, doi:10.1101/gad.2008511 (2011).
20 Wasson, J. A. *et al.* Maternally provided LSD1/KDM1A enables the maternal-to-zygotic transition and prevents defects that manifest postnatally. *eLife* **5**, doi:10.7554/eLife.08848 (2016).
21 Lambrot, R., Lafleur, C. & Kimmins, S. The histone demethylase KDM1A is essential for the maintenance and differentiation of spermatogonial stem cells and progenitors. *FASEB journal : official publication of the Federation of American Societies for Experimental Biology* **29**, 4402-4416, doi:10.1096/fj.14-267328 (2015).
22 Hayashi, S. & McMahon, A. P. Efficient recombination in diverse tissues by a tamoxifen-inducible form of Cre: a tool for temporally regulated gene activation/inactivation in the mouse. *Dev Biol* **244**, 305-318 (2002).
23 Sangiorgi, E. & Capecchi, M. R. Bmi1 is expressed in vivo in intestinal stem cells. *Nature genetics* **40**, 915-920, doi:10.1038/ng.165 (2008).
24 Yauch, R. L. *et al.* A paracrine requirement for hedgehog signalling in cancer. *Nature* **455**, 406-410, doi:10.1038/nature07275 (2008).
25 Schulz, C. *et al.* A lineage of myeloid cells independent of Myb and hematopoietic stem cells. *Science* **336**, 86-90, doi:10.1126/science.1219179 (2012).
26 Guy, J., Gan, J., Selfridge, J., Cobb, S. & Bird, A. Reversal of neurological defects in a mouse model of Rett syndrome. *Science* **315**, 1143-1147, doi:10.1126/science.1138389 (2007).
27 Pekny, M. & Nilsson, M. Astrocyte activation and reactive gliosis. *Glia* **50**, 427-434, doi:10.1002/glia.20207 (2005).
28 Yoshiyama, Y. *et al.* Synapse loss and microglial activation precede tangles in a P301S tauopathy mouse model. *Neuron* **53**, 337-351, doi:10.1016/j.neuron.2007.01.010 (2007).
29 Oakley, H. *et al.* Intraneuronal beta-amyloid aggregates, neurodegeneration, and neuron loss in transgenic mice with five familial Alzheimer's disease mutations: potential factors in amyloid plaque formation. *J Neurosci* **26**, 10129-10140, doi:10.1523/JNEUROSCI.1202-06.2006 (2006).
30 Duteil, D. *et al.* LSD1 promotes oxidative metabolism of white adipose tissue. *Nat Commun* **5**, 4093, doi:10.1038/ncomms5093[pii] (2014).
31 Takahashi, K. & Yamanaka, S. Induction of pluripotent stem cells from mouse embryonic and adult fibroblast cultures by defined factors. *Cell* **126**, 663-676 (2006).
32 Cameron, B. & Landreth, G. E. Inflammation, microglia, and Alzheimer's disease. *Neurobiol Dis* **37**, 503-509, doi:10.1016/j.nbd.2009.10.006 (2010).

33 Stephan, A. H., Barres, B. A. & Stevens, B. The complement system: an unexpected role in synaptic pruning during development and disease. *Annu Rev Neurosci* **35**, 369-389, doi:10.1146/annurev-neuro-061010-113810 (2012).

34 Selkoe, D. J. Alzheimer's disease is a synaptic failure. *Science* **298**, 789-791, doi:10.1126/science.1074069 (2002).

35 Lin, M. T. & Beal, M. F. Mitochondrial dysfunction and oxidative stress in neurodegenerative diseases. *Nature* **443**, 787-795, doi:10.1038/nature05292 (2006).

36 Zhang, B. *et al.* Integrated systems approach identifies genetic nodes and networks in late-onset Alzheimer's disease. *Cell* **153**, 707-720, doi:10.1016/j.cell.2013.03.030S0092-8674(13)00387-5 [pii] (2013).

37 Chen-Plotkin, A. S. *et al.* Variations in the progranulin gene affect global gene expression in frontotemporal lobar degeneration. *Hum Mol Genet* **17**, 1349-1362, doi:10.1093/hmg/ddn023ddn023 [pii] (2008).

38 Busser, J., Geldmacher, D. S. & Herrup, K. Ectopic cell cycle proteins predict the sites of neuronal cell death in Alzheimer's disease brain. *J Neurosci* **18**, 2801-2807 (1998).

39 Zhang, Y., James, M., Middleton, F. A. & Davis, R. L. Transcriptional analysis of multiple brain regions in Parkinson's disease supports the involvement of specific protein processing, energy metabolism, and signaling pathways, and suggests novel disease mechanisms. *Am J Med Genet B Neuropsychiatr Genet* **137B**, 5-16, doi:10.1002/ajmg.b.30195 (2005).

40 Rabin, S. J. *et al.* Sporadic ALS has compartment-specific aberrant exon splicing and altered cell-matrix adhesion biology. *Hum Mol Genet* **19**, 313-328, doi:10.1093/hmg/ddp498 (2010).

41 Neumann, M. *et al.* Ubiquitinated TDP-43 in frontotemporal lobar degeneration and amyotrophic lateral sclerosis. *Science* **314**, 130-133, doi:314/5796/130 [pii]10.1126/science.1134108 (2006).

42 Masters, C. L. *et al.* Neuronal origin of a cerebral amyloid: neurofibrillary tangles of Alzheimer's disease contain the same protein as the amyloid of plaque cores and blood vessels. *Embo J* **4**, 2757-2763 (1985).

43 Glenner, G. G. & Wong, C. W. Alzheimer's disease and Down's syndrome: sharing of a unique cerebrovascular amyloid fibril protein. *Biochem Biophys Res Commun* **122**, 1131-1135, doi:0006-291X(84)91209-9 [pii] (1984).

44 Bai, B. *et al.* U1 small nuclear ribonucleoprotein complex and RNA splicing alterations in Alzheimer's disease. *Proc Natl Acad Sci U S A* **110**, 16562-16567, doi:10.1073/pnas.1310249110 [pii] (2013).

45 Jawhar, S., Trawicka, A., Jenneckens, C., Bayer, T. A. & Wirths, O. Motor deficits, neuron loss, and reduced anxiety coinciding with axonal degeneration and intraneuronal Abeta aggregation in the 5XFAD mouse model of Alzheimer's disease. *Neurobiol Aging* **33**, 196 e129-140, doi:10.1016/j.neurobiolaging.2010.05.027 (2012).

46 Kim, D. *et al.* TopHat2: accurate alignment of transcriptomes in the presence of insertions, deletions and gene fusions. *Genome biology* **14**, R36, doi:10.1186/gb-2013-14-4-r36 (2013).

47 Trapnell, C. *et al.* Transcript assembly and quantification by RNA-Seq reveals unannotated transcripts and isoform switching during cell differentiation. *Nature biotechnology* **28**, 511-515, doi:10.1038/nbt.1621 (2010).
48 Gentleman, R. C. *et al.* Bioconductor: open software development for computational biology and bioinformatics. *Genome biology* **5**, R80, doi:10.1186/gb-2004-5-10-r80 (2004).
49 Suzuki, R. & Shimodaira, H. Pvclust: an R package for assessing the uncertainty in hierarchical clustering. *Bioinformatics* **22**, 1540-1542, doi:10.1093/bioinformatics/btl117 (2006).
50 Falcon, S. & Gentleman, R. Using GOstats to test gene lists for GO term association. *Bioinformatics* **23**, 257-258, doi:10.1093/bioinformatics/btl567 (2007).
51 Subramanian, A. *et al.* Gene set enrichment analysis: a knowledge-based approach for interpreting genome-wide expression profiles. *Proceedings of the National Academy of Sciences of the United States of America* **102**, 15545-15550, doi:10.1073/pnas.0506580102 (2005).
52 Lawrence, M., Gentleman, R. & Carey, V. rtracklayer: an R package for interfacing with genome browsers. *Bioinformatics* **25**, 1841-1842, doi:10.1093/bioinformatics/btp328 (2009).
53 Scharer, C. D., Barwick, B. G., Youngblood, B. A., Ahmed, R. & Boss, J. M. Global DNA methylation remodeling accompanies CD8 T cell effector function. *Journal of immunology* **191**, 3419-3429, doi:10.4049/jimmunol.1301395 (2013).
54 Wheeler, D. L. *et al.* Database resources of the National Center for Biotechnology Information. *Nucleic acids research* **29**, 11-16 (2001).

2.7 Acknowledgments

We thank M. Rosenfeld (U.C.S.D) for providing the LSD1 mice; N. Seyfried, R. Betarbet, M. Gearing, J. Fritz, and D. Cooper from the Emory ADRC (P50 AG025688), NINDS Emory Neuroscience Core Facilities (P30NS055077), Todd Golde and Pedro Cruz from The University of Florida Center for Translational Research in Neurodegenerative Disease for assistance with generating the *Lsd1* AAV6 virus, Javier Alcudia of the Stanford Gene Vector and Virus Core for help with the virus production, as well as A. Katz and S. Katz, for assistance with analyses of human tissue; J. Schroeder from the Emory Rodent Behavioral Core for help with behavioral assays; G. Pavlath for assistance with muscle histology; E. Corgiat for the myelination data; G. Bassell, V. Faundez, J. Boss, B. Kelly, C. Bean and T. Caspary for comments on the manuscript

and assistance throughout; R. Tenser for introducing us to A. Levey; and all of the Katz Lab for contributions throughout. D.J.K would like to thank J. Cohen, F. Turano, H. Lyman and S. Tilghman; D.A.M would like to thank L. Myrick; and M.A.C would like to thank R. Cordeiro and Y. France for help along the way. D.A.M was supported by the Emory PREP Post-Bac Program (5R25GM089615-04); and M.A.C and B.G.B by the GMB training grant (T32GM008490-21). B.G.B. was supported by NIH pre-doctoral fellowship F31AI112261-01. DW was supported by AG0476678 and KPS was supported by NS098615. The work was supported by a grant to D.J.K from the National Institute of Neurological Disorders and Stroke (1R01NS087142).

2.8 Figures and Tables

Figure 1. Neurodegeneration in *Lsd1*^{CAGG} mice.

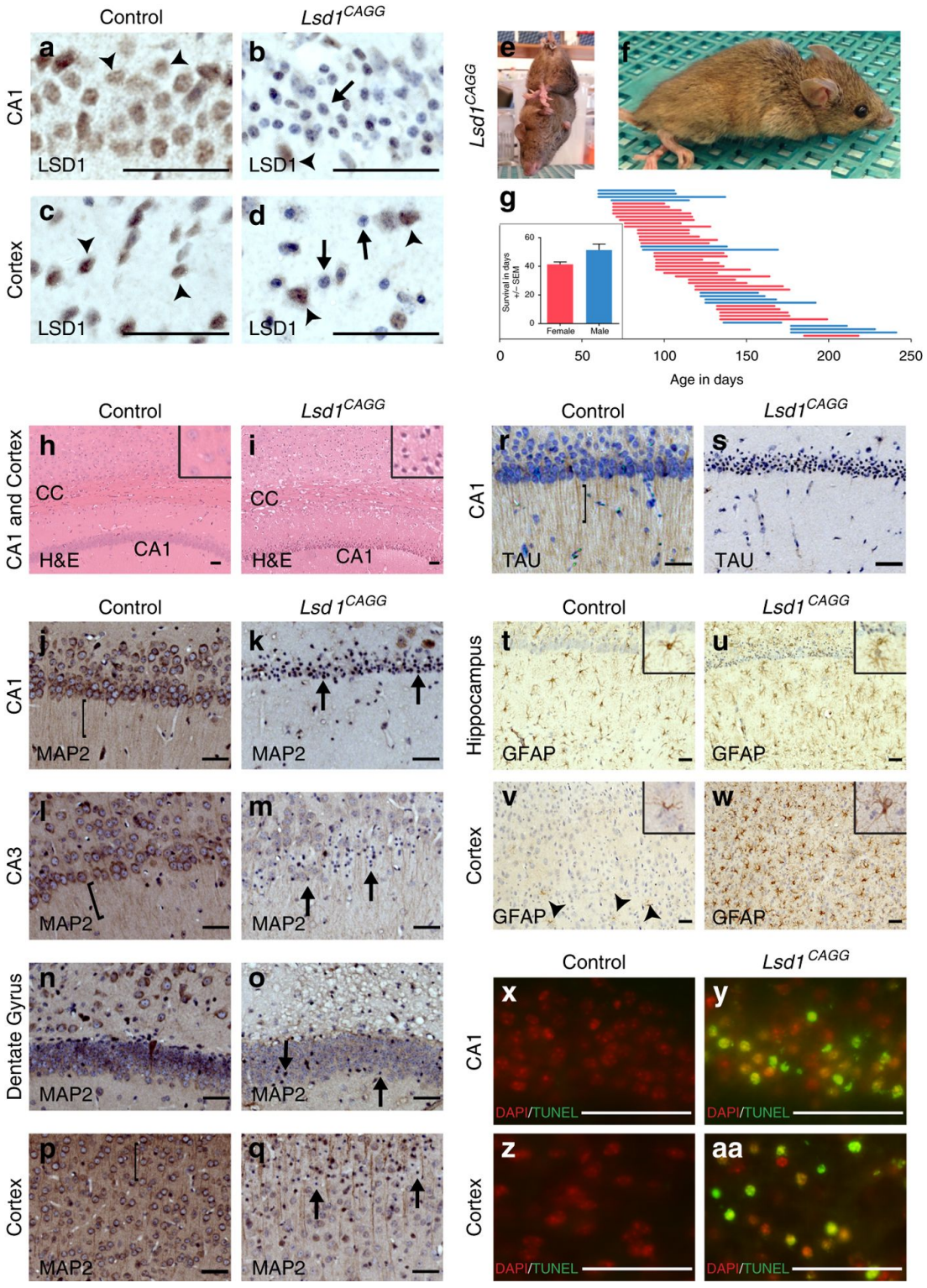

Figure 1. Neurodegeneration in *Lsd1^{CAGG}* mice.

(**a-d**) LSD1 immunohistochemistry (IHC) of control (**a,c**) and *Lsd1^{CAGG}* (**b,d**) CA1 (**a,b**) and cortex (**c,d**). Arrowheads highlight non-pyknotic LSD1 immunoreactive nuclei. Arrows highlight pyknotic LSD1 negative nuclei. (**e,f**) Representative images of *Lsd1^{CAGG}* mice with the terminal motor defect including hindlimb clasping (**e**) and failure to maintain posture (**f**). (**g**) The age of each individual male (blue) or female (red) mouse at the final tamoxifen injection (start of each line) to inducibly delete *Lsd1*, and the number of days (length of the line) until the terminal motor defect is reached. Inset shows survival in days for each sex. Data are shown as mean survival in days ± s.e.m., n=45 animals (**h,i**) H&E staining of tamoxifen injected *Cre* minus control (control) (**h**) and *Lsd1^{CAGG}* (**i**) CA1 and cortex. Insets are magnified views of non-pyknotic (**h**) and pyknotic (**i**) nuclei. CC denotes corpus callosum. (**j-q**) MAP2 IHC of control (**j, l, n, p**) and *Lsd1^{CAGG}* (**k, m, o, q**) CA1 (**j,k**), CA3 (**l,m**), dentate gyrus (**n,o**) and cortex (**p,q**). Brackets highlight dendrites and arrows highlight pyknotic nuclei. (**r,s**) Tau IHC of control (**r**) and *Lsd1^{CAGG}* (**s**) CA1. Bracket highlights axons. (**t-w**) GFAP IHC of control (**t,v**) and *Lsd1^{CAGG}* (**u,w**) hippocampus (**t,u**) and cortex (**v,w**). Arrowheads highlight sparse astrocytes in control cortex. Insets show magnified view of representative astrocytes. (**x-aa**) Merge of DAPI (red) and TUNEL (green) in control (**x,z**) and *Lsd1^{CAGG}* (**y,aa**) CA1 (**x,y**) and cortex (**z,aa**). All IHC (**j-w**) is counterstained with hematoxylin. All *Lsd1^{CAGG}* images are taken at the terminal phenotype. Scale bars= 50μm.

Figure 2. Loss of LSD1 results in learning and memory deficits

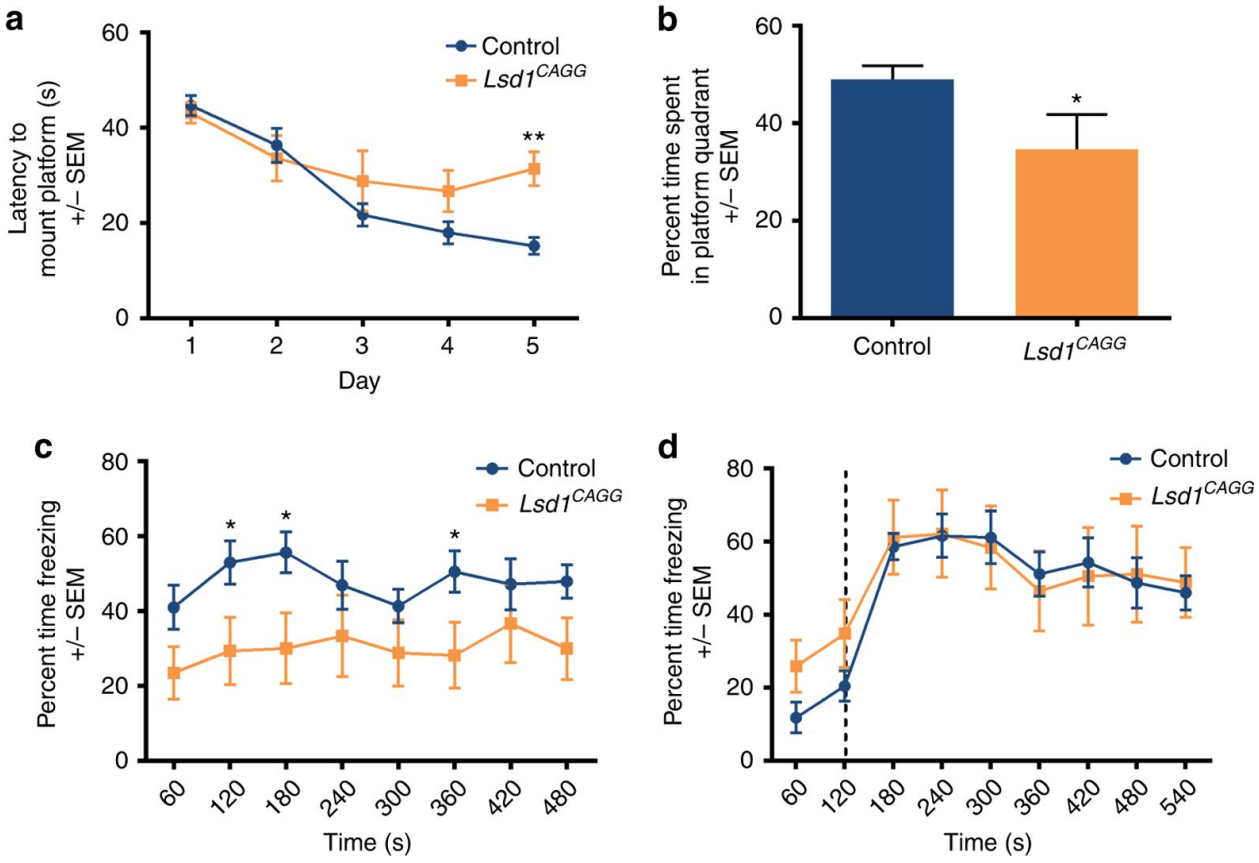

Figure 2. Loss of LSD1 results in learning and memory deficits

(**a**) Latency to mount platform (in seconds) in the Morris water maze across the 5 day training period of control (blue, $n = 15$) and $Lsd1^{CAGG}$ (orange, $n = 12$) mice. Data are shown as mean ± s.e.m. $^{**}P < 0.01$ on Day 5 compared by repeated measures two-way ANOVA with *post hoc* Sidak's multiple comparisons test. (**b**) Percent time spent swimming in platform quadrant during probe (day 6) after 5 days of water maze training for control (blue $n = 15$) and $Lsd1^{CAGG}$ mice (orange, $n = 11$) mice. Data are shown as mean ± s.e.m. $^{*}P < 0.05$ by unpaired t-test. (**c**) Percent time spent freezing during contextual fear response after fear conditioning of control (blue, $n = 12$) and $Lsd1^{CAGG}$ (orange, $n = 8$) mice. Data are shown as mean ± s.e.m. $^{*}P < 0.05$ by unpaired t-test at individual timepoints. $P = 0.052$ for difference between genotypes by repeated measures two-way ANOVA. (**d**) Percent time spent freezing during cued fear response after fear conditioning of control (blue, $n = 12$) and $Lsd1^{CAGG}$ (orange, $n = 8$) mice. Data are shown as mean ± s.e.m. Dashed line represents sound of tone.

Figure 3. Ectopic activation of stem cell genes in *Lsd1*^{CAGG} mice.

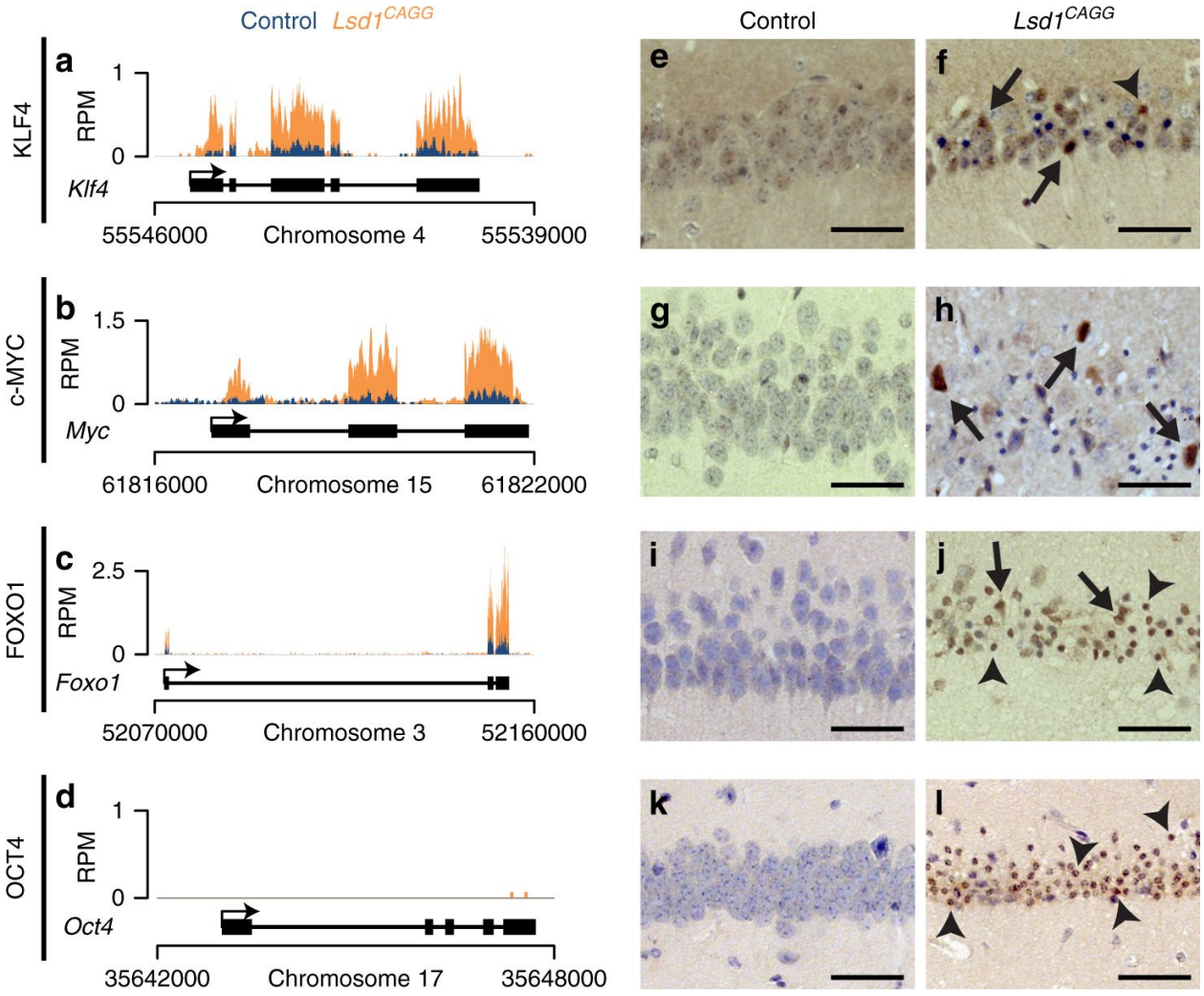

Figure 3. Ectopic activation of stem cell genes in *Lsd1*^{CAGG} mice.

(**a-d**) Genome browser style plot of RNA-seq reads per million (RPM) from control (blue) and overlaid *Lsd1*^{CAGG} (orange) hippocampi showing expression of the genes *Klf4* (**a**), *Myc* (**b**), *Foxo1*(**c**), *Oct4* (**d**). (**e-l**) Immunohistochemistry (IHC) with antibodies to KLF4 (**e,f**), c-MYC (**g,h**), FOXO1 (**i,j**), and OCT4 (**k,l**) in control (**e,g,i,k**) and *Lsd1*^{CAGG} (**f,h,j,l**) CA1 neuronal nuclei. Arrows denote non-pyknotic nuclei and arrowheads denote pyknotic nuclei. All IHC is counterstained with hematoxylin. All *Lsd1*^{CAGG} images are taken at the terminal phenotype. Scale bars= 50μm.

Figure 4. Loss of LSD1 induces common neurodegeneration pathways.

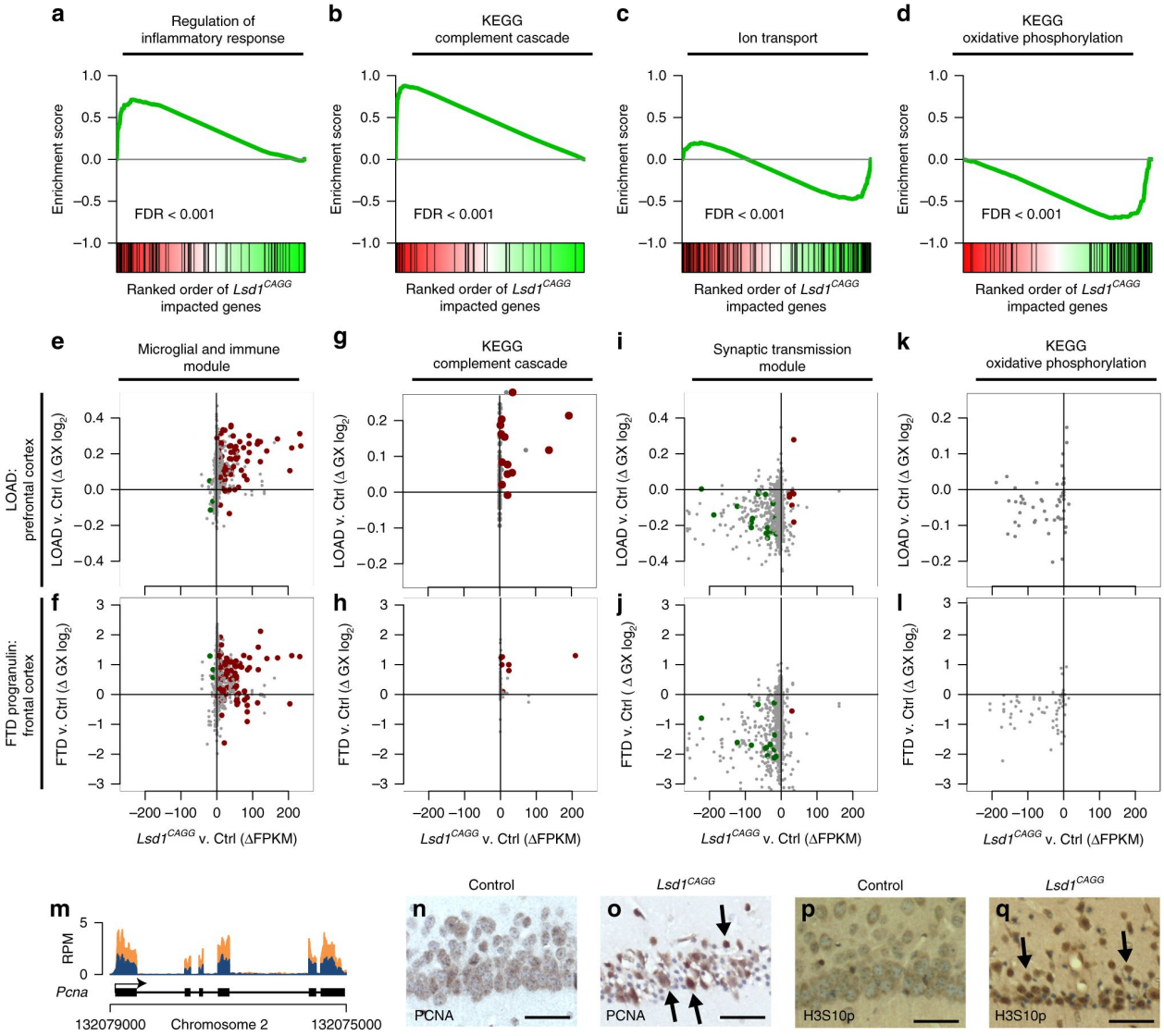

Figure 4. Loss of LSD1 induces common neurodegeneration pathways.

(**a-d**) Gene set enrichment plots of neurodegeneration pathways where *Lsd1*^{CAGG} impacted transcripts (x-axis) are sorted by magnitude of upregulation (red) to downregulation (green). The position of each gene from the gene set is represented as a black tick mark (x-axis). Enrichment score (y-axis) shows where enrichment of genes from the set occurs in the *Lsd1*^{CAGG} transcriptome. Gene sets shown are regulation of inflammatory response (**a**), Kyoto Encyclopedia of Genes and Genomes (KEGG) complement cascade (**b**), ion transport (**c**), and KEGG oxidative phosphorylation (**d**). FDR is shown for each plot. (**e-l**) Scatter plots showing correlated changes in gene expression of genes from the Microglial and Immune Module[36] (**e,f**), KEGG complement cascade (**g,h**), Synaptic Transmission Module[36] (**i,j**) and KEGG oxidative phosphorylation (**k,l**) gene sets between the *Lsd1*^{CAGG} and control hippocampus (FPKM, x-axes) compared to changes in $\log_2$ gene expression between late onset AD (LOAD) and control prefrontal cortex[36] (**e,g,i,k**; y-axis), or compared to changes between FTD-progranulin and control frontal cortex[37] (**f,h,j,l**; y-axis). The most significantly changed genes in the *Lsd1*^{CAGG} hippocampus (Supplementary Fig. 11d,e) are shown in red (upregulated) and green (downregulated). All other genes with a direct mouse/human orthologue are shown in grey. Genes with correlated expression changes are found in the top right and bottom left quadrants, while genes that do not correlate are found in the other quadrants. (**m**) Genome browser style plot (as described in Fig. 3a-d) showing *Pcna* expression in *Lsd1*^{CAGG} hippocampus (orange) compared to control (blue). (**n-q**) Immunohistochemistry with antibodies to PCNA (**n,o**), and H3S10p (**p,q**) in control (**n,p**) and *Lsd1*^{CAGG} (**o,q**) CA1 neuronal nuclei. Arrows denote non-pyknotic nuclei. All IHC is counterstained with hematoxylin. All *Lsd1*^{CAGG} images are taken at the terminal phenotype. Scale bars= 50μm.

Figure 5. Expression changes in *Lsd1*^{CAGG} mice correlate with those in AD and FTD.

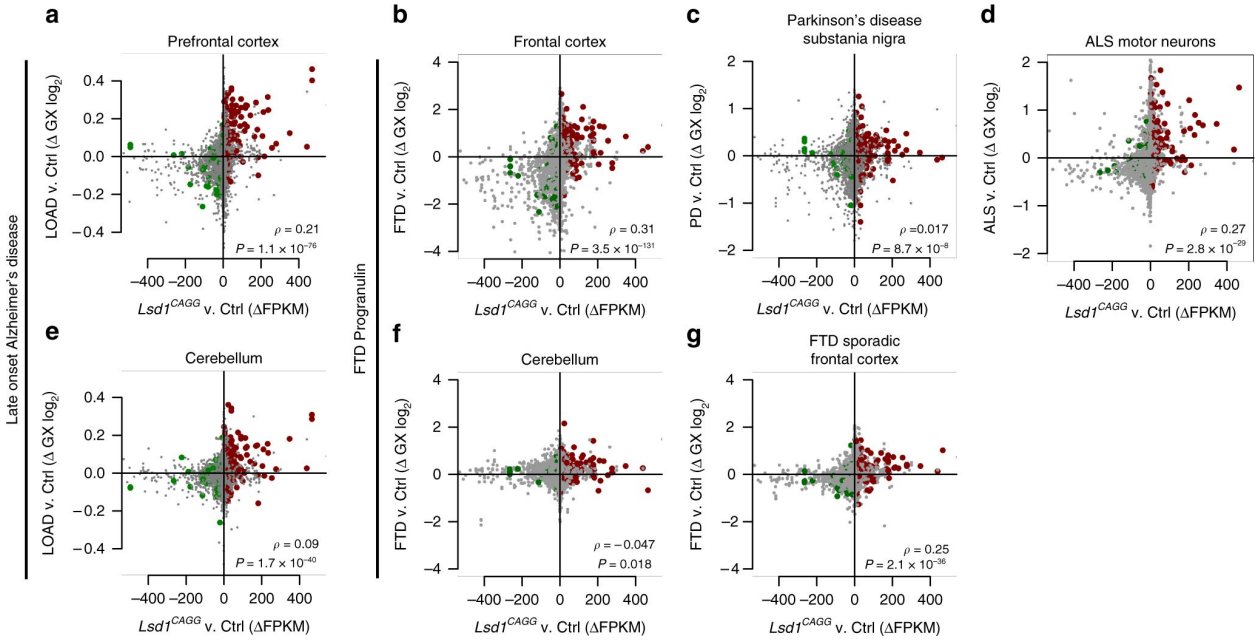

Figure 5. Expression changes in *Lsd1*^{CAGG} mice correlate with those in AD and FTD.

(**a-f**) Scatter plots (as described in Fig. 4**e-l**) showing genome-wide correlated changes in gene expression between the *Lsd1*^{CAGG} and control hippocampus (FPKM, x-axes) compared to $\log_2$ gene expression changes in late onset AD (LOAD) prefrontal cortex[36] (**a**; y-axis), FTD-progranulin frontal cortex[37] (**b**; y-axis), PD substantia nigra[39] (**c**; y-axis), ALS motor neurons[40] (d; y-axis), LOAD cerebellum[36] (**e**; y-axis), FTD-progranulin cerebellum[37] (**f**; y-axis), and sporadic FTD frontal cortex[37] (**g**; y-axis). *P*-values and ρ Pearson correlation coefficient are given.

Figure 6. LSD1 co-localization with pTau and pTDP-43 aggregates in AD and FTD.

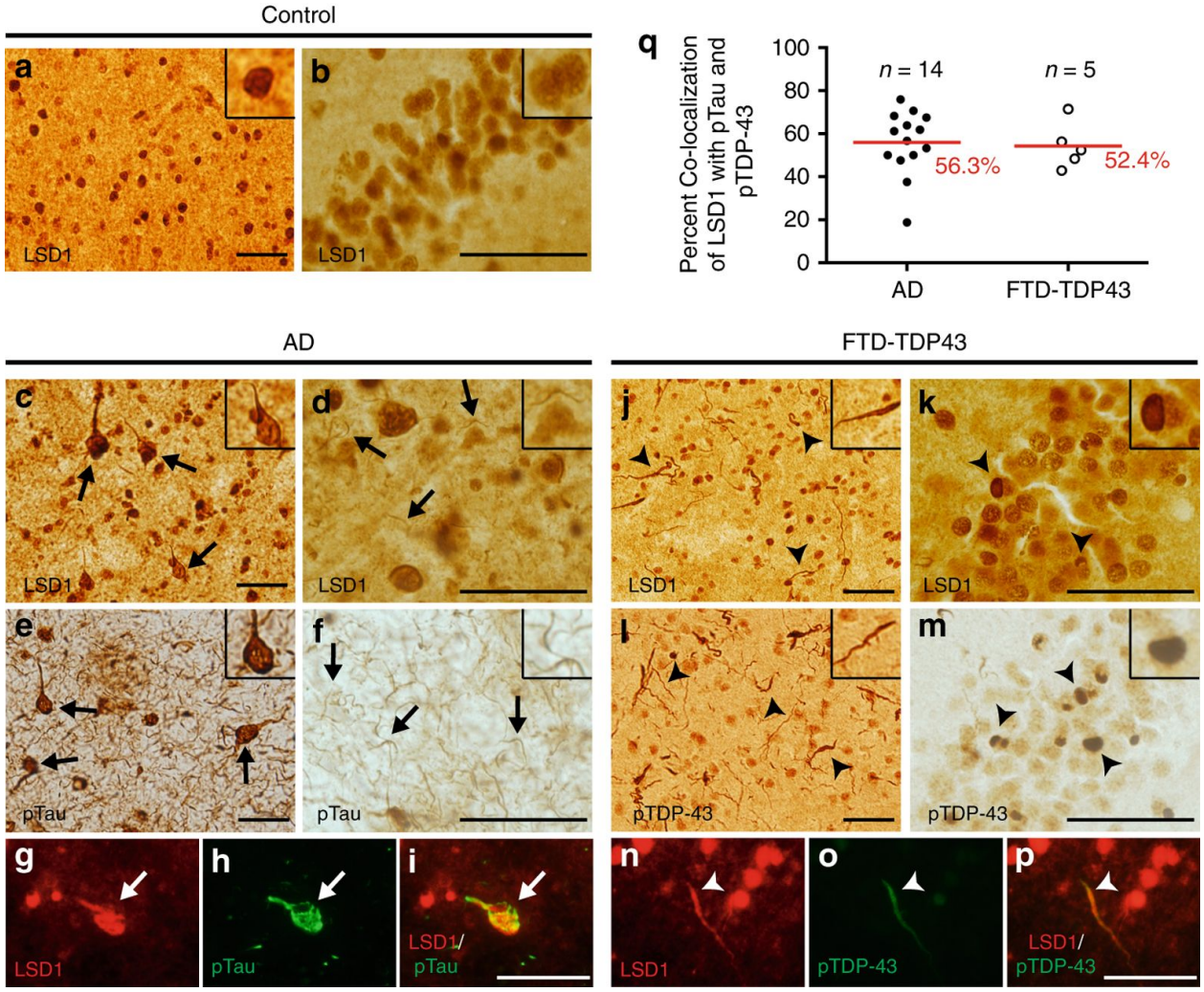

Figure 6. LSD1 co-localization with pTau and pTDP-43 aggregates in AD and FTD.

(**a,b**) LSD1 immunohistochemistry (IHC) showing expression of LSD1 in age-matched control frontal cortex (**a**) and hippocampus (**b**). (**c,d**) Representative IHC images showing LSD1 immunoreactivity localized to cytoplasmic tangle-like aggregates (**c**, arrows) and neurites (**d**, arrows) in AD frontal cortex. (**e,f**) IHC images showing pTau (AT8 epitope) neurofibrillary tangles (**e**, arrows) and neuropil threads (**f**, arrows) from the same AD frontal cortex as (**c,d**). (**g-i**) Representative image of LSD1 (**g**, red), pTau (**h**, green), and merged (**i**) immunofluorescence (IF) showing co-localization of LSD1 with a pTau neurofibrillary tangle in AD (arrow). (**j,k**) Representative IHC image showing LSD1 immunoreactivity localized to abnormal deposits in neurites (**j**, arrowheads) and cytoplasmic inclusions (**k**, arrowheads) in FTD-TDP43 frontal cortex (**j**) and hippocampus (**k**). (**l,m**) IHC images showing pTDP-43 in neurites and cytoplasmic inclusions (**l,m**, arrowheads) from the same FTD-TDP43 frontal cortex (**l**) and hippocampus (**m**) as (**j**) and (**k**), respectively. (**n-p**) Representative image of LSD1 (**n**, red), pTDP-43 (**o**, green) and merged (**p**) IF showing co-localization of LSD1 with pTDP-43 in a neurite in FTD-TDP43 (arrowhead). Insets are magnified views of LSD1 nuclear localization (**a,b**) and representative pathologies (**c-f**, **j-m**). Scale bars= 50μm. (**q**) The percentage of neurofibrillary tangles (pTau) with LSD1 colocalization in AD (n = 14 cases assayed, closed circles), and neurites (pTDP-43) with LSD1 colocalization in FTD-TDP43 (n = 5 cases assayed, open circles), with the average percentage shown (red bar).

Supplementary Figure 1. LSD1 expression in adult murine hippocampal and cortical neurons.

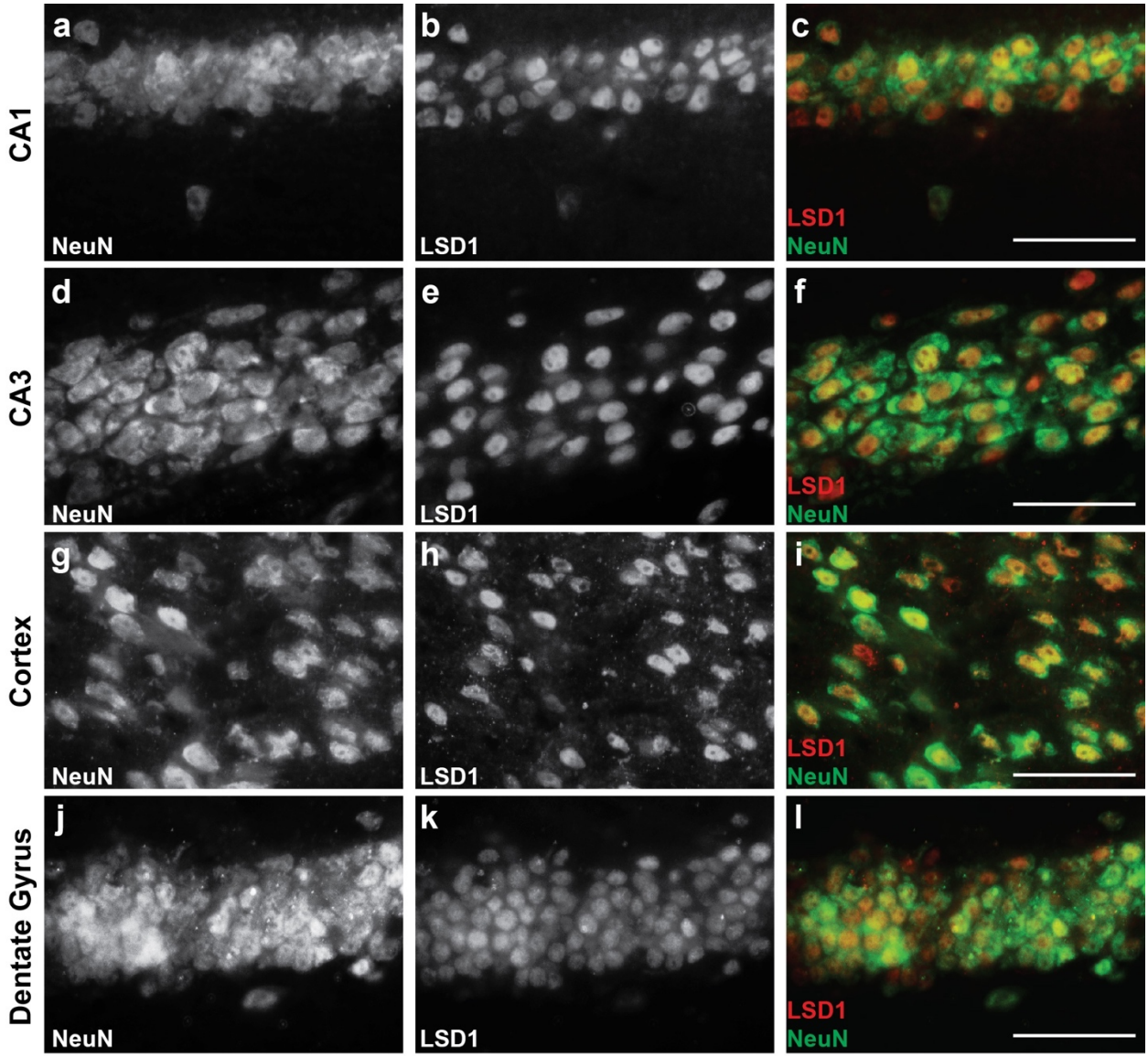

Supplementary Figure 1. LSD1 expression in adult murine hippocampal and cortical neurons.

(a-l) Immunofluorescence labelling with the neuronal nucleus marker NeuN (a,d,g,j,), LSD1 (b,e,h,k,) and merged (c,f,i,l) showing LSD1 protein in neurons of the CA1 (a-c) and CA3 (d-f) of the hippocampus, cortex (g-i) and dentate gyrus (j-l) of wild-type mice. Scale bars= 50μm.

Supplementary Figure 2. LSD1 expression in adult murine hippocampal and cortical astrocytes.

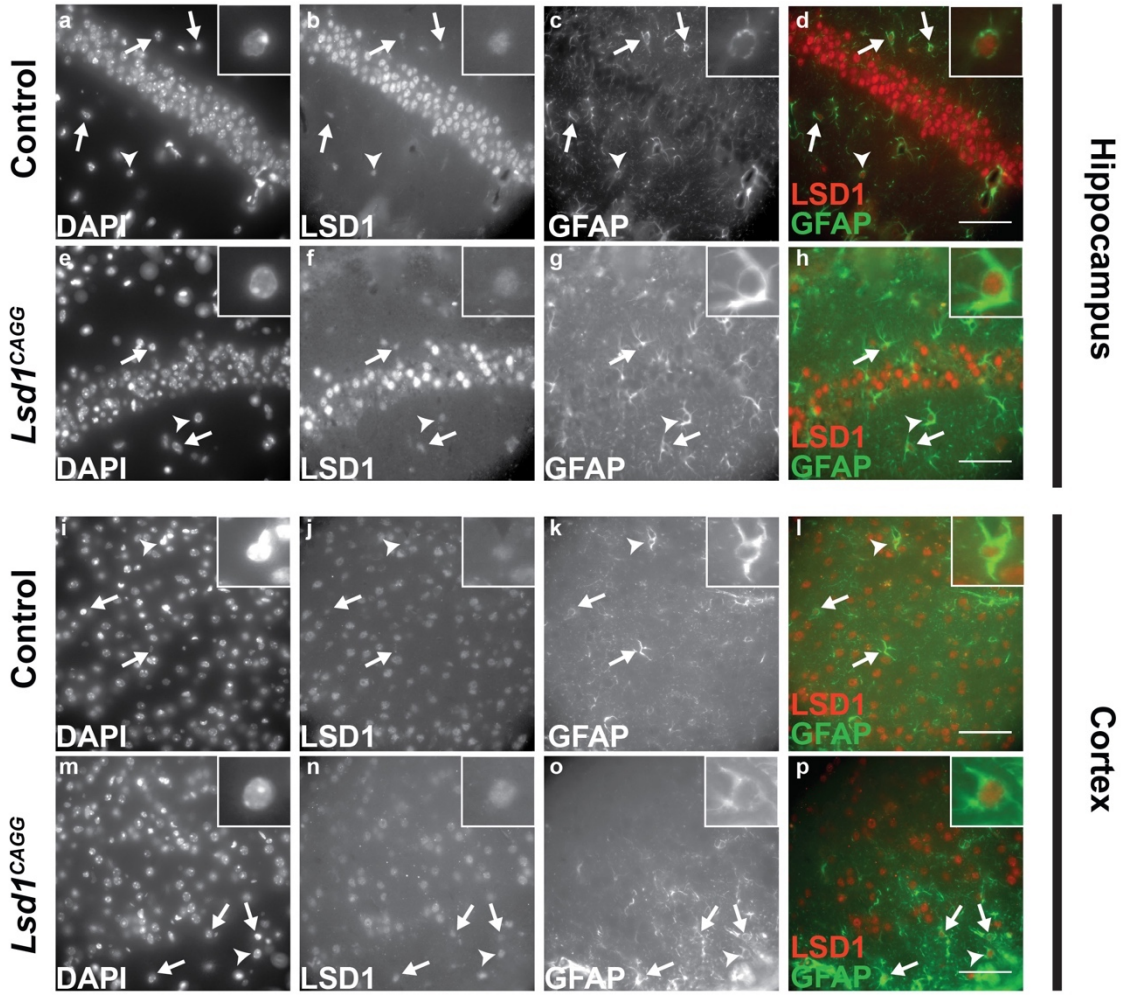

Supplementary Figure 2. LSD1 expression in adult murine hippocampal and cortical astrocytes.

(a-p) Immunofluorescence labeling of DAPI (a,e,i,m), LSD1 (b,f,j,n), GFAP (c,g,k,o) and LSD1/GFAP merge (d,h,l,p) showing LSD1 is present in GFAP positive astrocytes both in control hippocampus (a-d) and cortex (i-l), as well as *Lsd1*^{CAGG} hippocampus (e-h) and cortex (m-l), indicating LSD1 expression is not affected in astrocytes. Arrows denote representative nuclei. Arrowheads indicate nuclei magnified in inset. Scale bars= 50μm.

Supplementary Figure 3. LSD1 expression in adult murine hippocampal and cortical oligodendrocytes.

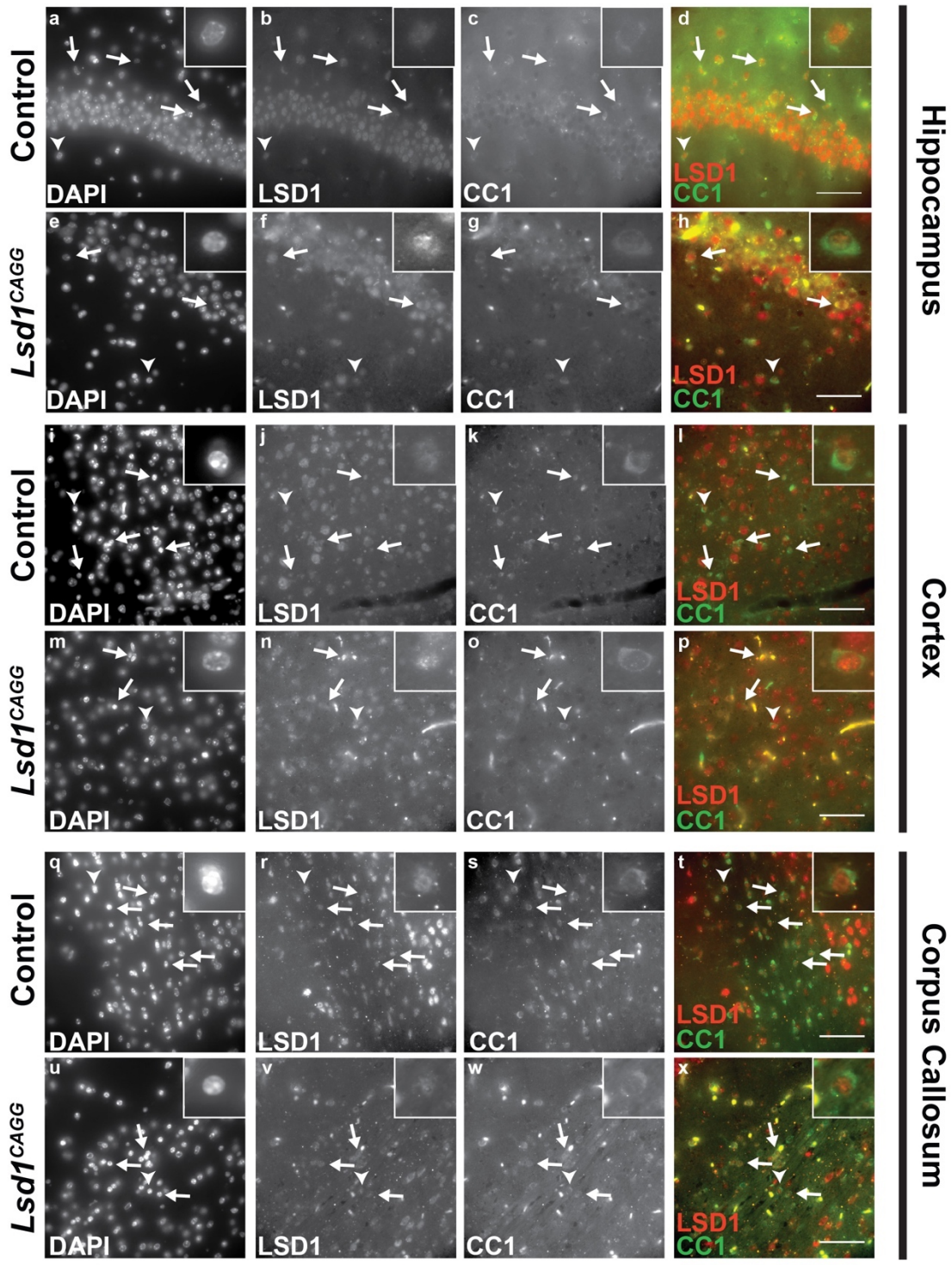

Supplementary Figure 3. LSD1 expression in adult murine hippocampal and cortical oligodendrocytes.

(a-x) Immunofluorescence labeling of DAPI (a,e,i,m,q,u), LSD1 (b,f,j,n,r,v), CC1 (c,g,k,o,s,w) and LSD1/CC1 merge (d,h,l,p,t,x) showing LSD1 is present in CC1 positive oligodendrocytes in the control hippocampus (a-d), cortex (i-l), and corpus callosum (q-t), as well as Lsd1CAGG hippocampus (e-h), cortex (m-l), and corpus callosum (u-x), indicating LSD1 expression is not affected in oligodendrocytes. Arrows denote representative nuclei. Arrowheads indicate nuclei magnified in inset. Scale bars= 50μm.

Supplementary Figure 4. LSD1 is not expressed in adult murine hippocampal and cortical microglia.

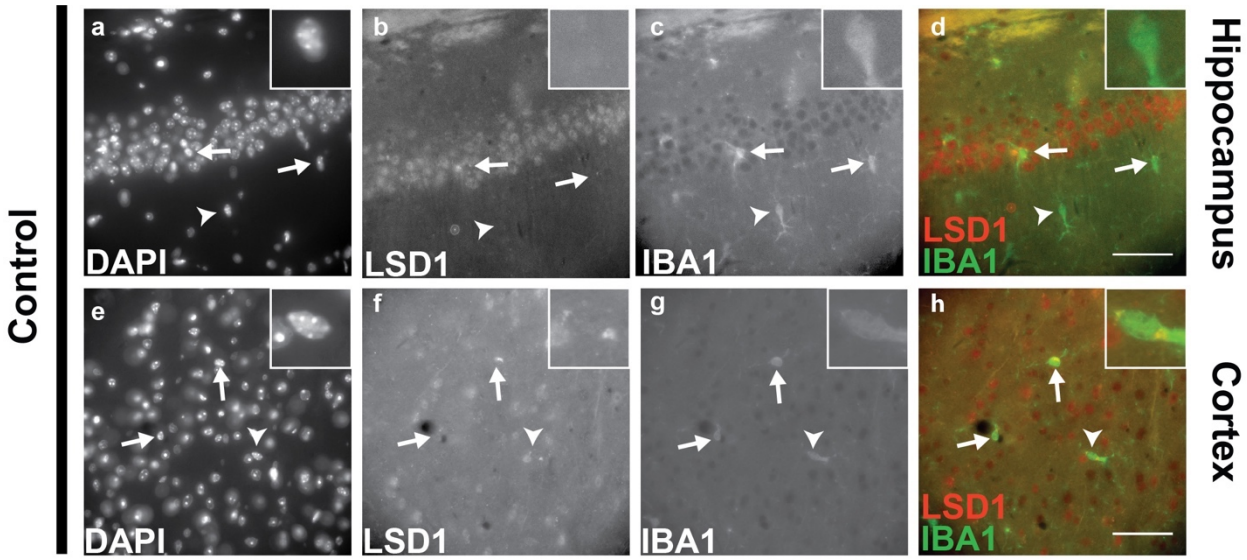

Supplementary Figure 4. LSD1 is not expressed in adult murine hippocampal and cortical microglia.

(a-h) Immunofluorescence labeling of DAPI (a,e,i,m), LSD1 (b,f,j,n), IBA1 (c,g,k,o) and LSD1/IBA1 merge (d,h,l,p) showing LSD1 is absent in IBA1 positive microglia in the hippocampus (a-d) and cortex (e-h) of control mice. Arrows denote representative nuclei. Arrowheads indicate nuclei magnified in inset. Scale bars= 50μm.

Supplementary Figure 5. Absence of spinal cord motor neuron and muscle defects in *Lsd1*^{CAGG} Mice.

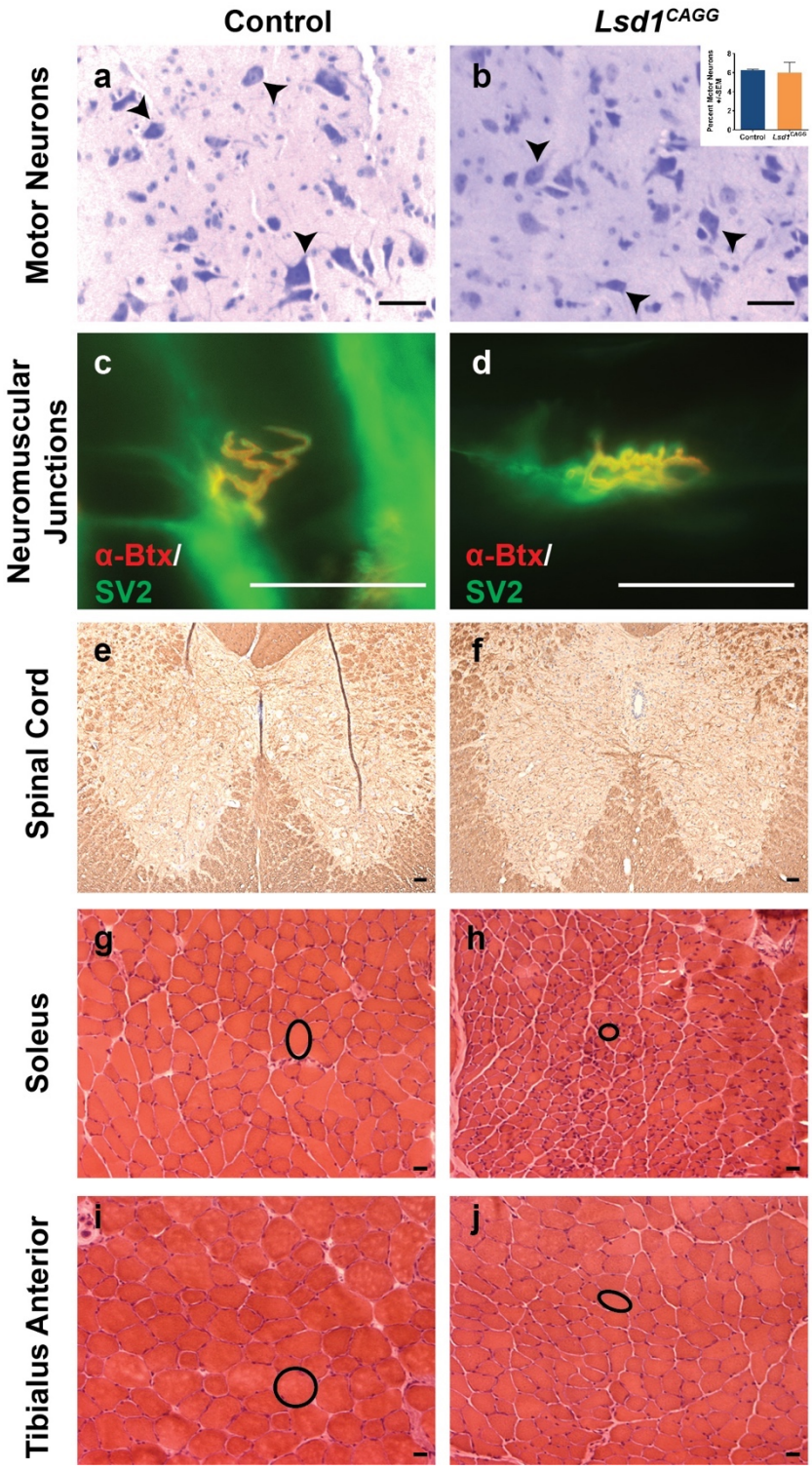

Supplementary Figure 5. Absence of spinal cord motor neuron and muscle defects in *Lsd1*^{CAGG} Mice.

(a,b) Thionin staining of control (a) and *Lsd1*^{CAGG} (b) ventral horn spinal cord motor neurons (arrowheads). Inset shows histogram of percentage motor neurons (per total ventral horn nuclei) for control (n = 3) and *Lsd1*^{CAGG} (n = 4). Values represent mean ± s.e.m. No significant difference between genotypes (p = 0.838, unpaired t test) (c,d). Immunofluorescence of neuromuscular junctions showing SV2 (presynaptic motor neurons, green) and fluorescent α-bungarotoxin (muscle acetylcholine receptors, red) in control (c) and *Lsd1*^{CAGG} (d). Colocalization SV2 and α-btx demonstrate an intact junction. (e,f) Immunohistochemistry (IHC) of myelin basic protein (MBP) in lower cervical spinal cord showing no difference in myelin amount or distribution between control (e) and *Lsd1*^{CAGG} (f). IHC is counterstained with hematoxylin. (g-j) H&E staining of soleus (g,h) and tibialus anterior muscles (i,j) showing muscle fiber size (circles) in controls (g,i) compared to reduced cell size in *Lsd1*^{CAGG} (h,j). Absence of gaps in the tissue and absence of centrally located nuclei indicate a lack of muscle degeneration. Scale bars= 50μm.

Supplementary Figure 6. Neurodegeneration in *Lsd1*^{CAGG} mice.

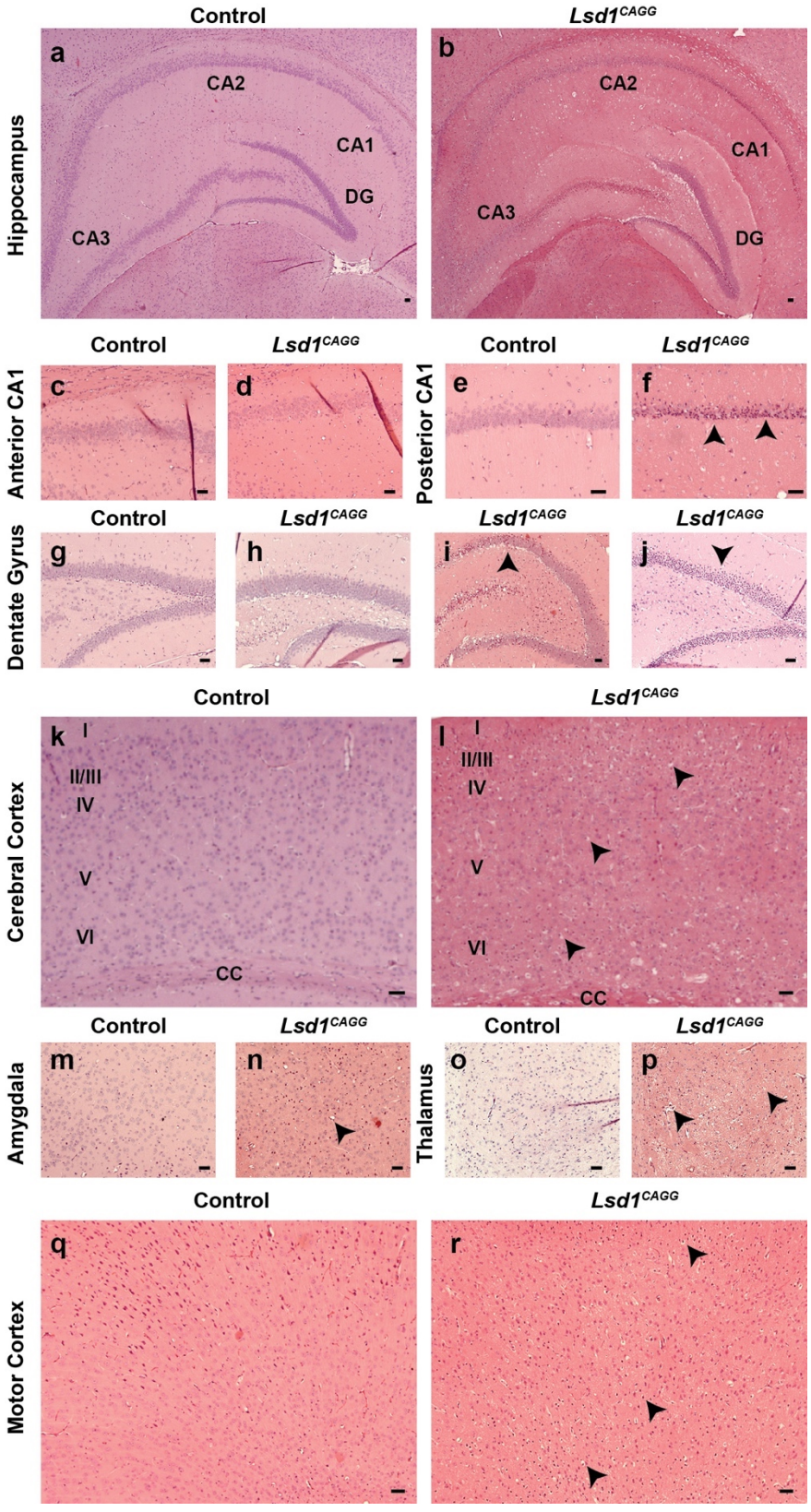

Supplementary Figure 6. Neurodegeneration in *Lsd1*^{CAGG} mice.

(a-r) H&E staining of control and *Lsd1*^{CAGG} hippocampus (a,b), anterior and posterior CA1 (c-f), dentate gyrus (g-j), cerebral cortex (k,l), amygdala (m,n), thalamus (o,p), and motor cortex (q,r). (a,b) Distribution of pyknosis in *Lsd1*^{CAGG} hippocampus with CA1 being most affected, and CA2 and CA3 moderately affected (b), compared to control with no pyknosis (a). (c-f) Increasing severity of pyknosis from anterior (d) to posterior (f) from the same *Lsd1*^{CAGG} hippocampus compared to control with no pyknosis (c,e). (g-j) Varying severity of pyknosis from three *Lsd1*^{CAGG} dentate gyruses; unaffected (h), moderately affected (i) completely affected (j) compared to control with no pyknosis (g). (k,l) Distribution of pyknosis in cerebral cortex of *Lsd1*^{CAGG} (l) in layers II/III, IV and VI, compared to control with no pyknosis (k), CC designates corpus callosum. (m-r) Distribution of pyknosis in the amygdala (n), thalamus (p) and motor cortex (r) of *Lsd1*^{CAGG} compared to control of same brain regions with no pyknosis (m,o,q). Arrowheads denote pyknotic nuclei. Scale bars= 50μm.

Supplementary Figure 7. LSD1 in different cell types

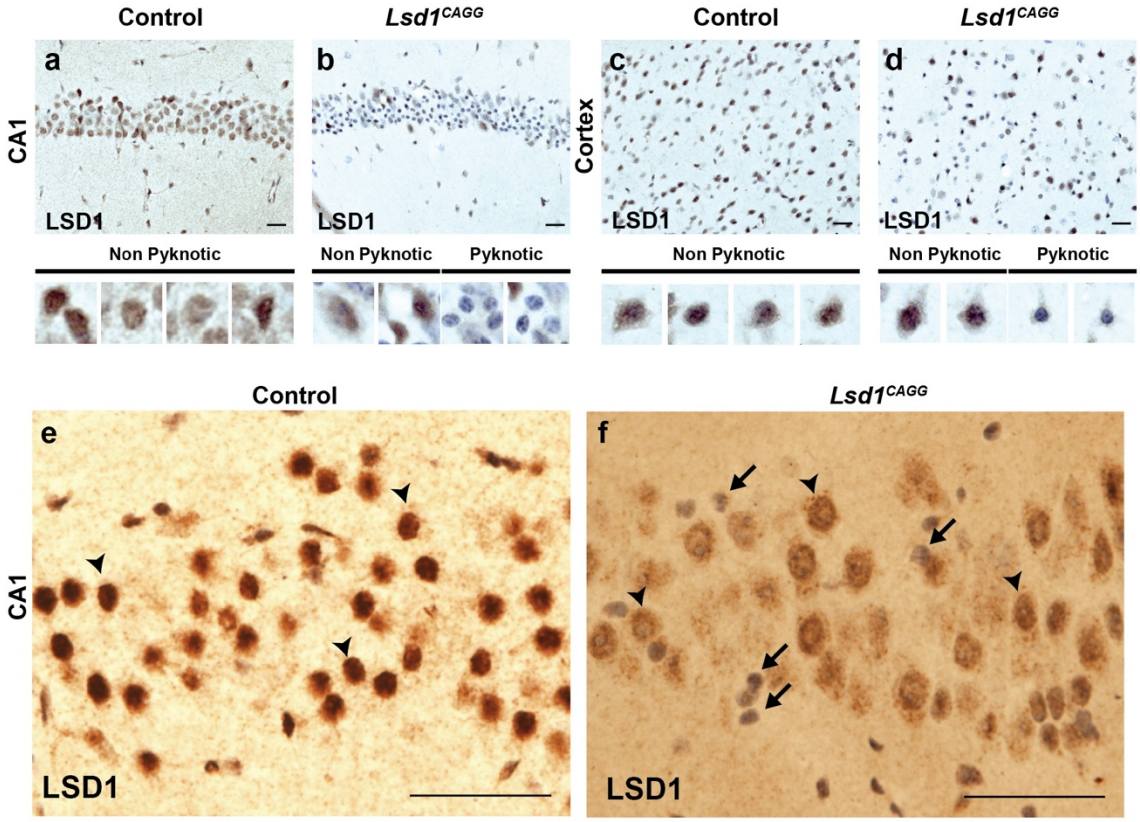

Supplementary Figure 7. LSD1 in different cell types

(a-d) LSD immunohistochemistry (IHC) in control (a,c) and *Lsd1*^{CAGG} (b,d) CA1 (a,b) and cerebral cortex (c,d) showing the breadth of pyknosis associated with absence of LSD1 immunoreactivity in *Lsd1*^{CAGG} (b,d) compared to control (a,c) where LSD1 immunoreactivity is ubiquitous and pyknosis is absent. Images are the source images from Figure 1a-d. Insets below highlight immunoreactive non-pyknotic neuronal nuclei and non-immunoreactive pyknotic neuronal nuclei. (e,f) LSD1 immunohistochemistry in control (e) and *Lsd1*^{CAGG} (f) CA1 ten weeks after a single, reduced dose of tamoxifen (1 mg/ 40g of body mass). Every neuronal nucleus in control and most neuronal nuclei in *Lsd1*^{CAGG} mice display normal LSD1 immunoreactivity and are not pyknotic (arrowheads). However, a small number of nuclei are non-immunoreactive for LSD1 and are also pyknotic (arrows), which is consistent with a cell autonomous effect on neuronal cell death.) All IHC (a-f) is counter stained with hematoxylin. Scale bars= 50μm.

Supplementary Figure 8. Absence of neurodegeneration in the *Lsd1*^{CAGG} cerebellum.

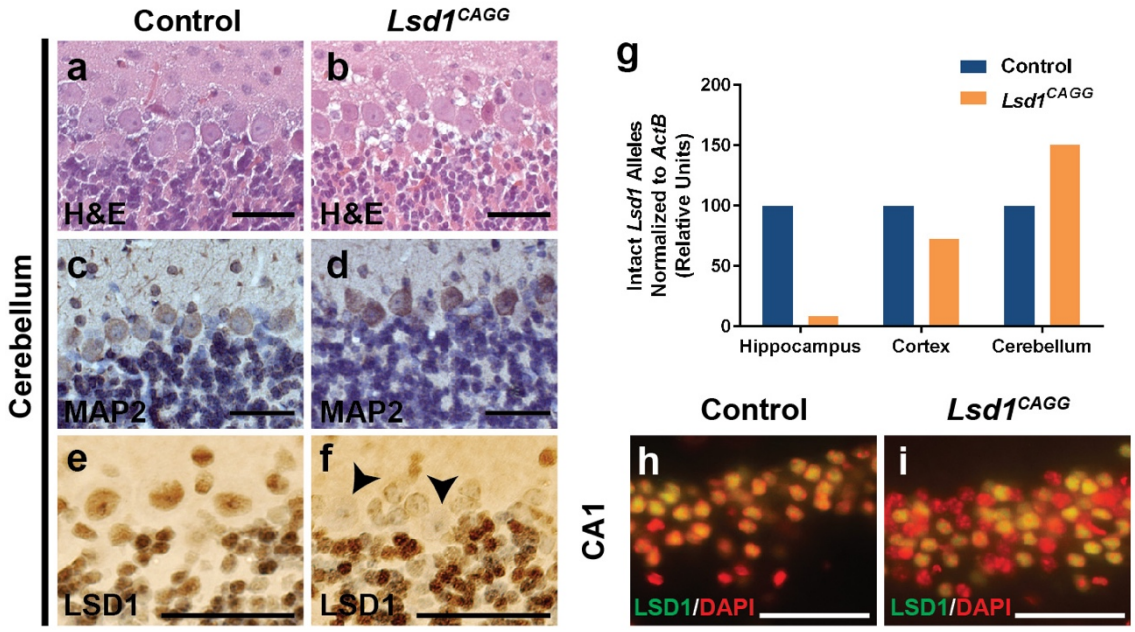

Supplementary Figure 8. Absence of neurodegeneration in the *Lsd1*^{CAGG} cerebellum.

(a,b) H&E staining of control (a) and *Lsd1*^{CAGG} (b) cerebellum showing similar cellular morphology and lack of pyknotic nuclei in *Lsd1*^{CAGG}. (c,d) MAP2 immunohistochemistry (IHC) in control (c) and *Lsd1*^{CAGG} (d) showing similar distribution in cerebellar neurons. (e,f) LSD1 IHC in control (e) and *Lsd1*^{CAGG} (f) cerebellum showing lack of LSD1 in some (arrowheads), but not all *Lsd1*^{CAGG} purkinje neurons. (g) Quantification of intact *Lsd1* alleles (revealing the extent of Lsd1 deletion) in control (blue) and *Lsd1*^{CAGG} (orange) hippocampus 24 hours after tamoxifen injection, and in cortex and cerebellum at terminal phenotype. Data are shown as relative units normalized to ActB, where the control value is set to 100. (h,i) Merge of LSD1 (green) immunofluorescence and DAPI (red) in control (h) and *Lsd1*^{CAGG} (i) CA1 nuclei showing LSD1 protein remaining in non-pyknotic nuclei approximately one week before the *Lsd1*^{CAGG} terminal motor phenotype. All IHC (c-f) is counterstained with hematoxylin. Scale bars= 50μm.

Supplementary Figure 9. LSD1 is not required for kidney and liver cell viability.

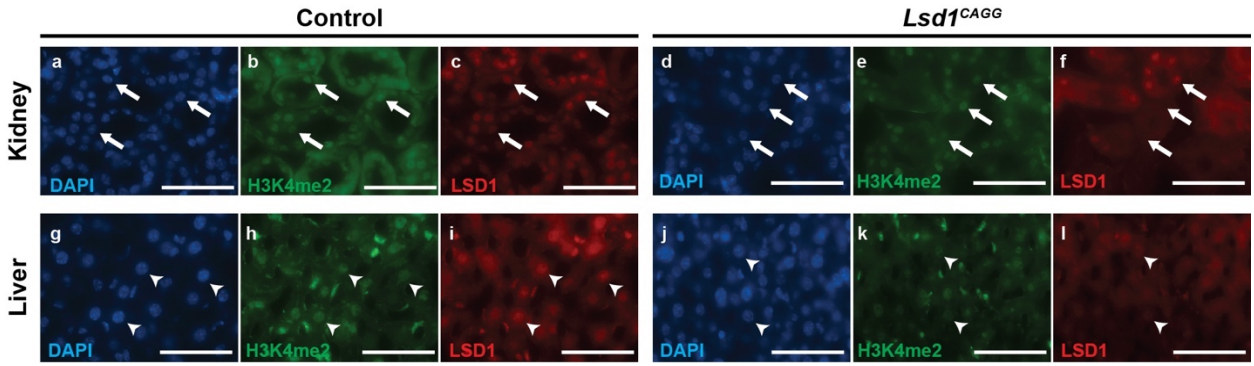

Supplementary Figure 9. LSD1 is not required for kidney and liver cell viability.

(a-l) Representative immunofluorescence images showing LSD1 (red), staining control H3K4me2 (green) and DAPI (blue) in mouse epithelial cells of the kidney nephron (a-f, arrows) and hepatocytes of the liver (g-l, arrowheads). LSD1 is normally ubiquitously expressed in controls (c,i). In Lsd1CAGG mice, LSD1 is absent (f,l), but kidney and liver morphology remains normal compared to controls (a,d,g,j). Absence of LSD1 immunoreactivity is not due to lack of antibody penetrance (b,e,h,k). Scale bars= 50μm.

Supplementary Figure 10. *Lsd1*^{CAGG} mice have learning and memory deficits.

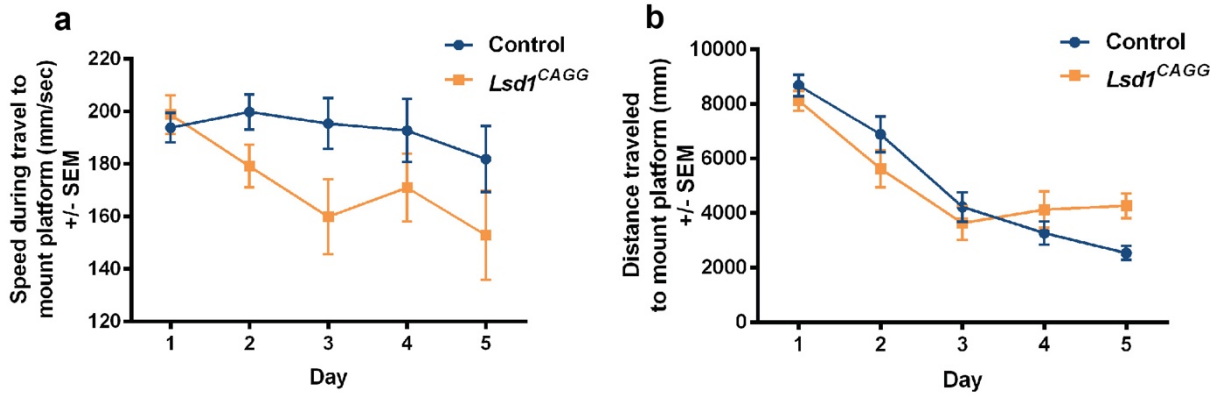

Supplementary Figure 10. *Lsd1*^{CAGG} mice have learning and memory deficits.

(a) Speed during travel to mount platform in Morris water maze across 5 day training period of control (blue, n = 15) and Lsd1CAGG (orange, n = 12) mice. Data are shown as mean ± s.e.m. No significant difference between genotypes by repeated measures two-way ANOVA. (b) Distance traveled to mount platform in Morris water maze across 5 day training period of control (blue, n = 15) and Lsd1CAGG (orange, n = 12) mice. Consistent with the increased latency to mount platform (Fig. 2a), Lsd1CAGG mice travel longer distance on Day 5. Data are shown as mean ± s.e.m.

Supplementary Figure 11. Differential expression of genes in *Lsd1*^{CAGG} hippocampus.

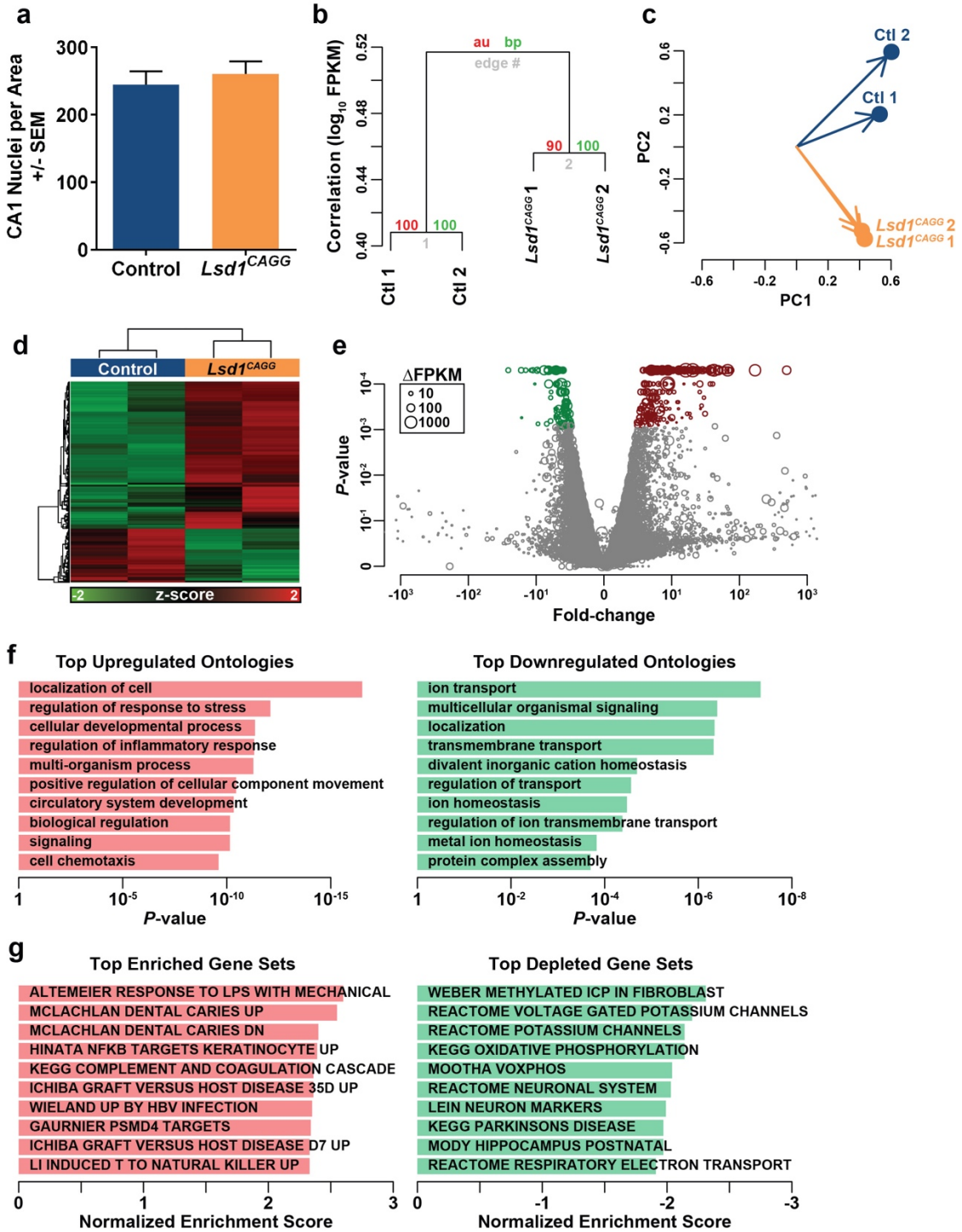

Supplementary Figure 11. Differential expression of genes in *Lsd1*^{CAGG} hippocampus.

(a) Total number of nuclei per area counted in control (n = 4) and terminal *Lsd1*^{CAGG} (n = 10) CA1. Data are shown as mean ± s.e.m. (b) Hierarchical clustering of gene expression across 24,412 transcripts (FPKM > 0.5) shows that control and Lsd1CAGG replicates significantly segregate by gene expression. The y-axis represents the log10 FPKM correlation. Approximate Unbiased P-values (AU, red) and Bootstrap Probabilities (BP, green) for each cluster are shown. (c) Principle component analysis (PCA) of 24,412 transcripts (FPKM > 0.5) shows consistent separation of control and *Lsd1*^{CAGG} samples in the first two principle components. (d) Heatmap of most significantly differentially expressed (281 upregulated, 124 downregulated) RNA-seq transcripts between *Lsd1*^{CAGG} and control hippocampi. Samples are hierarchically clustered by relative expression of differentially expressed transcripts. Relative higher (red) or lower (green) expression is indicated. (e) Volcano plot of fold-changes in gene expression (x-axis) by statistical significance (P-value; y-axis). Each circle represents a transcript and the normalized change in expression is represented by the size of the circle (legend). Those transcripts that are significantly (FDR < 0.05) differentially expressed are represented in red (281 upregulated) and green (124 downregulated). (f) Histogram of Gene Ontology analysis shows ontologies that are associated with those genes that are upregulated (red) and those genes that are downregulated (green) in the *Lsd1*^{CAGG} RNA-seq dataset. The top 10 ontologies are shown with P-values. (g) Histogram of Gene Set Enrichment Analysis shows the most enriched (red) and depleted (green) gene sets in the *Lsd1*^{CAGG} RNA-seq dataset. The top 10 gene sets are shown with normalized enrichment scores.

Supplementary Figure 12. Neural stem cell gene expression in *Lsd1*^{CAGG} mice.

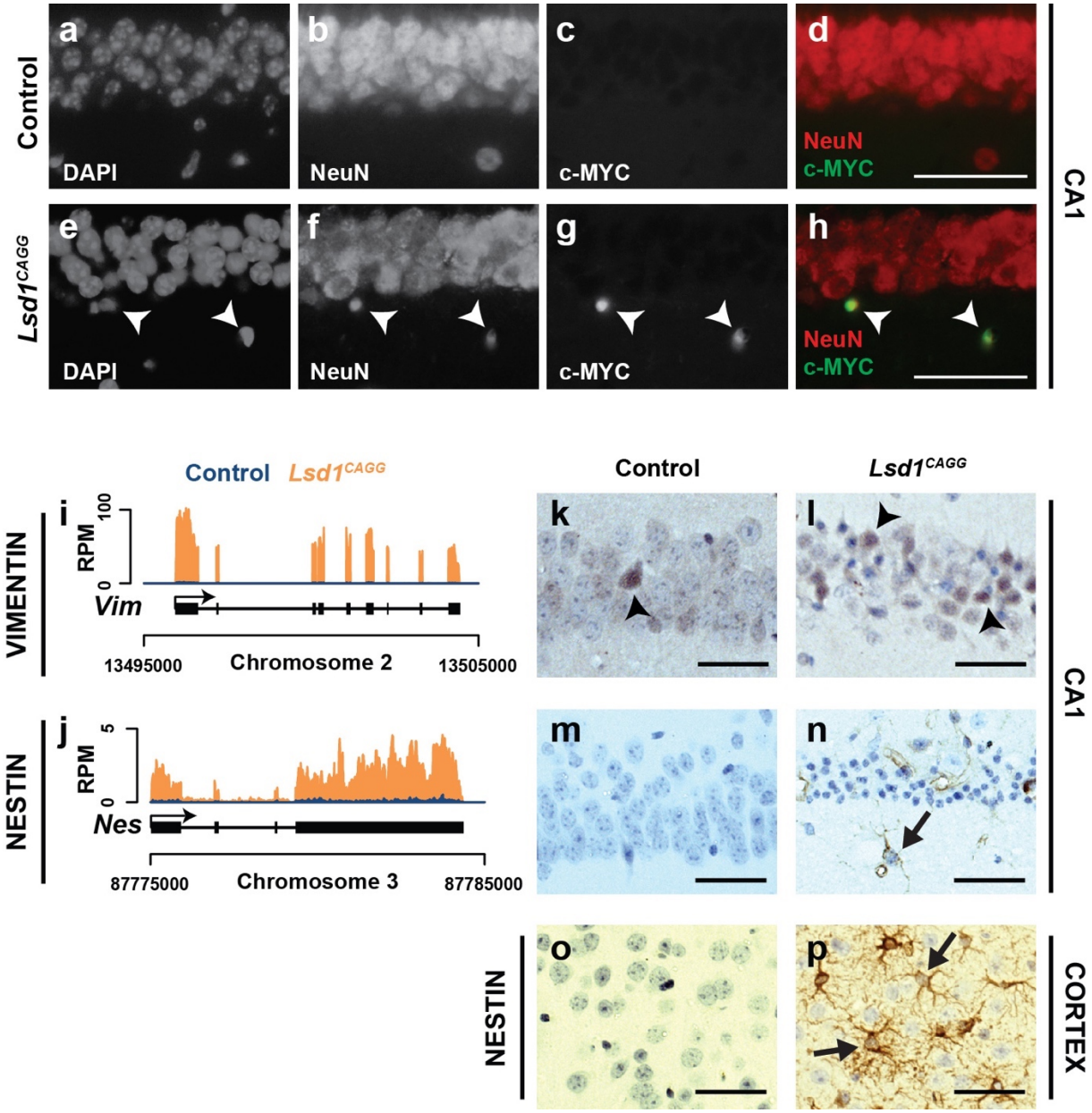

Supplementary Figure 12. Neural stem cell gene expression in *Lsd1*^{CAGG} mice

(a-h) Immunofluorescence labelling of DAPI (a,e), NeuN (b,f), c-MYC (c,g) and NeuN/c-MYC merge (d,h) in control (a-d) and *Lsd1*^{CAGG} (e-h) CA1. c-MYC protein is present in the nuclei of neurons in *Lsd1*^{CAGG} mice (e-h, arrowheads), but absent from neurons in control mince. (i,j) Genome browser style plot of RNA-seq reads per million (RPM) from control (blue) and overlaid *Lsd1*^{CAGG} (orange) hippocampus showing expression of the genes Vimentin (i) and Nestin (j). (k-p) Immunohistochemistry (IHC) with antibodies to VIMENTIN (k,l) and NESTIN (m-p) in control CA1 (k,m) and cortex (o), and *Lsd1*^{CAGG} CA1 (l,n) and cortex (p). VIMENTIN immunoreactivity was present in CA1 neurons in both control (k, arrowheads) and *Lsd1*^{CAGG} (l, arrowheads), with more immunoreactive neurons in Lsd1CAGG. NESTIN immunoreactivity was found in glial-shaped cells in Lsd1CAGG hippocampus (n) and cortex (p, arrows) and absent in control (m,o). All IHC is counterstained with hematoxylin. All Lsd1CAGG images were taken at the terminal phenotype. Scale bars= 50μm.

Supplementary Figure 13. LSD1 mislocalization is specific to AD and FTD.

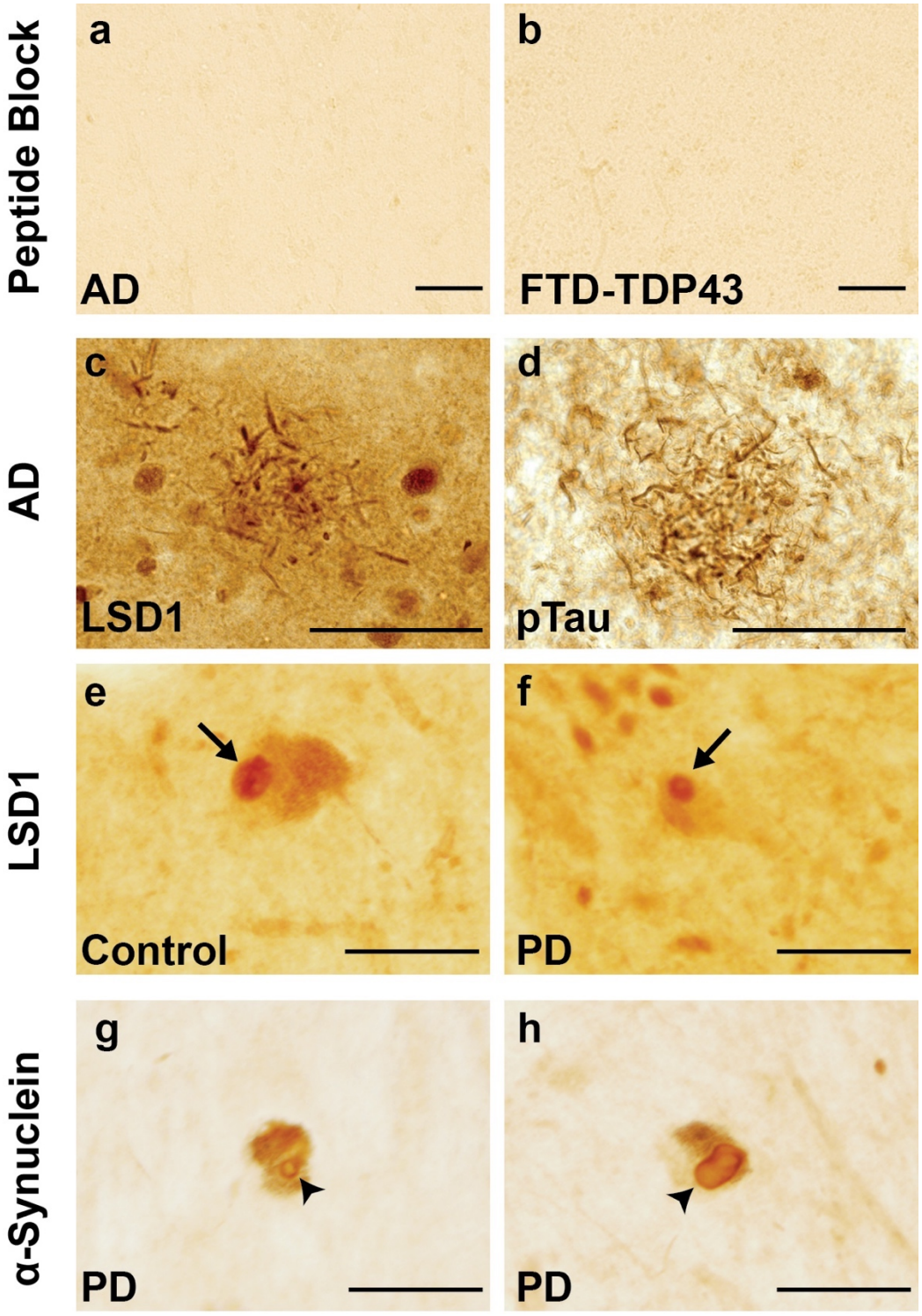

Supplementary Figure 13. LSD1 mislocalization is specific to AD and FTD.

(a,b) LSD1 IHC with primary antibody preincubated with the target peptide shows an absence of signal in AD (a) and FTD-TDP43 (b). (c,d) LSD1 (c) and pTau (AT8 epitope) (d) immunohistochemistry (IHC) showing immunoreactivity localized to neurites (c) and neuropil threads (d) around a senile plaque, but not to the amyloid core of the plaque. (e,f) LSD1 IHC in control (e) and PD (f) dopaminergic neurons of the substantia nigra shows LSD1 localized to the nucleus (arrows) and not Lewy bodies. (g,h) α-Synuclein IHC in PD shows formation of Lewy bodies in dopaminergic neurons of the substantia nigra (arrowheads). Scale bars= 50μm.

Supplementary Figure 14. Absence of pathological protein aggregates in *Lsd1*^{CAGG} mice.

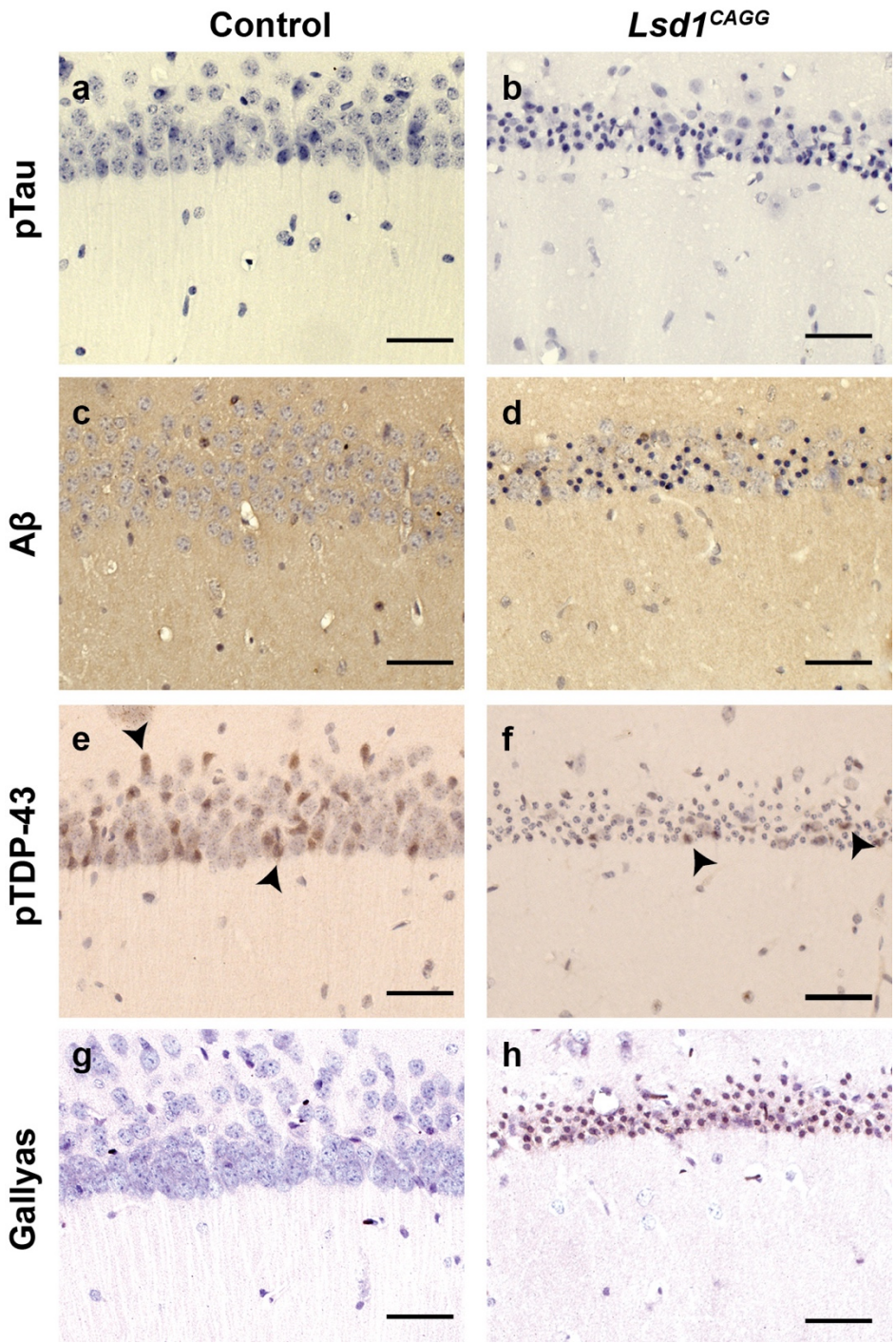

Supplementary Figure 14. Absence of pathological protein aggregates in *Lsd1^{CAGG}* mice.

(a-f) pTau (AT8 epitope) (a,b), Aβ (c,d), and pTDP-43 (e,f) immunohistochemistry in control (a,c,e) and *Lsd1^{CAGG}* (b,d,f) CA1 neurons showing absence of aggregate forms of the proteins. pTDP-43 is found sporadically in control nuclei (e, arrowheads) and shows a similar staining pattern in *Lsd1^{CAGG}* non-pyknotic nuclei (f, arrowheads), but there is no evidence of pTDP-43 aggregation. (g,h) Gallyas silver staining in control (g) and *Lsd1^{CAGG}* (h) CA1 neurons showing lack of any protein aggregation (positive stain is black). Scale bars= 50μm.

Supplementary Figure 15. Stem cell gene expression in human dementia.

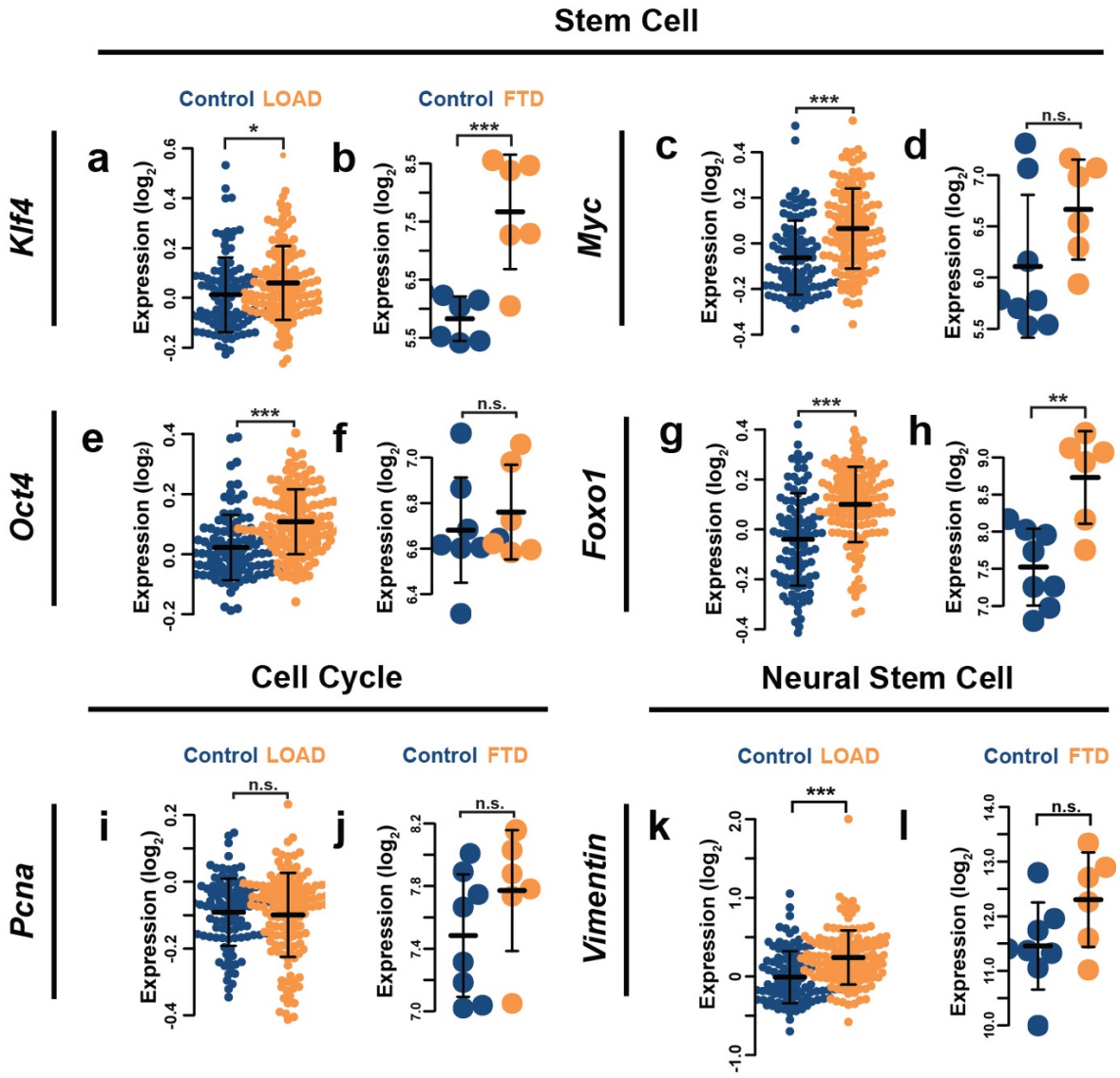

Supplementary Figure 15. Stem cell gene expression in human dementia.

(a-n) Beeswarm plots showing expression of Klf4 (a,b), Myc (c,d), Oct4 (e,f), Foxo1 (g,h), PCNA (i,j) and Vimentin (k,l) in control (blue) versus LOAD prefrontal cortex29 (a,c,e,g,i,k, orange), or control (blue) versus FTD-progranulin frontal cortex30 (b,d,f,h,j,l, orange). Values represent the log2 expression of each patient and bars represent mean ± s.d., *P < 0.05, **P < 0.01, ***P < 0.001, n.s.: not significant.

Supplementary Table 1. Primary antibodies used for immunohistochemistry (IHC) and immunofluorescence (IF) experiments.

Target	Manufacturer	Experiment	Dilution
NeuN	Millipore MAB377	Mouse IF	1:100
LSD1	Abcam 17721	Mouse IF	1:200
		Human IHC	1:500
		Human IF	1:500
		Mouse IHC	1:500
pTau (AT8 epitope)	ThermoFisher MN 1020	Human IHC	1:1,000
		Human IF	1:1,000
		Mouse IHC	1:1,000
pTDP-43	Cosmo Bio TIP-PTD-P02	Human IHC	1:1,000
		Mouse IHC	1:4,000
pTDP-43	Cosmo Bio TIP-PTD-M01	Human IF	1:1,000
α-Synuclein	J. Trojanowski and V. Lee Labs	Human IHC	1:10,000
Map2	Chemicon AB5622	Mouse IHC	1:500
Tau	Accurate BYA10741	Mouse IHC	1:200
GFAP	Dako Z0334	Mouse IHC	1:100
SV2	DSHB SV2	Mouse IF	1:50
Aβ	Signet 9220-02	Mouse IHC	1:1,000
KLF4	R&D Systems AF3158	Mouse IHC	1:100
c-MYC	Santa Cruz SC-40	Mouse IHC	1:100
OCT-4	BD Transduction Labs 611202	Mouse IHC	1:300
FOXO-1	Santa Cruz SC-11350	Mouse IHC	1:100
PCNA	Santa Cruz SC-56	Mouse IHC	1:250
H3S10p	Active Motif 39254	Mouse IHC	1:1000
NESTIN	Abcam ab11306	Mouse IHC	1:1000
VIMENTIN	Dako M072529-2	Mouse IHC	1:50
MBP	Millipore MAB386	Mouse IHC	1:100
CC1	Millapore OP80	Mouse IF	1:20
IBA1	ThermoFisher MA5-15810	Mouse IF	1:500

Shown for each antibody are the target antigen, manufacturer, experiments used and corresponding experimental dilution.

Chapter 3. The inhibition of LSD1 via sequestration contributes to tau-mediated neurodegeneration

Adapted from Amanda K. Engstrom, Alicia C. Walker, Rohitha A. Moudgal, **Dexter A. Myrick**, Stephanie M. Kyle, David J. Katz. The inhibition of LSD1 via sequestration contributes to tau-mediated neurodegeneration. *Proceedings of the National Academy of Sciences of the United States of America*, 117(46), 29133–29143. https://doi.org/10.1073/pnas.2013552117

Author Contributions: **D.A.M performed bioinformatics analysis on the RNA sequencing data. Figure 4A-B, Figure S6A, Figure S8A-J.** A.K.E and D.J.K. conceived and designed the study and wrote the manuscript. A.K.E. performed experiments with the help of A.C.W, S.M.K, and R.A.M under the direction of D.J.K. A.K.E, A.C.W, S.M.K, and R.A.M analyzed all other data and interpreted results. All authors discussed the results and commented on the manuscript.

3.1 ABSTRACT

Tauopathies are a class of neurodegenerative diseases associated with pathological tau. However, the mechanism through which tau contributes to neurodegeneration remains unknown. Previously, our lab implicated the histone demethylase LSD1 in tau-induced neurodegeneration by showing that LSD1 localizes to pathological tau aggregates in Alzheimer's disease cases, and that it is continuously required for the survival of hippocampal and cortical neurons in mice. Here, we utilize the P301S tauopathy mouse model to demonstrate that pathological tau can exclude LSD1 from the nucleus in neurons. In addition, we show that reducing LSD1 in these mice is sufficient to highly exacerbate tau-mediated neurodegeneration. Finally, we find that overexpressing LSD1 in the hippocampus of tauopathy mice, even after pathology has formed, is sufficient to significantly delay neurodegeneration. These results suggest that inhibiting LSD1 via sequestration contributes to tau-mediated neurodegeneration. Thus, LSD1 is a promising therapeutic target for tauopathies such as Alzheimer's disease.

3.2 INTRODUCTION

Tauopathies such as corticobasal degeneration, progressive supranuclear palsy, and frontotemporal lobar degeneration with tau inclusions are neurodegenerative diseases pathologically defined by different forms of tau positive intraneuronal deposits (*1-5*). In addition to these primary tauopathies, neuropathological observations of postmortem Alzheimer's disease (AD) brains show the presence neurofibrillary tangles (NFTs) of hyperphosphorylated tau protein, as well as plaques containing β-amyloid (Aβ) peptide (*6-9*). AD is the leading cause of age-related dementia, resulting from neuronal cell death in the frontal and temporal cortices, as well as the hippocampus (*7*). As dementia progresses, the spatial pattern of tau pathology highly correlates with the level of cognitive impairment (*10-13*). In addition, Aβ oligomers and/or plaques can enhance tau pathology in various mouse models (*24, 25*), and there is increasing evidence that accumulation of Aβ plaques can contribute to tau pathology (*3, 26, 27*). The most well-defined physiological role of tau is in stabilizing microtubules, particularly in neuronal axons (*2*). However, in the pathological state, tau becomes aberrantly phosphorylated (*2, 14, 15*), truncated (*1, 4*), and aggregates into oligomers and larger insoluble filaments (*16, 17*). This pathology is thought to trigger synaptic loss, dramatic genome-wide expression changes, increased inflammatory response, and neuronal cell death (*18-21*). These data suggest that pathological tau may be a downstream mediator of the neurotoxic effects leading to neuronal degeneration in AD.

Previously, our lab demonstrated that deleting the histone demethylase *Lsd1* in adult mice leads to significant neuronal cell death in the hippocampus and cortex with associated learning and memory defects (*28*). In this mouse model, loss of *Lsd1* induces genome-wide expression changes that significantly overlap with those observed in the brains of postmortem human AD cases, but not other neurodegenerative diseases, such as Parkinson's disease or amyotrophic

lateral sclerosis (ALS) cases. Consistent with this overlap, we observed LSD1 protein mislocalized to cytoplasmic NFTs, but not associated with Aβ plaques in AD cases or Lewy bodies of α-synuclein in Parkinson's disease cases (*28*). These data highlight the requirement for LSD1 in neuronal survival and suggest that the nuclear function of the histone demethylase LSD1 could be disrupted by mislocalization to pathological tau.

To investigate how LSD1 may contribute to tau-mediated neurodegeneration, we utilized the PS19 P301S tauopathy mouse model (hereafter referred to as PS19 Tau). PS19 Tau mice express a P301S mutated form of the human tau protein, originally identified in a frontotemporal dementia with parkinsonism (FTDP-17) patient, driven by the prion promoter throughout the nervous system (*29*). When expressed in mice, the P301S tau protein is prone to hyperphosphorylation and somatodendritic aggregation, without the presence of Aβ plaques. PS19 Tau mice develop a heavy pathological tau burden and have been well characterized for the temporal progression of tau pathology and disease-related phenotypes (*30, 31*). However, the mechanism of neuronal cell death caused by pathological tau is still unknown.

Here, we provide functional data that the inhibition of LSD1 function contributes to tau induced neurodegeneration. We demonstrate in PS19 Tau mice that pathological tau sequesters LSD1 in the cytoplasm of neurons throughout the brain. This results in depletion of LSD1 from the nucleus. Additionally, we provide genetic and molecular evidence that pathological tau contributes to neurodegeneration by disrupting LSD1. Finally, we show that overexpressing LSD1 in hippocampal neurons is sufficient to suppress neuronal cell death even after pathological tau has formed. We propose that pathological tau contributes to neuronal cell death by sequestering LSD1 in the cytoplasm, depleting the nuclear pool of LSD1 that is required for neuronal survival.

3.3 RESULTS

Tau pathology depletes LSD1 from the nucleus in the PS19 Tau mouse model

Previously, we showed in human AD cases that LSD1 protein inappropriately colocalizes with NFTs in the cell body of hippocampal and cortical neurons, while in unaffected controls LSD1 was properly localized exclusively to the nucleus (*28*). However, because neurons in AD cases with intracellular NFTs presumably die and are cleared, it was difficult to determine whether tau prevents LSD1 from localizing to the nucleus in a dying neuron. To address this possibility, we performed LSD1 immunofluorescence on 12 month old PS19 Tau mice, which have significant tau pathology (*29*). Because PS19 Tau mice undergo neurodegeneration over a shortened period, there are more neurons undergoing neurodegeneration at any given time point. Thus, we reasoned that it may be possible to observe LSD1 depletion from the nucleus. Similar to what we observe in humans, LSD1 protein in 12 month old Wild Type mice was localized to the nucleus of neurons in the cerebral cortex (Fig. 1A-C) and the hippocampus (Fig. S1 A-C). However, in 12 month old PS19 Tau mice, LSD1 protein was sequestered in the cytoplasm and depleted from the nucleus both in the cerebral cortex (Fig. 1D-F) and the hippocampus (Fig. S1 D-F). These are both regions where we observe substantial cytoplasmic tau pathology (Fig. 1G-I; Fig. S1 G-I). Similarly, in other brain regions that accumulate tau pathology, such as the thalamus and amygdala, LSD1 was localized to the nucleus in 12 month old Wild Type control mice (Fig. S1 J-O), but abnormally localized to the cytoplasm in PS19 Tau mouse littermates (Fig. S1 P-U). Overall, we observed sequestration of LSD1 in 6 out of 7 mice analyzed. In each of the 6 mice, there were varying levels of sequestration ranging from LSD1 found in both the nucleus and cytoplasm (Fig. S1 V-X), to depletion from the nucleus (Fig. S1 Y-DD).

3.3.1 Reduction of LSD1 increases the mouse tauopathy phenotype

If the presence of pathological tau in the cytoplasm is leading to neuronal cell death through the sequestration and nuclear depletion of LSD1, we would expect that lowering the overall levels of LSD1 would accelerate depletion and exacerbate the progression of disease. To test this, we made PS19 Tau mice heterozygous for *Lsd1* (hereafter referred to as PS19;$Lsd1^{\Delta/+}$, Fig. S2 A). *Lsd1* heterozygotes (hereafter referred to as $Lsd1^{\Delta/+}$) have a functioning copy of *Lsd1* and don't have phenotypes associated with LSD1 loss of function (*32-34*). Thus, *Lsd1* heterozygosity does not completely compromise LSD1 function. Instead mice that are heterozygous for *Lsd1* are sensitized to mechanisms affecting LSD1 localization and function. Consistent with this, we observed a 30% reduction in transcript levels (Fig. S2 B) and a 35% reduction in protein levels (Fig. S2 C,D) in $Lsd1^{\Delta/+}$ mice compared to their $Lsd1^{+/+}$ littermates. Surprisingly, PS19 Tau mice have a 20% increase in LSD1 protein levels compared to $Lsd1^{+/+}$ littermates. Nevertheless, consistent with the reduction in LSD1 that we observe in $Lsd1^{\Delta/+}$ mice, PS19;$Lsd1^{\Delta/+}$ mice have a similar 26% reduction in transcript levels (Fig. S2 B) and a 31% reduction in protein levels (Fig. S2 C,D) compared to PS19 Tau littermates. In addition, all genotypes were born at normal Mendelian ratios with equal male/female ratios.

As expected, $Lsd1^{\Delta/+}$ mice had normal survival (Fig. 2A). In contrast, PS19 Tau mice had a reduced overall survival (Fig. 2A) (*29*). When one copy of *Lsd1* was removed from PS19 Tau mice, their reduced survival was significantly exacerbated (P-value = 0.0017, Fig. 2A). As expected, there was little effect on the onset of reduced viability. The initial decline in the survival of PS19;$Lsd1^{\Delta/+}$ mice started only slightly earlier than PS19 Tau mice, but after the appearance of pathological tau in neurons (Fig. S6 K-M) (*29*). This suggests that pathological tau may have to be present before *Lsd1* heterozygosity has deleterious effects. Subsequently,

PS19;*Lsd1*$^{\Delta/+}$ mice had a 14% reduction in median lifespan compared to PS19 Tau mice and reached median survival 44 days earlier then PS19 Tau mice. In addition, there was a further exacerbation of reduced lifespan as pathology became more severe. PS19;*Lsd1*$^{\Delta/+}$ mice reached the point when there was only 10% of the population remaining 83 days earlier than PS19 Tau mice, and all but one of the last 25% of PS19;*Lsd1*$^{\Delta/+}$ mice died between 11.5-13.5 months, compared to 13.5-19 months in PS19 Tau mice. As a result, 28% of PS19 Tau mice were still alive after all but one of the PS19;*Lsd1*$^{\Delta/+}$ mice had died (Fig. 2A).

PS19 Tau mice develop paralysis starting with hind limb clasping which progresses until they are unable to feed (*29*). In our hands, PS19 Tau mice displayed intermittent hind limb clasping starting at approximately 6 months of age. At 12 months, these mice had a severe clasp, but were still mobile. This is delayed compared to what was originally reported by Yoshiyama and colleagues (*29*). PS19;*Lsd1*$^{\Delta/+}$ mice also displayed intermittent hind limb clasping beginning at approximately 6 months of age. However PS19;*Lsd1*$^{\Delta/+}$ mice became terminally paralyzed at a faster rate compared to PS19 Tau mouse littermates. At 12 months, when PS19 Tau mice were still mobile, PS19;*Lsd1*$^{\Delta/+}$ mice were severely paralyzed and typically terminal (Movie S1). To quantitatively assess paralysis we performed rotarod and grid performance tests. In the rotarod, we assessed the ability of the mice to stay on the rotating rod (latency to fall) (Fig. 2B), the speed of the rod at which they fall off the rotarod (rotations per minute) (Fig. 2C), and the total distance traveled (Fig. 2D). All genotypes performed the same at 6 months and 8 months (Fig. 2B-D). However, at 10 months, when PS19 Tau mice still performed normally, PS19;*Lsd1*$^{\Delta/+}$ mice had a significant deficit in mobility (P-value < 0.01, Fig. 2B,C). A deficit in PS19;*Lsd1*$^{\Delta/+}$ mice was also observed at 10 months in the total distance traveled (Fig. 2D) and in grid performance testing (Fig. S3 A), though neither were statistically significant.

To further investigate the exacerbation of paralysis we examined the spinal cord motor neurons. Healthy motor neurons from *Lsd1*$^{+/+}$ control mice express LSD1 (Fig. S3 B-D) and are classically identified by circular nuclei at the center of a large cell body. In contrast to the healthy motor neurons we observed in 12 month old PS19 Tau mice (Fig. S3 E), many of the motor neurons in PS19;*Lsd1*$^{\Delta/+}$ mice at 12 months had abnormal morphology, with the nucleus skewed to the edge of the cell body (Fig. S3 E vs. S3 F) and a ballooned cell body (Fig. S3 F). Within the cell body we found aberrant hyperphosphorylated NFH (heavy chain neurofilament), which is a sign of activated neuronal stress pathways (Fig S3 G vs. S3 H) (*35, 36*). This abnormal morphology is highly reminiscent of a well-established process known as chromatolysis, which is characterized by swelling of the neuronal cell body, disruption of Nissl granules, and pyknotic or shrunken nuclei abnormally skewed to the edge of the cell body (*37, 38*). Chromatolysis, which is linked to neuronal stress and often leads to apoptosis (*38*), has been observed in AD and other neurodegenerative diseases (*37, 39-41*).

3.3.2 Reduction of LSD1 exacerbates PS19 Tau neurodegeneration

In addition to accelerating the paralysis phenotype, reducing the level of *Lsd1* in PS19 Tau mice exacerbated neuronal cell death in the brain. At 6 months and 8 months, we observed no difference between genotypes in the overall morphology in the hippocampus (Fig. S4 A-H) based on histological analysis. There was also no difference between *Lsd1*$^{+/+}$ and *Lsd1*$^{\Delta/+}$ mice at 10 months or 12 months (Fig. 3A,B; Fig. S4 I,J,M,N; Fig. S5 A,B,E,F,I,J,M,N). At 10 months, PS19 Tau mice had very little cell loss in the hippocampus compared to *Lsd1*$^{+/+}$ and *Lsd1*$^{\Delta/+}$ control mice (Fig. S4 I-K, M-O). In contrast, at 10 months, PS19;*Lsd1*$^{\Delta/+}$ mice had dramatic cell loss both in the CA1 region of the hippocampus and throughout the posterior hippocampus (Fig.

S4 L,P). At 12 months, the PS19 Tau mice had a slight decrease in CA1 and CA3 neurons spanning the hippocampal pyramidal cell layer compared to *Lsd1*$^{+/+}$ control mice (17% and 19.4% respectively, Fig. 3A,B; Fig. S5 A-C, E-G). In comparison, PS19;*Lsd1*$^{\Delta/+}$ mice had a 52% and 54% decrease in the CA1 and CA3 respectively (Fig. 3A,B; Fig. S5 D,H) compared to *Lsd1*$^{+/+}$ control mice. This resulted in decreased overall brain size (Fig. 3C) and brain weight (Fig. 3D) in PS19;*Lsd1*$^{\Delta/+}$ mice compared to PS19 Tau and *Lsd1*$^{\Delta/+}$ mouse littermates. Additionally, at 12 months there were increased levels of cell loss in the Dentate Gyrus (Fig. S5 I-L), and throughout the posterior hippocampus (Fig. S5 M-P).

Along with the histology, we monitored the progression of neuronal cell death in the same individual over time by performing magnetic resonance imaging (MRI) at 6 months and again at 10 months (Movie S2). At 6 months, there was no sign of cell loss or ventricular dilatation in *Lsd1*$^{\Delta/+}$, PS19 Tau, or PS19;*Lsd1*$^{\Delta/+}$ mice (Fig. 3E-G). However, at 10 months the MRI showed that there was dramatic ventricular dilatation in PS19;*Lsd1*$^{\Delta/+}$ mice, as evidenced by high-intensity areas in T2- weighted imaging, with substantial hippocampal and neocortical atrophy (Fig. 3J vs. 3H, Movie S2). At this timepoint, PS19 Tau mice had some ventricular dilatation and hippocampal atrophy throughout the hippocampus (Fig. 3I), but much less than PS19;*Lsd1*$^{\Delta/+}$ mice (Fig. 3J, Movie S2. 0:51sec vs. 1:00sec).

3.3.3 Tau pathology is not affected by change in LSD1 levels

Since LSD1 is a chromatin regulator, it is possible that reducing LSD1 protein levels affects the PS19 Tau transgene. However, we confirmed that there was no difference between PS19 Tau mice and PS19;*Lsd1*$^{\Delta/+}$ mice in the endogenous mouse *Mapt* RNA expression, nor in the human P301S MAPT transgene expression (Fig. S6 A). It is also possible that LSD1 affects tau

pathology. To test this, we performed immunohistochemistry staining for a hyperphosphorylated form of tau (AT8). As expected, we did not observe any AT8 positive staining in *Lsd1*$^{\Delta/+}$ at 6, 8, or 10 months (Fig. S6 B,E,H). Additionally, we observed very little AT8 positive immunoreactivity at 6 months in both PS19 Tau or PS19;*Lsd1*$^{\Delta/+}$ mice (Fig. S6 C,D). At 8 months both PS19 Tau and PS19;*Lsd1*$^{\Delta/+}$ mice had low but consistent levels of AT8 positive immunoreactivity (Fig. S6 F,G), and by 10 months both PS19 Tau and PS19;*Lsd1*$^{\Delta/+}$ mice developed the same high level of AT8 positive tau immunoreactivity (Fig. S6 I,J). This was consistent throughout both the CA1 and CA3 regions of the hippocampus and the cerebral cortex (Fig. S6 K-M). We also did not observe any difference between PS19 Tau mice and PS19;*Lsd1*$^{\Delta/+}$ mice when assaying PHF1 (an alternative phospho-tau antibody) immunoreactivity in the CA1 region of the hippocampus at 8 months (Fig. S7 A-C, G) and 10 months (Fig. S7 D-F, G), nor in the CA3 region of the hippocampus or the cerebral cortex at 8 and 10 months (Fig. S7 H,I).

3.3.4 The functional interaction between tau pathology and LSD1 inhibition is specific

To test the specificity of the functional interaction between tau pathology and LSD1, we investigated the overlap in the effected molecular pathways associated with both pathological tau and *Lsd1* heterozygosity. To address this, we performed RNA sequencing on the hippocampus of 9 month *Lsd1*$^{+/+}$, *Lsd1*$^{\Delta/+}$, PS19 Tau, and PS19;*Lsd1*$^{\Delta/+}$ littermates. As opposed to analyzing transcriptional changes at the terminal stage of disease, this time point allows us to assess molecular changes prior to the onset of neuronal cell death. This is also the time point that we observed the earliest signs of exacerbation of paralysis in PS19;*Lsd1*$^{\Delta/+}$ mice. Because of this early stage in the progression of the disease, we would not expect dramatic changes in

transcription overall. Nevertheless, if tau pathology is inhibiting LSD1 function, we would expect that the genome-wide expression changes induced by tau might be exacerbated by a reduction in LSD1. The RNA-seq analysis detected 54 significant gene expression changes in PS19 Tau mice compared to $Lsd1^{+/+}$ (Fig S8 A,B), and 271 significant gene expression changes in PS19;$Lsd1^{\Delta/+}$ mice compared to $Lsd1^{+/+}$ (Fig S8 C,D). Importantly, $Lsd1^{\Delta/+}$ mice had only 4 gene expression changes observed genome-wide (Fig. S8 E,F), indicating that the partially reduced level of LSD1 expression had very little effect on transcription on its own. This is consistent with the lack of phenotype in these animals.

We first examined the relationship between tau-induced expression changes and the effects of *Lsd1* heterozygosity by comparing the transcriptional changes observed in PS19 Tau mice with PS19;$Lsd1^{\Delta/+}$ mice. In PS19 Tau mice that do not yet have significant neurodegeneration, we identified 54 genes (36 up and 18 down) that were differentially expressed. Of these 54 genes, 50 were changed in the same direction in PS19;$Lsd1^{\Delta/+}$ mice (93%). In addition, amongst the 50 genes changed in the same direction, 36 (72%) had exacerbated expression in PS19;$Lsd1^{\Delta/+}$ mice compared to PS19 Tau mice (Fig. 4A). Based on this overlap, we further compared the expression changes between PS19 Tau mice and PS19;$Lsd1^{\Delta/+}$ mice genome-wide. Amongst the transcripts that were changed in both PS19 Tau mice and PS19;$Lsd1^{\Delta/+}$ mice compared to $Lsd1^{+/+}$ mice, 71% changed in the same direction (either up or down). Consistent with this overlap in gene expression, Gene Set Enrichment Analysis demonstrated that the pathways that are affected in both PS19 Tau mice and PS19;$Lsd1^{\Delta/+}$ mice are very similar (Fig. S8 G-J). However, the genes affected in both sets of mice tended to be further exacerbated in PS19;$Lsd1^{\Delta/+}$ mice compared to PS19 Tau mice. Amongst the 71% of genes that changed in the same direction in both PS19 Tau mice and

PS19;*Lsd1*$^{\Delta/+}$ mice, 76% of these transcripts had a higher fold-change in PS19;*Lsd1*$^{\Delta/+}$ mice compared to PS19 Tau mice (Fig. 4B).

3.3.5 Overexpression of LSD1 rescues neurodegeneration in the hippocampus of PS19 Tau mice

Our data demonstrate that reduction of LSD1 protein exacerbates the tauopathy phenotype in PS19 Tau mice. Based on this, we considered the possibility that overexpression of LSD1 might counter the loss of LSD1 from the nucleus and protect against neurodegeneration in PS19 Tau mice. To address this possibility, we injected PS19 Tau mice with a neuronal specific virus (AAV-DJ driven by the synapsin promoter) expressing either the full length LSD1 protein with an N-terminal HA tag (hereafter referred to as PS19- LSD1 inj) or a control virus expressing only the HA tag (hereafter referred to as PS19- HA inj). Additionally, to control for the effects of viral injection, we injected Wild Type littermates with the HA only expressing virus (hereafter referred to as WT- HA inj). All injections were performed directly into the hippocampus at 8-8.5 months, when tau pathology is already present throughout the nervous system. Immunolabeling for the HA tag demonstrated that the virus is specific to NeuN+ neurons (Fig. S9 A-D), with no HA expression observed in IBA+ microglia (Fig. S9 E-H), or GFAP+ astrocytes (Fig. S9 I-L). It also confirmed that virally expressed LSD1 is nuclear (Fig. S9 M) and confined to the hippocampus (Fig. S9 N). After 3 months of overexpression, 11-11.5 month old mice were euthanized, and the brains were analyzed. Injections resulted in a ~6-fold increase in expression of LSD1 in the hippocampus compared to endogenous LSD1 in the PS19- HA inj mice, but no increase in the cerebellum (Fig. S9 O,P). As expected, because the viral injections were restricted to the hippocampus, the mice injected with LSD1 still developed paralysis (Movie S3). This

confirms that the tau transgene is expressed and functioning. Additionally, we did not observe a difference in total levels of AT8 positive tau immunoreactivity (Fig. S9 Q-T). Therefore, any modulation to the phenotype was not due to changes in tau pathology.

Injected mice were evaluated for cell death by neuronal cell counts in the hippocampus. Injection of LSD1 virus into the hippocampus of PS19 Tau mice rescued the neurodegeneration phenotype. At 11 months, compared to WT-HA inj control mice, 70% of the PS19-HA inj mice had hippocampal cell counts that were below the lowest WT-HA inj control, while none of the Tau mice injected with the LSD1 virus were below this level. Overall, we observed significantly more neurons (P-value <0.05) spanning the pyramidal cell layer (84% of WT- HA inj CA1 counts) compared to their PS19- HA inj littermates (59% of WT- HA inj CA1 counts), such that overall the neuronal cell count in PS19- LSD1 inj mice was not statistically different from the WT- HA inj (Fig. 5A-D). Additionally, in the histological analysis we observed a large number of cells infiltrating the hippocampus in PS19- HA inj mice compared to WT- HA inj littermates (Fig. 5B vs. 5C). Marker analysis demonstrated that this was due to a strong inflammatory response, with a large increase in the number of GFAP+ astrocytes (Fig. S10 A-C vs. D-F) and TRL2+ activated microglia (Fig. S10 J-L vs. M-O, S-V vs. W,Z, EE). Injection of PS19 Tau mice with LSD1 virus rescued this inflammatory response. For example, all but one (9 out of 10 analyzed) of the PS19- LSD1 inj mice had a reduction in the number of GFAP+ astrocytes (Fig. S10 G-I vs. D-F) and TRL2+ activated microglia (Fig. S10 P-R vs. M-O, AA-DD vs. W-Z, EE). Of note, the one PS19- LSD1 inj mouse where we did observe increased glial cells, similar to PS19- HA inj mice, had the lowest neuronal cell count (74% of WT- HA inj CA1 neurons). It is possible that this mouse was already undergoing neurodegeneration prior to the injection of the LSD1 overexpression virus.

Although the number of hippocampal neurons in PS19- LSD1 inj mice did not differ from WT- HA inj controls, in 6 of the 10 PS19- LSD1 inj mice we observed cells with abnormal blebbed nuclei at varying numbers throughout the hippocampus (Fig. 5E). These abnormal cells are rare in PS19- HA inj mice, which have a reduced overall number of cells in the pyramidal cell layer compared to WT- HA inj control mice. One possibility is that these abnormal cells with blebbing nuclei represent an intermediate state between a healthy neuron and a dying neuron that is prolonged by rescue via LSD1 overexpression. Interestingly, these abnormal cells also differed in the localization of HA-tagged LSD1. The four mice with normal nuclei had HA-tagged LSD1 protein localized uniformly throughout the nucleus (Fig. 5F). In contrast, the six mice with abnormal nuclear blebbing had some HA-tagged LSD1 that was mislocalized to the cytoplasm (Fig. 5G). This includes the one PS19- LSD1 inj mouse that had an elevated number of astrocytes and TRL2 positive microglia. Thus, the blebbing state correlates with when the viral produced LSD1 begins to be sequestered in the cytoplasm, similar to the endogenously produced LSD1.

3.4 DISCUSSION

In this study we investigate a potential downstream mediator of tau pathology in neurodegenerative disease. We find that modulation of the chromatin modifying enzyme LSD1 can alter neurodegeneration in a tauopathy mouse model. Previously, we showed that LSD1 colocalizes with tau pathology in the cell body of neurons in AD cases (*28*). This suggested that LSD1 might be disrupted in tauopathies such as AD, by being excluded from the nucleus. To address this directly, we utilize the PS19 tauopathy mouse model. In these mice, we find that LSD1 is sequestered in the cytoplasm, in some cases being completely depleted from the nucleus. This provides the first cytological evidence that pathological tau can prevent LSD1 from

properly localizing to the nucleus in hippocampal and cortical neurons, where we have previously shown it is continuously required.

Based on the ability of pathological tau to sequester LSD1, we hypothesized that neuronal cell death may be due, at least partly, to LSD1 being sequestered in the cytoplasm and depleted from the nucleus. In this case, reducing LSD1 levels should make it easier for tau to deplete LSD1 from the nucleus, resulting in a faster progression of neurodegeneration and/or a more severe neurodegenerative phenotype. Importantly, LSD1 heterozygosity alone induces only 4 significant gene expression changes and does not lead to any neurodegeneration. This suggests that any effects observed in PS19;*Lsd1*$^{\Delta/+}$ mice are not simply due to LSD1 haploinsufficiency. Normally, PS19 Tau mice develop paralysis and neurodegeneration, along with reduced survival. In contrast, when we reduce LSD1 in the PS19 Tau mice, PS19;*Lsd1*$^{\Delta/+}$ mice die significantly earlier, most likely due to the increased rate of paralysis. Additionally, PS19;*Lsd1*$^{\Delta/+}$ mice have increased neuronal cell death and clearance in the hippocampus. This suggests that pathological tau functions through LSD1 to cause neurodegeneration *in vivo* in mice.

PS19;*Lsd1*$^{\Delta/+}$ mice have a 31% reduction in LSD1 protein levels compared to PS19 Tau mice from birth. This reduction should theoretically make mice sensitive to LSD1 depletion at any time. However, tau pathology starts at 6-8 months in PS19 Tau mice. As a result, if *Lsd1* heterozygosity is functioning by making it easier for pathological tau to deplete LSD1 from the nucleus, we would not expect to see any exacerbation until after pathological tau is present. The exacerbation of the PS19 Tau mouse neurodegenerative phenotype does not occur until after pathological human tau was present. This suggests that the effect of *Lsd1* heterozygosity requires the presence of pathological tau, placing LSD1 downstream of tau. Consistent with LSD1 being

downstream of pathological tau, we found no evidence that *Lsd1* heterozygosity affects the expression of the tau transgene, or the buildup of pathological tau in PS19 Tau mice.

To test whether the functional interaction between pathological tau and reduced LSD1 is specific, we used RNA-seq to determine whether the downstream molecular pathways altered in PS19 Tau mice are exacerbated in PS19;$Lsd1^{\Delta/+}$ mice. This analysis was performed at the time of earliest signs of neuronal distress, allowing us to assess molecular changes prior to cell death and clearance. LSD1 heterozygosity induces only 4 significant expression changes. In addition, the pathways are affected in both PS19 Tau mice and PS19;$Lsd1^{\Delta/+}$ mice are very similar. This suggests that reducing LSD1 did not induce any additional neurodegeneration pathways. In contrast, when LSD1 is reduced in PS19 Tau mice, the genome-wide expression changes induced by pathological tau are specifically exacerbated. This suggests that the functional interaction that we observe between pathological tau and reduced LSD1 is occurring through the tau pathway.

Our previous data implicated LSD1 in the tau-mediated neurodegeneration pathway. Utilizing the PS19 Tau mouse model, we now show a functional interaction between pathological tau and LSD1. Importantly, because PS19 Tau mice do not have Aβ plaque accumulation, this functional interaction is specific to tau. Based on these data we propose the following model (Movie S4): in healthy hippocampal and cortical neurons, LSD1 is translated in the cytoplasm and transported into the nucleus where it is continuously required to repress inappropriate transcription. In tauopathy, pathological tau accumulates in the cytoplasm blocking LSD1 from nuclear import. This interferes with the continuous requirement for LSD1, resulting in neuronal cell death. Recently, it has been observed that the nuclear pore breaks down in AD

(*42-44*). It should be noted that this mechanism would potentially exacerbate the model that we propose.

This model makes a direct prediction: if tau is predominantly functioning through LSD1, then increasing the levels of LSD1 should rescue the tau-induced neurodegenerative phenotype. To address this, we overexpressed LSD1 in the hippocampal neurons of PS19 Tau mice. Overexpression of LSD1 specifically in hippocampal neurons rescues the neuronal cell death and limits the inflammatory response. This rescue is neuronal specific, suggesting that the functional interaction between LSD1 and tau is occurring in neurons. In addition, this rescue occurs despite there being no effect on tau aggregation. This negates the possibility that the tau transgene is simply not functioning when LSD1 is overexpressed. The ability of LSD1 overexpression to overcome tau-mediated neurodegeneration in the presence of pathological tau aggregates, provides further evidence that pathological tau is functioning through the inhibition of LSD1. Importantly, overexpressing LSD1 should not prevent it from being sequestered. Rather overexpressing LSD1 should make it more difficult for pathological tau to sequester all of the LSD1 protein, allowing some LSD1 to be transported to the nucleus. Thus, overexpressing LSD1 would be expected to temporarily rescue the ability of pathological tau to kill neurons. Consistent with this, LSD1 overexpression delays the effect of pathological tau rather than permanently rescuing. In 60% of the mice, the surviving neurons have abnormal morphology, and the overexpressed version of LSD1 is also sequestered. observation that neurons fail to maintain their morphology when the overexpressed LSD1 begins to be sequestered in the cytoplasm provides further support for the model that tau mediates neurodegeneration through the sequestration of LSD1. Nevertheless, our data suggest that overexpression of LSD1 cannot permanently overcome pathological tau. To permanently overcome pathological tau, it would

likely be necessary to permanently disrupt the interaction between pathological tau and LSD1. This work is currently ongoing in the lab. Overall, our data establish LSD1 as a major downstream effector of tau-mediated neurodegeneration. Based on these data, we propose that the LSD1 pathway is a potential late stage target for intervention in tauopathies, such as AD.

3.5 MATERIALS AND METHODS

All mouse work, including surgical procedures, were approved by and conducted in accordance with the Emory University Institutional Animal Care and Use Committee.

3.5.1 Mouse tissue fixation

Mice were given a lethal dose of isoflurane via inhalation, then transcardially perfused with ice cold 4.0% paraformaldehyde in 0.1M phosphate buffer. Brain and spinal cord were dissected and post fixed in cold paraformaldehyde solution for 2 hours. Brain weights and sizes were taken from mice that were euthanized by cervical dislocation. Brain was dissected, immediately weighed, imaged, and fixed in cold 4.0% paraformaldehyde in 0.1M phosphate buffer overnight. In all cases, tissues were transferred to cold PBS, then serially dehydrated and embedded in paraffin and serially sectioned into 8μm coronal sections.

3.5.2 Histology and histological studies

Hematoxylin and eosin staining was performed according to standard procedures. Briefly, sections were dewaxed with xylenes and serial ethanol dilutions then stained with Eosin using the Richard-Allan Scientific Signature Series Eosin-Y package (ThermoScientific). To derive unbiased estimates of neuronal loss in the hippocampus, the number of primordial neurons in CA1 and CA3 (corresponding approximately to bregma coordinates -2.0 mm and -3.0 mm) were counted from 2 randomly selected regions in the field of a Zeiss Axiophot ocular graticule grid

and measured manually using digital micrographs of H&E-stained preparations. Investigators were blinded to the genotype or treatment.

3.5.3 Immunohistochemistry and immunofluorescence

Sections were dewaxed with xylenes and serial ethanol dilutions, then treated with 3% hydrogen peroxide at 40°C for 5 minutes to quench endogenous peroxidase activity, blocked in 2% serum at 40°C for 15 minutes, and incubated with primary Ab (Table S1) overnight at 4°C. Slides were washed, then incubated with biotinylated secondary Ab (Biotinylated Goat α Rabbit, 1:200, Vector Labs BA-1000 or Biotinylated Goat α Mouse, 1:200, Vector Labs BA-9200) at 37°C for 30 minutes. Signal amplification was then carried out by incubating at 37°C for 1 hour with Vector Labs Elite ABC reagent (PK-6200). Slides were developed with DAB for 1-5 minutes, counterstained with hematoxylin for 1 minutes, and coverslipped. For immunofluorescence, dewaxed sections were first rinsed with TBS. Antigen retrieval was performed by microwaving at 10% power 2X for 5 minutes in 0.01M sodium citrate. Slides were then cooled, washed with TBS, permeabilized in 0.5% Triton X-100 for 20 minutes, followed by blocking in 10% goat serum 20 minutes. Primary Abs (Table S1) were incubated overnight at 4°C. Slides were then washed and incubated in secondary Abs (Invitrogen A1 1001 and Invitrogen A11012) for 1 hour at room temperature, followed by TBS washes, counterstained with DAPI, and then coverslipped. For the assessment of tau accumulation, six random sections (sampling from CA1, CA3, and cerebral cortex) per sample were manually counted using digital micrographs of AT8 stained preparations in the field of a Zeiss Axiophot ocular graticule grid. Investigators were blinded to the genotype or treatment. Imagining for immunofluorescence of LSD1 staining was performed on a spinning-disk confocal Nikon-Tie controlled with the software NIS Elements (Nikon). Imaging for all other immunofluorescence staining was performed on an Eclipse Ti2

inverted microscope (Nikon, Toyko, Japan) controlled with the software NIS Elements (Nikon). Image J software ((NIH, http://imagej.nih.gov/ij/) was used for viewing all images.

3.5.4 Protein Quantification

Protein levels were determined by homogenizing brains in 1 ml/g of tissue in ice-cold lysis buffer (150mM NaCl, 1% Triton X-100, 0.5% Na-deoxycholate, 1% SDS, 50mM Tris, pH8.0) in a dounce homogenizer, followed by end-over-end spin at 4°C for 2 hours, and centrifugation at 20,000 x g for 20 minutes at 4°C. Protein concentrations were determined following standard BCA protocol (Pierce BCA Protein Assay Kit). Equal amounts of protein for each sample were loaded and run on a 12% SDS-PAGE gel, transferred (Semi-dry transfer using BIO RAD Trans-Blot Turbo Transfer System), blocked in 5% BSA, and probed with primary Ab (Table S1) over night at 4°C. Blots were rinsed and stained with HRP-conjugated secondary Ab, and detected by chemiluminescence using ChemiDoc MP Imaging System (BIO RAD). Protein levels were normalized using total protein calculated using BIO RAD ImageLab software.

3.5.5 Quantitative analysis of paralysis

We performed experiments on PS19 Tau, *Lsd1*$^{\Delta/+}$, PS19;*Lsd1*$^{\Delta/+}$ mice at 6, 8, and 10 months. For the rotarod experiments, mice were given two practice trials and then placed on the rotating cylinder at 4rpm. Rotational speed then gradually increased over a 5-minute test session up to a maximum rotational speed of 40rpm. Latency to fall off of the accelerating rotarod was used as the dependent variable. We calculated the latency to fall, maximum speed in rotations per minute, and distance traveled. For grid performance, mice were placed on a horizontal grid that was then inverted so mice are hanging upside down by their paws. Mice were videotaped for 10 seconds, and then scored for forepaw and back paw distance traveled. Mice that could not hold

onto grid for 10 seconds were censored. Investigators were blinded to the genotypes for both experiments.

3.5.6 MRI of brain atrophy

MRI studies were conducted on PS19 Tau, *Lsd1*$^{\Delta/+}$, PS19;*Lsd1*$^{\Delta/+}$ mice at 6 months and 10 months (*n*=3/genotype). Mice were anesthetized with isoflurane, and monitored for heart rate and temperature changes while anesthetized. MRI measurements were performed using a 9.4 T/20 cm horizontal bore Bruker magnet, interfaced to an AVANCE console (Bruker, Billerica, MA, USA). A two-coil actively decoupled imaging set-up was used (a 2 cm diameter surface coil for reception and a 7.2 cm diameter volume coil for transmission). Axial T2-weighted images were acquired with a RARE (Rapid Acquisition with Refocused Echos) sequence. Its imaging parameters were as follows: TR = 3000 ms, Eff.TE = 64 ms, RARE factor = 4, field of view (FOV) = 23.04 × 23.04 mm2, matrix = 192 × 192, Avg = 4, slice thickness (thk) = 0.6 mm, number of slice(NSL)=20. Specific emphasis was placed on the neocortex and hippocampus in the coronal images (1.0 – 4.0 mm posterior to the bregma).

3.5.7 RNA sequencing

9 month old *Lsd1*$^{+/+}$, *Lsd1*$^{\Delta/+}$, PS19 Tau, and PS19;*Lsd1*$^{\Delta/+}$ littermates (n=2 mice/genotype) were euthanized by cervical dislocation, hippocampi were dissected and snap frozen with liquid nitrogen in 1mL Trizol, and stored at -80°C. For RNA isolation, samples were thawed at 37°C then kept on ice prior to homogenization with Polytron homogenizer with a 5 second pulse. After a 5 minute incubation at room temperature, one tenth the sample volume of 1-bromo-3chloropropane was added, mixed by inversion and incubated for 3 minutes at room temperature. Samples were then centrifuged at 13,000 X g for 15 minutes at 4°C to separate the aqueous and organic layers. As much of the aqueous layer was recovered as possible, then RNA was

precipitated with isoproponal. Pellets were then washed with 75% ethanol and resuspended in 50μL of dionized water. RNA library preparation and sequencing were performed by HudsonAlpha Genomic Services Lab. RNA was Poly(A) selected and 300bp size selected. Libraries were sequenced for 25 million 50bp paired end reads.

3.5.8 RNA sequencing analysis

The sequencing data were uploaded to the Galaxy web platform, and *we used the public server at* usegalaxy.org *to analyze the data ((45, 46)).* FASTQ files were quality assessed using FASTQC (v.0.11.7), trimmed using Trimmomatic (v.0.36.5) and minimum QC score of 20 and minimum read length of 36bp. Paired-end reads were subsequently mapped to the GRCm38 genome using HISAT2 (v.2.1.0). Unmapped, unpaired and multiply mapped reads were removed using Filter SAM or BAM (v.1.1.2). Assignment of transcripts to GRCm38 genomic features was performed using Featurecounts (v.1.6.0.6) and the Ensembl GRCm38.93 gtf file. Differentially expressed transcripts were determined using DESEQ2 (v.2.11.40.2) (*(46))*. For all datasets, a cutoff of adjusted p-value < 0.3 and abs (log_2 fold change) > 0.58 was applied. TPM values were calculated from raw data obtained from Featurecounts output. Subsequent downstream analysis was performed using R and normalized counts and adjusted P-values from DESEQ2 (v.2.11.40.2). Heatmaps were produced and hierarchical clustering was done using the gplots package (v. 3.0.1) and normalized counts (*(47)*). Volcano plots were produced using the enhanced volcano package (v.0.99.16) and adjusted p-values (*(48)*). Additionally, Gene Set Enrichment Analysis (Pre-ranked list) was performed using the online platform WebGestalt (*(49-52))*. Custom R-scripts available upon request.

3.5.9 Stereotaxic surgery and viral infusion

All surgical procedures were approved by and conducted in accordance with the Emory University Institutional Animal Care and Use Committee. Mice were anesthetized with isoflurane (3% induction, 1-2% maintenance) and administered the analgesic meloxicam (5 mg/kg). Using a Stoeling Quintessential Stereotaxic Injector pump and Hamilton syringe, mice were injected with either the AAV-DJ-LSD1- HA virus or the control AAV-DJ- HA virus into both hippocampi. Each virus was injected into the rostral (AP: -2.5, ML:± 2.2, DV: -1.6, relative to bregma) and caudal (AP: -3.1, ML:± 3.0, DV: -3.5) hippocampus of both hemispheres (four injection sites total). Infusion volumes were 0.5 µL per injection site, administered at a rate of 0.15 µL/min. Following surgery, mice were monitored daily for the duration of the experiment. Brains were extracted 3 months post-surgery which allows sufficient time for viral expression. Injection accuracy was confirmed by HA positive staining, and those mice where staining was outside the hippocampus or that did not fully reach hippocampus were censored.

3.6 REFERENCES

1. M. E. Orr, A. C. Sullivan, B. Frost, A Brief Overview of Tauopathy: Causes, Consequences, and Therapeutic Strategies. *Trends in pharmacological sciences* **38**, 637-648 (2017).
2. Y. Wang, E. Mandelkow, Tau in physiology and pathology. *Nat Rev Neurosci* **17**, 5-21 (2016).
3. D. M. Holtzman *et al.*, Tau: From research to clinical development. *Alzheimers Dement* **12**, 1033-1039 (2016).
4. C. M. Wischik *et al.*, Isolation of a fragment of tau derived from the core of the paired helical filament of Alzheimer disease. *Proc Natl Acad Sci U S A* **85**, 4506-4510 (1988).
5. M. Goedert, C. M. Wischik, R. A. Crowther, J. E. Walker, A. Klug, Cloning and sequencing of the cDNA encoding a core protein of the paired helical filament of Alzheimer disease: identification as the microtubule-associated protein tau. *Proc Natl Acad Sci U S A* **85**, 4051-4055 (1988).
6. J. Hardy, D. J. Selkoe, The amyloid hypothesis of Alzheimer's disease: progress and problems on the road to therapeutics. *Science* **297**, 353-356 (2002).
7. S. H. Barage, K. D. Sonawane, Amyloid cascade hypothesis: Pathogenesis and therapeutic strategies in Alzheimer's disease. *Neuropeptides* **52**, 1-18.
8. G. S. Bloom, Amyloid-β and Tau: The Trigger and Bullet in Alzheimer Disease PathogenesisAmyloid-β and TauAmyloid-β and Tau. *JAMA Neurology* **71**, 505-508 (2014).
9. C. Duyckaerts, B. Delatour, M.-C. Potier, Classification and basic pathology of Alzheimer disease. *Acta Neuropathologica* **118**, 5-36 (2009).
10. P. V. Arriagada, J. H. Growdon, E. T. Hedley-Whyte, B. T. Hyman, Neurofibrillary tangles but not senile plaques parallel duration and severity of Alzheimer's disease. *Neurology* **42**, 631-639 (1992).
11. E. Karran, M. Mercken, B. De Strooper, The amyloid cascade hypothesis for Alzheimer's disease: an appraisal for the development of therapeutics. *Nat Rev Drug Discov* **10**, 698-712 (2011).
12. T. Gomez-Isla *et al.*, Neuronal loss correlates with but exceeds neurofibrillary tangles in Alzheimer's disease. *Ann Neurol* **41**, 17-24 (1997).
13. A. Bejanin *et al.*, Tau pathology and neurodegeneration contribute to cognitive impairment in Alzheimer's disease. *Brain* **140**, 3286-3300 (2017).
14. D. P. Hanger, J. C. Betts, T. L. Loviny, W. P. Blackstock, B. H. Anderton, New phosphorylation sites identified in hyperphosphorylated tau (paired helical filament-tau) from Alzheimer's disease brain using nanoelectrospray mass spectrometry. *J Neurochem* **71**, 2465-2476 (1998).
15. M. Morishima-Kawashima *et al.*, Hyperphosphorylation of tau in PHF. *Neurobiol Aging* **16**, 365-371; discussion 371-380 (1995).
16. T. Arendt, J. T. Stieler, M. Holzer, Tau and tauopathies. *Brain Research Bulletin* **126**, 238-292 (2016).
17. R. J. Castellani, G. Perry, Tau Biology, Tauopathy, Traumatic Brain Injury, and Diagnostic Challenges. *J Alzheimers Dis* **67**, 447-467 (2019).
18. E. Masliah *et al.*, Altered expression of synaptic proteins occurs early during progression of Alzheimer's disease. *Neurology* **56**, 127-129 (2001).

19. M. Ingelsson *et al.*, Early Abeta accumulation and progressive synaptic loss, gliosis, and tangle formation in AD brain. *Neurology* **62**, 925-931 (2004).
20. J. W. Kinney *et al.*, Inflammation as a central mechanism in Alzheimer's disease. *Alzheimer's & Dementia: Translational Research & Clinical Interventions* **4**, 575-590 (2018).
21. J. M. Rubio-Perez, J. M. Morillas-Ruiz, A review: inflammatory process in Alzheimer's disease, role of cytokines. *TheScientificWorldJournal* **2012**, 756357-756357 (2012).
22. H. Braak, D. R. Thal, E. Ghebremedhin, K. Del Tredici, Stages of the pathologic process in Alzheimer disease: age categories from 1 to 100 years. *J Neuropathol Exp Neurol* **70**, 960-969 (2011).
23. H. Braak, K. Del Tredici, The pathological process underlying Alzheimer's disease in individuals under thirty. *Acta Neuropathol* **121**, 171-181 (2011).
24. D. E. Hurtado *et al.*, A{beta} accelerates the spatiotemporal progression of tau pathology and augments tau amyloidosis in an Alzheimer mouse model. *Am J Pathol* **177**, 1977-1988 (2010).
25. Z. He *et al.*, Amyloid-beta plaques enhance Alzheimer's brain tau-seeded pathologies by facilitating neuritic plaque tau aggregation. *Nat Med* **24**, 29-38 (2018).
26. S. H. Choi *et al.*, A three-dimensional human neural cell culture model of Alzheimer/'s disease. *Nature* **515**, 274-278 (2014).
27. H. Braak, E. Braak, Frequency of Stages of Alzheimer-Related Lesions in Different Age Categories. *Neurobiology of Aging* **18**, 351-357 (1997).
28. M. A. Christopher *et al.*, LSD1 protects against hippocampal and cortical neurodegeneration. *Nature Communications* **8**, 805 (2017).
29. Y. Yoshiyama *et al.*, Synapse Loss and Microglial Activation Precede Tangles in a P301S Tauopathy Mouse Model. *Neuron* **53**, 337-351.
30. A. Bellucci *et al.*, Induction of Inflammatory Mediators and Microglial Activation in Mice Transgenic for Mutant Human P301S Tau Protein. *The American Journal of Pathology* **165**, 1643-1652 (2004).
31. M. Iba *et al.*, Tau pathology spread in PS19 tau transgenic mice following locus coeruleus (LC) injections of synthetic tau fibrils is determined by the LC's afferent and efferent connections. *Acta Neuropathol* **130**, 349-362 (2015).
32. C. T. Foster *et al.*, Lysine-specific demethylase 1 regulates the embryonic transcriptome and CoREST stability. *Molecular and cellular biology* **30**, 4851-4863 (2010).
33. L. Jin *et al.*, Loss of LSD1 (lysine-specific demethylase 1) suppresses growth and alters gene expression of human colon cancer cells in a p53- and DNMT1(DNA methyltransferase 1)-independent manner. *The Biochemical journal* **449**, 459-468 (2013).
34. D. B. Lyons *et al.*, An epigenetic trap stabilizes singular olfactory receptor expression. *Cell* **154**, 325-336 (2013).
35. B. I. Giasson, W. E. Mushynski, Aberrant stress-induced phosphorylation of perikaryal neurofilaments. *J Biol Chem* **271**, 30404-30409 (1996).
36. Y. L. Liu *et al.*, Alternation of neurofilaments in immune-mediated injury of spinal cord motor neurons. *Spinal Cord* **47**, 166 (2008).
37. L. D. F. Moon, Chromatolysis: Do injured axons regenerate poorly when ribonucleases attack rough endoplasmic reticulum, ribosomes and RNA? *Dev Neurobiol* **78**, 1011-1024 (2018).
38. B. G. Cragg, What is the signal for chromatolysis? *Brain Res* **23**, 1-21 (1970).

39. S. Sil, A. R. Goswami, G. Dutta, T. Ghosh, Effects of naproxen on immune responses in a colchicine-induced rat model of Alzheimer's disease. *Neuroimmunomodulation* **21**, 304-321 (2014).
40. J. Riancho *et al.*, Compensatory Motor Neuron Response to Chromatolysis in the Murine hSOD1(G93A) Model of Amyotrophic Lateral Sclerosis. *Front Cell Neurosci* **8**, 346 (2014).
41. A. M. Cataldo, D. J. Hamilton, R. A. Nixon, Lysosomal abnormalities in degenerating neurons link neuronal compromise to senile plaque development in Alzheimer disease. *Brain Res* **640**, 68-80 (1994).
42. B. Eftekharzadeh *et al.*, Tau Protein Disrupts Nucleocytoplasmic Transport in Alzheimer's Disease. *Neuron* **99**, 925-940.e927 (2018).
43. L. G. Sheffield, H. B. Miskiewicz, L. B. Tannenbaum, S. S. Mirra, Nuclear Pore Complex Proteins in Alzheimer Disease. *Journal of Neuropathology & Experimental Neurology* **65**, 45-54 (2006).
44. B. Frost, F. H. Bardai, M. B. Feany, Lamin Dysfunction Mediates Neurodegeneration in Tauopathies. *Curr Biol* **26**, 129-136 (2016).
45. E. Afgan *et al.*, The Galaxy platform for accessible, reproducible and collaborative biomedical analyses: 2016 update. *Nucleic Acids Res* **44**, W3-w10 (2016).
46. E. Afgan *et al.*, The Galaxy platform for accessible, reproducible and collaborative biomedical analyses: 2018 update. *Nucleic Acids Research* **46**, W537-W544 (2018).
47. B. B. Gregory R. Warens, Lodewijk Bonebakker, Robert Gentleman, Wolfgang Huber Andy Liaw, Thomas Lumley, Martin Maechler, Arni Magnusson, Steffen Moeller, Marc Schwartz, Bill Venables. (2019).
48. K. Blighe, in *R. package version 1.2.0*. (2019).
49. J. Wang, D. Duncan, Z. Shi, B. Zhang, WEB-based GEne SeT AnaLysis Toolkit (WebGestalt): update 2013. *Nucleic Acids Res* **41**, W77-83 (2013).
50. J. Wang, S. Vasaikar, Z. Shi, M. Greer, B. Zhang, WebGestalt 2017: a more comprehensive, powerful, flexible and interactive gene set enrichment analysis toolkit. *Nucleic Acids Res* **45**, W130-w137 (2017).
51. Y. Liao, J. Wang, E. J. Jaehnig, Z. Shi, B. Zhang, WebGestalt 2019: gene set analysis toolkit with revamped UIs and APIs. *Nucleic Acids Res* **47**, W199-w205 (2019).
52. B. Zhang, S. Kirov, J. Snoddy, WebGestalt: an integrated system for exploring gene sets in various biological contexts. *Nucleic Acids Res* **33**, W741-748 (2005).

3.7 ACKNOWLEDGMENTS

We thank M. Rosenfeld (U.C.S.D) for providing *Lsd1* deletion mice; N. Seyfried, R. Betarbet, Mr. Gearing, from the Emory ADRC (P50 AG025688), NINDS Emory Neuroscience Core Facilities (P30NS055077) for tissue processing and providing PHF1 antibody, J. Alcudia of the Stanford Gene Vector and Virus Core for the help with virus generation and production; J. Schroeder from Emory Rodent Behavioral Core for help with Rotatord and Grid Performance

assays supported by the Emory Neuroscience NINDS Core Facilities (P30NS055077) with further support provided by the Georgia Clinical & Translational Science Alliance of the National Institutes of Health under Award Number UL1TR002378; and J. Park from the Emory Center for Systems Imagining for preforming MRI supported by the National Center for Advancing Translational Sciences of the National Institutes of Health under Award Number UL1TR000454. We would also like to thank M.J. Rowley and V. Corces for assistance on RNA sequencing analysis, K. Porter-Stransky and D. Weinshenker for providing PS19 Tau mouse and teaching stereotaxic surgery procedure, L.R. Lym and Dr. Lerit for assistance with confocal imagining; D. Weinshenker, A. Levey, C. Bean and T. Caspary for comments on the manuscript and assistance throughout. Additionally, the authors would like to thank fellow Katz lab members for assistance experimentally and intellectually. **Funding:** A.K.E was supported by the National Institute of General Medicine training grant (T32 GM008367-26) and an NRSA from National Institute of Neurological Disorders and Stroke (NINDS) (F31 NS098663-02). D.A.M was supported by a research supplement to promote diversity in health-related research from the NINDS (1R01NS087142). S.M.K was supported the NINDS Training in Translational Research in Neurology grant (5T32 NS007480-17). The work was supported by a grant to D.J.K from the National Institute of Neurological Disorders and Stroke (1R01NS087142). **Author Contributions:** A.K.E and D.J.K. conceived and designed the study and wrote the manuscript. A.K.E. performed experiments with the help of A.C.W, S.M.K, and R.A.M under the direction of D.J.K. D.A.M performed bioinformatics analysis on the RNA sequencing data. A.K.E, A.C.W, S.M.K, and R.A.M analyzed all other data and interpreted results. All authors discussed the results and commented on the manuscript. **Competing Interests:** The authors declare that they have no competing interests. **Data and materials availability:** FastQ files for the RNA

sequencing experiments are bring deposited in the GEO and will be available upon publication. Results from DESEQ2 are available in Data S1. Correspondence and requests for materials should be addressed to D.J.K. (djkatz@emory.edu).

3.8 FIGURES AND TABLES

Figure 1. LSD1 sequestration and tau accumulation in PS19 Tau mice.

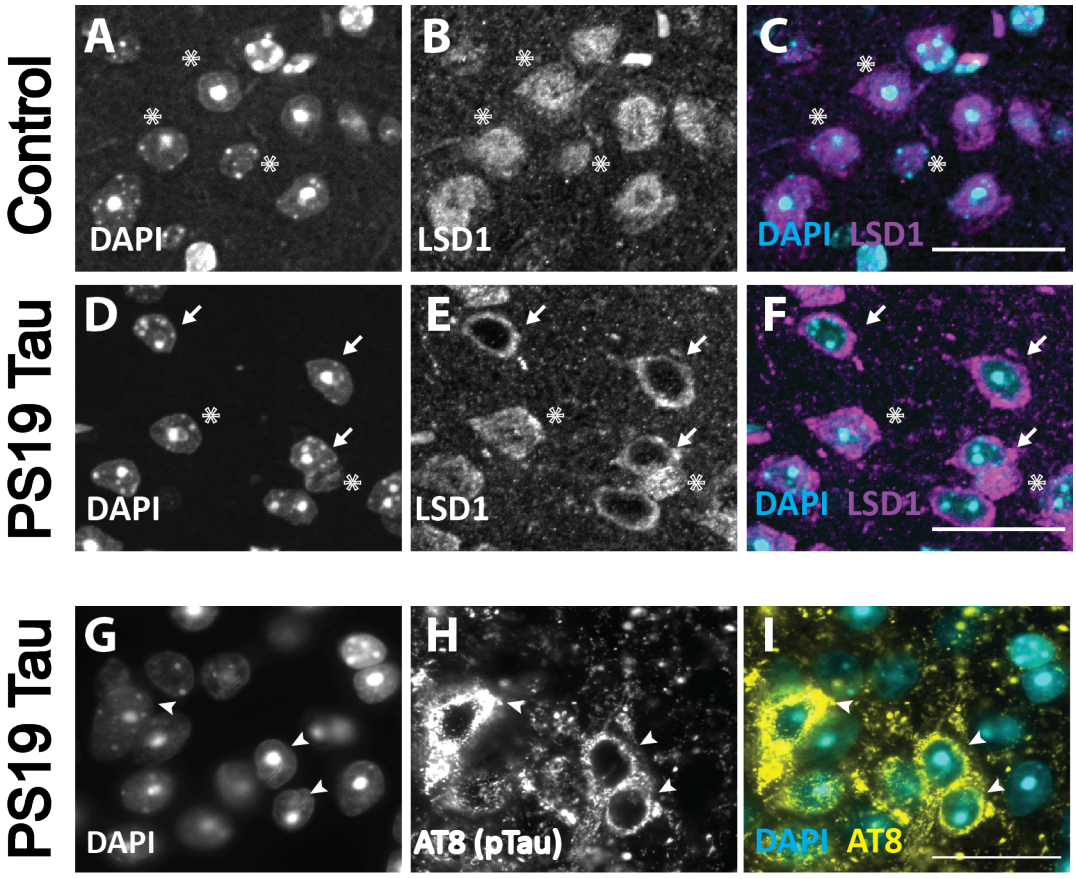

Fig 1. LSD1 sequestration and tau accumulation in PS19 Tau mice.

A-C, Representative immunofluorescence of 12 month old control Wild Type mice showing DAPI (**A**), LSD1 (**B**), and merged (**C**) in the cerebral cortex where LSD1 is localized specifically to DAPI positive nuclei. **D-F**, Representative image of the cerebral cortex in 12 month old PS19 Tau mice. Staining for DAPI (**D**), LSD1 (**E**), and merged (**F**) shows that LSD1 is localized outside the nucleus, and depleted from the DAPI positive nucleus. Arrows denote cells where LSD1 is localized outside of the nucleus, and asterisks denote LSD1 localized specifically to the nucleus. **G-I,** Representative immunofluorescence of 12 month old PS19 Tau mouse with staining for DAPI (**G**), AT8 positive hyper-phosphorylated tau (**H**) and merge (**I**) where hyper-phosphorylated tau accumulates in the cytoplasm of the cell body. Arrowheads denote hyper-phosphorylated tau. Scale bars=25μm.

Fig. 2: Reduction of *Lsd1* exacerbates the PS19 Tau mouse paralysis phenotype.

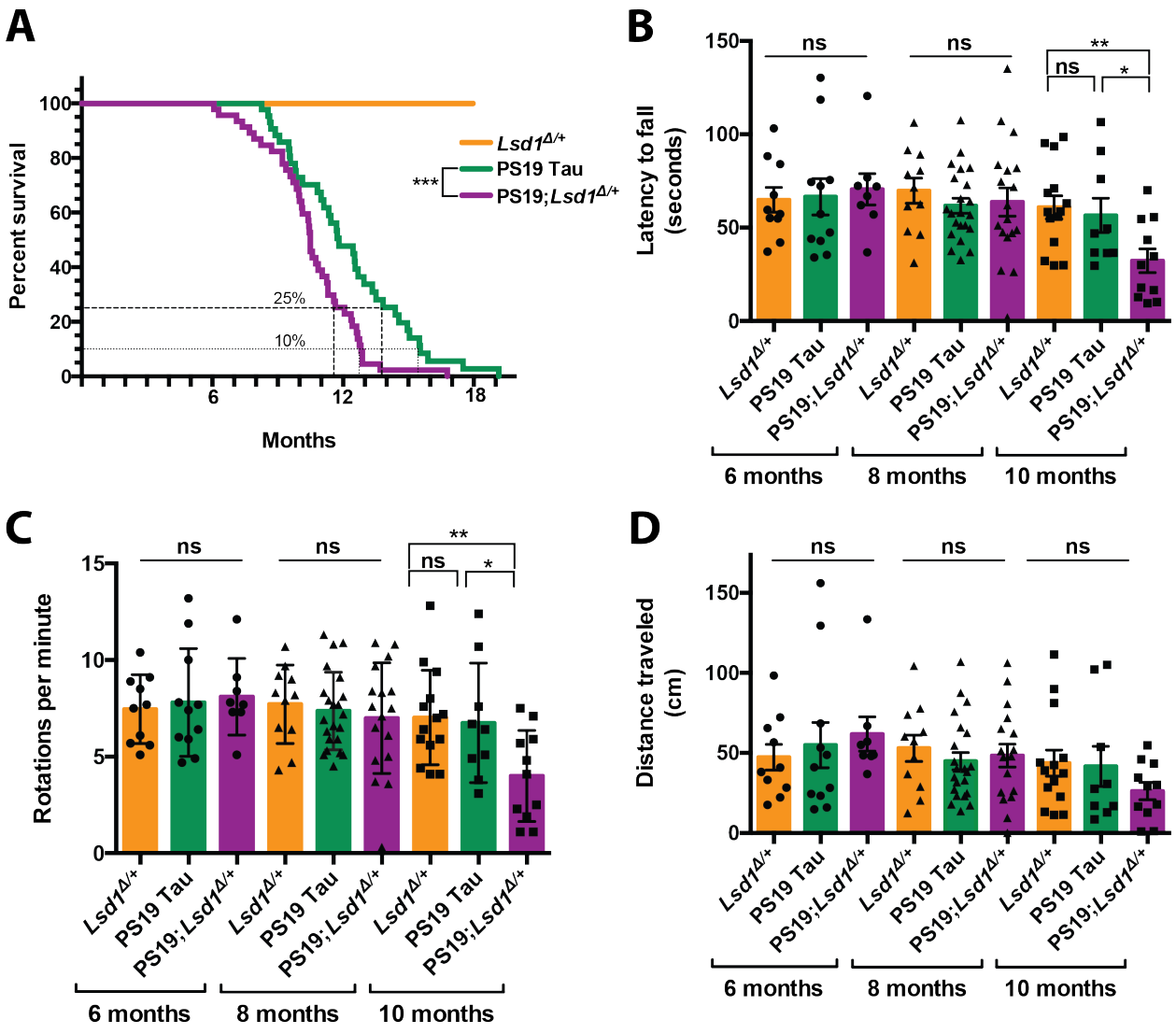

Fig. 2: Reduction of *Lsd1* exacerbates the PS19 Tau mouse paralysis phenotype.

A, Lifespan curve showing that no $Lsd1^{\Delta/+}$ mice died before 18 months (orange, *n*=20). PS19;$Lsd1^{\Delta/+}$ mice (purple, *n*=44) have a significant reduction in survival compared to PS19 Tau mice with wild-type levels of *Lsd1* (green, *n*=37)(Log-rank Mantle-Cox test ***P<0.005). **B-D**, Rotarod testing of latency to fall (in seconds) (**B**), rotations per minute (when the mouse fell) (**C**), and distance traveled (in centimeters) (**D**) for mice at age 6, 8 and 10 months. $Lsd1^{\Delta/+}$ (orange, *n*=10,11,14), PS19 Tau (green, *n*=11,22,9), and PS19;$Lsd1^{\Delta/+}$ (purple, *n*=8,17,11). Values are mean ± SEM (two-way analysis of variance (ANOVA) with Tukey's post hoc test *P<0.05 **P<0.01, ns=not significant).

Fig. 3: Reduction of *Lsd1* exacerbates neurodegeneration in PS19 Tau mice.

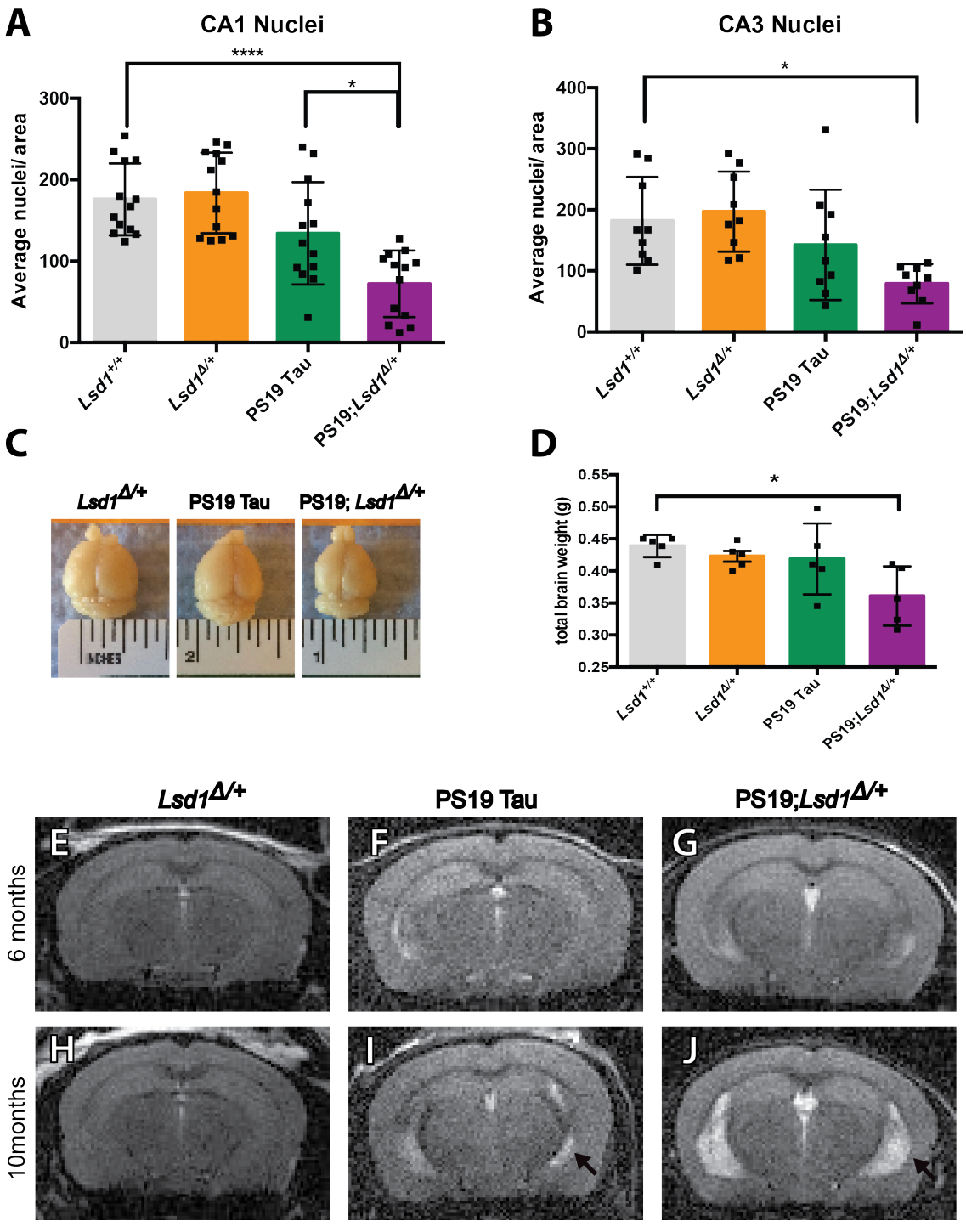

Fig. 3: Reduction of *Lsd1* exacerbates neurodegeneration in PS19 Tau mice.

A,B, Average nuclei per area in the CA1 (**A**) and CA3 (**B**) regions of the hippocampus in 12 month old *Lsd1*$^{+/+}$, *Lsd1*$^{\Delta/+}$, PS19 Tau, and PS19;*Lsd1*$^{\Delta/+}$ mice. Quantification from histology represented in **Fig. S5 A-H**. Values are mean ± SD (**A**, *n*=13 & **B,** *n*=9). **C,** Representative image of the brains of 12 month old *Lsd1*$^{\Delta/+}$, PS19 Tau, and PS19;*Lsd1*$^{\Delta/+}$ littermates. **D,** Total brain weight of 12 month old littermates represented in **Fig. 3C.** Values are mean ± SD (*n*=5). For all graphs: one-way analysis of variance (ANOVA) with Tukey's post hoc test (two-sided) *P<0.05,****P<0.001. **E-J,** Representative image of T2- weighted RARE coronal MRI taken from 6 months (**E-G**) and 10 months (**H-jJ**) of age in *Lsd1*$^{\Delta/+}$ (**E,H**), PS19 (**F,J**), and PS19;*Lsd1*$^{\Delta/+}$ (**G,J**) mice (*n*=3). Arrow denotes region of hippocampal atrophy.

Fig. 4. Molecular overlap between loss of LSD1 function and tauopathy

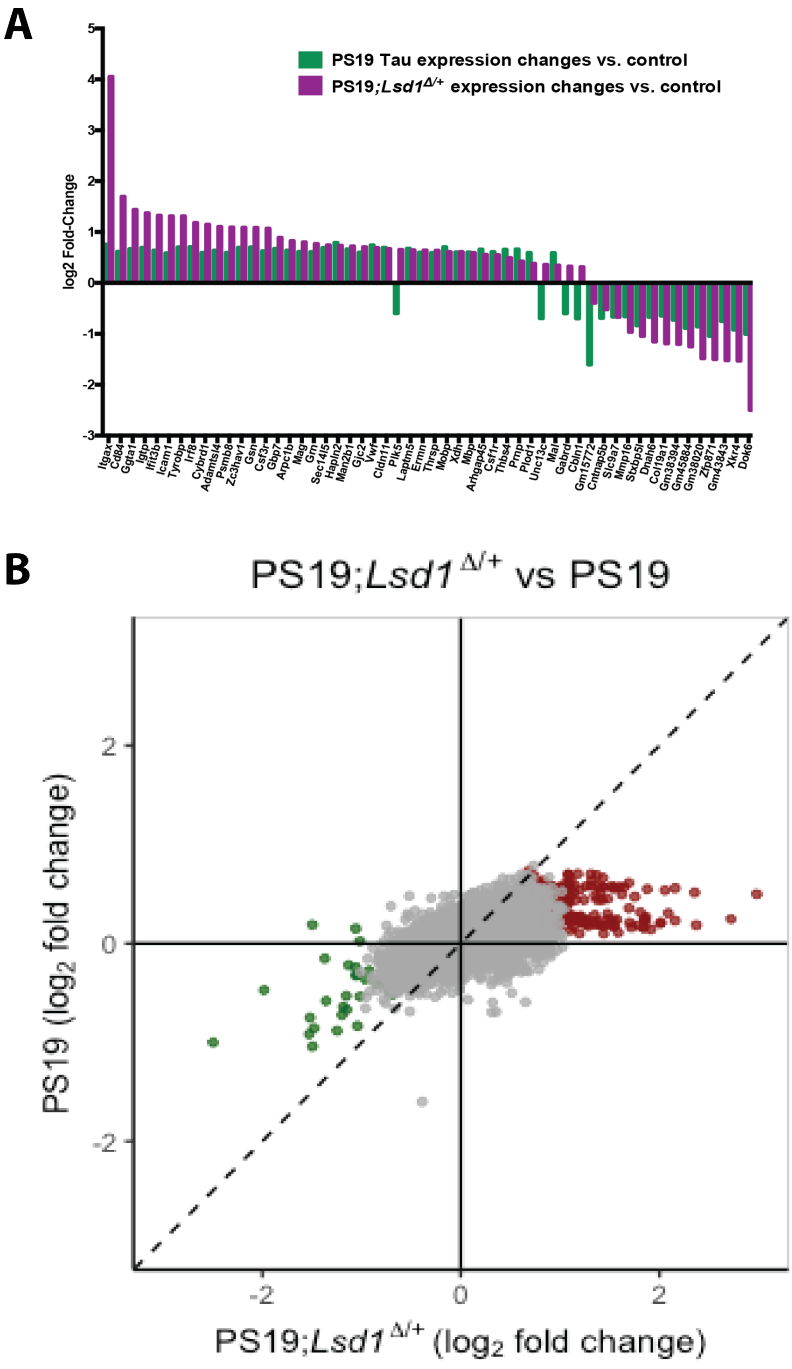

Fig. 4. Molecular overlap between loss of LSD1 function and tauopathy.

A, Histogram (log_2 fold change) of the 54 genes that have significant changes in expression in the PS19 Tau mouse (green) and their corresponding expression changes in the PS19;*Lsd1*$^{\Delta/+}$ mouse (purple). **B,** Scatter plot showing the correlation between the genome-wide log_2 fold change in gene expression between PS19 Tau and PS19;*Lsd1*$^{\Delta/+}$. The most significantly changed genes in PS19;*Lsd1*$^{\Delta/+}$ mouse are shown in red (upregulated) and green (downregulated). All other genes are shown in grey. Dotted line represents 1:1 relationship between gene expression changes in PS19 Tau vs. PS19;*Lsd1*$^{\Delta/+}$. Exacerbated genes fall to the right of the dotted line in the positively correlated quadrant and to the left of the dotted line in the negatively correlated quadrant. Genes with correlated expression changes are found in the top right and bottom left quadrants, while genes that do not correlate are found in the opposite quadrants.

Fig. 5. LSD1 overexpression rescues the neurodegenerative phenotype in the hippocampus of 11 month old PS19 Tau mice.

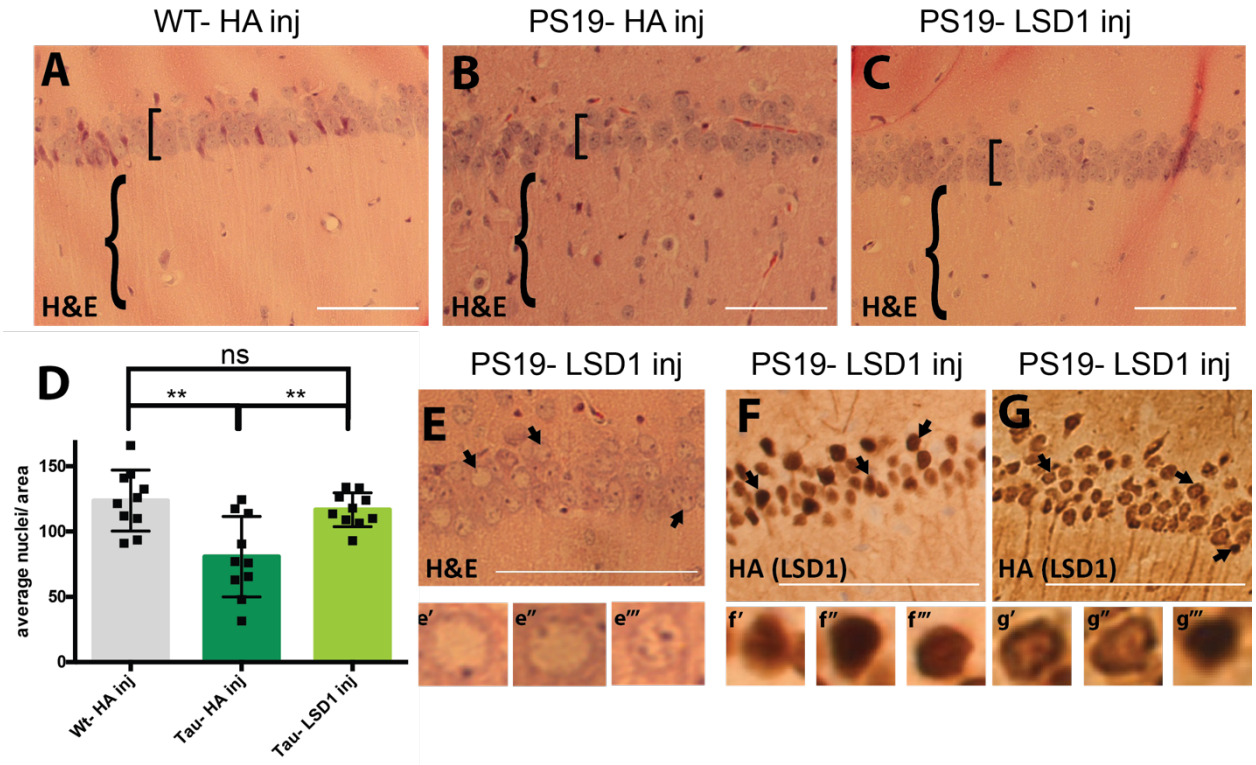

Fig. 5. LSD1 overexpression rescues the neurodegenerative phenotype in the hippocampus of 11 month old PS19 Tau mice.

A-C, Representative image of H&E stained CA1 region of the hippocampus of 11 month old Wild Type mice injected with HA control virus (WT- HA inj) (**A**), PS19 Tau mice injected with HA control virus (PS19- HA inj) (**B**), and PS19 Tau mice injected with *Lsd1* overexpressing virus (PS19- LSD1 inj) (**C**). Square brackets denote thickness of pyramidal layer of the CA1 of the hippocampus and curvy brackets denote hippocampal region with or without infiltrating cells. **D,** Quantification of the average number of nuclei in the pyramidal layer of the hippocampus per area per mouse from histology represented in **Fig. 5A-C**. Values are mean ± SD (n=10, one-way analysis of variance (ANOVA) with Tukey's post hoc test, **p<0.01, ns=not significant). **E,** Representative H&E of PS19- LSD1 inj mouse with abnormal nuclei blebbing in the CA1 region of the hippocampus. **E'-E''',** High magnified image of cells denoted by arrows in **Fig. 5E** of individual nuclei that are either abnormally blebbed (**E', E"**) or normal (**E'''**). **F,G,** Immunohistochemistry staining of HA(LSD1) in 11 month PS19- LSD1 inj mice. HA is either localized specifically to the nucleus in all nuclei (**F**) or in only a few nuclei while it is partially sequestered in the cytoplasm in others (**G**). **F'-F''',** High magnified image of cells denoted by arrows in **Fig. 5F** of nuclear HA localization in individual nuclei. **G'-G''',** High magnified image of cells denoted by arrows in **Fig. 5G** of individual nuclei with HA(LSD1) either sequestered to the cytoplasm (**G', G"**) or confined to the nucleus (**G'''**). Scale bars=50μm.

Fig. S1. Sequestration of LSD1 in PS19 Tau mice.

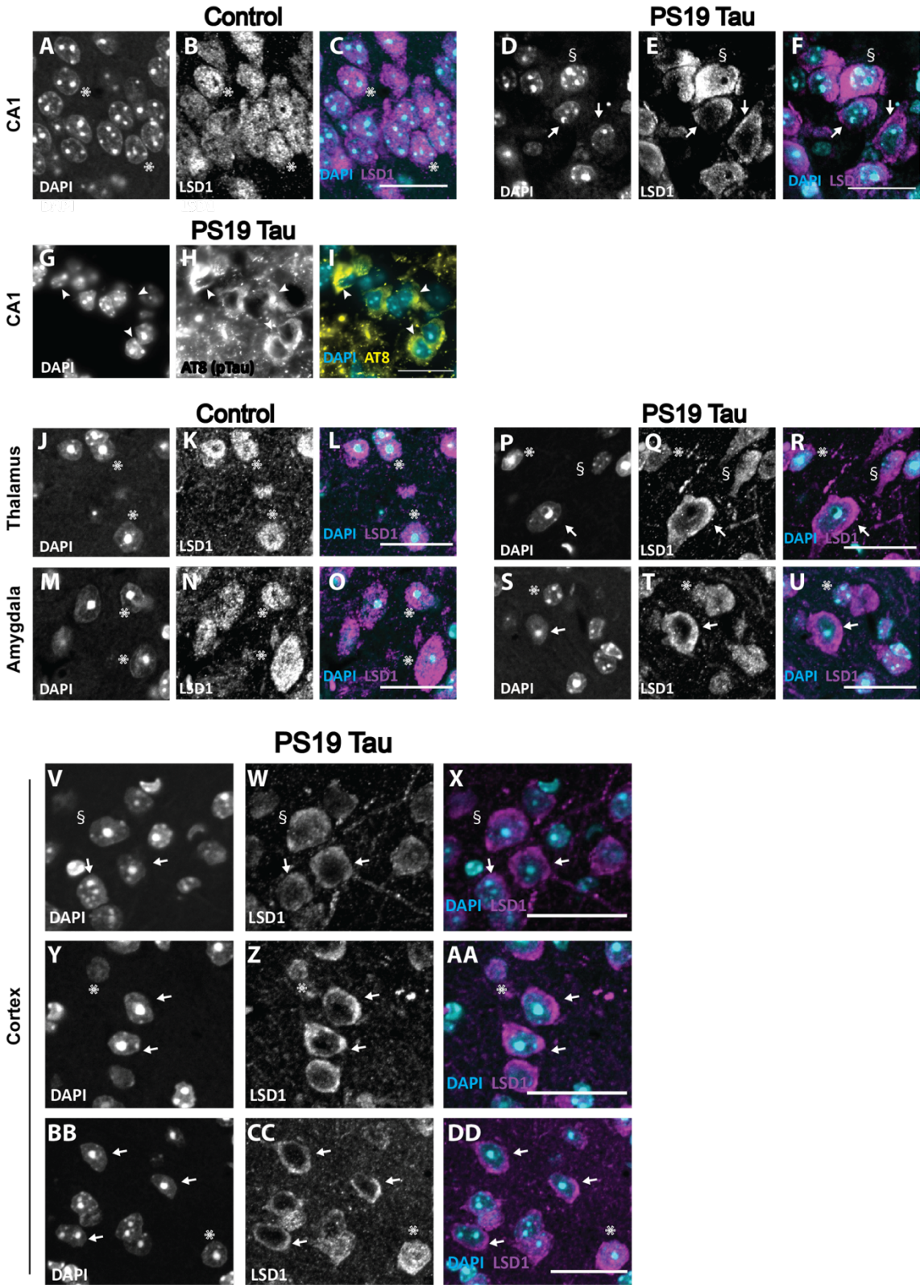

Fig. S1. Sequestration of LSD1 in PS19 Tau mice.

A-**F**, Representative immunofluorescence showing DAPI (**A,D**), LSD1 (**B,E**), and merged (**C,F**) images in the CA1 region of the hippocampus in 12 month old Wild Type (**A-C**) and PS19 mice (**D-F**). **G-I**, Representative immunofluorescence showing DAPI (**G**), AT8 positive hyper-phosphorylated tau (**H**), and merged (**I**) in the CA1 region of the hippocampus of 12 month old PS19 Tau mice showing hyper-phosphorylated tau accumulation in the cytoplasm of the cell bodies. Arrowheads denote hyper-phosphorylated tau. **J-U,** Representative immunofluorescence showing DAPI (**J,M,P,S**), LSD1 (**K,N,Q,T**), and merged (**L,O,R,U**) images in the thalamus (**J-L,P-R**) and amygdala (**M-O,S-U**). In 12 month old control Wild Type mice (**J-O**), LSD1 is localized specifically to the DAPI positive nuclei, but in 12 month old PS19 Tau mice (**P-U**) LSD1 is localized outside of the nucleus. **V-DD,** Additional examples of immunofluorescence showing DAPI (**V,Y,BB**), LSD1 (**W,Z,CC**), and merged (**X,AA,DD**) of the cerebral cortex of 12 month old PS19 Tau mice. Arrows denote cells where LSD1 is localized outside of the nucleus, asterisks denote LSD1 localized specifically to the nucleus, and § denotes cells where LSD1 is both nuclear and cytoplasmic. *n*=7 mice analyzed (images representative of 6 of the 7 mice analyzed). Scale bars=25μm.

Fig. S2: Generation of PS19 Tau mice with reduced levels of LSD1

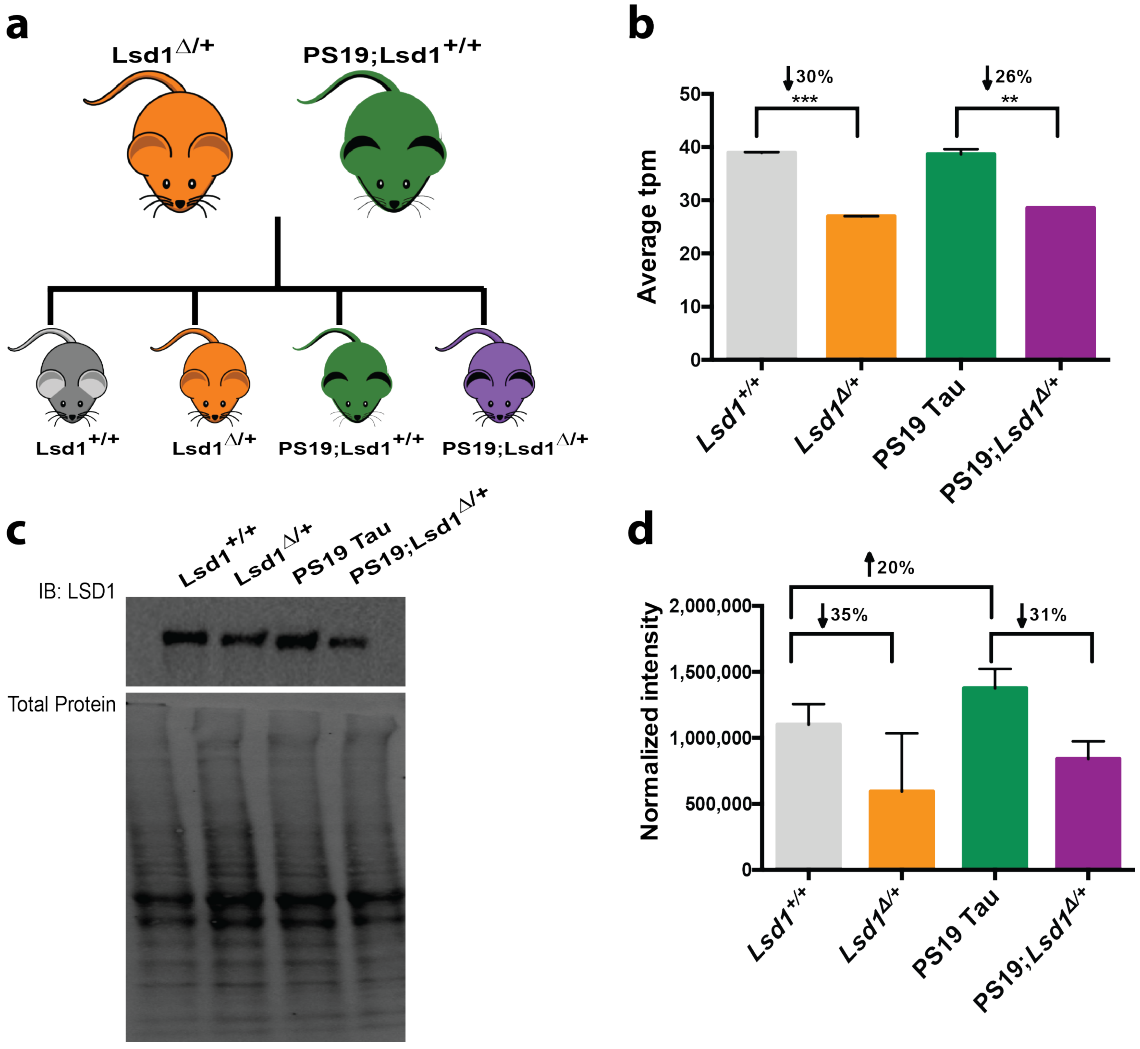

Fig. S2: Generation of PS19 Tau mice with reduced levels of LSD1.

a, PS19 Tau mice carrying the P301S human tau transgene that are wild-type for *Lsd1* were crossed with *Lsd1* heterozygous mice. These crosses generated four genotypes: Wild Type mice (*Lsd1*$^{+/+}$, grey), *Lsd1* heterozygous mice (*Lsd1*$^{\Delta/+}$, orange), PS19 Tau mice that are wild-type for *Lsd1* (PS19;*Lsd1*$^{+/+}$ referred to as PS19 Tau, green), and PS19 Tau mice that are heterozygous for *Lsd1* (PS19;*Lsd1*$^{\Delta/+}$, purple). Colors designated here are maintained throughout all figures. **b,** Average transcripts per million (tpm) from RNA-sequencing of *Lsd1* expression in the hippocampus of *Lsd1*$^{+/+}$, *Lsd1*$^{\Delta/+}$, PS19 Tau, and PS19;*Lsd1*$^{\Delta/+}$ mice. *Lsd1*$^{\Delta/+}$ mice had a 30% reduction in expression compared to *Lsd1*$^{+/+}$ mice, and PS19;*Lsd1*$^{\Delta/+}$ had a 26% reduction in expression compared to PS19 Tau mice. Values are mean ± SD (n=2, one-way analysis of variance (ANOVA) **P<0.01, ***P<0.005). **c,** Representative image of protein levels in the brain of *Lsd1*$^{+/+}$, *Lsd1*$^{\Delta/+}$, PS19 Tau, and PS19;*Lsd1*$^{\Delta/+}$ mice from LSD1 immunoblot and corresponding total protein blot. **d,** Quantification of immunoblot for LSD1 normalized to total protein loaded per sample as represented in **Fig. S2c**. Compared to *Lsd1*$^{+/+}$ mice, *Lsd1*$^{\Delta/+}$ mice had a 35% reduction and PS19 Tau mice had 20% increase in LSD1 protein levels. PS19; *Lsd1*$^{\Delta/+}$ mice had a 31% reduction in LSD1 protein level compared to PS19 Tau mice. Values are mean ± SD (n=3, one-way analysis of variance (ANOVA)).

Fig. S3: Reduction of *Lsd1* affects spinal cord in PS19 Tau mice

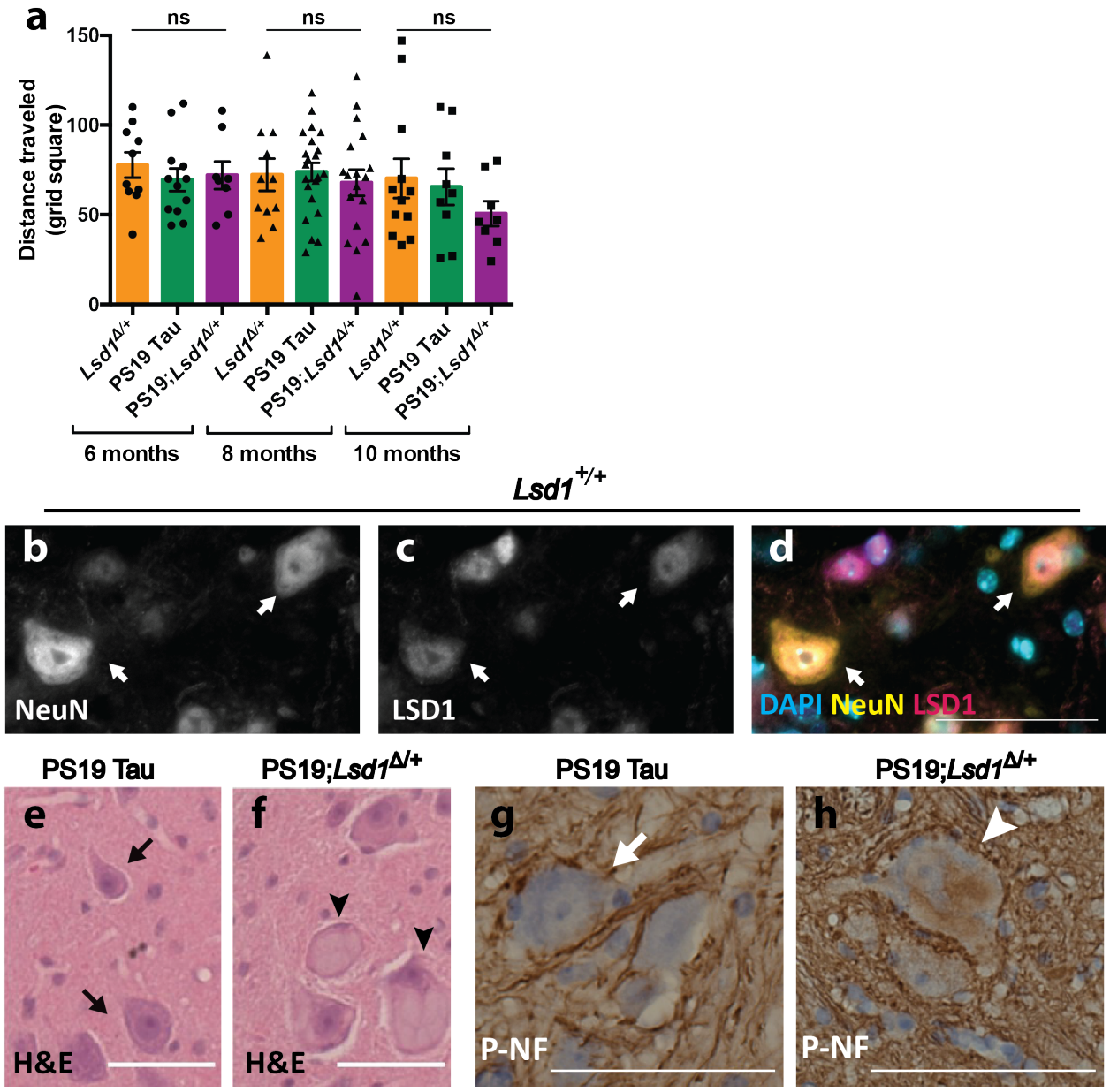

Fig. S3: Reduction of *Lsd1* affects spinal cord in PS19 Tau mice

a, Grid performance test measuring the distance traveled (grid squares traversed) with both forelimbs and hindlimbs in 6, 8, and 10 month old mice. $Lsd1^{\Delta/+}$ (orange, n=10,11,12), PS19 Tau (green, n=12,22,9), and PS19;$Lsd1^{\Delta/+}$ (purple, n=8,18,8). Values are mean ± SEM (two-way analysis of variance (ANOVA) with Tukey's post hoc test. ns=not significant). **b-d,** Immunofluorescence staining of NeuN (**b**), LSD1 (**c**), and merged with DAPI (**d**) in spinal cord motor neurons of 12 month old $Lsd1^{+/+}$ control mice. **e,f,** Representative image of hematoxylin and eosin (H&E) staining of motor neurons in 12 month old PS19 Tau mice (**e**) and PS19;$Lsd1^{\Delta/+}$ (**f**) littermates. **g,h,** Representative image of immunohistochemistry staining for phospho-nuerofilament (brown) counterstained with DAPI (blue) in the motor neurons of 12 month old PS19 Tau mice (**g**) and PS19;$Lsd1^{\Delta/+}$ (**h**) littermates. Arrows denote healthy motor neurons. Arrowheads denote abnormal motor neurons. Scale bars=50μm.

Fig. S4: There is no exacerbation of neurodegeneration in PS19 Tau mice with reduced *Lsd*1 until 10 months of age.

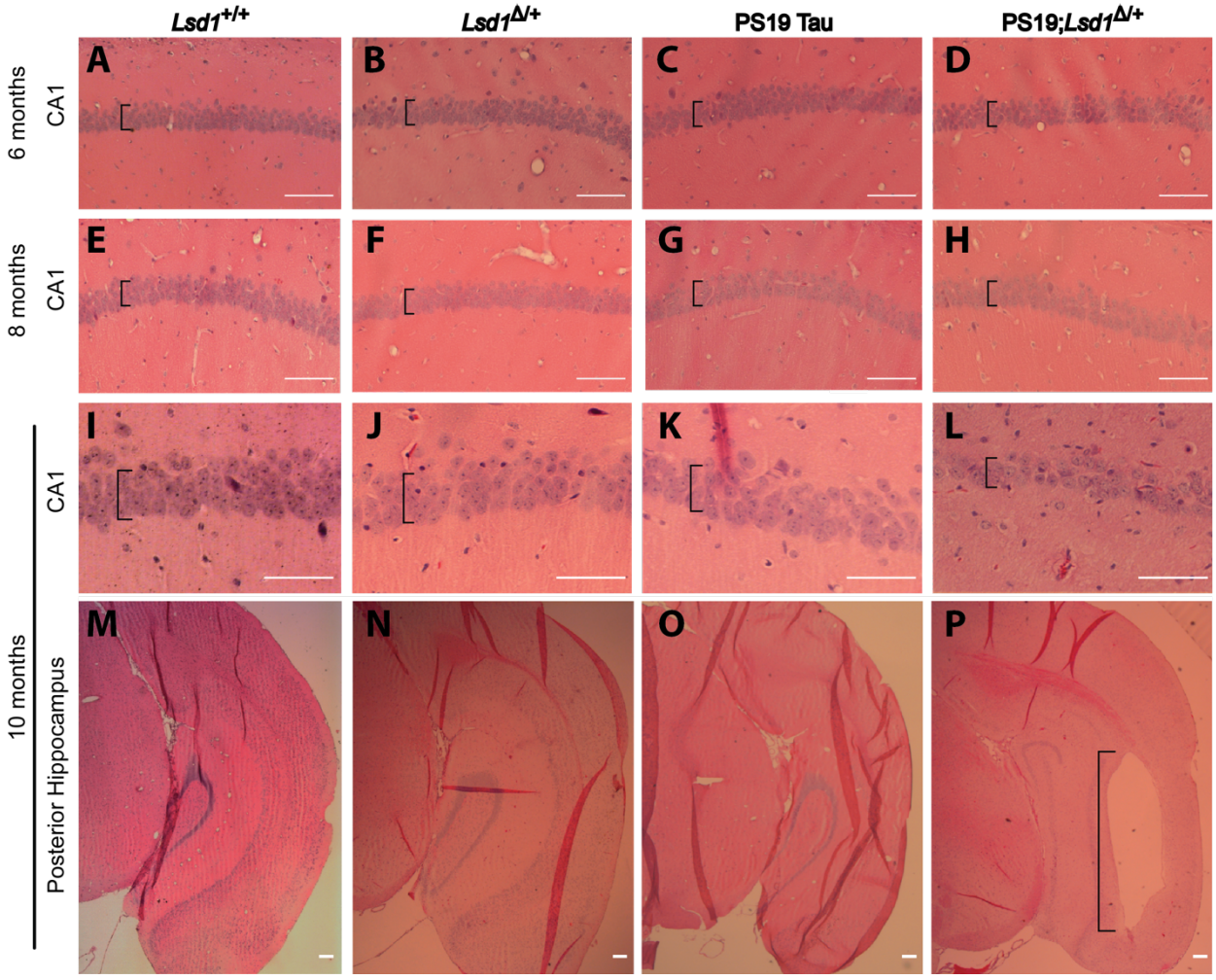

Fig. S4: There is no exacerbation of neurodegeneration in PS19 Tau mice with reduced *Lsd*1 until 10 months of age.

a-p, Representative image of H&E staining of *Lsd1*$^{+/+}$ (**a,e,i,m**), *Lsd1*$^{\Delta/+}$ (**b,f,j,n**), PS19 Tau (**c,g,k,o**), and PS19;*Lsd1*$^{\Delta/+}$ (**d,h,l,p**) littermates at 6 months (**a-d**), 8 months (**e-h**) and 10 months (**i-p**) in the CA1 (**a-l**) and posterior hippocampus (**m-p**). Brackets denote thickness of pyramidal layer of the CA1 (**a-l**), and region of cell clearance in posterior hippocampus (**p**). Scale bars=50μm.

Fig. S5: Increased neurodegeneration throughout the hippocampus and cortex of 12 month old mice.

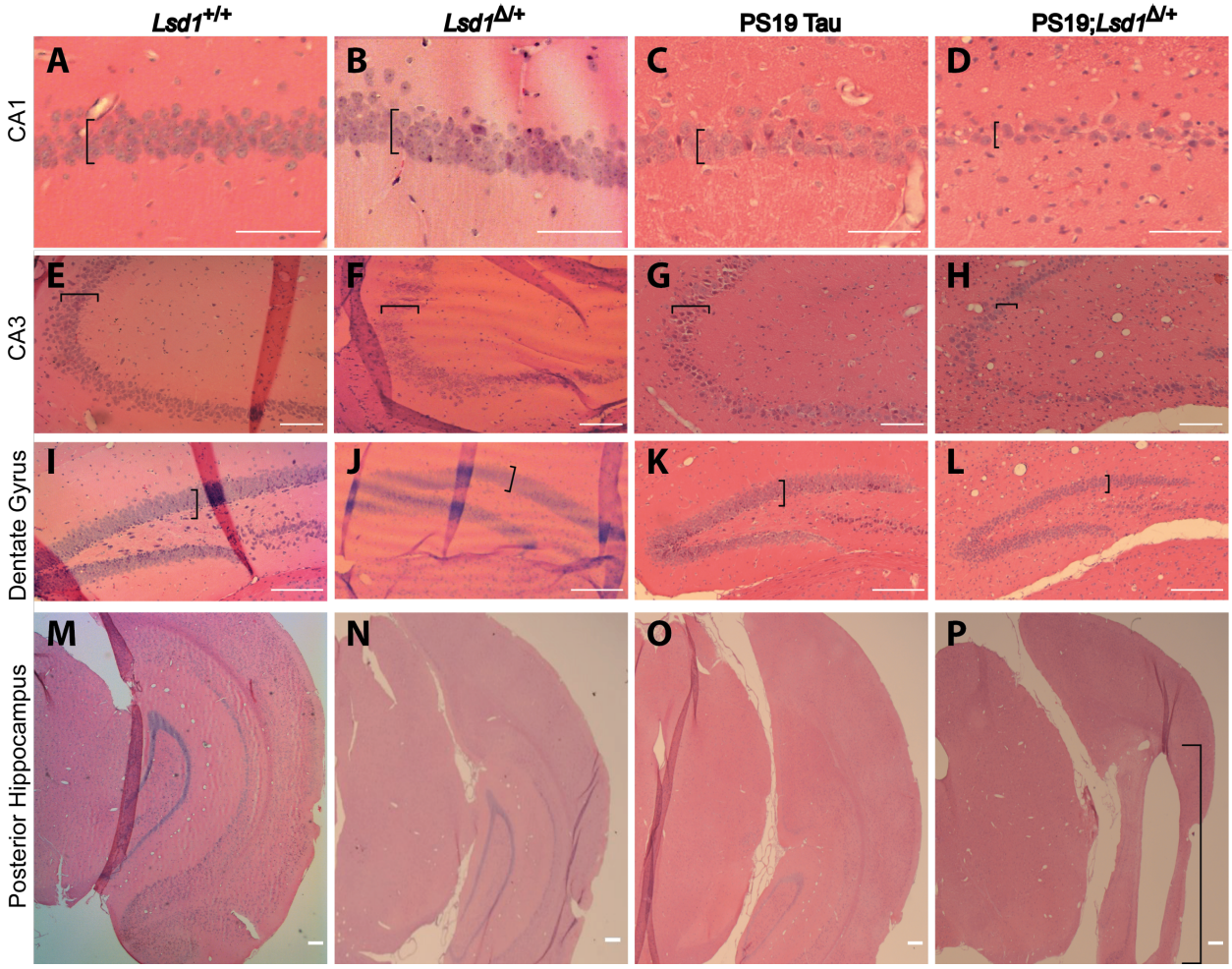

Fig. S5: Increased neurodegeneration throughout the hippocampus and cortex of 12 month old mice.

a-p, H&E staining of 12 month old *Lsd1*$^{+/+}$ (**a,e,i,m**), *Lsd1*$^{\Delta/+}$ (**b,f,j**,**n**), PS19 Tau (**c,g,k,o**), and PS19;*Lsd1*$^{\Delta/+}$ (**d,h,l,p**) littermates in the CA1 (**a-d**) and CA3 (**e-h**) regions of the hippocampus, the dentate gyrus (**i-l**), and the posterior hippocampus (**m-p**). Brackets denote thickness of pyramidal layer of the CA1 (**a-d**), CA3 (**e-h**), the granule cell layer of the Dente Gyrus (**i-l**), and region of cell clearance in posterior hippocampus (**p**). Scale bars=50μm.

Fig. S6: Reduction of *Lsd1* does not affect AT8 positive tau pathology.

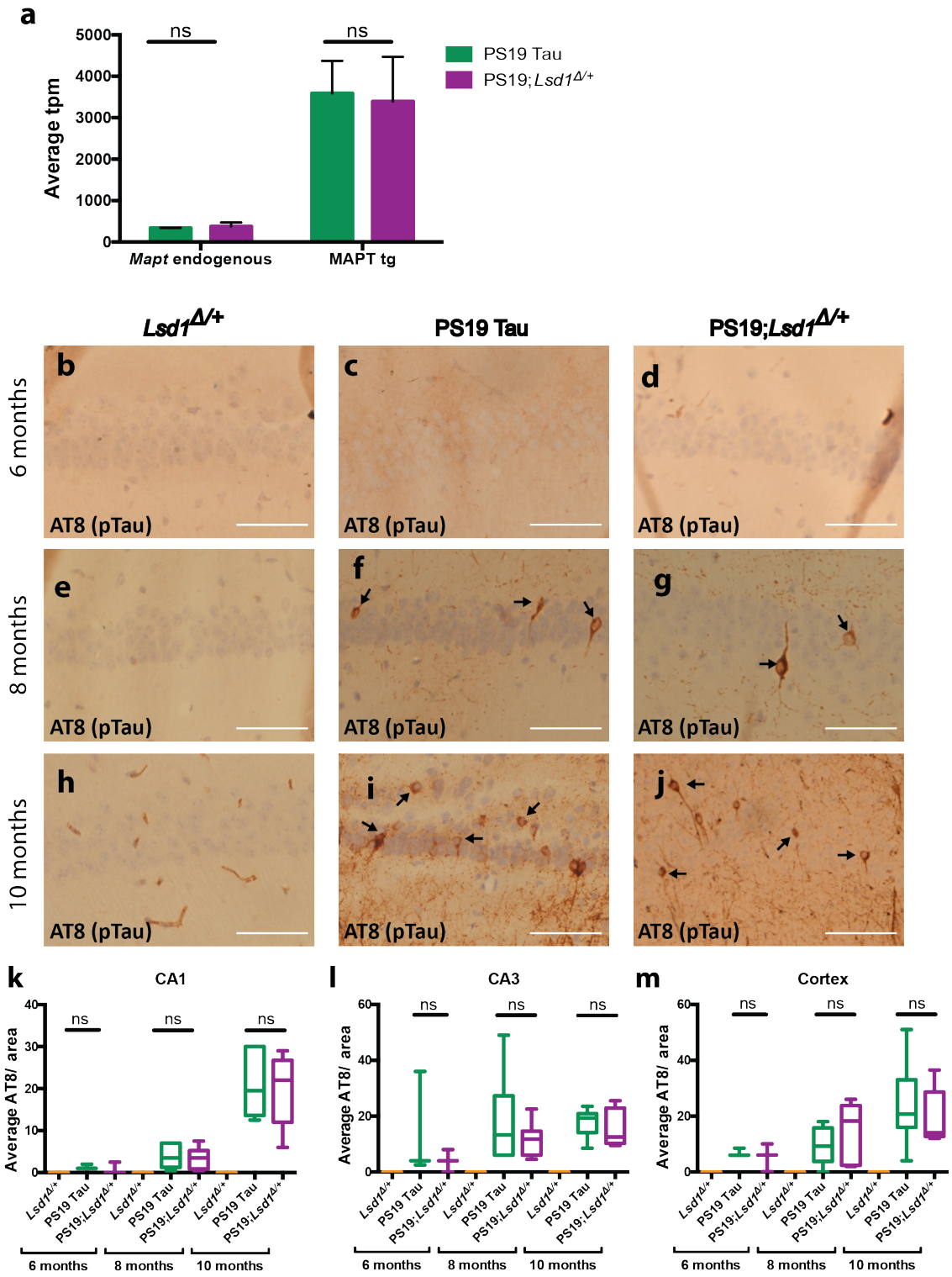

Fig. S6: Reduction of *Lsd1* does not affect AT8 positive tau pathology.

a, Average transcripts per million (tpm) from RNA sequencing of endogenous MAPT and the expression of the human P301S MAPT transgene in the hippocampus of PS19 Tau, and PS19; $Lsd1^{\Delta/+}$ mice. Values are mean ± SD (n=2). **b-j,** Representative image of immunohistochemistry staining of phosphorylated tau (AT8 antibody) of the CA1 region of the hippocampus in $Lsd1^{\Delta/+}$ (**b,e,h**) , PS19 Tau (**c,f,i**), and PS19;$Lsd1^{\Delta/+}$ (**d,g,j**) littermates at 6 months (**b-d**), 8 months (**e-g**), and 10 months (**h-j**). Arrows denote AT8 positive immunoreactivity. Scale bars=50μm. **k-m,** Quantification of the average AT8 positive tau immunoreactivity per area from histology represented in **Fig. S6b-j** in the CA1 (**k**) and CA3 (**l**) regions of the hippocampus, and the cerebral cortex (**m**) (6 months n=3, 8 months n=6, and 10 months n=6, box plot edges are 25th and 75th percentile, central line is the median, and whiskers are max and min). For all graphs: one-way analysis of variance (ANOVA) with Tukey's post hoc test (two-sided), ns=not significant.

Fig. S7: Reduction of *Lsd1* does not affect PHF1 positive tau pathology.

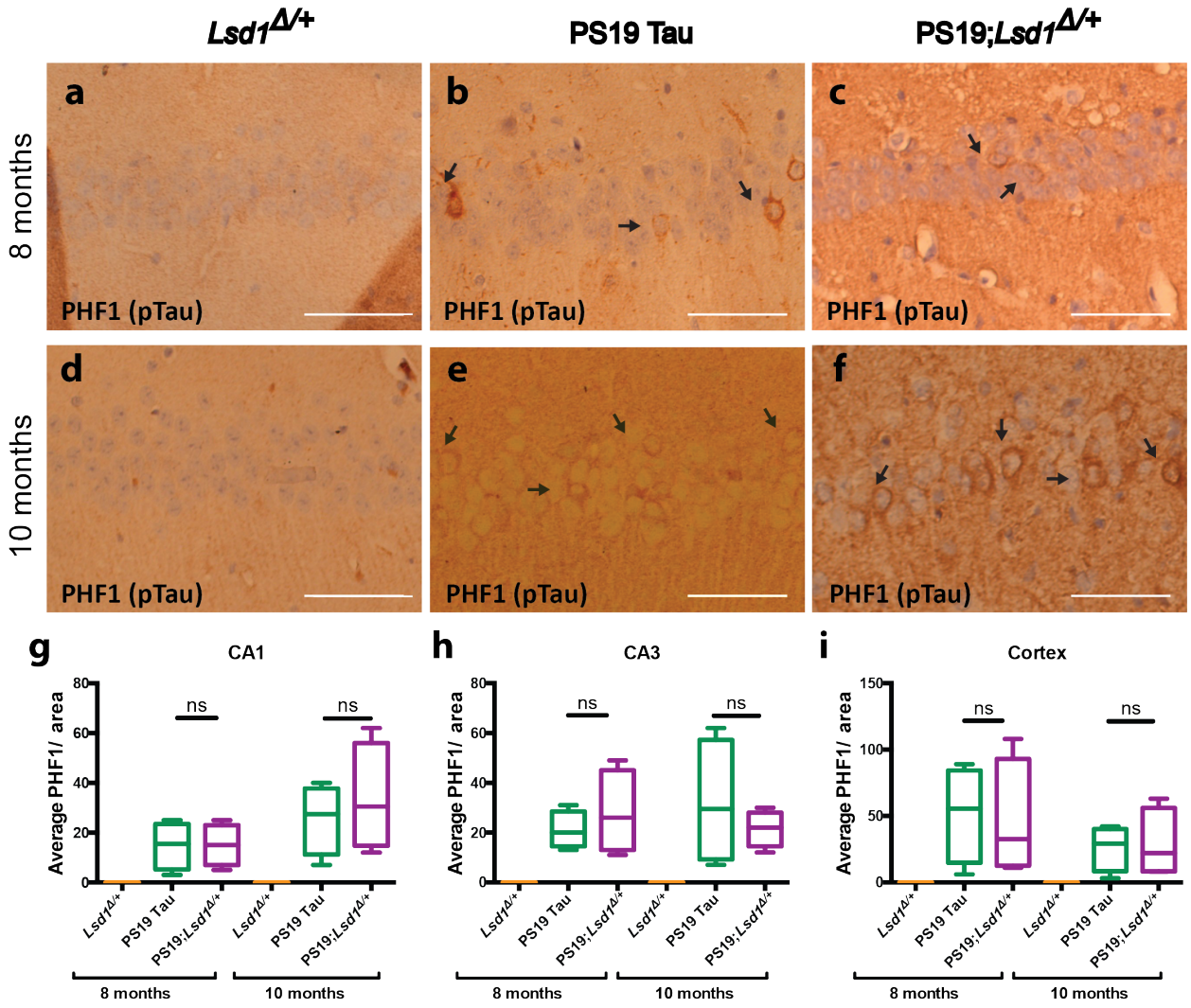

Fig. S7: Reduction of *Lsd1* does not affect PHF1 positive tau pathology

a-f, Representative image of immunohistochemistry staining of PHF1 in the CA1 region of the hippocampus in $Lsd1^{\Delta/+}$ (**a,d**), PS19 Tau (**b,e**), and PS19;$Lsd1^{\Delta/+}$ (**c,f**) littermates at 8 months (**a-c**) and 10 months (**d-f**). Arrows denote PHF1 positive immunoreactivity. Scale bars=50μm. **g-i,** Quantification of average PHF1 positive tau immunoreactivity per area from histology represented in **Fig.** S7**a-f** in the CA1 (**g**) and CA3 (**h**) regions of the hippocampus, and the cerebral cortex (**i**) (*n*=4 box plot edges are 25th and 75th percentile, central line is the median, and whiskers are max and min). For all graphs: one-way analysis of variance (ANOVA) with Tukey's post hoc test (two-sided), ns=not significant.

Fig. S8: Differential expression in 9 month old *Lsd1*$^{\Delta/+}$, PS19 Tau, and PS19;*Lsd1*$^{\Delta/+}$ hippocampus.

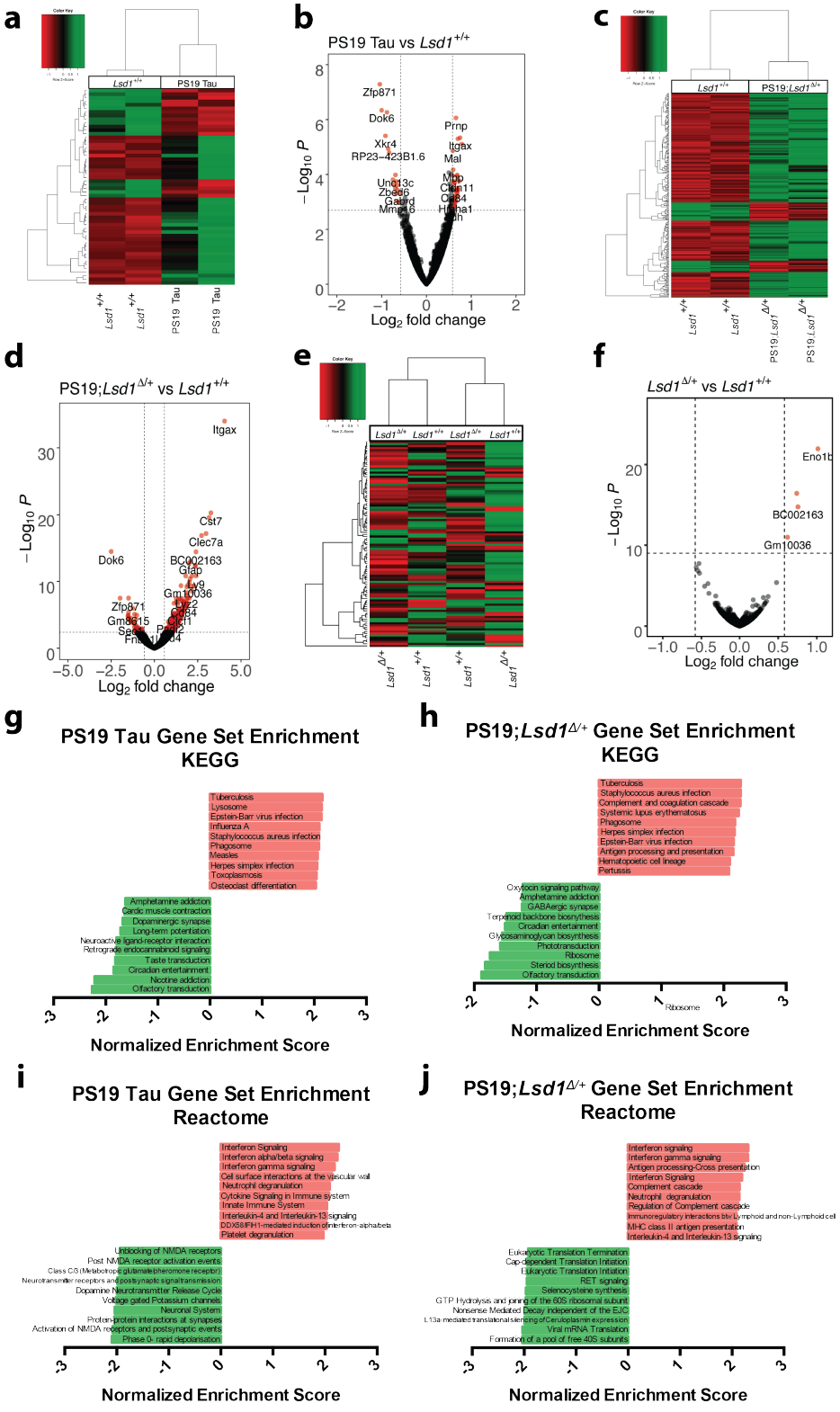

Fig. S8: Differential expression in 9 month old *Lsd1*$^{\Delta/+}$, PS19 Tau, and PS19;*Lsd1*$^{\Delta/+}$ hippocampus.

a,c,e, Heatmap of differentially expressed RNA-seq transcripts between *Lsd1*$^{+/+}$ and PS19 Tau (**a**), PS19; *Lsd1*$^{\Delta/+}$ (**c**), and *Lsd1*$^{\Delta/+}$ (**e**) mouse hippocampus. Samples are hierarchically clustered by relative expression of differentially expressed transcripts. Relative higher (red) and lower (green) expression is indicated. **b,d,f,** Volcano plot of $\log_2$ fold-changes in gene expression (x-axis) by statistical significance ($-\text{Log}_{10}$ P-value; y-axis) in PS19 Tau (**b**), PS19; *Lsd1*$^{\Delta/+}$ (**d**), and *Lsd1*$^{\Delta/+}$ (**f**) compared to *Lsd1*$^{+/+}$ mouse hippocampus. Each dot represents a transcript, and the dotted line represents a significance $\log_2$ fold change cut off of 0.5. **g-j,** Histogram of Gene Set Enrichment Analysis compared to KEGG pathways (**g,h**) and the Reactome (**i,j).** The top ten most enriched (red) and depleted (green) gene sets in the PS19 Tau (**g,i**) and PS19; *Lsd1*$^{\Delta/+}$ (**h,j**) are shown with normalized enrichment scores.

Fig. S9: LSD1 overexpression in hippocampal neurons of PS19 Tau mice.

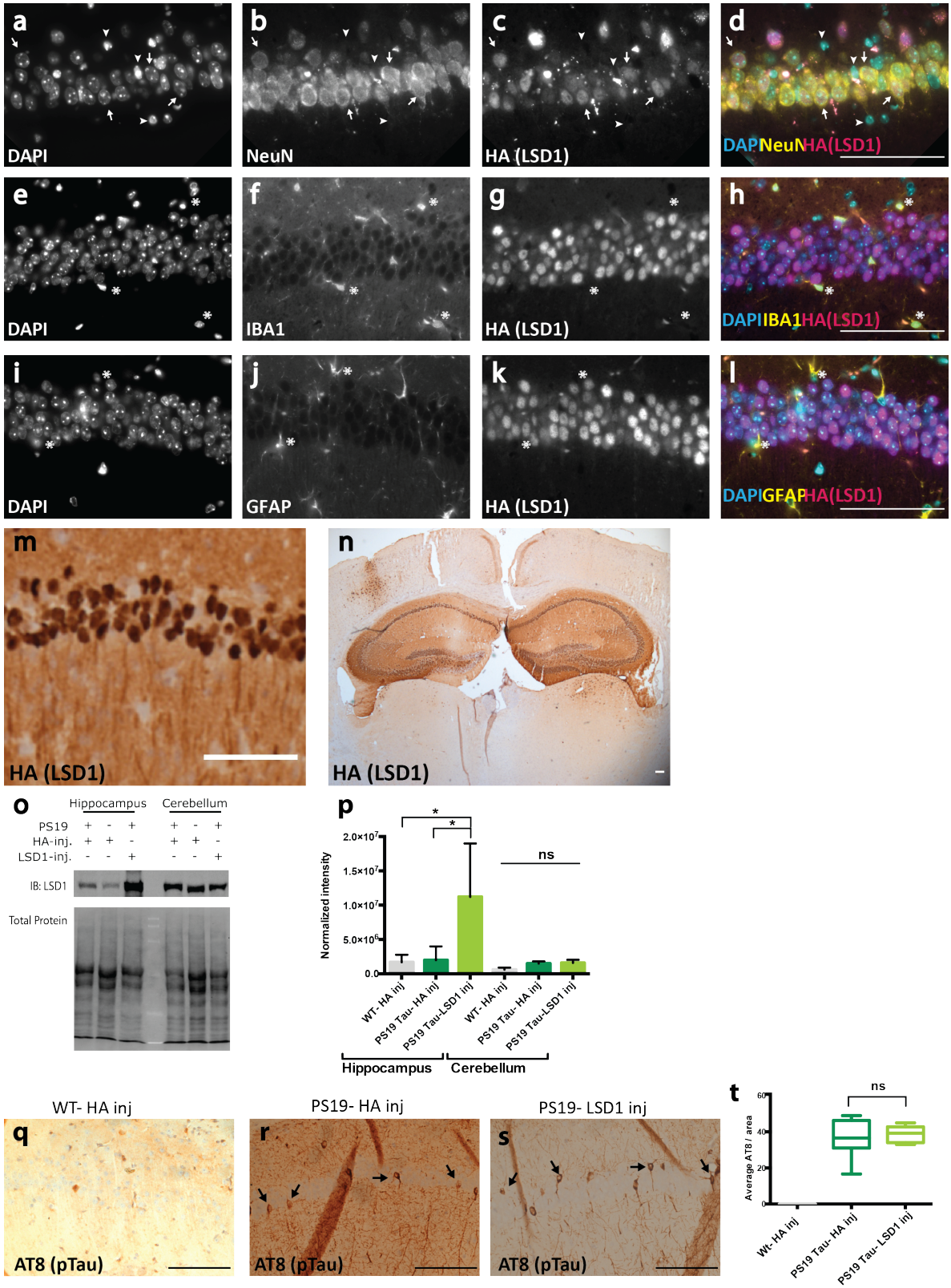

Fig. S9: LSD1 overexpression in hippocampal neurons of PS19 Tau mice

a-d, Representative immunofluorescence labeling in a WT- HA inj mouse showing DAPI (**a**), NeuN (**b**), HA (which represents the LSD1 virus, hereafter denoted as HA(LSD1)) (**c**), and merged (**d**). Viral produced LSD1 is present in NeuN+ neurons. Arrows denote NeuN+ cells that have HA expression. Arrowheads denote cells that lack NeuN staining and also lack HA expression. **e-h,** Representative immunofluorescence labeling showing DAPI (**e**), IBA1 (**f**), HA(LSD1) (**g**), and merged (**h**). Asterisks denote cells stained positive for IBA1 (**e-h**), which lack HA expression. **i-l,** Representative immunofluorescence labeling showing DAPI (**i**), GFAP (**j**), HA(LSD1) (**k**), and merged (**l**) images. Asterisks denote cells stained positive for GFAP (**i-l**), which lack HA expression. **m-n,** Immunohistochemistry staining for HA(LSD1) showing expression localized to the nucleus of neurons (**m**) specifically within the hippocampus (**n**). **o,** Representative image of immunoblot for LSD1 protein and corresponding total protein blot in the hippocampus versus the cortex of mice injected with either LSD1 or HA only expressing virus. **p,** Quantification of immunoblot for LSD1 normalized to total protein loaded per sample as represented in **Fig. S9o** shows overexpression in the hippocampus, but not the cortex. Values are mean ± SD (n=3, one-way analysis of variance (ANOVA) with Tukey's post hoc test (two-sided), *P<0.05, ns=not significant. **q-r,** Representative image of immunohistochemistry staining of phosphorylated tau (AT8 antibody) in the CA1 region of the hippocampus in 11 month old WT- HA inj (**q**), PS19- HA inj (**r**), and PS19- LSD1inj (**s**) mice. Arrows denote AT8 positive immunoreactivity. Scale bars=50μm. (**t**) Quantification of average AT8 positive tau immunoreactivity per area from histology represented in **Fig. S9q-s**. Box plot edges are 25th and 75th percentile, central line is the median, and whiskers are max and min (n=8, one-way analysis of variance (ANOVA) with Tukey's post hoc test (two-sided), ns=not significant).

Fig. S10: LSD1 overexpression reduces the gliosis in PS19 Tau mice.

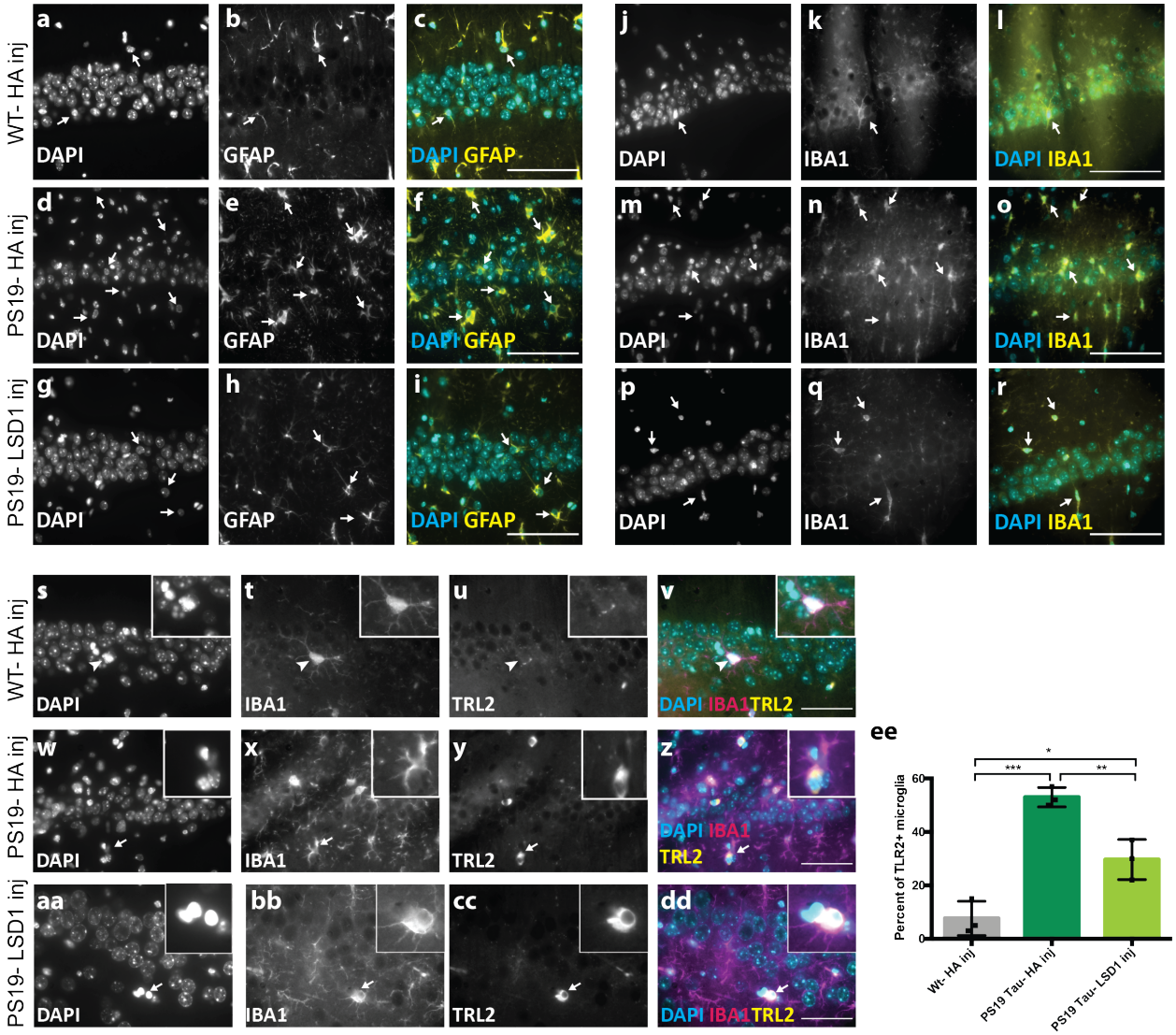

Fig. S10: LSD1 overexpression reduces the gliosis in PS19 Tau mice.

a-i, Representative immunofluorescence showing DAPI (**a,d,g**), astrocyte marker GFAP (**b,e,h**), and merged (**c,f,i**) images in WT- HA inj (**a-c**), PS19- HA inj (**d-f**), and PS19- LSD1 inj (**g-i**). Arrows denote GFAP+ astrocytes. **j-r,** Representative immunofluorescence showing DAPI (**j,m,p**), microglia marker IBA1 (**k,n,q**), and merged (**l,o,r**) images in WT- HA inj (**j-l**), PS19-HA inj (**m-o**), and PS19- LSD1 inj (**p-r**). Arrows denote IBA1+ microglia. **s-dd,** Representative immunofluorescence labeling showing DAPI (**s,w,aa**), microglia marker IBA1 (**t,x,bb**), activated microglia marker TRL2 (**u,y,cc**), and merged (**v,z,dd**) images in WT-Ha inj (**s-v**), PS19-HA inj (**w-z**), and PS19-LSD1 inj (**aa-dd)**. Inset of microglia that is IBA1 positive but TRL2 negative (**s-v,** denoted by arrowhead) or both IBA1 and TRL2 positive (**w-dd**, denoted by arrow). All images are from the CA1 region of the hippocampus Scale bars=50μm. **ee,** Quantification of the percentage of microglia that are TRL2+ in WT- HA inj, PS19- HA inj, and PS19- LSD1 inj mice represented in **Fig. S10s-dd**. Values are mean ± SD are (*n*=3, one- way analysis of variance (ANOVA) with Tukey's post hoc test, *p<0.05, **p<0.01, ***p<0.005).

Chapter 4. Discussion

4.1 Summary of Findings and Significance

Our data suggests the model that accumulation of cytoplasmic pathological tau aggregates leads to sequestration of LSD1 protein in the cytoplasm. LSD1 is continually required in the nucleus for neuronal survival (1, 2). Data from ours and other labs suggest that LSD1 (and its complexes) functions as a repressor of chromatin and prevents the inappropriate transcription of non-neuronal genes in neurons (3–5). It is possible that LSD1 sequestration is the result of an interaction between pathological TAU and the N-terminal intrinsically disordered domain (IDR) of LSD1. This interaction masks the NLS signal and prevents the nuclear localization of LSD1 by the importin complex. Furthermore, the prevention of LSD1 accumulation in the nucleus results in inappropriate gene transcription and neuronal cell death.

In order to determine the role of Lsd1 in terminally differentiated cells, we deleted Lsd1 from adult mouse neurons. Loss of LSD1 leads to massive neuronal cell death, paresis and significant learning and memory defects. We observed a significant increase in pyknotic nuclei, TUNEL positive neuronal nuclei and complete loss of TAU and MAP2 staining in LSD1 mutant hippocampus. These data all strongly indicate massive neuronal loss following the loss of LSD1. Additionally, we observed significantly increased latency to mount platform in the Morris water maze test in LSD1 mutants compared to controls. We also performed genome-wide RNA sequencing to identify broad changes in gene expression. Genome-wide expression changes observed in the hippocampus of human AD (and FTD) patients are highly correlated with those observed in the hippocampus of LSD1 mutant mice (6, 7). This correlation appears to be specific to tauopathy and not neuronal cell death/ neurodegeneration in general. For example, expression changes in other neurodegenerative diseases, such as PD, are not correlated with those observed in LSD1 mutant mice (8).

Furthermore, LSD1 inappropriately colocalizes with pathological TAU in human AD patients. LSD1 immunohistochemistry was performed on post-mortem AD and age-matched control cases. We observed LSD1 inappropriately associated with cytoplasmic NFTs and neurites but not amyloid plaque pathology. To confirm this finding, we performed dual immunofluorescence with antibodies to LSD1 and pTau. LSD1 colocalizes with pTAU in over 50% of NFTs in the AD cases analyzed. These data suggest a critical role for LSD1 in tau-mediated neurodegeneration.

To further investigate the role of LSD1 in tau-mediated neurodegeneration we utilized the P310S tau mouse. A mouse model for tauopathy overexpressing mutant human MAPT protein found in AD and other tauopathies (9, 10). We observed the sequestration of LSD1 protein from the nucleus in these mice after the accumulation of pTAU aggregates. Furthermore, in LSD1 heterozygous mice (40% reduction of LSD1 expression), the exclusion of LSD1 from neuronal nuclei was accelerated and exacerbated. In the context of the P301S tau mouse, reduction of LSD1 protein levels ultimately leads to the exacerbation of the p301s mediated neurodegeneration. LSD1 heterozygosity alone has no observable phenotypic effect on mice and no significant gene expression changes. However, P301S; LSD1+/- mice exhibit significantly more signs of neurodegeneration and shorter life spans. Furthermore, gene expression changes observed in P301S;LSD1+/- mice are observed in highly similar genes/ genetic pathways as P301S but significantly exaggerated. In addition to the reduction of LSD1, we also observed that the overexpression of LSD1 can prevent or at least delay the sequestration of LSD1 from the nucleus and delay the onset of tau-mediated neurodegeneration. This occurs even in the presence of significant tau pathology. Moreover, LSD1 overexpression also ameliorates the aberrant gene expression observed in P301s mice.

Taken together, these data and our model suggests that LSD1 is a critical downstream regulator of tau-mediated neurodegeneration in mice and in human AD. LSD1 also represents a potential therapeutic target for the treatment and/or prevention of tau-mediated neurodegeneration. Particularly because we have observed that targeting LSD1 expression has significant effects on disease progression even after presence of a significant pathological tau burden. More broadly, this data illustrates that terminally differentiated cells, such as neurons, may require continuous prevention of inappropriate gene expression through homeostatic epigenetic mechanisms that maintain cell fate. Congruent with these findings, we also observe that LSD1 is required to maintain testis stem cell fate in both development and adulthood (Appendix A).

4.2 Future Directions

There are several avenues for potential therapeutic interventions targeting LSD1 in neurodegenerative disease. Firstly, it may be possible to overexpress LSD1 directly or indirectly through the reactivation of LSD2 (11). However, based on our data, this approach may only delay or temporarily ameliorate the neurodegenerative process. Additionally, one could modulate LSD1 levels therapeutically by more broadly influencing the balance of chromatin state at the LSD1 locus through chromatin modifiers (12, 13). Furthermore, we hypothesize that the pathological tau interacts with the IDR of LSD1. Therefore, inhibiting this specific interaction could be therapeutically relevant in the treatment of tauopathy (14–16).

Future directions include utilizing the overexpression of the truncated LSD1 protein containing only the IDR to potentially saturate the binding epitope of pathological tau allowing full length LSD1 to avoid cytoplasmic sequestration and remain localized to neuronal nuclei.

Additionally, one could disrupt LSD1 IDR – pathological tau interactions by utilizing a high throughput biochemical assay to screen for compounds that bind the LSD1 IDR and prevent phase transition.

4.4 References

1. A. K. Engstrom, *et al.*, The inhibition of LSD1 via sequestration contributes to tau-mediated neurodegeneration. *P Natl Acad Sci Usa* 117, 29133–29143 (2020).

2. M. A. Christopher, *et al.*, LSD1 protects against hippocampal and cortical neurodegeneration. *Nat Commun* 8, 805 (2017).

3. R. Armisén, R. Fuentes, P. Olguín, M. E. Cabrejos, M. Kukuljan, Repressor Element-1 Silencing Transcription/Neuron-Restrictive Silencer Factor Is Required for Neural Sodium Channel Expression during Development of Xenopus. *J Neurosci* 22, 8347–8351 (2002).

4. T. Kuwabara, J. Hsieh, K. Nakashima, K. Taira, F. H. Gage, A Small Modulatory dsRNA Specifies the Fate of Adult Neural Stem Cells. *Cell* 116, 779–793 (2004).

5. N. Ballas, C. Grunseich, D. D. Lu, J. C. Speh, G. Mandel, REST and Its Corepressors Mediate Plasticity of Neuronal Gene Chromatin throughout Neurogenesis. *Cell* 121, 645–657 (2005).

6. B. Zhang, *et al.*, Integrated Systems Approach Identifies Genetic Nodes and Networks in Late-Onset Alzheimer's Disease. *Cell* 153, 707–720 (2013).

7. A. S. Chen-Plotkin, *et al.*, Variations in the progranulin gene affect global gene expression in frontotemporal lobar degeneration. *Hum Mol Genet* 17, 1349–1362 (2008).

8. Y. Zhang, M. James, F. A. Middleton, R. L. Davis, Transcriptional analysis of multiple brain regions in Parkinson's disease supports the involvement of specific protein processing, energy metabolism, and signaling pathways, and suggests novel disease mechanisms. *Am J Medical Genetics Part B Neuropsychiatric Genetics* 137B, 5–16 (2005).

9. Y. Yoshiyama, *et al.*, Synapse Loss and Microglial Activation Precede Tangles in a P301S Tauopathy Mouse Model. *Neuron* 53, 337–351 (2007).

10. A. Bellucci, *et al.*, Induction of Inflammatory Mediators and Microglial Activation in Mice Transgenic for Mutant Human P301S Tau Protein. *Am J Pathology* 165, 1643–1652 (2004).

11. R. Fang, *et al.*, Human LSD2/KDM1b/AOF1 Regulates Gene Transcription by Modulating Intragenic H3K4me2 Methylation. *Mol Cell* 39, 222–233 (2010).

12. B. D. Strahl, C. D. Allis, The language of covalent histone modifications. *Nature* 403, 41–45 (2000).

13. T. Kouzarides, Chromatin Modifications and Their Function. *Cell* 128, 693–705 (2007).

14. I. Diner, *et al.*, Aggregation Properties of the Small Nuclear Ribonucleoprotein U1-70K in Alzheimer Disease*. *J Biol Chem* 289, 35296–35313 (2014).

15. V. Uversky, Amyloidogenesis of Natively Unfolded Proteins. *Curr Alzheimer Res* 5, 260–287 (2008).

16. Y. Chen, *et al.*, Crystal structure of human histone lysine-specific demethylase 1 (LSD1). *Proc National Acad Sci* 103, 13956–13961 (2006).

Chapter 5. Extended Materials and Methods

5.1 RNA Sequencing Analysis

5.1.1 Quality Control

Sequencing data (FASTQ files) were uploaded to the Galaxy web platform, (public server at http://usegalaxy.org). Paired-end data from each sample (forward and reverse) were put together into a data collection (2 files per collection). Quality assessment on each data collection of FASTQ files was performed using FASTQC (v.0.11.7). FASTQC returned many quality assessment metrics. The sequence quality histogram illustrated the mean quality (or Phread) score per base across the 50bp reads. An average Phread score of 20 or greater and minimum length of 36 base pairs after trimming was required to retain the read for further downstream analysis. FASTQC also provided information such as sequence length distribution, sequence duplication levels, overrepresented sequences and adapter content. We ensured these metrics were within the acceptable range and no adapter content was present. Sequence trimming was performed using Trimmomatic (v.0.36.5). Default settings were used unless noted otherwise below. Trimmomatic parameters utilized within the Galaxy web platform:

- select “paired-end” (as collection)
- “Perform initial ILLUMINACLIP step?” = NO
- Use default setting for 1st trimmomatic operation
- Sliding window trimming, Number of bases to average across = 4,
- Average quality score required = 20
- Insert 2nd trimmomatic operation
- from dropdown list select “minlen”
- minimum length of reads to be kept: 36bp

5.1.2 Sequence Mapping

Paired-end reads were mapped to the GRCm38 genome using HISAT2 (v.2.1.0). GRCm38 (DNA primary assembly) FASTA file was downloaded from the Ensembl FTP site on 7/24/18

and uploaded to the galaxy web platform. Default settings were used unless noted otherwise below. HISAT2 parameters utilized within the Galaxy web platform:

- Select ‘use genome from history”
- Select uploaded GRCm38 DNA primary assembly FASTA file
- “Paired-end reads”
- “Unstranded”
- Under ‘summary options’ select ‘output summary’ and ‘print summary to file’

5.1.3 Sequence Mapping Quality Control

Unmapped, unpaired and multiply mapped reads were then removed using Filter SAM or BAM (v.1.1.2). Filter SAM or BAM parameters utilized within the Galaxy web platform:

- Select BAM file generated by HISAT2
- Set “minimum MAPQ quality score” to 40
- Set “filter on bitwise flag” to yes
- Select “read is paired” and “read is mapped in a proper pair”

HISAT2 MAPQ scores range from 0-60:
60 - uniquely mapped read, regardless of number of mismatches / indels
1 - multiply mapped, perfect match or few mismatches / indels
0 - unmapped, or multiply mapped and with lots of mismatches / indels

Utilizing a minimum MAPQ quality score > 40 allowed for the removal of non-uniquely mapped reads. Additionally, BAM files from the Filter SAM or BAM utility were analyzed for mapping quality using Flagstat.

5.1.4 Differential Expression

Assignment of transcripts to GRCm38 genomic features was performed using Featurecounts (v.1.6.0.6). GRCm38.93 GTF file was downloaded from Ensembl FTP site on 7/21/18 and uploaded to the galaxy web platform. Featurecounts parameters utilized within the Galaxy web platform:

- Select BAM files generated by Filter SAM or BAM utility
- “Unstranded”
- Select annotation file “in your history”
- Select Ensembl GTF file previously uploaded
- “Output format”: DESEQ2 compatible
- Select yes for “create gene length file” (needed calculate TPM or FPKM)
- Under “options for paired-end reads” menu, enable ‘count fragments instead of reads”

Differentially expressed transcripts were determined using DESEQ2 (v.2.11.40.2). Tabular count files from Featurecounts were used to analyze differential expression between genotypes. Within DESEQ2, the factor was genotype with the different levels being experimental genotype vs control/ WT genotype. The analysis was run independently for each experimental-control pair. DESEQ2 was also utilized to generate normalized count tables. These counts represent expression values normalized for differences in sequencing depth and composition bias to allow for direct comparison between samples via heatmap visualizations. DESEQ2 parameters utilized within the Galaxy web platform:

- Select output from Featurecounts utility (.tabular count files)
- Factor = genotype
- Factor level 1 = experimental samples of the same genotype
- Factor level 2 = control samples
- Repeat for each genotype compared to control
- Under “Files have header?” select “yes” (output from featurecounts have a header)
- Under “Output normalized counts table?” select “yes”

Normalized count files from featurecounts and DESEQ2 output files were downloaded from the galaxy web platform onto a physical drive stored in the Katz lab. Subsequent analyses were performed using R.

5.2 RNA Sequencing Data Processing

5.2.1 Transcripts per million reads (TPM) expression values

The following R script was used to determine gene expression in terms of transcripts per million reads (TPM). Raw count files and the feature length file from Featurecounts was the input data. The analysis was performed independently for each genotype. The following is a representative example.

```
#TPM = (read count / gene length in kilobases) / (sum of count/gene length column / 10^6)
## Read in Lsd1 control raw counts files and feature length file
controla.counts <- tbl_df(read.delim("controlA_SRR5535973.featurecounts.tabular",
                          stringsAsFactors = FALSE, header = TRUE))
controlb.counts <- tbl_df(read.delim("controlB_SRR5535974.featurecounts.tabular",
                          stringsAsFactors = FALSE, header = TRUE))
control.lengths <- tbl_df(read.delim("controlB_SRR5535974.featurelengths.tabular",
                           stringsAsFactors = FALSE, header = TRUE))

#Combine dataframes by Ensembl IDs
control <- control.lengths %>%
  left_join(controla.counts,by = "Geneid" ) %>%
  left_join(controlb.counts,by = "Geneid") %>%

#Convert feature lengths column from base pairs to kb
  mutate(control.length.kb = Length/1000) %>%
  rename(controlb.count = SRR5535974_controlB_.fastqsanger,
         controla.count = SRR5535973_controlA_.fastqsanger) %>%

#Calculate RPK for each sample
  mutate(controlaRPK = controla.count/control.length.kb,
         controlbRPK = controlb.count/control.length.kb)

#Calculate scaling factor for each sample
controla.scalingfactor <- sum(control$controlaRPK)/1000000
controlb.scalingfactor <- sum(control$controlbRPK)/1000000

#Calculate TPM for each sample
control <- control %>%
  mutate(controlaTPM = controlaRPK/controla.scalingfactor,
                controlbTPM = controlbRPK/controlb.scalingfactor) %>%

#Calculate mean value for both samples
  mutate(avg.controlTPM = rowMeans(select(.,controlaTPM,controlbTPM))) %>%
  arrange(desc(avg.controlTPM))
```

5.2.2 Identification of differentially expressed genes (DEGs)

For all datasets, a cutoff of adjusted p-value < 0.3 and abs (log_2 fold change) > 0.58 was applied.

This was performed using the following R script.

```
#Load Tidyverse package
library(tidyverse)

#Read in DESEQ2 results file
sample <- tbl_df(read.delim("Galaxy1-
        [DESeq2_result_file_on_LSD1mutant_vs_LSD1control].tabular", header = FALSE, sep
        = "\t", stringsAsFactors = FALSE))

#Add column identifiers
colnames(sample) <- c("ensembl.geneid","base.mean","log2fc","stderr","wald-
        stats","p.value","p.adj")

#Filter out genes with NA values for P.adjusted or log2 Fold-Change
#Apply p-adjusted and Log2 Fold-Change cutoffs
#Arrange in descending order by log2fc values
DEGs <- sample %>%
        select(ensembl.geneid, log2fc, p.adj, p.value ) %>%
        filter(!is.na(p.adj) & !is.na(log2fc)) %>%
        filter(p.adj < 0.3 & abs(log2fc) > 0.58 ) %>%
        arrange(desc(log2fc))

#Output CSV file with list of DEGs and corresponding gene symbols
write.csv(DEGs,"lsd1mut.DEGs.csv", row.names = FALSE)
```

5.2.3 Convert Ensembl IDs to Gene Symbols

The following R script was used to match mouse Ensembl Gene IDs in expression data to

corresponding mouse gene symbols.

```
## install GenomicFeatures and EnsDb.Mmusculus.v79 package to read in mouse gene
## identifiers
BiocManager::install ("GenomicFeatures")
BiocManager::install ("EnsDb.Mmusculus.v79")
library(GenomicFeatures)
library (EnsDb.Mmusculus.v79)
```

```
## Pull gene identification data from Ensembl Database
keys <- keys(EnsDb.Mmusculus.v79)
anno.result <- select(EnsDb.Mmusculus.v79, keys=keys,
        columns=c("GENEID","SYMBOL","GENENAME","ENTREZID"),keytype="GENEID)

## Subset annotation file for Ensembl ID and Gene Symbol
annot <- select(anno.result, GENEID, SYMBOL)

## Join annotation table and sample gene expression data by Ensembl IDs
Sample.symbol <- left_join(sample, annot, by = c("ensembl.geneid" = "GENEID"))
```

5.2.4 Heatmaps

Heatmaps and hierarchical clustering were generated using the "complex heatmap package" in

R. Input was normalized counts files from DESEQ2. Example R Script:

```
#read in deseq2 results file
sample1.counts <- read.delim("Galaxy204-[Normalized_counts_file_on_.tabular",
                        header = TRUE, sep = "\t", stringsAsFactors = FALSE)

#assign column header names
colnames(sample1.counts)  <- c("geneid", "sample1", "sample2","sample3", "sample4" )

#read in csv with DEGs
sample1.DEGs <- tbl_df(read.csv("sample1.DEGs.csv", stringsAsFactors = FALSE))

#Create matrix for generating heatmap
samples <- sample1.counts %>%

#join dataframes by geneid
#Subset normalized counts file for DEGs
        inner_join(sample1.DEGs, by = "geneid") %>%
        arrange(p.value) %>%

#log2 transform count data
        mutate("sample.1"= log2(sample1 + 1), "sample.2"= log2(sample2 +1),
        "sample.3"= log2(sample3 +1), "sample.4"= log2(sample4 +1)) %>%

#subset data to only contain the log2 transformed counts
        select("sample.1", "sample.2", "sample.3", "sample.4") %>%

# convert dataframe to matrix
        data.matrix()
```

```
#Install the “Complex Heatmap” package and “circlize” package (for colors)
install_github("jokergoo/ComplexHeatmap")
install.packages("circlize")
library(ComplexHeatmap)
library(circlize)

#Set heatmap colors
col_fun = colorRamp2(c(-2, 0, 2), c("light green", "black", "red"))

#Scale data
sample_scaled = t(scale(t(samples)))

#Generate final heatmap
#Cluster both rows and columns
#Hierarchical Clustering method = Complete
#Hierarchical Clustering distance algorithm = pairwise distance function
Heatmap(samples,
        name = "samples",
        col = col_fun,
        cluster_rows = TRUE,
        cluster_columns = TRUE,
        clustering_method_rows = "complete",
        clustering_method_columns = "complete",
        clustering_distance_rows = function(x, y) 1 - cor(x, y),
        clustering_distance_columns = function(x, y) 1 - cor(x, y),
        heatmap_legend_param = list (title = 'Z-scores',
                 legend_height = unit(4, "cm"),
                title_position = "lefttop-rot"
    ))
```

5.2.5 Volcano plots

Volcano plots were produced using the “Enhanced Volcano” package in R. A volcano plot is a scatterplot for the visual comparison of statistical significance (-log10 P-value, y axis) and magnitude of change (Log2 Fold-Change values, x axis). Example R Script:

```
# Install and load Enhanced Volcano package
BiocManager::install("EnhancedVolcano", version = "devel")
library(EnhancedVolcano)

## Enhanced volcano only seems to work when you read in a tab delim text file (not read.csv()
## or tbl_df(read.csv))
```

```
## Read in deseq2 output file
lsd1mut2 <- read.delim("lsd1mut.gs.rmna.txt", header = TRUE, sep = "\t", dec = ".")

# Plot volcano plot
plot2 <- EnhancedVolcano( lsd1mut2,
                    lab = lsd1mut2$gene.symbol,
                    x = "log2fc",
                    y = "p.value",
                    pCutoff = 0.007131771,
                    FCcutoff = 2,
                    xlab = bquote(~Log[2]~ "fold change"),
                    ylab = bquote(~-Log[10]~italic(P)),
                    transcriptPointSize = 1.5,
                    transcriptLabSize = 3.0,
                    title = "LSD1 cKO vs WT",
                    col = c("black", "black", "black", "red3"),
                    colAlpha = 0.5,
                    xlim = c(-8,8.5),
                    ylim = c(0,65),
                    cutoffLineType = "dashed",
                    cutoffLineCol = "black",
                    cutoffLineWidth = 0.5,
                    legendPosition = "none",
                    DrawConnectors = FALSE,
                    widthConnectors = 0.2,
                    colConnectors = "grey30",
                    border = "full",
                    borderWidth = 1.5,
                    borderColour = "black",
                    gridlines.major = FALSE,
                    gridlines.minor = FALSE)
```

5.2.6 Gene Set Enrichment Analysis (GSEA)

Gene Set Enrichment Analysis (Pre-ranked list) was performed using the online platform WebGestalt. The metric used for determining rank was the standard:

Sign ($\log_2$ Fold-Change) * -$\log_{10}$ (P-Value). The ranked list file (*.rnk) was created using the following r script.

```
## Load tidyverse package
```

```
library(tidyverse)

## Read in NCBI Homologene data
hom <- read.table( "homologene.data", sep = "\t", header = TRUE, quote = "", stringsAsFactors
= FALSE)

## Read PS19_Lsd1 deseq2 output
ps19_lsd1 <- read.csv("transhet.gs.rmna.csv", stringsAsFactors = FALSE)

## subset homologene table
#mouseId = 10090
#humanId = 9606

## subset homologene table for taxid and human gene symbol
homology.human <- hom %>%
  filter(taxId == "9606") %>%
  select(id, geneSymbol) %>%
  rename(geneid_human = geneSymbol)

## subset homologene table for taxid and mouse gene symbol
 homology.mouse <- hom %>%
  filter(taxId == "10090" ) %>%
  select(id, geneSymbol) %>%
  rename(geneid_mouse = geneSymbol)

## Add column of taxids corresponding to mouse gene symbols
x <- ps19_lsd1 %>%
  left_join(homology.mouse, by = c("gene.symbol" = "geneid_mouse")) %>%

## Add column of human gene symbols corresponding to taxids
  left_join(homology.human, by = "id") %>%

## Include only log2fc, p value and human gene symbols columns and filter out NA values
  select(log2fc, p.value, geneid_human) %>%
  filter(!is.na(geneid_human), !is.na(log2fc), !is.na(p.value)) %>%

## Calculate metric for GSEA pre-ranked list
  mutate(fcSign = sign(log2fc),
         logP = -log10(p.value),
         metric = logP*fcSign) %>%

## Select human gene symbol and metric (sorted by metric value)
  select(geneid_human, metric) %>%
  arrange(desc(metric))

## Write ranked expression file (.rnk) for running GSEA on Web Gestalt platform
```

```
write.table(x, file = "ps19_lsd1.expression.rnk", quote = FALSE, sep = "\t", row.names =
FALSE,  col.names = FALSE)
```

5.3 Data Visualization

5.3.1 Comparison to Human Gene Expression Data

(Chapter 2, Figure 5)

Normalized gene expression data from different human neurodegenerative diseases were downloaded from the NCBI Gene Expression Omnibus (GEO) database. Data from late onset Alzheimer's disease (LOAD) was obtained via the GSE44772 gene set. This large study looked at 1,647 postmortem brain tissues from LOAD and control subjects. Expression profiling was performed by Rosetta/Merck Human 44k 1.1 (GPL4372) microarray and data were processed using the Rosetta Revolver system. This analysis required several tables. "GSE44772_sample_sheet.csv" (table containing sample identifiers, such as brain region and control vs LOAD) and "GSE44772_series_matrix.txt" (table containing all the normalized expression data) were downloaded from NCBI Series GSE44772. "GPL3472.txt" (table containing Rosetta Probe IDs and corresponding Entrez Gene IDs) was obtained from NCBI GEO platform GPL4372.

Data from Frontotemporal lobar degeneration (FTLD-U) was obtained via the GSE13162 gene set. This study looked at brain tissue from 17 FTLD-U subjects and 11 controls. Expression profiling was performed using the Affymetrix U133A 2.0 microarray platform and Robust Multichip Analysis (RMA) normalization. We also obtained the series matrix file, sample sheet and table containing Probe IDs for the Affymetrix Human Genome U133A 2.0 Array (GPL571) from the NCBI GEO database.

Data from Parkinson's Disease (PD) was obtained via the GSE20295 gene set. This study looked at brain tissue from 15 PD subjects and 15 controls. Expression profiling was performed using the Affymetrix U133A microarray platform and RMA normalization methods. Affymetrix U133A 2.0 microarray platform and Robust Multichip Analysis (RMA) normalization. We also obtained the series matrix file, sample sheet and table containing Probe IDs for the Affymetrix Human Genome U133A Array (GPL96) from the NCBI GEO database.

These analyses also required the NCBI homologene database to map human and mouse genes. All of these tables are stored on a physical drive in the Katz lab and are available upon request. Comparison to LOAD expression data is presented as a representative example for all human disease comparisons performed. The analysis was ultimately performed using the following R script.

```
library(tidyverse)
library(data.table)

## read in homologene table
hom <- read.table("homologene.data", sep = "\t", header = TRUE, quote = "")

## subset homologene table for mouse and human
#mouseId = 10090
#humanId = 9606

homology.human <- hom %>%
  filter(taxId == "9606") %>%
  select(id, geneId) %>%
  rename(geneid_human = geneId)

homology.mouse <- hom %>%
  filter(taxId == "10090" ) %>%
  select(id, geneId) %>%
  rename(geneid_mouse = geneId)

#read in manifest sample data for GSE44772 (LOAD)
manifest = read.csv("GSE44772_sample_sheet.csv", stringsAsFactors = FALSE)
```

```
#read in LOAD data
data <- read.table("GSE44772_series_matrix.txt", sep = "\t", header = T, comment = "!",
stringsAsFactors = F, fill = T, na.strings =  c("","null"))


#read in annotation file
annot <- read.table("GPL4372.txt", sep = "\t", header = T, quote = "")
annotation <- select(annot, ID, EntrezGeneID)

#combine the data & annot info
# add a column of entrez gene IDs that correspond to the microarray IDs
data <- data %>%
        left_join(annotation, by = c("ID_REF" = "ID")) %>%

# add a column of homology IDs that match entrez geneids in AD data
        left_join(homology.human, by = c("EntrezGeneID" = "geneid_human")) %>%

# add a column of mouse Entrez IDs that match homology IDs in AD data
#remove rows that have an NA in geneid_mouse column
        left_join(homology.mouse, by = "id") %>%
        filter(!is.na(geneid_mouse))

# create new dataframe with average expression (690 individuals)
        ADmean = data.frame(ID = data$EntrezGeneID, mouse.entrez = data$geneid_mouse,
              Mean.ACR = rowMeans(data[, as.character(manifest$Accession[manifest$Group
        == "A" & manifest$Tissue == "CR" ])], na.rm = TRUE),
              Mean.NCR = rowMeans(data[, as.character(manifest$Accession[manifest$Group
        == "N" & manifest$Tissue == "CR" ])], na.rm = TRUE),
              Mean.APFC = rowMeans(data[, as.character(manifest$Accession[manifest$Group
        == "A" & manifest$Tissue == "PFC" ])], na.rm = TRUE),
              Mean.NPFC = rowMeans(data[, as.character(manifest$Accession[manifest$Group
        == "N" & manifest$Tissue == "PFC" ])], na.rm = TRUE),
              Mean.AVC = rowMeans(data[, as.character(manifest$Accession[manifest$Group
        == "A" & manifest$Tissue == "VC" ])], na.rm = TRUE),
              Mean.NVC = rowMeans(data[, as.character(manifest$Accession[manifest$Group
        == "N" & manifest$Tissue == "VC" ])], na.rm = TRUE)
)

#Alternative using dplyr
#create vector of Accession numbers for each group for calculating row means
#ACR <- manifest %>%
#  select(Accession, Group, Tissue) %>%
#  filter(Group == "A", Tissue == "CR")
#ACR = ACR$Accession
#data <- mutate( data, Mean.ACR = rowMeans(select(., ACR), na.rm = T))
```

```
#Compute delta values for each condition
ADmean <- mutate(ADmean, log2fc.CR = Mean.ACR/Mean.NCR,
                 log2fc.PFC = Mean.APFC/Mean.NPFC,
                 log2fc.VC = Mean.AVC/Mean.NVC,
                 delta.CR = Mean.ACR - Mean.NCR,
                 delta.PFC = Mean.APFC - Mean.NPFC,
                 delta.VC = Mean.AVC - Mean.NVC
                 )

##read in mouse expression data
all.tpm <- read.csv("all.tpm.csv", stringsAsFactors = FALSE)

##add entrez ids to lsd1 tpm data
annotation2 <- read.csv("annotation.csv", stringsAsFactors = FALSE)
lsd1.tpm <- all.tpm %>%
  left_join(annotation2, by = c("Geneid" = "GENEID")) %>%
  select(Geneid, gene.symbol, ENTREZID, lsd1mutaTPM, lsd1mutbTPM, avg.lsd1mutTPM,
controlaTPM, controlbTPM, avg.controlTPM) %>%
  filter(!is.na(ENTREZID))

## add delta and fold change to TPM data
delta.tpm <- lsd1.tpm %>%
  mutate( delta.lsd1mutant = avg.lsd1mutTPM - avg.controlTPM,
          log2fc.lsd1mutant = log2((avg.lsd1mutTPM+1) / (avg.controlTPM+1))
          )

## Remove genes from mouse TPM data with no expression (TPM < 1)
delta.tpm <- delta.tpm[!(delta.tpm$avg.lsd1mutTPM < 1  ),]

## Read in mouse data with log2fc and pvalues for labeling up and downregulated genes
lsd1mutant <- read.csv("lsd1mut.gs.rmna.csv", stringsAsFactors = FALSE)

## create new dataframe with upregulated genes (log2fc > 2 & p.adj < 0.1)
up <-lsd1mutant %>%
  filter(p.adj < 0.1 & log2fc > 2 ) %>%
  left_join(annotation2, by = c("ensembl.geneid" = "GENEID" )) %>%
  select(ENTREZID) %>%
  filter(!is.na(ENTREZID))

## create new dataframe with downregulated genes (log2fc < -2 & p.adj < 0.1)
down <-lsd1mutant %>%
  filter(p.adj < 0.1 & log2fc < -2 ) %>%
  left_join(annotation2, by = c("ensembl.geneid" = "GENEID" )) %>%
  select(ENTREZID) %>%
  filter(!is.na(ENTREZID))
```

```
## Merge mouse TPM and LOAD patient means by mouse entrez id. Output only mouse entrez
id found in both datasets
merge <- delta.tpm %>%
  inner_join( ADmean, by =  c("ENTREZID" = "mouse.entrez")) %>%

## Create new column in merged dataframe called "condition"
## Used for labelling the up and down genes in plot
  mutate(condition = ifelse(ENTREZID %in% up$ENTREZID, "up",
                            ifelse(ENTREZID %in% down$ENTREZID, "down","others")))

## Spearman correlation test
# define values to test correlation
x <- merge$delta.lsd1mutant
y <- merge$delta.PFC

# Run actual test using cor.test
test = cor.test(x, y, method = "spearman") # rho = .2 p = 4.225 E-134

# Display actual p-value instead of "p< 2.2e-16"
test$p.value

# Run linear model test
lm = lm(x ~ y)  # p < 2.2e-16
summary(lm)

# Look at range of values to set x and y axis limits
range(merge$delta.lsd1mutant)
range(merge$delta.PFC)

## Create scatterplot of correlation of LOAD and mouse expression data
pfc <-ggplot(merge, aes(x= delta.lsd1mutant, y = delta.PFC, colour= condition),
           na.rm = TRUE) +
  geom_point(size =2, alpha=.75)   +
  theme(legend.position="none",
        panel.grid.major = element_blank(),
        panel.grid.minor = element_blank(),
        axis.line = element_line(colour = "black"),
        panel.background = element_blank(),
        panel.border = element_rect(colour = "grey", fill=NA),
        plot.title = element_text(hjust = 0.5)) +
  scale_color_manual(
    values = c("up" = "dark red",
               "down" = "dark green",
               "others" = "dark grey"))+
  geom_hline(yintercept=0)+
  geom_vline(xintercept=0)+
```

```
  xlim(-5000,5000) +
  ylim(-1,1)+
  xlab(expression(paste(italic("Lsd1"^"CAGG"), " vs Ctrl (" , Delta, "TPM")))) +
  ylab(expression(paste("LOAD vs Ctrl (", Delta, "Gx ", log[2],")"))) +
  ggtitle("Prefrontal Cortex")

pfc +
  annotate("text", x = 2300, y = -.85, label = expression(paste( rho, "= "))) +
  annotate("text", x = 1750, y = -1, label = expression(paste( "p = ")))
```

5.3.2 Bar Plot

(Chapter 3, Figure 4a)

R script for creating bar plot to compare expression changes (log_2 Fold-Change) of a subset of genes between P19 Tau mouse and the PS19;*Lsd1*$^{\Delta/+}$ mouse.

```
library(tidyverse)
library(ggplot2)

## Read in DEG tables
tau.deg <- read.csv("tau.degs.csv", stringsAsFactors = FALSE)
transhet.deg <- read.csv("transhet.gs.rmna.csv", stringsAsFactors = FALSE)

## Expression of PS19 DEGs in PS19;Lsd1
overlap <- tau.deg %>%
  inner_join( transhet.deg, by= "ensembl.geneid") %>%
  filter(!is.na(gene.symbol.x)) %>%
  select(gene.symbol.x, log2fc.x, log2fc.y) %>%
  rename(gene.symbol = gene.symbol.x  , log2fc.tau  = log2fc.x , log2fc.transhet= log2fc.y )
overlap4 <- overlap %>%
  melt( id.vars = "gene.symbol") %>%
  filter(!is.na(value))

##Plot expression (log2FC) of genes shared btw the two datasets
plot <-
  ggplot(data = overlap4, aes(x= reorder(gene.symbol, -value), y= value, fill = variable)) +
  geom_bar(stat = "identity", width = 1, position = "dodge")+
  scale_y_continuous(breaks=seq(-4,6,1)) +
  scale_fill_manual(values = c("#339900", "#990066"),
                    name = "Variable",
                    labels = c(expression("PS19 Tau expression changes vs. control"),
                               expression(paste("PS19;",italic("Lsd1")^Delta,""^ "/+", ""^ "/+",
                                                "expression changes vs. control"))))+
```

```
  xlab(NULL)+
  ylab("log2 Fold-Change")

plot +
  theme(panel.border = element_blank(),
        panel.grid.major = element_blank(),
        panel.grid.minor = element_blank(),
        panel.background = element_blank(),
        axis.line = element_line(colour = "black"),
        axis.text.x=element_text(angle=70,hjust=1),
        legend.position = c(.5,.9),
        legend.title = element_blank(),
        legend.direction = "vertical",
        legend.text.align = 0,
  )
```

5.3.3 Scatterplot

(Chapter 3, Figure 4b)

R script for creating scatterplot to compare expression changes (log_2 Fold-Change) genome-wide between P19 Tau mouse and the PS19;*Lsd1*$^{\Delta/+}$ mouse.

```
library(tidyverse)
## Read in expression data from DESEQ2
tau <- read.csv("tau.gs.rmna.csv", stringsAsFactors = FALSE)
transhet <- read.csv("transhet.gs.rmna.csv", stringsAsFactors = FALSE)

## Join together the data from each genotype
corr4 <- inner_join(transhet, tau, by = "ensembl.geneid")

## create new dataframe with upregulated genes (log2fc > .58 & p.adj < 0.3)
up4 <-transhet %>%
  filter(p.adj < 0.3 & log2fc > 0.58 )

## create new dataframe with downregulated genes (log2fc < -.58 & p.adj < 0.3)
down4 <-transhet %>%
  filter(p.adj < 0.3 & log2fc < -0.58 )

## Add new column for identifying DEGs by color
corr4 <- mutate(corr4, condition = ifelse(ensembl.geneid %in% up4$ensembl.geneid, "up",
```

```
                    ifelse(ensembl.geneid %in% down4$ensembl.geneid,
                    "down","others")))

## Plot scatterplpot using ggplot2
p4 <- ggplot(corr4, aes(x= log2fc.x, y = log2fc.y, colour= condition), na.rm = TRUE) +
  geom_point(size =1, alpha=.75)   +
  theme(legend.position="none",
        panel.grid.major = element_blank(),
        panel.grid.minor = element_blank(),
        axis.line = element_line(colour = "black"),
        panel.background = element_blank(),
        panel.border = element_rect(colour = "grey", fill=NA),
        plot.title = element_text(hjust = 0.5)) +
  scale_color_manual(
    values = c("up" = "dark red",
               "down" = "dark green",
               "others" = "dark grey"))+
  geom_hline(yintercept=0)+
  geom_vline(xintercept=0)+
  xlim(-2.5,2.5) +
  ylim(-2.5,2.5)+
  xlab(expression(paste("PS19;",italic("Lsd1")^Delta,""^ "/+ ","(", log[2], " fold change)"))) +
  ylab(expression(paste("PS19 (", log[2], " fold change)"))) +
  ggtitle(expression(paste("PS19;", italic("Lsd1")^Delta, ""^ "/+", " vs PS19")))
p4 +
geom_abline(intercept = 0, slope = 1, linetype = "dashed")
```

Appendix A. KDM1A/LSD1 regulates the differentiation and maintenance of spermatogonia in mice

Adapted from **Dexter A. Myrick,** Michael A. Christopher, Alyssa M. Scott, Ashley K. Simon, Paul G. Donlin-Asp, William G. Kelley, and David J. Katz. KDM1A/LSD1 regulates the differentiation and maintenance of spermatogonia in mice. PLoS ONE. 2017; 12(5):e0177473. doi: 10.1371/journal.pone.0177473. PubMed PMID: 28498828; PubMed Central PMCID: PMC5428937.

Author Contributions: D.A.M and D.J.K conceived and designed the study as well as the writing of the manuscript. D.A.M performed experiments with the assistance of A.M.S, A.K.S and P.G.D. D.A.M analyzed all data and interpreted results under the direction of D.J.K. The manuscript was edited by all the coauthors. W.G.K provided financial assistance and guidance throughout.

A1. Abstract

The proper regulation of spermatogenesis is crucial to ensure the continued production of sperm and fertility. Here, we investigated the function of the H3K4me2 demethylase KDM1A/LSD1 during spermatogenesis in developing and adult mice. Conditional deletion of *Kdm1a* in the testis just prior to birth leads to fewer spermatogonia and germ cell loss before 3 weeks of age. These results demonstrate that KDM1A is required for spermatogonial differentiation, as well as germ cell survival, in the developing testis. In addition, inducible deletion of *Kdm1a* in the adult testis results in the abnormal accumulation of meiotic spermatocytes, as well as apoptosis and progressive germ cell loss. These results demonstrate that KDM1A is also required during adult spermatogenesis. Furthermore, without KDM1A, the stem cell factor OCT4 is ectopically maintained in differentiating germ cells. This requirement for KDM1A is similar to what has been observed in other stem cell populations, suggesting a common function. Taken together, we propose that KDM1A is a key regulator of spermatogenesis and germ cell maintenance in the mouse.

A2. Introduction

In mammals, sperm are continuously produced over the lifetime of adult males. This continuous production of sperm is maintained by the ongoing differentiation of spermatogonia (1). Recently, the histone demethylase KDM1A (lysine specific demethylase 1A) has been implicated in the differentiation of multiple cell types (2-4). Therefore, to gain insight into the mechanism of spermatogonial differentiation, we investigated the function of KDM1A in mouse spermatogenesis.

In male mice, primordial germ cells colonize the developing testis and become prospermatogonia or gonocytes (hereafter referred to as prospermatogonia) by embryonic day 12.5 (E12.5). After birth, these prospermatogonia become undifferentiated spermatogonia and also transition directly to differentiated spermatogonia. The differentiated spermatogonia then become haploid spermatozoa and complete the first wave of spermatogenesis, which takes approximately 35 days (5). Following the first wave of spermatogenesis, the undifferentiated spermatogonia continue to undergo meiosis and produce mature spermatozoa (1). This process occurs continuously throughout the lifetime of adult males.

Accumulating evidence has implicated the histone modification di-methylation of lysine 4 on histone H3 (H3K4me2) in the maintenance of transcriptional states during development (6-9). However, if H3K4me2 functions in the maintenance of transcription, then this histone methylation may have to be reprogrammed to allow for changes in cell fate. This function may be accomplished by the activity of histone demethylases such as KDM1A. KDM1A is an amine-oxidase type histone demethylase that is part of the CoREST (co RE1-silencing transcription factor) complex and specifically demethylates H3K4me2 *in vitro* (10, 11). KDM1A associates with CoREST in pachytene spermatocytes (12), though it is unknown whether it also interacts with CoREST in other germ cells. KDM1A has also been shown to associate with the androgen

receptor (AR) complex in the mouse testis (13). When associated with the AR complex *in vitro*, KDM1A has specificity for H3K9me2 (13).

In mammals, loss of KDM1A in the mouse embryo results in embryonic lethality prior to E7, when tissues are first beginning to be specified (14, 15). Furthermore, KDM1A has been implicated in the differentiation of several mouse cell types *in vitro* (16-19) and in the terminal differentiation of pituitary cells during pituitary organogenesis *in vivo* (14). Recently, KDM1A has also been demonstrated to have a role in stem cell differentiation (2-4). During the differentiation of mouse ES cells *in vitro*, KDM1A is required to remove H3K4 methylation at the promoters and enhancers of stem cell genes (3). For example, KDM1A binds to the promoter, as well as the proximal and distal enhancers, of the critical stem cell gene *Oct4*. When KDM1A is depleted, H3K4 methylation at these stem cell genes is not properly removed and the expression of these genes is inappropriately maintained during mES cell differentiation (3). This may cause the differentiation defect observed in KDM1A-depleted mouse ES cells (3, 15, 20). In addition, KDM1A is thought to act in a similar fashion during hematopoietic stem cell differentiation *in vivo* in the mouse (2).

In the testis, *Oct4* is expressed in undifferentiated spermatogonia. It is required for the maintenance of spermatogonia *in vitro* and facilitates the colonization of the testis following spermatogonial transplantation *in vivo* (21). In addition, KDM1A has been shown to directly bind *Oct4* in a mouse germ cell line (GC-1 cells)(22). Since KDM1A has been implicated in the transcriptional repression of critical transcription factors, such as *Oct4*, during stem cell differentiation, we hypothesized that KDM1A may also be required for differentiation during spermatogenesis. Consistent with this hypothesis, Lambrot et al. recently provided the first evidence that KDM1A functions during the first wave of spermatogenesis in the maintenance

and differentiation of spermatogonia (23). Using the identical *Kdm1a* conditional deletion mouse, our findings agree with these conclusions. In addition, we extended these findings by utilizing a tamoxifen inducible *Cre* allele to analyze the function of KDM1A in adult spermatogenesis. This analysis suggests that KDM1A has an ongoing role in adult spermatogenesis. Finally, our data suggest that KDM1A regulates the transcription of *Oct4* during spermatogonial differentiation. Taken together, our results provide further evidence that KDM1A is a key regulator of spermatogenesis in mice.

A3. Results

A3.1 KDM1A is dynamically expressed in the murine testis

We first asked if KDM1A protein is present in prospermatogonia and spermatogonia. Consistent with prior observations (23, 24), immunofluorescence with a KDM1A antibody demonstrates that KDM1A protein is found in prospermatogonia and Sertoli Cells in testicular cords at 1 day post partum (dpp) (Fig 1A,B). In addition, in juvenile testes KDM1A is present in spermatogonia, as well as in Sertoli cells (Fig 1C-D). KDM1A is subsequently absent in preleptotene spermatocytes, and then present again in pachytene spermatocytes and round spermatids, but not in mature spermatozoa (Fig 1C-F, inset Fig 1H). Also, consistent with previously reported immunohistochemistry (24), this localization pattern is the same in adult testes (Fig 1G-J). In particular, in adult mice KDM1A is present in PLZF positive spermatogonia (Fig 1I,J). KDM1A is also present in adult Sertoli Cells (Fig 1G,H).

A3.2 Loss of KDM1A causes defects in the maintenance and differentiation of spermatogonia

To determine the role of KDM1A in spermatogenesis we conditionally deleted *Kdm1a* by crossing floxed *Kdm1a* mice (14) to a *Ddx4*/*Vasa-Cre* transgenic line (25) and a tamoxifen

inducible *Cagg-Cre* transgenic line (26). The resulting *Kdm1a*$^{flox/flox}$*;Vasa-Cre* and *Kdm1a*$^{flox/flox}$*;Cagg-Cre* mice are hereafter referred to as *Kdm1a*^{Vasa} and *Kdm1a*^{Cagg}. Littermate *Kdm1a*$^{flox/+}$*;Vasa-Cre* or *Kdm1a*$^{flox/flox}$ without *Vasa-Cre* are used as controls in all subsequent *Kdm1a*^{Vasa} experiments. Tamoxifen-injected *Cre* minus littermates are used as controls in all subsequent *Kdm1a*^{Cagg} experiments. In comparison to endogenous *Vasa,* which is expressed earlier, *Vasa-Cre* is strongly induced in the germline between E15 and E18, with near complete recombination occurring by birth (25). In the male germline, prospermatogonia are fully established well before the onset of *Vasa-Cre* (27). As a result, deletion of *KDM1A* with *Vasa-Cre* can be used to determine the role of KDM1A in the differentiation and maintenance of germ cells. *Kdm1a*^{Vasa} males are sterile and exhibit a dramatic reduction in the size of adult testes (Fig 2A). To further investigate this phenotype, we examined histology and markers in control and *Kdm1a*^{Vasa} testes at 1, 6, 8, 10 and 21dpp, as well as in adults (Fig 2A-Q, S1A-R and S2A-H Figs). Without KDM1A, adult testes lack germ cells (Fig 2B,C), and immunohistochemistry with the Sertoli cell marker SOX9 confirms that germ cells are lost prior to 21dpp (Fig 2D,E). Thus, KDM1A is required to maintain germ cells, including spermatogonia.

Examination of *Kdm1a*^{Vasa} testes at earlier time points suggests that the loss of germ cells is due to a defect in both spermatogonial differentiation and maintenance. At 1dpp, *Kdm1a*^{Vasa} testicular cords contain the same number of germ cells as controls (Fig 2F,G,N). Thus, as expected from the timing of *Vasa-Cre* expression, KDM1A does not affect the specification of prospermatogonia. In control 6dpp testes, we observe OCT4+ undifferentiated spermatogonia and KIT+ differentiating spermatogonia. (Fig 2H,O,Q and S1 Fig A,M). In mutants at 6dpp we observe identical numbers of OCT4+ undifferentiated spermatogonia (Fig 2I,O and S1 Fig B). Thus, without KDM1A, OCT4+ spermatogonia are normal. However, by 6dpp, *Kdm1a*^{Vasa}

mutants show the first signs of a defect in the maintenance of undifferentiated spermatogonia. This is indicated by the lower numbers of PLZF+ spermatogonia compared to controls (Fig 2P and S1 Fig G,H). At 6dpp there is also a defect in spermatogonial differentiation, as indicated by the lower numbers of KIT+ differentiating spermatogonia, as well as an overall decrease in germ cell number (Fig 2H,I,N,Q and S1M,N and S2A,B Figs). At 8dpp and 10dpp, there continues to be fewer PLZF+ spermatogonia (Fig 2P and S1 Fig I-L). Also, by 10dpp there is now a significant decrease in the number of OCT4+ spermatogonia compared to controls (Fig 2O and S1 Fig C-F). This indicates a progressive defect in the maintenance of undifferentiated spermatogonia (Fig 2J-M). Furthermore, at 8dpp we continue to observe far fewer KIT+ differentiating spermatogonia (Fig 2Q and S1 Fig O,P). Finally, by 10dpp in many control testicular cords spermatogonia have differentiated to produce spermatocytes and there is a rapid expansion in the number of germ cells (Fig 2L,N and S2 Fig E). In contrast, *Kdm1a*^{Vasa} mutant cords contain very few spermatocytes, and even at later stages, post-meiotic spermatids are never observed (Fig 2M,N and S2 Fig F).

At 10dpp, we also observe germ cell apoptosis. For example, over 40% (*Kdm1a*^{Vasa} average: 4.2 vs control average: 1.8 per cord) of the remaining germ cells in *Kdm1a*^{Vasa} testes are positive for the apoptosis marker Cleaved Caspase-3 (Fig 3A-C) and many of these germ cells are TUNEL positive (Fig 3D,E). We also observe the apoptosis hallmark, fragmented DNA, in some remaining germ cells (inset Fig 3B). Overall, the combination of spermatogonia maintenance defect, differentiation defect and germ cell apoptosis results in a large deficit in the number of germ cells at 10dpp (Fig 2L-N and S2 Fig E,F) and the loss of germ cells by 21dpp (Fig 2D,E and S2 Fig G,H).

Kdm1a^{Vasa} males lack germ cells by 21dpp and never complete a spermatogenic cycle. Therefore, to better understand the fate of germ cells in *Kdm1a*^{Vasa} mutants, we conditionally deleted *Kdm1a* with the tamoxifen inducible *Cagg-Cre* transgene in adult mice (26). Since the *Cagg-Cre* transgene is active throughout the adult mouse somatic cells in the testis, as well as other tissues, may be affected. Nevertheless, since spermatogenesis is continuously ongoing in the adult male, the inducibility of the *Cre* transgene enabled us to determine if KDM1A has an ongoing function during spermatogenesis in adults.

Using a similar inducible deletion approach with another spermatogonia expressed gene, *Nanos2,* it has been demonstrated that 12 weeks is sufficient to cause a complete loss of all germ cells (28). However, at time points beyond 9 weeks, *Kdm1a*^{Cagg} mice begin to have defects in the nervous system and die (M. Christopher, D. Myrick et al., reported elsewhere). As a result, analyses of *Kdm1a*^{Cagg} testes were done at or before 9 weeks to avoid complications due to these defects. At 9 weeks after the last tamoxifen injection the most affected tubules contain mostly Sertoli cells (Fig 4A,B). This demonstrates that KDM1A has an ongoing role in adult spermatogenesis. Also, the observation that Sertoli cells remain (Fig 4B,C) and are morphologically normal in even the most affected seminiferous tubules, indicates that these cells may not be affected, even though these cells express KDM1A (Figs 1 and 4B). However, future studies will be necessary to determine definitively whether this is the case. Approximately 7-9 weeks after the last tamoxifen injection, the majority of tubules are highly disorganized, with many germ cells abnormally clumped (Fig 4E,F,J) or out of place. In particular, we observe spematogonia-like cells near or in the lumen (Fig 4E), abnormal spacing around cells with vacuoles interspersed (Fig 4G,H), and some tubules lacking a lumen altogether (Fig 4E,L).

In *Kdm1a*^{Cagg} testes, we also observe defects that are similar to what we observe during the first wave of spermatogenesis. For example, many germ cells display the classic crescent shaped apoptotic morphology (Fig 4F,I). These crescent shaped nuclei are not observed in tamoxifen injected littermate controls. To confirm that these cells are undergoing apoptosis, we performed immunofluorescence with the apoptosis marker Cleaved Caspase-3 (Fig 4M,N). This analysis demonstrated a 4.5-fold increase in the number of apoptotic nuclei compared to controls (Fig 4O). We also observe many tubules with far fewer germ cells than normal (Fig 4B,G-I). Quantification of germ cells demonstrated a 1.8-fold (*Kdm1a*^{Cagg}: 120/tubule vs. control: 221/tubule) decrease in germ cells (Fig 4D). There are also many giant spermatocyte-like apoptotic cells present (Fig 4J). Furthermore, in *Kdm1a*^{Cagg} testes we observe many germ cells with chromosomal abnormalities and multi-nucleated germ cells (Fig 4K,L). These defects indicate a potential block to meiotic entry. To confirm this block, we performed immunofluorescence with the meiotic marker synaptonemal complex protein 1 (SYCP-1)(Fig 4P,Q). This analysis demonstrated a 3.8-fold (*Kdm1a*^{Cagg}:105.5/tubule vs. control: 27.7/tubule) increase in the number of SYCP-1 positive nuclei compared to tamoxifen-injected littermate controls, indicating arrest during early meiotic prophase (Fig 4R).

A3.3 Loss of KDM1A does not derepress *Line1* and *IAP* retrotransposons

Miwi2 and *Dnmt3l* mutant mice exhibit a loss of germ cells that is similar to *Kdm1a* mutants (29, 30). MIWI2 is an RNA binding protein of the *Piwi* family that functions in the production of germline PIWI interacting RNA's (piRNAs) (29). Without MIWI2, germ cells arrest in meiosis and seminiferous tubules degenerate over time. This ultimately results in the loss of germ cells in adult males (29). DNMT3L associates with the *de novo* methyltransferase

complex and is required for proper *de novo* methylation in mammals (31). Without *Dnmt3l*, male mice exhibit severe defects that are identical to *Miwi2* (30). The testis phenotypes in both *Miwi2* and *Dnmt3l* mutants are thought to be caused by the reactivation of retrotransposons, leading to meiotic catastrophe. Specifically, in *Dnmt3l* and *Miwi2* mutants, *Line1* and *IAP* retrotransposons fail to properly acquire DNA methylation and are inappropriately expressed (29, 30). Therefore, to determine if the *Kdm1a* mutant phenotype could be due to a similar mechanism, we examined DNA methylation and the expression of *Line1* and *IAP* elements in $Kdm1a^{Vasa}$ and $Kdm1a^{Cagg}$ testes. In $Kdm1a^{Cagg}$ testes, we do not detect any expression of *IAP* retrotransposons (S3 Fig A,B). Nor do we detect a decrease in DNA methylation at *Line1* or *IAP* elements (S3 Fig E). We do observe *Line1* expression in spermatocytes of $Kdm1a^{Cagg}$ testes (S3 Fig C). However, we also detect this same expression in control adult testes (S3 Fig D). To our knowledge, this is the first time that the expression of *Line1* retrotransposons has been examined in spermatocytes of adult seminiferous tubules (32, 33). This expression is surprising since retrotransposition in these gametes could have a large negative impact. We also do not observe increased expression of *Line1* elements, or any decrease in DNA methylation at *Line1* and *IAP* elements in $Kdm1a^{Vasa}$ mutants at 10dpp (S3 Fig F-H). Importantly, because the methylation analysis was performed on whole testis in one control versus one mutant, it is possible that loss of *IAP* or *Line1* methylation could have been missed in a specific testis cell type. Nevertheless, the unaffected methylation pattern is consistent with the lack of expression defect, which was performed in a cell type specific fashion. Based on the similarity of the germ cell loss and meiotic progression defect with those observed in *Miwi2* and *Dnmt3l* mutants, it was possible that the *Kdm1a* functions as part of the mechanism to regulate transposons in the testis. However, the overall lack of retrotransposon defects indicates that this is not likely.

A3.4 KDM1A binds to the *Oct4* locus in the adult testis

KDM1A represses critical genes, such as *Oct4,* during the differentiation of mouse ES cells *in vitro* and hematopoietic stem cells *in vivo* (2, 3). This raises the possibility that KDM1A could also repress the transcription of *Oct4* during spermatogonial differentiation. Consistent with this possibility, KDM1A binds directly to the *Oct4* locus in mouse ES cells and in a mouse germ cell line (GC-1 cells)(3, 22). To determine if KDM1A also binds directly to *Oct4* in the mouse testis, we performed KDM1A chromatin immunoprecipitation (ChIP) in wild-type whole adult testes. We observe a 6.3-average fold enrichment of KDM1A at the promoter of *Oct4* compared to a no antibody control (Fig 5A and S4 Fig A). There is also significant binding at the proximal enhancer of *Oct4* (a 3.0-average fold enrichment), but no significant binding at the distal enhancer (Fig 5A and S4 Fig A). This demonstrates that KDM1A binds directly to *Oct4* in the mouse testis. Importantly since the ChIP analysis was performed on whole testis it is not possible to determine whether KDM1A binding occurs in germ cells or somatic support cells. However, since there are far fewer somatic cells than germ cells in the testis, it is unlikely that the observed enrichment could be explained by KDM1A binding in somatic cells alone (34).

A3.5 KDM1A is required for the repression of *Oct4*

The binding of KDM1A to *Oct4* is consistent with a model where KDM1A is required for the repression of *Oct4* during spermatogenesis. If this is the case, OCT4 might be ectopically expressed in *Kdm1a* mutants. Because $Kdm1a^{Vasa}$ mutants undergo almost no differentiation, we looked for ectopic expression by performing OCT4 immunofluorescence in $Kdm1a^{Cagg}$ mutants. In controls, OCT4 protein is confined to spermatogonia (Fig 6A-C). Likewise, in 28% of the seminiferous tubules from $Kdm1a^{Cagg}$ mutants, OCT4 is confined to spermatogonia (Fig 6G).

However, in the majority of *Kdm1a*^{Cagg} mutant seminiferous tubules (72%), OCT4 protein is present throughout the seminiferous tubule in meiotic spermatocyte-like and post-meiotic spermatid-like germ cells (Fig 6D-F). Quantification of OCT4+ cells demonstrates a 9.1-fold increase in OCT4+ nuclei per seminiferous tubule (*Kdm1a*^{Cagg}: average 18.4/tubule vs. control: 1.9/tubule)(Fig 6G). This suggests that KDM1A is required to repress *Oct4* expression during spermatogenesis.

A3.6 H3K4me2 at the *Oct4* locus

The binding of KDM1A to *Oct4* suggests that KDM1A may repress OCT4 by removing H3K4me2. If this is the case, we would expect an increase in H3K4me2 in *Kdm1a* mutants versus controls. To test this possibility, we performed H3K4me2 chromatin immunoprecipitation (ChIP) on 10-day old whole testes in *Kdm1a*^{Vasa} mutants. *Kdm1a*^{Vasa} mutants were used, rather than *Kdm1a*^{Cagg} mutants, because *Kdm1a*^{Vasa} mutants are more uniformly affected. In addition, this analysis was conducted at 10dpp, despite the extensive germ cell loss compared to controls, because at this time point, there is a severe spermatogenesis defect but still a large enough number of germ cells present for ChIP analysis. To account for the fewer germ cells in *Kdm1a*^{Vasa} testes, we normalized the fold change of the H3K4me2 ChIP results, based on the difference in percentage of germ cells in *Kdm1a*^{Vasa} 10dpp testes versus controls (S4 Fig B). After normalization, we detect a large increase in H3K4me2 at the promoter and proximal enhancers of *Oct4* (Fig 5B and S4 Fig C). These data suggest that KDM1A may repress OCT4 during spermatogenesis by removing H3K4me2.

A4. Discussion

Recently, Lambrot *et al.* provided the first evidence that KDM1A functions during the first wave of spermatogenesis (23). Using an identical combination of conditional *Kdm1a* allele and *Vasa-Cre* transgene, our data agree with their conclusions. Specifically, they find that despite the loss of KDM1A, spermatogonia are still properly established (23). At 6dpp, we observe no effect on the number OCT4+ spermatogonia. In addition, there are PLZF+ spermatogonia present, though at reduced numbers. These findings confirm the conclusion that KDM1A is not required for the establishment of spermatogonia.

Although KDM1A is not required for the establishment of spermatogonia, Lambrot *et al.* demonstrated that loss of KDM1A has a severe effect on the maintenance and differentiation of spermatogonia (23). At 6dpp, we show that loss of KDM1A results in a defect in the number of Kit+ and PLZF+ spermatogonia. This defect becomes more pronounced at 8dpp and 10dpp, and by 10dpp we observe many germ cells undergoing apoptosis. We also begin to see a decline in the number of OCT4+ spermatogonia. By 21dpp, loss of KDM1A results in the loss of germ cells. Thus our results confirm the findings of Lambrot *et al.* (23) that KDM1A is required for the maintenance and differentiation of spermatogonia.

To determine if KDM1A also has an ongoing role in adult spermatogenesis, we inducibly deleted *Kdm1a* with the *Cagg-Cre* transgene. Loss of KDM1A during adult spermatogenesis also results in a severe spermatogenesis defect. Specifically we observe a block in the entry to meiosis coupled with a failure to maintain germ cells. These defects in adult spermatogenesis are broadly similar to what we and others (23) observe during the first wave of spermatogenesis, in that in both cases, there is a defect in differentiation coupled to a loss of germ cells. Thus, the function of KDM1A in spermatogenesis appears to be maintained in adult spermatogenesis. Nevertheless, the defect observed during adult spermatogenesis appears to be distinct from the

neonatal defect because we also observe the accumulation of meiotic spermatocytes. The accumulation of spermatocytes may be due to activation of a meiotic checkpoint. It is well established that the first wave of spermatogenesis in rodents is distinct from subsequent waves. In particular, during the first wave, prospermatogonia directly become differentiated spermatogonia. It is possible that this difference contributes to the difference in spermatogenesis defects that we observe between neonatal and adult spermatogenesis. In addition, our use of the inducible *Cagg-Cre* transgene makes it possible to detect additional defects due to the distinct timing of deletion in the asynchronous seminiferous tubules. It is possible that this distinct timing enabled us to uncover the meiotic arrest.

The use of the *Cagg-Cre* inducible system enabled us to identify a role for KDM1A in adult spermatogenesis. However, because the *Cagg-Cre* transgene induces KDM1A deletion everywhere, we cannot rule out the possibility that loss of KDM1A in Sertoli cells, or even other tissues, contributes to the observed adult spermatogenesis phenotype. To demonstrate that the $Kdm1a^{Cagg}$ spermatogenesis phenotype is due to the function of KDM1A in germ cells, we would need an inducible germ cell *Cre* transgene. However, at the moment, no inducible germ cell *Cre* transgene exists. Nevertheless, both we and others have demonstrated a role for KDM1A specifically in germ cells during the first wave of spermatogenesis (23). Thus, we favor a model where KDM1A is required in germ cells during adult spermatogenesis as well.

Because seminiferous tubules are not synchronized in the adult, the timing of deletion in individual seminiferous tubules enables us to observe potential post-meiotic defects. In both the histology and cleaved caspase staining, we observe round spermatid-like cells that appear to be undergoing apoptosis. In addition, we observe some seminiferous tubules that have round spermatids, but no sperm. These data indicate that some of the *Kdm1a* mutant germ cells that

progress through meiosis may still be defective. Thus, there may also be a requirement for KDM1A post-meiotically.

In order to determine why KDM1A is required for spermatogonial differentiation, we investigated two alternative mechanisms. First, based on the similarity of the *Kdm1a* mutant phenotype to *Dnmt3l* and *Miwi2* mutants, we considered the possibility that the observed *Kdm1a* defects are due to meiotic catastrophe caused by the reactivation of retrotransposons. However, we do not detect any defect in the repression of *Line1* or *IAP* retrotransposons. Thus we conclude that the *Kdm1a* phenotype is distinct from *Dnmt3l* and *Miwi2* mutants. This could be because DNMT3L and MIWI2 may act earlier in the germline, before the activation of *Vasa-Cre*. In this case, our experiments could not determine whether KDM1A might also act on retrotransposons earlier. Nevertheless, the similarity between the phenotypic effects in these mutants, hints that they could share a common spermatogenesis checkpoint.

The second potential mechanism that we investigated in our mutants is the failure to repress stem cell gene transcription. If KDM1A is required to repress critical spermatogonia genes during spermatogenesis, then we might expect these genes to be ectopically expressed in *Kdm1a* mutants. In $Kdm1a^{Cagg}$ mutants, we find that OCT4 protein is maintained in meiotic spermatocyte-like and post-meiotic spermatid-like germ cells. This suggests that KDM1A is required for the repression *Oct4* during spermatogenesis. Consistent with this, we find that KDM1A binds directly to the *Oct4* locus and loss of KDM1A leads to an increase in H3K4me2 at *Oct4.* Based on these data, along with similar expression defects that are observed during differentiation in other stem cell populations (2, 3), it is possible that KDM1A may enable spermatogonial differentiation by repressing the expression of critical genes associated with the undifferentiated cell fate.

The data presented here, as well as in Lambrot *et al.* (23), establish clearly that KDM1A has a critical function during the first wave of spermatogenesis, in the maintenance and differentiation of spermatogonia. In addition, we show here that KDM1A has an ongoing function in adult spermatogenesis, repressing the expression of *Oct4*, enabling meiotic progression and preventing germ cell loss. Taken together, these results demonstrate that KDM1A is an important regulator of spermatogenesis.

A5. Materials and Methods

A5.1 Ethics Statement

All animal procedures were performed in accordance with the regulations of the NIH Office of Laboratory Animal Welfare and were approved by the Emory University Institutional Animal Care and Use Committee (DAR-2003573-092319N).

A5.2 Mice

Mice were housed in a specific pathogen free facility in individually ventilated cages. Mice were given water and diet *ad libitum*. The facility is accredited by the American Association for the Accreditation of Laboratory Animal Care (AAALAC). Mice were monitored daily by members of the laboratory and by animal health technicians. Prior to the experimental endpoint, the mice experienced minimal pain or stress during routine handling and tail biopsies. No animals became ill or died prior to the experimental endpoint. Animals at the experimental endpoint were euthanized by CO_2 inhalation.

A5.3 Generation of KDM1A conditional mutant mice

Generation of the *Kdm1a*$^{flox/+}$ and *Kdm1a*$^{-/-}$ alleles was performed by mating *Kdm1a*$^{flox/flox}$ (14) and *Vasa cre*$^{+/+}$ (25) animals. The resulting *Kdm1a*$^{flox/+}$*;Vasa-cre*$^{+/-}$ males were again mated to

Vasa-cre$^{+/+}$ females and F2 *Kdm1a*$^{flox/+}$ *Vasa cre*$^{+/-}$ males acquired from this cross were mated to *Kdm1a*$^{flox/flox}$ females to produce *Kdm1a*$^{-/-}$ mutant animals. Primers used for genotyping were: *Kdm1a* floxed (F: 5'-CTCTGTAGCTGTCGAGCTGCTG, R: 5'-GAGGATGGCTCACATTGGTAC), *Kdm1a* deleted (F: 5'-GAACTCCACAGTCATTGATACC, R: 5'-GAGGATGGCTCACATTGGTAC) and Cre (F: 5'-GAACCTGATGGACATGTTCAGG, R: 5'-AGTGCGTTCGAACGCTAGAGCCTGT). Generation of the inducibly deleted alleles was performed by mating *Kdm1a*$^{flox/flox}$ (14) and *Cagg-cre*$^{+/+}$ (26) animals. *Kdm1a*$^{flox/+}$ *Cagg-cre*$^{+/-}$ animals were intercrossed to generate *Kdm1a*$^{flox/flox}$ *Cagg-cre*$^{+/-}$ animals. 10mg/ml tamoxifen (Sigma) in corn oil was administered by intraperitoneal injection at 75mg/kg. Animals were injected once a day on days 1,2,4,5 and 7 (5 times total). Controls were *Kdm1a*$^{flox/flox}$ *Cagg-cre*$^{-/-}$ animals and were injected on the same schedule. In most cases, controls were littermates. In the case that a littermate control was not available an age-matched *Kdm1a*$^{flox/flox}$ *Cagg-cre*$^{-/-}$ control was used.

A5.4 Histological Methods

For immunofluorescence, testes were fixed for 1-3 hours at 4°C in 4% paraformaldehyde, followed by a 2 hour PBS wash and then transferred to 30% sucrose overnight at 4°C. The tissue was then embedded in O.C.T. compound (Tissue-Tek) and stored at -80°C. 10µm sections were incubated with primary antibody in wash solution (1% heat-inactivated goat serum, 0.5% triton X-100 in PBS) overnight at 4°C in a humidified chamber. Slides were incubated in secondary antibody (1:500 in wash solution) at room temperature for 2 hours in humidified chamber. KDM1A polyclonal Abcam ab17721, SOX9 polyclonal Millipore ab5535, SYCP-1 polyclonal Abcam ab15090, OCT4 monoclonal BD Transduction Laboratories 611202: Fig 5, OCT4 polyclonal Abcam ab19847: Figs 2 and 3, PLZF monoclonal Santa Cruz sc-28319: Fig 5,

CLEAVED CASPASE-3 polyclonal Cell Signaling Technology 9661, Alexa Fluor 488 goat-α mouse IgG and, Alexa Fluor 594 goat-α rabibit IgG, Invitrogen.

For histology and immunohistochemistry**,** testes were fixed in Bouin's solution overnight, dehydrated in ethanol and xylenes and embedded in paraffin. For histology, 10µm sections were stained with Hematoxylin and Eosin. For immunohistochemistry, antigen retrieval was performed using a microwave in 0.01M Citrate then remaining steps were carried out per manufacturer's instructions using the VECTASTAIN Elite ABC kit (Vector PK6101). Primary antibodies were diluted in Tris-Cl pH 7.5 with 1% BSA and 0.1% Brij. DAB solution was prepared per manufacturer's instructions (Vector SK4110) and developed to desired darkness. Slides were then counterstained with hematoxylin (Genetex GTX7334). SOX9 polyclonal Millipore AB5535, PLZF polyclonal Santa Cruz SC22839, KIT polyclonal R&D Systems AF1356. Quantification was performed manually by counting the number of positive cells within seminiferous tubules. Greater than 30 seminiferous tubules per section were analyzed and at least n= 2 animals in all experiments. Statistical analysis was performed using Mann-Whitney U test ($p < .05$).

A5.5 TUNEL Assay

TUNEL assays were performed on 10µm frozen sections, per the manufacturer's specifications (Roche In situ cell death detection kit, Fluorescein).

A5.6 In Situ Hybridization

DIG-labeled in situ hybridization was performed on frozen sections as previously described (35). Line1 and IAP probes are from Bourc'his et al. (30).

A5.7 Bisulfite Analysis

Whole testes were digested overnight with Proteinase K in 37° water bath followed by phenol extraction and ethanol precipitation to isolate genomic DNA. Bisulfite conversion was performed with the Zymo EZ DNA Methylation kit, per the manufacturer's specifications. Bisulfite converted genomic DNA was amplified by PCR and individual TA cloned PCR products were sequenced. Primers: IAP (F: 5'-TTGATAGTTGTGTTTTAAGTGGTAAATAAA, R: 5'-AAAACACCACAAACCAAAATCTTCTAC) and LINE1 (F: 5' GTTAGAGAATTTGATAGTTTTTGGAATAGG, R: 5'-CCAAAACAAAACCTTTCTCAAACACTATAT). Methylation analysis was performed using BiQ Analyzer software (36).

A5.8 Chromatin Immunoprecipitation

Whole testes were homogenized in 2-10ml of phosphate-buffered saline with 1% formaldehyde and protease inhibitors (Roche Diagnostics). For adult testes both testes from a single adult animal were used. For neonatal testes, testes were pooled from 3-6 animals. The tissue was homogenized using 10 strokes in a dounce homogenizer and incubated for 10 minutes at room temperature. The cross-linking reaction was terminated by the addition of glycine [final 0.125M]. The samples were centrifuged for 2 minutes at 2000rpm and washed three times with 2-10ml cold PBS with protease inhibitors. After the last wash the pellet was resuspended in 400ul of lysis buffer from the Millipore ChIP assay kit (Millipore) with protease inhibitors. The samples were sonicated for 30minutes (45 second pulse, 15 seconds off on high setting) at 4°C using a Diagenode Bioruptor UCD-200, then centrifuged for 10 minutes at 13,000rpm at 4°C. The supernatant was split equally into two-2ml eppendorf tubes, for immunoprecipitation and for no antibody control. Each sample was diluted to 2ml total volume of ChIP dilution buffer and

immunoprecipitation was carried out on 1.5ml, per the manufacturer's instructions using 10µg of either KDM1A antibody (KDM1A polyclonal Abcam ab17721) or H3K4me2 antibody (H3K4me2 monoclonal Millipore 05-1338). The remaining 500µl was used for an input sample. Precipitated DNA was analyzed using quantitative PCR on a Bio-Rad CFX96 Real-Time PCR machine. Primers: *Oct4* promoter (F: 5'-CTGTAAGGACAGGCCGAGAG, R: 5'-CAGGAGGCCTTCATTTTCAA), *Oct4* proximal enhancer (F: 5'-TCAGGGTAGGCTCTCTGCAC, R: 5'-TCCCCTCACACAAGACTTCC) and *Oct4* distal enhancer (F: 5'-TGAACTGTGGTGGAGAGTGC, R: 5'-GCCAAGTTCACAAAGCTTCC).

A6. References

1. de Rooij DG. Proliferation and differentiation of spermatogonial stem cells. Reproduction. 2001;121(3):347-54.
2. Kerenyi MA, Shao Z, Hsu YJ, Guo G, Luc S, O'Brien K, et al. Histone demethylase Lsd1 represses hematopoietic stem and progenitor cell signatures during blood cell maturation. Elife. 2013;2:e00633.
3. Whyte WA, Bilodeau S, Orlando DA, Hoke HA, Frampton GM, Foster CT, et al. Enhancer decommissioning by LSD1 during embryonic stem cell differentiation. Nature. 2012;482(7384):221-5.
4. Zhu D, Holz S, Metzger E, Pavlovic M, Jandausch A, Jilg C, et al. Lysine-specific demethylase 1 regulates differentiation onset and migration of trophoblast stem cells. Nat Commun. 2014;5:3174.
5. Jan SZ, Hamer G, Repping S, de Rooij DG, van Pelt AM, Vormer TL. Molecular control of rodent spermatogenesis. Biochim Biophys Acta. 2012;1822(12):1838-50.
6. Ng HH, Robert F, Young RA, Struhl K. Targeted recruitment of Set1 histone methylase by elongating Pol II provides a localized mark and memory of recent transcriptional activity. Mol Cell. 2003;11(3):709-19.
7. Mito Y, Henikoff JG, Henikoff S. Genome-scale profiling of histone H3.3 replacement patterns. Nature genetics. 2005;37(10):1090-7.
8. Martin C, Zhang Y. The diverse functions of histone lysine methylation. Nat Rev Mol Cell Biol. 2005;6(11):838-49.
9. Muramoto T, Muller I, Thomas G, Melvin A, Chubb JR. Methylation of H3K4 Is required for inheritance of active transcriptional states. Curr Biol.20(5):397-406.
10. You A, Tong JK, Grozinger CM, Schreiber SL. CoREST is an integral component of the CoREST- human histone deacetylase complex. Proc Natl Acad Sci U S A. 2001;98(4):1454-8.
11. Shi Y, Lan F, Matson C, Mulligan P, Whetstine JR, Cole PA, et al. Histone demethylation mediated by the nuclear amine oxidase homolog LSD1. Cell. 2004;119(7):941-53.
12. Zhang J, Bonasio R, Strino F, Kluger Y, Holloway JK, Modzelewski AJ, et al. SFMBT1 functions with LSD1 to regulate expression of canonical histone genes and chromatin-related factors. Genes & development. 2013;27(7):749-66.
13. Metzger E, Wissmann M, Yin N, Muller JM, Schneider R, Peters AH, et al. LSD1 demethylates repressive histone marks to promote androgen-receptor-dependent transcription. Nature. 2005;437(7057):436-9.
14. Wang J, Scully K, Zhu X, Cai L, Zhang J, Prefontaine GG, et al. Opposing LSD1 complexes function in developmental gene activation and repression programmes. Nature. 2007;446(7138):882-7.
15. Wang J, Hevi S, Kurash JK, Lei H, Gay F, Bajko J, et al. The lysine demethylase LSD1 (KDM1) is required for maintenance of global DNA methylation. Nature genetics. 2009;41(1):125-9.
16. Su ST, Ying HY, Chiu YK, Lin FR, Chen MY, Lin KI. Involvement of histone demethylase LSD1 in Blimp-1-mediated gene repression during plasma cell differentiation. Mol Cell Biol. 2009;29(6):1421-31.

17. Saleque S, Kim J, Rooke HM, Orkin SH. Epigenetic regulation of hematopoietic differentiation by Gfi-1 and Gfi-1b is mediated by the cofactors CoREST and LSD1. Molecular cell. 2007;27(4):562-72.
18. Musri MM, Carmona MC, Hanzu FA, Kaliman P, Gomis R, Parrizas M. Histone demethylase LSD1 regulates adipogenesis. J Biol Chem. 2010;285(39):30034-41.
19. Choi J, Jang H, Kim H, Kim ST, Cho EJ, Youn HD. Histone demethylase LSD1 is required to induce skeletal muscle differentiation by regulating myogenic factors. Biochem Biophys Res Commun. 2010;401(3):327-32.
20. Macfarlan TS, Gifford WD, Agarwal S, Driscoll S, Lettieri K, Wang J, et al. Endogenous retroviruses and neighboring genes are coordinately repressed by LSD1/KDM1A. Genes Dev. 2011;25(6):594-607.
21. Dann CT, Alvarado AL, Molyneux LA, Denard BS, Garbers DL, Porteus MH. Spermatogonial stem cell self-renewal requires OCT4, a factor downregulated during retinoic acid-induced differentiation. Stem Cells. 2008;26(11):2928-37.
22. Godmann M, May E, Kimmins S. Epigenetic mechanisms regulate stem cell expressed genes Pou5f1 and Gfra1 in a male germ cell line. PLoS One. 2010;5(9):e12727.
23. Lambrot R, Lafleur C, Kimmins S. The histone demethylase KDM1A is essential for the maintenance and differentiation of spermatogonial stem cells and progenitors. FASEB J. 2015.
24. Godmann M, Auger V, Ferraroni-Aguiar V, Di Sauro A, Sette C, Behr R, et al. Dynamic regulation of histone H3 methylation at lysine 4 in mammalian spermatogenesis. Biol Reprod. 2007;77(5):754-64.
25. Gallardo T, Shirley L, John GB, Castrillon DH. Generation of a germ cell-specific mouse transgenic Cre line, Vasa-Cre. Genesis. 2007;45(6):413-7.
26. Hayashi S, McMahon AP. Efficient recombination in diverse tissues by a tamoxifen-inducible form of Cre: a tool for temporally regulated gene activation/inactivation in the mouse. Dev Biol. 2002;244(2):305-18.
27. Bowles J, Koopman P. Retinoic acid, meiosis and germ cell fate in mammals. Development. 2007;134(19):3401-11.
28. Sada A, Suzuki A, Suzuki H, Saga Y. The RNA-binding protein NANOS2 is required to maintain murine spermatogonial stem cells. Science. 2009;325(5946):1394-8.
29. Carmell MA, Girard A, van de Kant HJ, Bourc'his D, Bestor TH, de Rooij DG, et al. MIWI2 is essential for spermatogenesis and repression of transposons in the mouse male germline. Dev Cell. 2007;12(4):503-14.
30. Bourc'his D, Bestor TH. Meiotic catastrophe and retrotransposon reactivation in male germ cells lacking Dnmt3L. Nature. 2004;431(7004):96-9.
31. Bourc'his D, Xu GL, Lin CS, Bollman B, Bestor TH. Dnmt3L and the establishment of maternal genomic imprints. Science. 2001;294(5551):2536-9.
32. Soper SF, van der Heijden GW, Hardiman TC, Goodheart M, Martin SL, de Boer P, et al. Mouse maelstrom, a component of nuage, is essential for spermatogenesis and transposon repression in meiosis. Developmental cell. 2008;15(2):285-97.
33. Brown JP, Bullwinkel J, Baron-Luhr B, Billur M, Schneider P, Winking H, et al. Correction: HP1gamma function is required for male germ cell survival and spermatogenesis. Epigenetics & chromatin. 2012;5(1):18.
34. Russell LD, Ren HP, Sinha Hikim I, Schulze W, Sinha Hikim AP. A comparative study in twelve mammalian species of volume densities, volumes, and numerical densities

of selected testis components, emphasizing those related to the Sertoli cell. The American journal of anatomy. 1990;188(1):21-30.
35. Schaeren-Wiemers N, Gerfin-Moser A. A single protocol to detect transcripts of various types and expression levels in neural tissue and cultured cells: in situ hybridization using digoxigenin-labelled cRNA probes. Histochemistry. 1993;100(6):431-40.
36. Bock C, Reither S, Mikeska T, Paulsen M, Walter J, Lengauer T. BiQ Analyzer: visualization and quality control for DNA methylation data from bisulfite sequencing. Bioinformatics. 2005;21(21):4067-8.

A7. Acknowledgements

We would like to thank D. Bourc'His for providing the *in situ* probes; D. Cutler for assistance in mapping the bisulfite clones; and B. Kelly, B. Shur, C. Easley, C. Bean, T. Caspary and members of the Katz lab for helpful discussions on the work and the manuscript. Thank you to M. Rosenfeld for providing the $Lsd1^{fl/fl}$ mice and D. Castrillon for providing the *Vasa-Cre* mice.

A8. Figures and Tables

Fig 1. Expression of KDM1A in the testis.

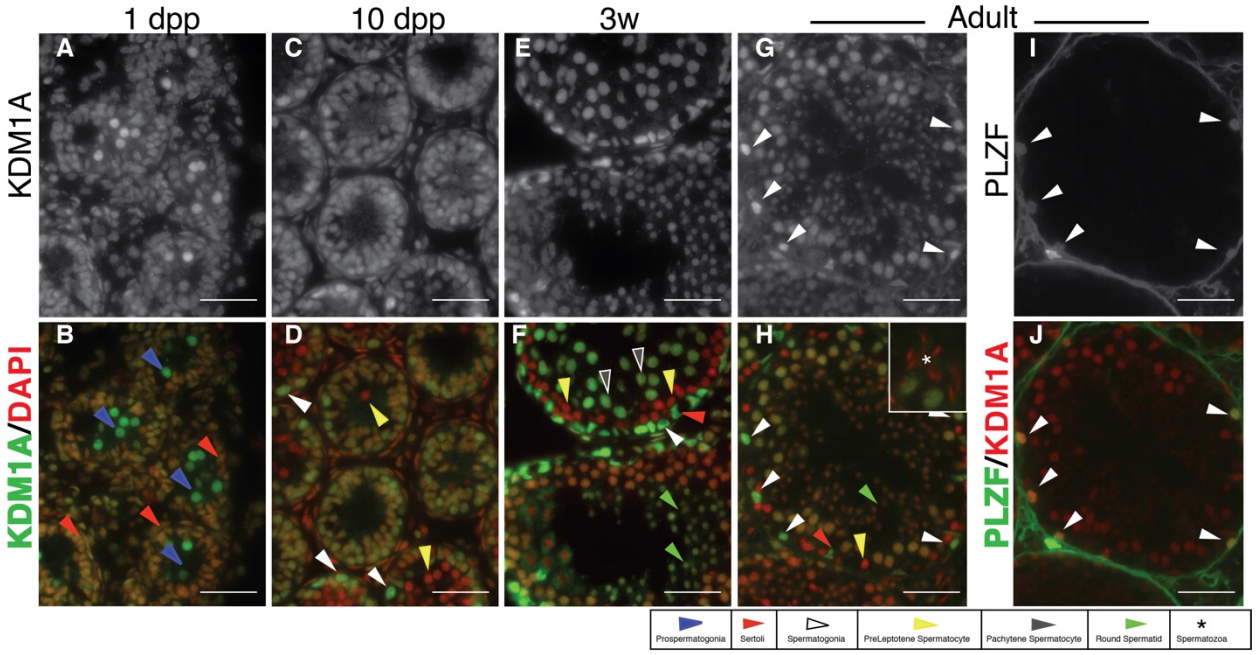

Fig 1. Expression of KDM1A in the testis.

KDM1A (A,C,E,G), PLZF (I) and combined DAPI (red) and KDM1A (green) (B,D,F,H) immunofluorescence from wild-type testes. (J) Combined PLZF (green) and KDM1A (red) IF. Asterisk in magnified inset (H) indicates mature spermatozoa. White arrowheads in (I,J) indicate spermatogonia marked by PLZF. The expression of KDM1A in these same PLZF+ spermatogonia is shown in G,H (white arrowheads). In all other panels, spermatogenic cell types are labeled as described in legend (dpp= days post partum). Cell types were identified based on morphology and location within the testicular cord or seminiferous tubule. Scale bars, 25 μm.

Fig 2. Spermatogonia differentiation and maintenance defect in *Kdm1a*^{Vasa} mutants.

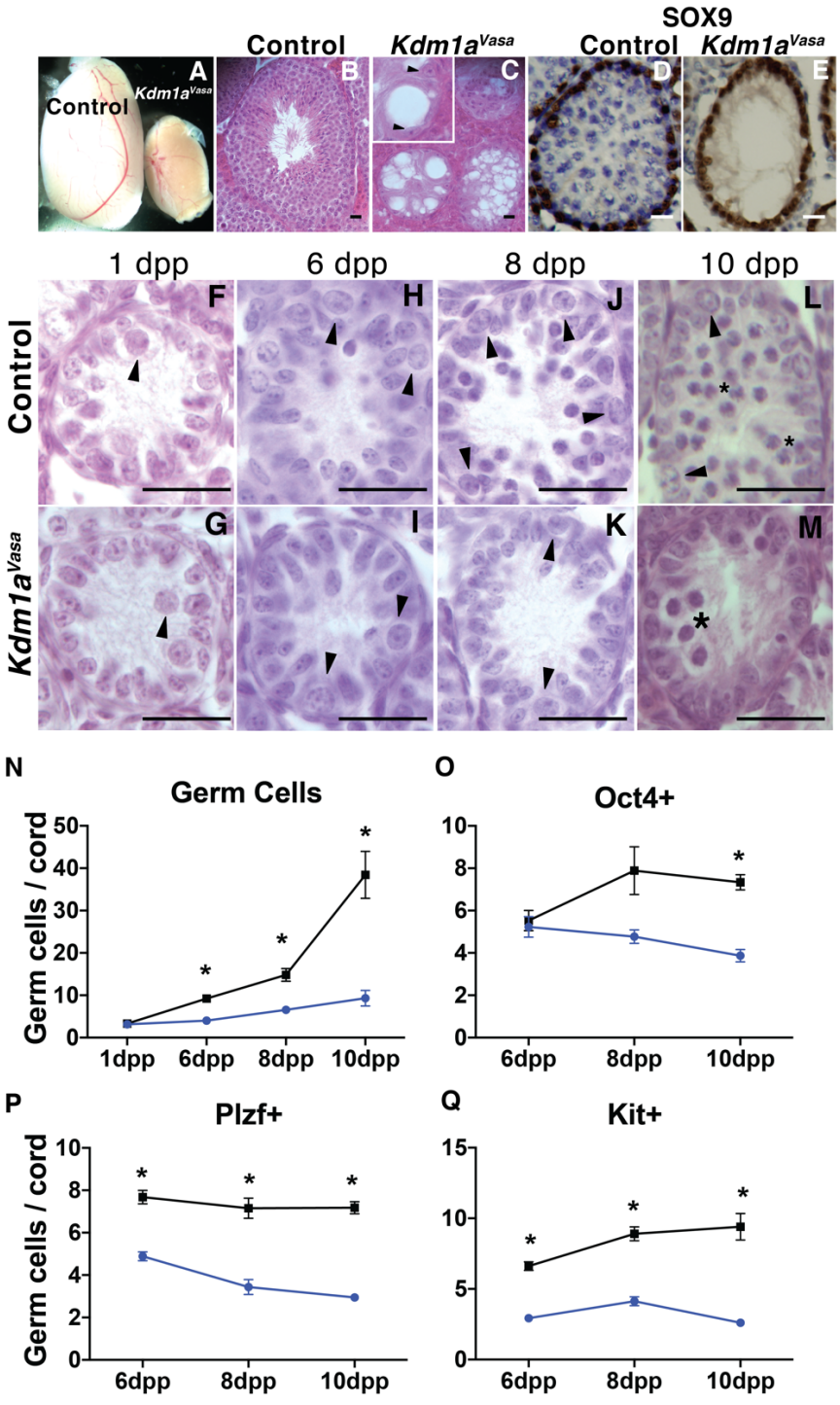

Fig 2. Spermatogonia differentiation and maintenance defect in *Kdm1a*^{Vasa} mutants.

(A) Representative images of control and *Kdm1a*^{Vasa} mutant adult testes. Histology from control (B) and *Kdm1a*^{Vasa} (C) adult testes. Arrowheads indicate Sertoli cells (C). SOX9 immunohistochemistry (brown) counterstained with hematoxylin (blue) from control (D) and *Kdm1a*^{Vasa} (E) testes at 21days post partum (dpp). Histology from control (F,H,J,L) and *Kdm1a*^{Vasa} testes (G,I,K,M) at 1dpp (F,G), 6dpp (H,I), 8dpp (J,K) and 10dpp (L,M). Arrowheads indicate spermatogonia (F-L), and asterisk indicates spermatocytes (L) and abnormal spermatocytes (M). (N) Germ cells per testis cord quantified from histology (F,G) at 1dpp, and SOX9 immunofluorescence (S2 Fig) at 6dpp, 8dpp and 10dpp (the adult testis size was not quantified). Quantification of OCT4+ (O), PLZF+ (P) and KIT+ (Q) germ cells per cord from immunofluorescence (S1 Fig) (n=>30 testis cords counted from multiple animals, Mann-Whitney U test, $p<.001$). (N-Q) The control is shown in black and Kdm1a^{Vasa} is shown in blue. Scale bars, 25 μm.

Fig 3. Germ cell apoptosis in *Kdm1a*^{Vasa} mutants.

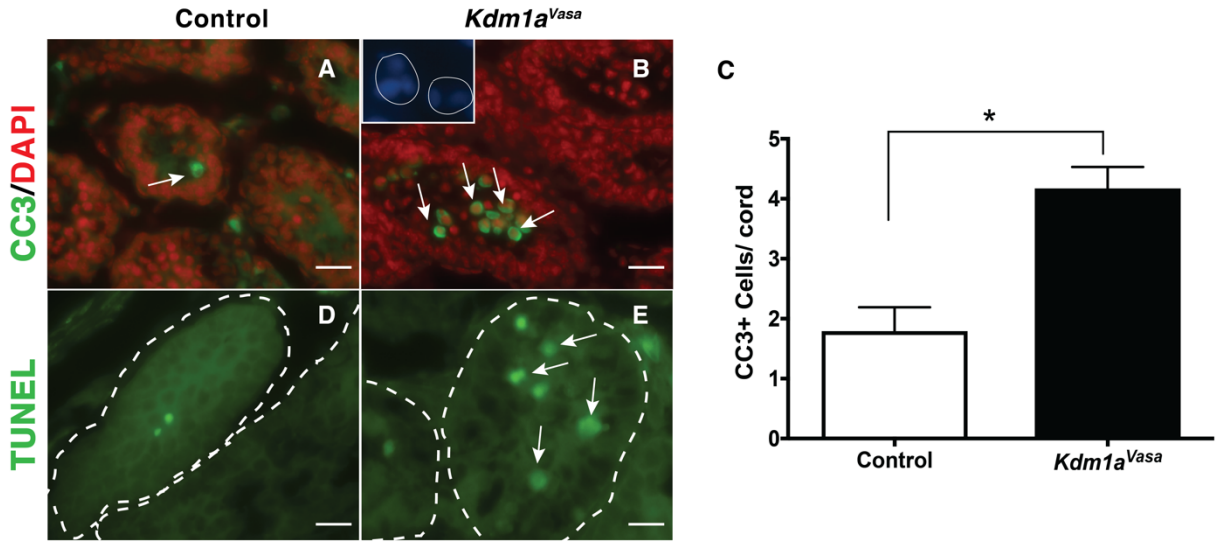

Fig 3. Germ cell apoptosis in *Kdm1a*^{Vasa} mutants.

Quantification of Cleaved Caspase-3 (CC3) positive germ cells per testicular cord (C) from control (A) and *Kdm1a*^{Vasa} (B) testes (n=>30 testis cords counted from multiple animals), Mann-Whitney U test, p<.001). Arrows (A,B) indicate CC3 positive nuclei. Magnified inset (B) shows fragmented DNA in germ cells from a different Kdm1a^{Vasa} testis (DAPI: blue). TUNEL (green) from control (D) and *Kdm1a*^{Vasa} mutants (E) at 10dpp. Testicular cord boundaries are indicated by dashed lines. Scale bars, 25 μm.

Fig 4. Germ cell maintenance and meiotic defects in *Kdm1a*^{Cagg} adult testes.

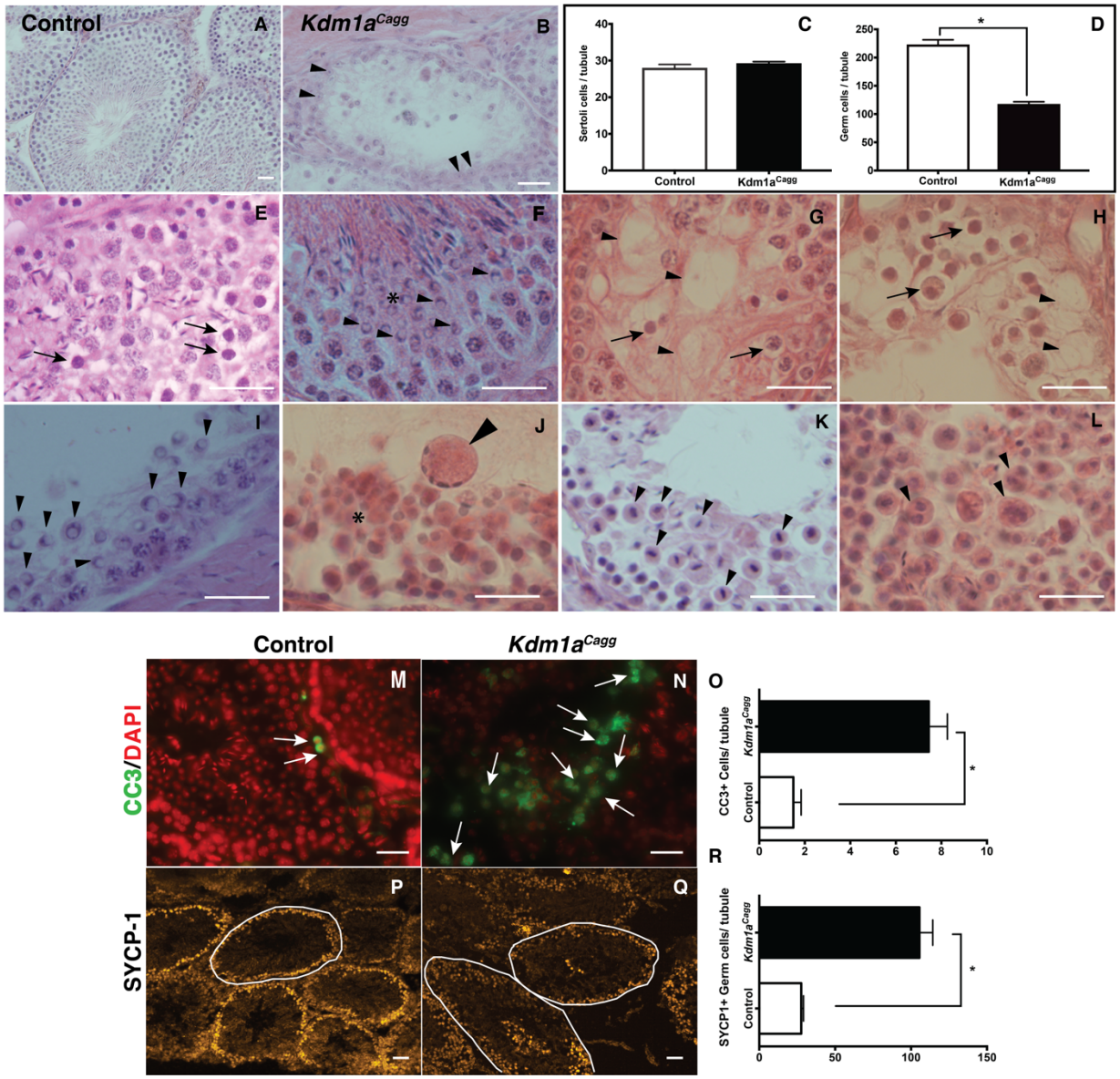

Fig 4. Germ cell maintenance and meiotic defects in *Kdm1a*^{Cagg} adult testes.

Histology from control (A) and *Kdm1a*^{Cagg} testes (B,E-L), 7-9 weeks after the last tamoxifen injection to *delete Kdm1a,* showing mostly Sertoli cells remaining (arrowheads in B), spematogonia-like cells near or in the lumen (arrows in E), seminiferous tubule lacking a lumen (E,L), abnormally clumped germ cells (asterisk in F,J), abnormal spacing around cells (arrow in G,H) with vacuoles interspersed (arrowheads in G,H), germ cells with crescent shaped apoptotic morphology (arrowheads in F,I), giant spermatocyte-like apoptotic cells (arrowhead in J), chromosomal abnormalities (arrowheads in K), and multi-nucleated germ cells (arrowheads in L). Quantification of SOX9+ Sertoli cells (C) and germ cells per seminiferous tubule (D) in control and *Kdm1a*^{Cagg} testis (n=3, controls and n=4, *Kdm1a*^{Cagg} mutants, >25 seminiferous tubules per animal, Mann-Whitney U test, $p<.05$). Apoptosis marker CLEAVED CASPASE-3 (CC3)(green) merged with DAPI (red) (M,N) and meiotic marker SYCP-1 (yellow) (P,Q) and from control (M,P) and *Kdm1a*^{Cagg} mutants (N,Q). Quantification of the CC3 (O) and SYCP-1 (R) immunofluorescence (n= >30 seminiferous tubules counted from multiple animals, Mann-Whitney U test, $p<.05$). Scale bars, 25 μm.

Fig 5. KDM1A and H3K4me2 chromatin immunoprecipitation at *Oct4*.

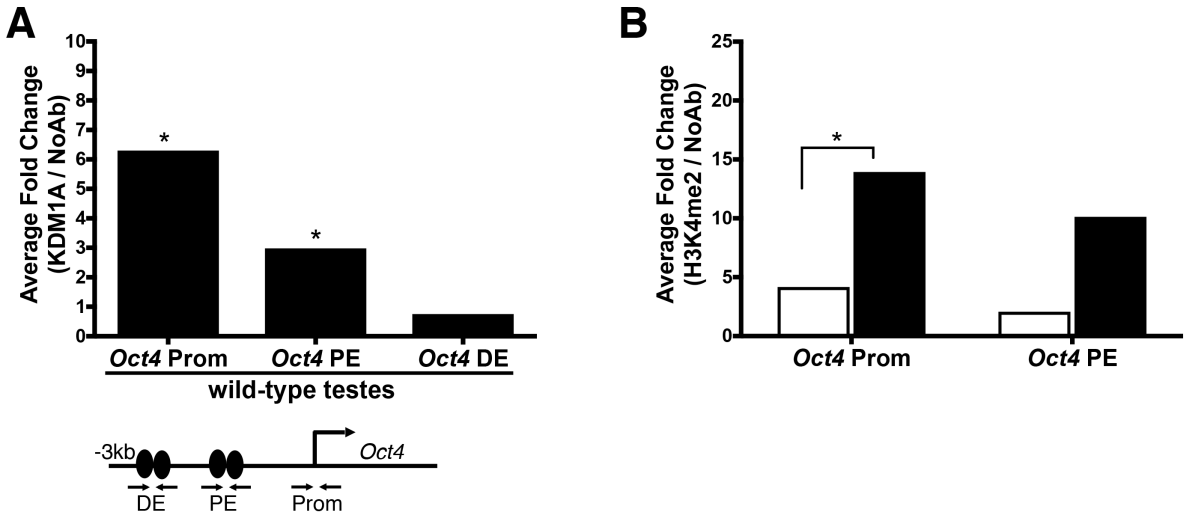

Fig 5. KDM1A and H3K4me2 chromatin immunoprecipitation at *Oct4*.

Average fold enrichment (KDM1A/no Ab) from chromatin immunoprecipitation (ChIP) at *Oct4* in wild-type adult testes calculated from S4 Fig A (n=2, Unpaired t-test, $p<.05$). (B) Average fold enrichment (H3K4me2/no Ab) from ChIP at *Oct4* in $Kdm1a^{Vasa}$ (black) and control (white) testes calculated from S4 Fig C (n= 3 animals, Unpaired t-test, $p<.05$). The location of the *Oct4* promoter (prom) primers and the *Oct4* distal (DE) and proximal enhancer (PE) primers are shown below panel A.

Fig 6. Ectopic expression of spermatogonia genes in *Kdm1a*^{Cagg} testes.

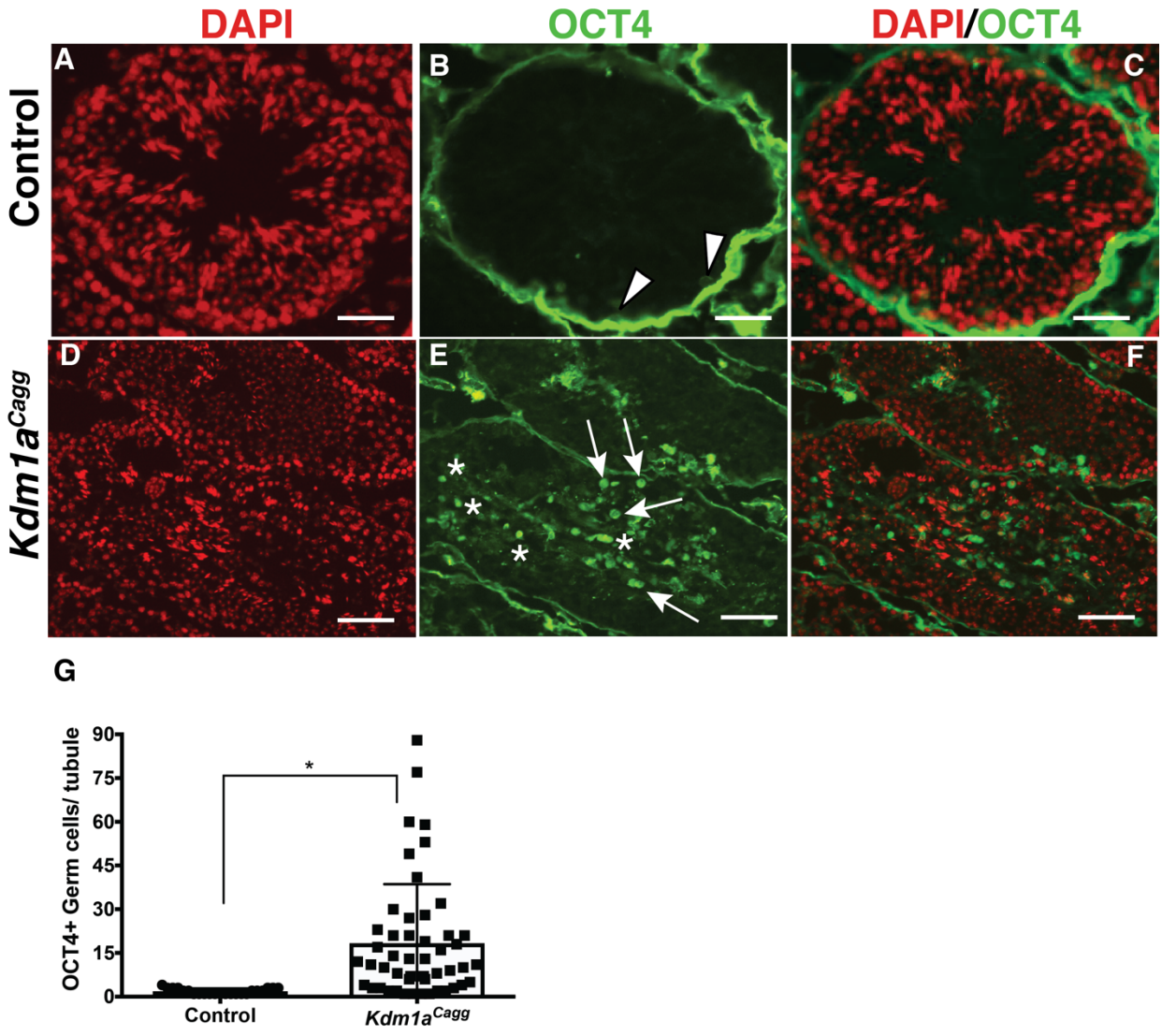

Fig 6. Ectopic expression of spermatogonia genes in *Kdm1a*^{Cagg} testes.

DAPI (A,D), OCT4 (B,E), and combined (C,F) immunofluorescence from wild-type (A-C) and *Kdm1a*^{Cagg} testes (D-F). Arrowheads in (B) indicate spermatogonia marked by OCT4, whereas arrows in (E) indicate OCT4 protein in spermatocyte-like cells. Asterisk (E) indicates OCT4 protein in post-meiotic spermatid-like cells. Quantification of the OCT4 (G) ectopic protein phenotype (n=>50 tubules counted from multiple animals, Mann-Whitney U test, p<.001). Scale bars, 25 μm.

S1 Fig. Germ Cell Markers in *Kdm1a*^{Vasa} mutants.

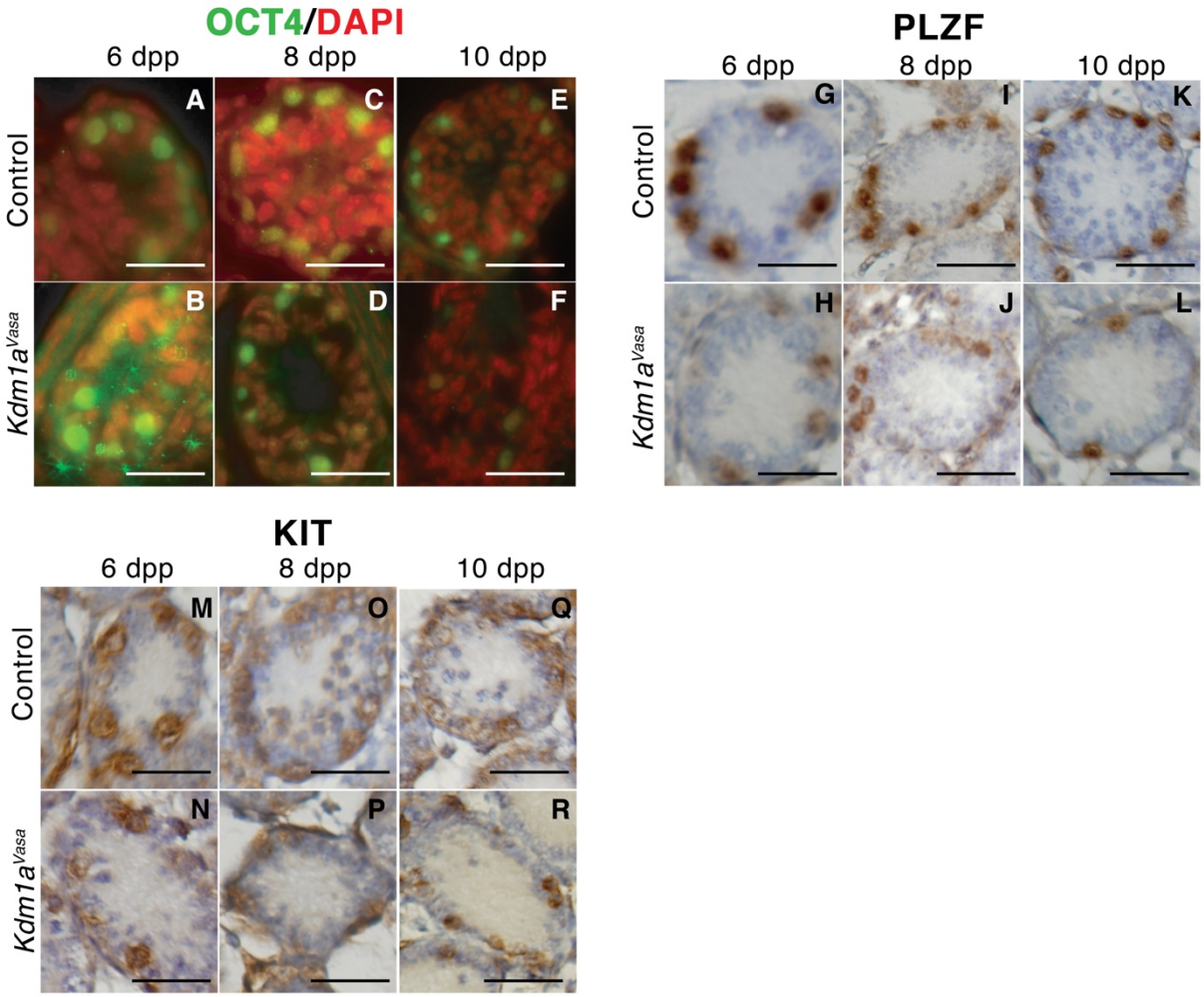

S1 Fig. Germ Cell Markers in *Kdm1a*^{Vasa} mutants

OCT4+ (A-F), PLZF+ (G-L) and KIT+ (M-R) germ cells from control (A,C,E,G,I,K,M,O,Q) and *Kdm1a*^{Vasa} (B,D,F,H,J,L,N,P,R) testes at 6 days post partum (dpp)(A,B,G,H,M,N), 8dpp (C,D,I,J,O,P) and 10dpp (E,F,K,L,Q,R). Images correspond to the quantification in Fig 2. Scale bars, 25 μm.

S2 Fig. Germ cells in *Kdm1a*^{Vasa} mutants.

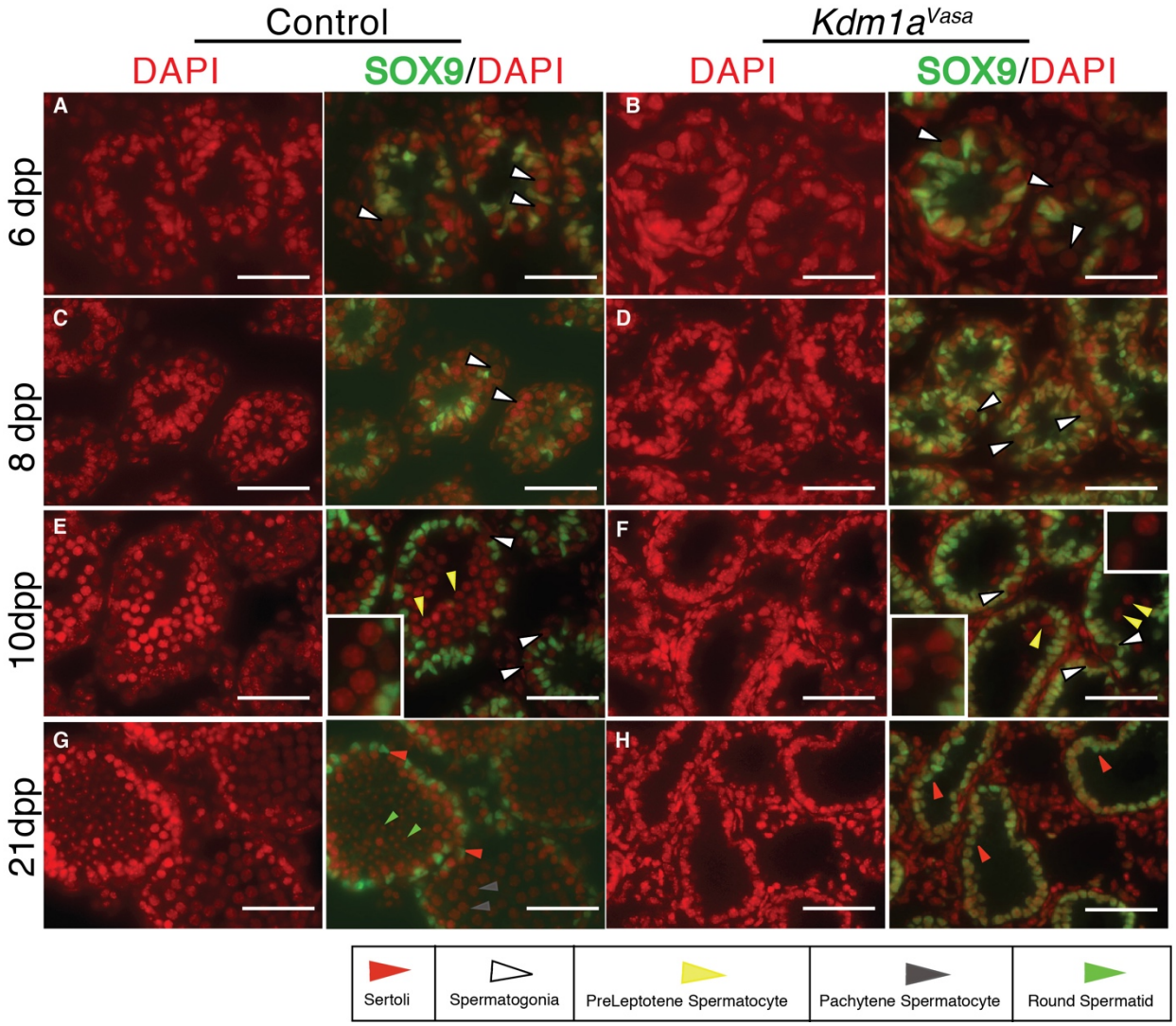

S2 Fig. Germ cells in *Kdm1a*^{Vasa} mutants.

DAPI (red), and merged (DAPI: red, SOX9: green) from control (A,C,E,G) and *Kdm1a*^{Vasa} (B,D,F,H) testes at 6dpp (A,B), 8dpp (C,D), 10dpp (E,F) and 21dpp (G,H) showing germ cells (absence of SOX9). Insets indicate normal spermatocytes (E) and spermatocytes with abnormal morphology (F). Spermatogenic cell types are labeled as described in legend (dpp= days post partum). Scale bars, 25 μm.

S3 Fig. Retrotransposon expression and DNA methylation in *Kdm1a* mutants.

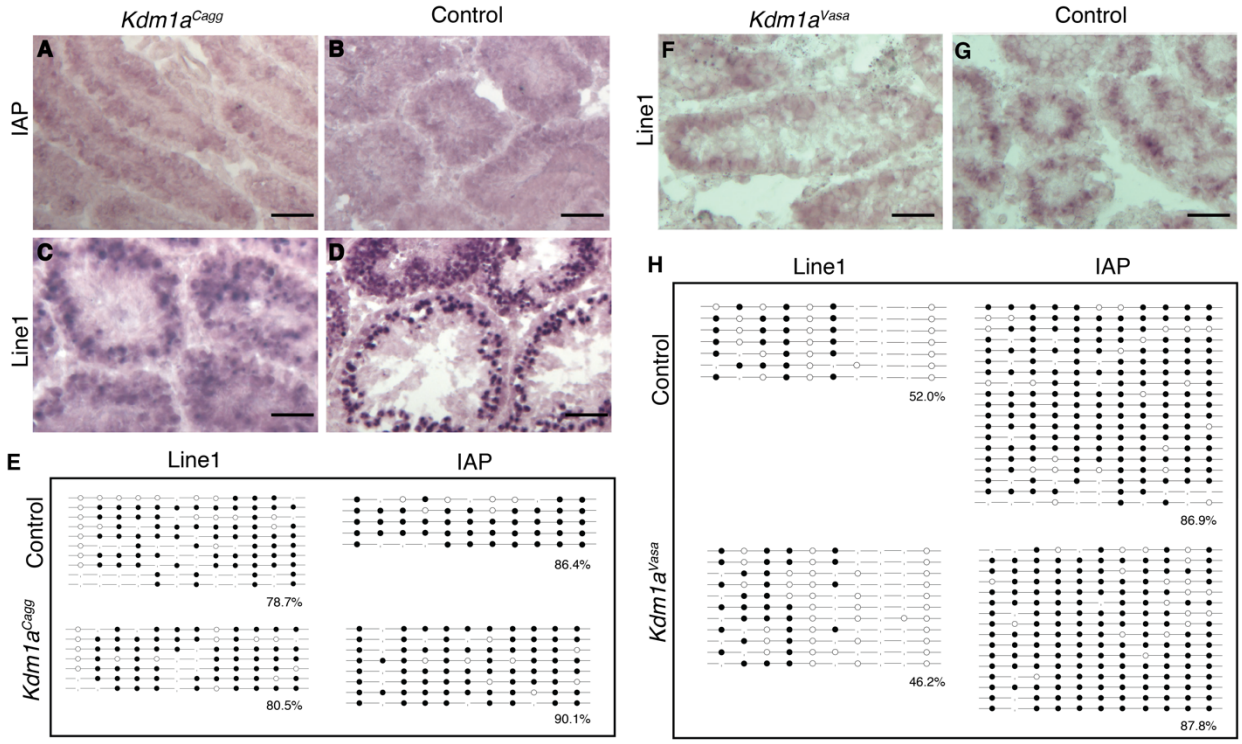

S3 Fig. Retrotransposon expression and DNA methylation in *Kdm1a* mutants.

IAP (A,B) and *Line1* (C,D,F,G) in situ (dark purple) hybridization on adult $Kdm1a^{Cagg}$ (A,C), adult control (B,D), $Kdm1a^{Vasa}$ 10dpp (F) and control 10dpp (G) testes. Bisulfite analysis at the *Line1* and *IAP* locus in adult $Kdm1a^{Cagg}$ (E) and $Kdm1a^{Vasa}$ (H) 10dpp testes versus controls. Circles represent CpG dinucleotides. Filled in circles indicate methylated CpG's. Hash marks indicate CpG's not assayed due to sequence alignment. Each row represents an individually TA cloned bisulfite PCR product (E,H). Percentage of CpG methylation at *IAP* and *Line1* in $Kdm1a^{Cagg}$ (E) and $Kdm1a^{Vasa}$ (H) testis versus controls is indicated below each diagram. Each methylation analysis was performed on one mutant versus one control. Individual *Line1* and *IAP* clones likely contain different number of CpG residues due to amplification from multiple loci in the genome. Scale bars, 25 μm.

S4 Fig. KDM1A and H3K4me2 chromatin immunoprecipitation.

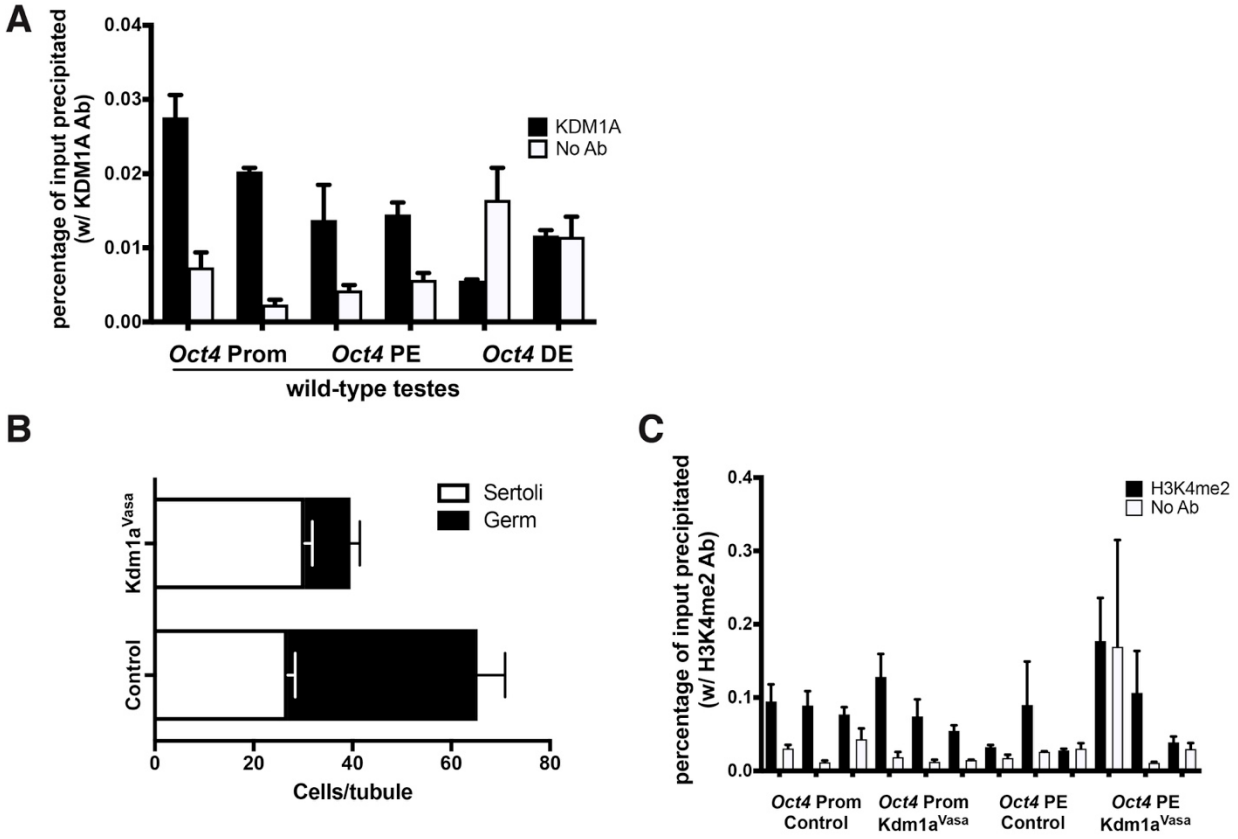

S4 Fig. KDM1A and H3K4me2 chromatin immunoprecipitation.

Chromatin immunoprecipitation (ChIP) at *Oct4* (A) showing the percentage input precipitated with a KDM1A antibody (Ab) (black bars) or no Ab (white bars) in wild-type adult testes (n=2). This data was used to calculate the average fold change in Fig 5A. Quantification of Sertoli cells and germ cells (B) in $Kdm1a^{Vasa}$ and control testes used for normalization of average fold enrichment in (Fig 5). ChIP at *Oct4* showing the percentage input precipitated with an H3K4me2 Ab (black bars) or no Ab (C) in control versus $Kdm1a^{Vasa}$ testes at the *Oct4* promoter (prom) and proximal enhancer (PE) (n=3). This data was used to calculate the average fold change in Fig 5B. Primer locations are the same as the KDM1A ChIP.